Understanding the chemical reactivity mechanism between the solid electrolyte and sintering aids to decrease the densification temperature of Li1+xAlxTi2-x(PO4)3

Morgan Guilleux

Sorbonne Université

ED 397 – Physique et Chimie des Matériaux

Laboratoire de Chimie de la Matière Condensée de Paris

Understanding the chemical reactivity mechanism between the solid electrolyte and sintering aids to decrease the densification temperature of $Li_{1+x}Al_xTi_{2-x}(PO_4)_3$

By Morgan Guilleux

PhD thesis in Material Chemistry

Directed by Arnaud Perez and Christel Laberty-Robert

Presented and defended on 21st October 2024 in front of the jury,

Dr. Vincent Seznec	Associate Professor, LRCS, UPJV	Referee
Prof. Cécile Pagnoux	Professor, IRCER, UL	Referee
Dr. Damien Dambournet	Associate Professor, PHENIX, SU	Examiner
Prof. Domitille Giaume	Professor, IRCP, PSL	President
Dr. Arnaud Perez	Associate Researcher, LCMCP, SU	Supervisor
Prof. Christel Laberty-Robert	Professor, LCMCP, SU	Director

A ma mère,

Remerciements

Je tiens tout d'abord à exprimer ma profonde gratitude à mon encadrant de thèse, Arnaud Perez, pour la confiance qu'il m'a accordée en me proposant ce sujet de thèse. Je le remercie également pour sa disponibilité, sa bienveillance, et tout l'enrichissement scientifique qu'il a su partager avec moi. Travailler à ses côtés a été un véritable plaisir et une expérience formatrice. Je souhaite également remercier chaleureusement Christel Laberty-Robert, ma directrice de thèse, pour les nombreuses discussions, tant scientifiques que personnelles, qui ont ponctué ces années. Sa gentillesse et sa rigueur ont été pour moi une source précieuse de motivation et d'inspiration.

Mes remerciements s'adressent aux membres du jury pour avoir accepté d'évaluer mon travail : à la présidente du jury Domitille Giaume ; aux rapporteurs Vincent Seznec et Cécile Pagnoux ; ainsi qu'à Damien Dambournet. Je suis reconnaissante pour leurs conseils avisés et les échanges enrichissants lors de la soutenance. Ces discussions ont été pour moi particulièrement stimulantes.

Je tiens à remercier les directeurs du LCMCP, Christian Bonhomme (alias Chef Suprême) et François Ribot pour leur accueil chaleureux et leur humour sans égal. Grâce à eux, le laboratoire bénéficie d'une ambiance aussi conviviale que dynamique ! Un immense merci à Diana et Corinne, ainsi qu'à Hélène, avec qui j'ai partagé d'innombrables fous rires. Ton rire communicatif, Hélène, restera gravé dans ma mémoire !

Je n'oublie pas les autres permanents d'RMES : Damien Bregiroux, avec qui j'ai eu la chance de collaborer, notamment autour de la SPS. Merci pour ces échanges passionnants entre céramistes ! Merci à Natacha Krins, dont la bonne humeur et la gentillesse sont contagieuses ! Je tiens également à remercier chaleureusement l'ensemble des non-permanents de l'équipe d'RMES, des plus anciens aux petits nouveaux : Agathe, Mimi, Ronan, Bastien, Adeline, Kethso(ce), Rémi (7b), Jamal, Navid, Eli, Elyes, Anna, Lydia, Romain, Antony, Margarita, Antonin, Kim et Alexis. Vous avez tous contribués à rendre ces années de thèses si riches, conviviales et surtout inoubliables.

Un immense merci aux permanents du laboratoire avec qui j'ai eu la chance de collaborer, notamment Christel, Cristina et Mohamed. Votre expertise, vos conseils et vos échanges ont été précieux et ont marqué mon parcours. Merci également à tous les autres permanents avec qui j'ai pu partager des discussions enrichissantes tout au long de ces années. Je tiens aussi à

remercier chaleureusement l’ensemble des non-permanents du laboratoire pour leur énergie et leur bonne humeur, qui ont largement contribué à rendre cette expérience aussi agréable qu’enrichissante. Une mention toute spéciale à Clara, Amandine, Alicia et Florence, qui sont devenues de véritables amies.

Un grand merci à mes amies de fac, Kiki, future docteure, et Mel, fraîchement docteure, pour votre soutien indéfectible et votre présence tout au long de ces trois années. Même si nous n’étions pas dans le même labo, votre amitié m’a donné la force d’avancer. Merci également à Greg !

Aux ami(e)s de Solvay, un immense merci pour vos conseils, votre patience et, surtout, votre bonne humeur : Ella ("Ella tempête"), Aymeric (de la team Digitale), le Babtiste (et son sac à dos), le X, Annabelle, et, bien sûr, ma petite Mo ! Vous avez donné vie à la "Fédération des motivées", qui n’aura jamais été aussi motivée ! Pensée émue à Sébastian.

Enfin, je tiens à remercier ma mère, à qui je dois tout. Les mots ne seront jamais suffisants pour exprimer toute ma gratitude envers toi. Même si tu n’as pas toujours compris exactement ce que je faisais, tu as toujours été là pour m’écouter, me soutenir et m’encourager, quoi qu’il arrive. Ton amour inconditionnel et ta présence ont été ma force tout au long de ce chemin. Merci d’avoir cru en moi, même dans les moments où j’avais du mal à y croire moi-même. Merci à mes deux amours, Mia et Livi qui ont été de véritables soutiens émotionnels depuis leur venue.

Table of contents

General introduction

The climate system is being disrupted by greenhouse gas emissions (carbon dioxide, methane, etc.) resulting from industrial advancements and human activities. Since 1850, these emissions have increased by a factor of 10, leading to a 0.9 °C rise in the Earth's surface temperature[1,2]. If no action is taken, the Intergovernmental Panel on Climate Change (IPCC) report predicts a temperature increase of 3.2 °C by 2100. This warming causes irreversible effects on the environment, biodiversity, and human health. Examples include ocean acidification and oxygen depletion, accelerated ice melt, rising sea levels, and an increase in the intensity of extreme weather events such as droughts, heatwaves, and tropical cyclones[3].

To mitigate global warming, it is essential to reduce greenhouse gas emissions. In line with this goal, the United Nations Climate Change Conference (COP21) held in Paris in 2015 established the Paris Agreement, which aims to cut emissions by 45 % by 2030 and move towards net-zero emissions by 2050 (Figure 0-1).

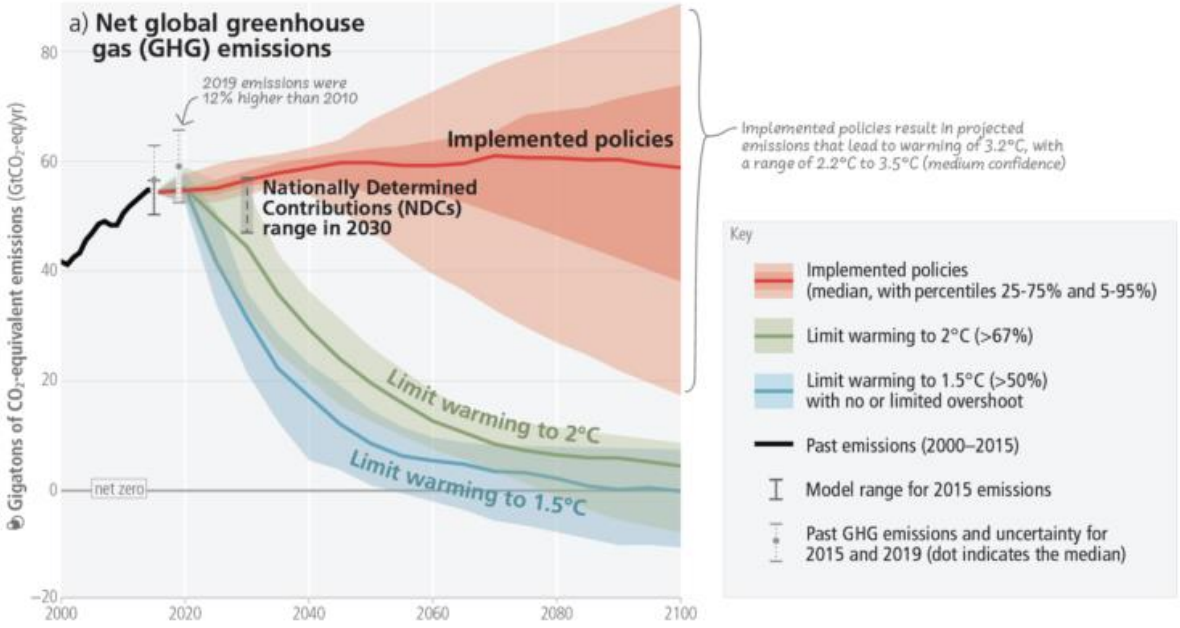

Figure 0-1: Evolution of global greenhouse gas emission depending on the desired emission reduction scenarios (in blue and green) and the policies currently in place (in red). From IPCC[2]

The transport sector was responsible for a quarter of greenhouse gas emissions in the European Union in 2019, according to the European Environment Agency[4].

One way to reduce these emissions would be to transition to electric vehicles, which are equipped with motors and energy storage systems that do not produce CO_2. Currently, the technology used for both stationary and mobile applications is Li-ion batteries. However, this technology is limited by its energy density (260 Wh/kg), which constrain the performance of

electric vehicles, particularly their range[5]. One way to enhance the performance of Li-ion batteries is to use Li-metal as a negative electrode. With its very low potential (0 V vs Li^+/Li), it can be combined with high-potential positive electrodes (5 V vs Li^+/Li), theoretically doubling the initial energy density from ~260 Wh/kg to ~400 Wh/kg[5]. However, Li-metal is incompatible with the liquid electrolyte, responsible for lithium-ion transport between electrodes, as its incorporation leads to dendrite formation and potential short circuits[6]. Furthermore, employing high-potential positive electrodes is not feasible, as the liquid electrolyte oxidizes at high potentials. Additionally, this liquid electrolyte poses significant safety concerns due to its flammability, making it a critical obstacle in the technology[5].

An alternative to liquid electrolyte is the use of solid electrolyte, which, in principle, can prevent dendrite formation and maintain stability at high potentials. Solid electrolytes must exhibit key characteristics, including ionic conductivity greater than 10^{-4} S/cm at room temperature, low electronic conductivity, and a wide electrochemical stability window[7]. However, despite the many types of solid electrolytes, such as polymers, sulphides, and oxides, none of these families fully meet all the required characteristics to be competitive with liquid electrolyte. Each family has its own specific advantages and challenges[8].

In this thesis, I focused on one of the challenges related to solid oxide electrolytes: their densification through a high-temperature treatment step, the sintering. Sintering serves several purposes, such as minimizing porosity and grain boundaries, improving ionic conductivity, and maximizing interfaces between different grains[9]. Specifically, the solid electrolyte $Li_{1+x}Al_xTi_{2-x}(PO_4)_3$ (LATP) was selected because of its advantage of being stable at high potentials (4.1 V vs Li^+/Li), making it a good candidate for the composite positive electrode[9].

The sintering temperature depends both on the material and the sintering technique employed. For LATP, conventional sintering must be conducted above 1000 °C to reduce porosity below 5 % and achieve ionic conductivities on the order of 10^{-4} S/cm at room temperature[10]. However, this high temperature poses an energy challenge and also causes LATP to react with the active material in the composite positive electrode, eventually leading to the degradation of both materials[11]. Although there are techniques available to decrease the sintering temperature of LATP, they do not allow for temperatures below 800°C, or the resulting ionic conductivities remain insufficient[12,13]. Therefore, this thesis focuses on exploring methods to lower the densification temperature of LATP.

Thus, in **Chapter I**, we will present the state of the art on various sintering methods for LATP and solid oxide electrolytes in general. The transition from the Li-ion technology to all-solid-state batteries will be introduced, along with an overview of the different families of solid electrolytes. We will discuss the different synthesis methods and properties of LATP and detail the challenges related to high sintering temperatures.

Chapter II will focus on the impact of particle size and morphology on the sintering of LATP. This chapter will primarily establish the fundamentals concerning synthesis, conventional sintering densification, and ionic conduction properties.

In **Chapter III**, the use of lithium salts as a sintering aid will be investigated. Initially, we will explore the reactivity mechanism of LATP with lithium salts, focusing on the systematic formation of consistent impurities. The relationship between this reactivity and densification will be studied to explain the improved density observed at lower temperatures with the addition of lithium salts. Finally, we will assess the ionic conduction properties of LATP with and without lithium salts to determine their beneficial impact.

Based on the study conducted in the previous chapter, **Chapter IV** will investigate the use of a eutectic mixture of lithium salts with a low melting temperature and which does not react with LATP. This mixture of salts has not been previously used as a sintering aid for LATP. The impact of this salt will be examined in both conventional sintering and Spark Plasma Sintering (SPS) to leverage the combined effects of these techniques.

Chapter I: State of the art

I. From Li-ion technology to Solid-State Batteries

I.1. Introduction to the Li-ion technology and its limits

Since their commercialisation in the 1990s by Sony, Li-ion batteries (LIBs) have revolutionised numerous sectors due to their high energy density, long cycle life and cost[14–16]. These batteries are composed of a negative electrode, a polymer separator and a positive electrode. All the components are immersed in a liquid electrolyte, which consists of lithium salt dissolved, i.e. $LiPF_6$, in organic carbonates solvents[17]. This last component allows to transport the lithium ion to and from the electrodes. In most cases, layered oxides such as $LiCoO_2$ are used as the positive electrode, whereas graphite is primarily used as the negative electrode[18]. During charging, lithium ions move from an electrode to the other one through the liquid electrolyte, and electrons follow an external path to balance the charge. During the battery charge, the reactions at the positive and negative electrodes are summarised by the equations (1) and (2) respectively:

$$LiCoO_2 \rightarrow Li_{1-x}CoO_2 + xLi^+ + xe^- \qquad (1)$$

$$C_6 + xLi^+ + xe^- \rightarrow Li_XC_6 \qquad (2)$$

During discharging, the process reverses. This reversible movement of lithium ions between the electrodes allows the battery to charge and discharge efficiently.

Although this technology has become indispensable in a variety of applications, ranging from portable electronic devices to electric vehicles, the use of flammable solvents for the liquid electrolyte poses safety issues. Moreover, Li-ion batteries have reached their limit in term of energy density[16], as the liquid state of the electrolyte limits the use of Li-metal as the negative electrode. This compatibility issue leads to dendrite formation and potential short circuits[6].

I.2. Transition to Solid-State Batteries (SSBs)

One way to overcome these problems is to switch to solid-state batteries (SSBs) where the liquid electrolyte is replaced by a solid electrolyte. The operation principle remains the same. As shown in Figure I-1, two design exist. The first one (to the right) consists of two porous electrodes filled by solid electrolyte, which are physically separated by solid electrolyte particles that act both as separator and electrolyte for the lithium-ion transport. The second one (to the left) is similar, but the porous negative electrode is replaced by Li-metal[19]. Both

architectures address safety concerns, but the latter design is ideal because an increase in both volumetric and gravimetric energy densities is expected thanks to the high theoretical gravimetric capacity of the Li-metal (3700 mAh/g). Theoretically, this transition could double the initial energy density from ~260 Wh.kg^{-1} to ~400 Wh.kg^{-1}[5].

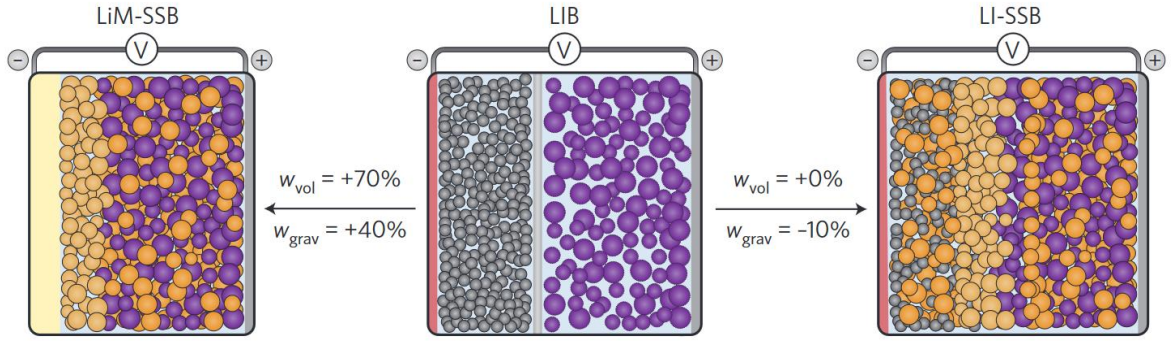

Figure I-1: Typical design for SSBs with Li-metal as negative (to the left), conventional Li-ion batteries (in the middle) and SSBs with composite electrodes (to the right). From Janek et al. [5]

Additionally, liquid electrolytes are not stable at high voltage, indicating that SSBs could also incorporate high-voltage positive electrodes (materials with a 5 V redox potential)[20,21]. Globally, other benefits are expected such as high thermal stability[20], long-term stability and mechanical properties[5].

Finally, this design offers a potential decrease of the cell thickness. This thickness decrease enables the downsizing of the battery cell, module, and pack. By minimising the overall volume of battery components, more energy can be stored within a given space, leading to a higher volumetric energy density compared to conventional LIBs. This is particularly advantageous in applications where space is limited, such as the electrical vehicles field[22].

I.3. Challenges about the realization of SSBs

However, the transition from Li-ion batteries to all-solid-state batteries is not without challenges, as illustrated by the Figure I-2. Main challenges are briefly discussed:

First of all, void formation is inevitable despite the application of high pressure (>350 MPa) during the fabrication of a prototype. Indeed, several phenomena result in the formation of this porosity. For example, the morphology and the particle size of the components implies a weak connection between them, unlike in Li-ion battery where all the components are immerged in the liquid electrolyte. What's more, the volume variation of the electrodes during the cycling induces some crack and contact loss between active material and solid electrolyte particles. The resultant porosity could lead to the formation of lithium dendrites and increase the contact

resistance due to non-optimal lithium ion diffusion and charge transfer[23].

Another challenge concerns the chemical compatibility of each component in the battery. Indeed, compatibility issues imply spontaneous chemical reactions that could generate new interphases at the interfaces. These interphases are called differently as a function of their localisation in the battery: it is called solid electrolyte interphase (SEI) at the negative electrode side, and cathode electrolyte interphase (CEI) at the positive electrode side. This phenomenon can be beneficial if the new interphase conducts lithium ions without being electrons conductive. Otherwise, it leads to the degradation of the battery performance[5,24].

In addition to chemical compatibility, the solid electrolyte must be stable across the applied voltage range. Indeed, the oxidation of the solid electrolyte at high voltage and/or its reduction at low voltage leads to its decomposition and the formation of degradation products. As for the chemical reactivity that was explained previously, this results on the degradation of the battery. The challenge is that the electrochemical stability window of most solid electrolytes does not meet this requirement[23,25,26].

Finally, the presence of grain boundaries when two particles with different electrochemical potentials come into contact are also challenging. This interaction leads to the formation of a Li-deficient space-charge layer at the interface due to the transfer of Li-ion from one particle to the other[23].

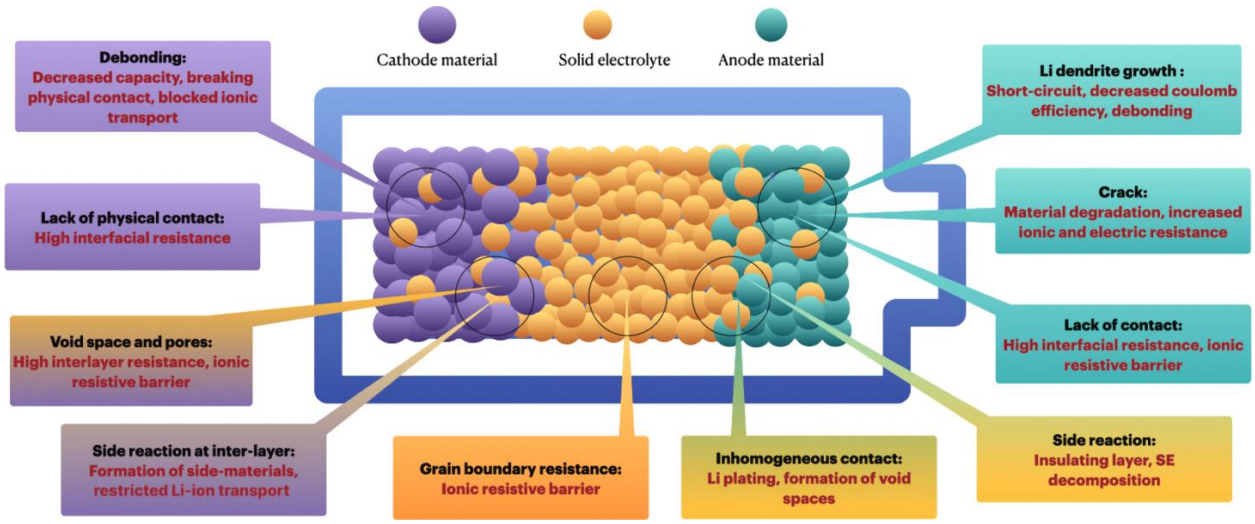

Figure I-2: Schematic illustration of main interfacial issues and limitations in SSBs. Orange spheres are solid electrolyte particles; purple spheres are active material particles; green spheres represent Li-metal particles. From Moradi et al. [27]

II. The solid electrolyte: state of the art

The majority of the issues explained previously largely depends on the nature of the solid electrolyte. Before discussing the various families of solid electrolyte, it is important to outline some essential characteristics that define a good candidate:

- A solid electrolyte must demonstrate high ionic conductivity, ideally greater than 10^{-4} S/cm at room temperature[14]. However, it is reported that an ionic conductivity of 10^{-3} S/cm is preferable for a solid electrolyte to be truly competitive with liquid electrolytes. Indeed, liquid electrolytes typically exhibit an ionic conductivity of around 10^{-2} S/cm at room temperature[28].
- It must have a very low electronic conductivity (< 10^{-12} S/cm) to prevent the passage of electrons from one electrode to another within the cell[20,29].
- Additionally, a wide electrochemical stability window (0-5 V versus Li^+/Li) is crucial to prevent oxidation at high voltage and reduction at low voltage during cycling[30].

These three points are the essential characteristics, but other requirements are also crucial, such as safety considerations, thermal stability (greater than 150 °C), low overall cost, and good mechanical properties to ensure ease manufacturing and processing[7,9].

Three main families of solid electrolyte have been identified, but none of them meet all of these characteristics. As presented in Figure II-1, each has its own advantages and disadvantages when used in all-solid-state batteries[8].

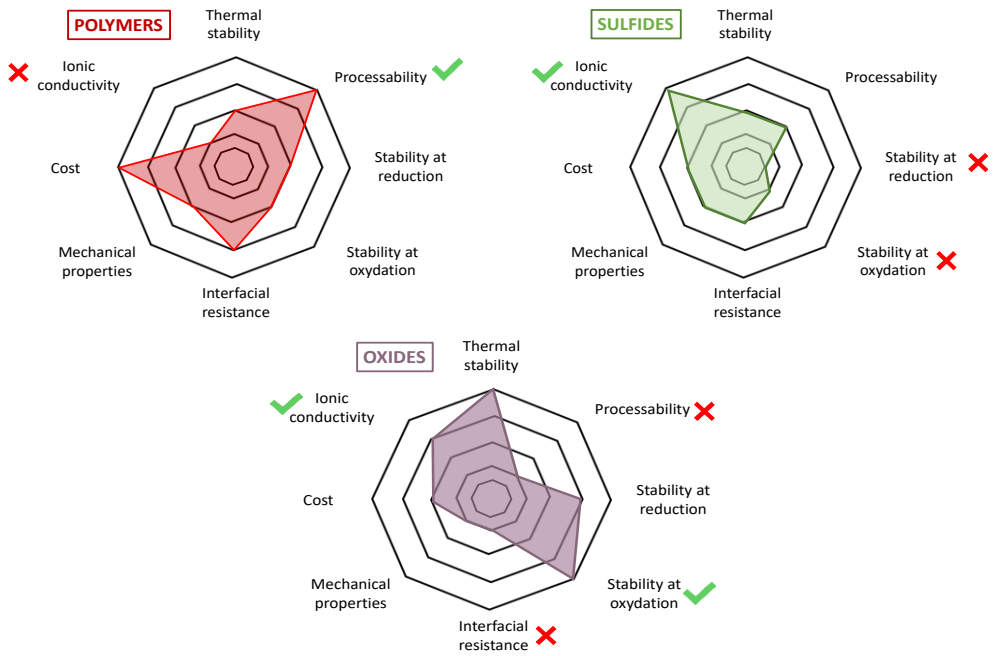

Figure II-1: Summary of the properties of three major families of solid electrolyte: polymers, sulphides, and oxides. Adapted from Zhao et al. [8]

II.1. The Solid Polymer Electrolytes

The **Solid Polymer Electrolytes** (SPEs) demonstrate excellent electrochemical performance, high safety, as well as good flexibility and processability[31,32]. One of the most well-known systems consists of a polymer host combined with an alkali-metal salt (Li, Na, K), where the polymer acts as a solid solvent in which the salt is dissolved[33,34].

However, despite these advantageous properties, this family faces significant challenges, primarily due to their low ionic conductivity and limited thermal stability[27]. Even with the incorporation of lithium salts, their ionic conductivities are in the range of 10^{-5} to 10^{-6} S/cm at room temperature[27,34,35]. Among the various polymers investigated, polyethylene oxide (PEO) combined with lithium salts is the most extensively studied due to its stable interface with Li-metal anode[36–38]. Blue Solution has commercialised a battery called LMP®, which is a system utilising PEO with lithium salt, $LiFePO_4$ as the positive electrode, and a Li-metal foil as the negative electrode[39]. However, this system requires operation at around 60 °C to achieve an ionic conductivity of 10^{-4} S/cm.

II.2. The Solid Inorganic Electrolytes

The **sulphide based electrolytes** are well known for their exceptional ionic conductivities at room temperature, which are comparable to that of typical organic liquid electrolyte[40–42]. For example, Seino et al. reported a very good ionic conductivity of $1.7x10^{-2}$ S/cm at room temperature for the $70Li_2S$-$30P_2S_5$ glass ceramic[41]. Another promising sulphide-based electrolyte is the argyrodite, Li_6PS_5X (with X = Cl, Br, I), which has demonstrated ionic conductivities in the range of 10^{-3} S/cm at room temperature[43]. This performance can be explained by the characteristics of sulphur atoms, which are softer and more polarisable compared to oxygen atoms. As a result, there is less interaction with the lithium atoms, leading to increased mobility[44,45]. In addition, they exhibit a good flexibility and excellent mechanical properties. However, they suffer from a limited electrochemical stability window, typically constrained by high potentials[25,26,46]. Additionally, they are unstable in the presence of moisture, which leads to the release of the toxic gas H_2S[45,47,48].

In contrast, most of the **oxide-based electrolytes** have the particularity to address safety concerns as they are stable, even at high temperature[7]. Moreover, they exhibit sufficient ionic conductivities in the range of 10^{-3}-10^{-5} S/cm at room temperature. Several families exist, including LiSICON, NaSICON, Garnet, Perovskites, anti-Perovskites, LiPON and others[49].

Among these families, two materials are widely studied in the literature: the Garnet-type solid electrolyte $Li_7La_3Zr_2O_{12}$ (LLZO)[50,51] and the NaSICON-type $Li_{1+x}Al_xTi_{2-x}(PO_4)_3$ (LATP)[9,20,52].

- **Garnet type $Li_7La_3Zr_2O_{12}$**

Oxides with garnet structure are promising candidates for SSBs as they have good ionic conductivities ranging from 10^{-3} to 10^{-4} S/cm at room temperature, a good stability against Li-metal and a wide electrochemical stability window[7,20,53]. However, the cubic phase of LLZO (c-LLZO), which exhibits the highest ionic conductivity, typically requires specific conditions to be stabilised at room temperature, often through doping with elements like Al, Ta, or Ga[54,55]. Despite its advantageous properties, c-LLZO is not stable in the presence of water, as it reacts to form LiOH. Subsequently, LiOH can react with CO_2 to form Li_2CO_3. The formation of Li_2CO_3 is problematic because it induces a phase transition from the cubic to the tetragonal phase, which significantly reduces ionic conductivity[55–57]. Moreover, the LLZO is composed of lanthanide atom, a rare-earth metal, whose availability and geographical distribution are limited[44].

- **NaSICON type $Li_{1+x}Al_xTi_{2-x}(PO_4)_3$**

In contrast, solid electrolytes with a NaSICON structure, such as LATP, exhibit similar ionic conductivities, ranging from 10^{-3} to 10^{-4} S/cm at room temperature, while offering excellent stability in ambient conditions and at high potentials (up to 4.1 V vs Li^+/Li)[58,59]. Moreover, the glass ceramic version of LATP and LAGP, which was reported for the first time by Ohara company, exhibits a high ionic conductivity of 5.10^{-3} S/cm at 27 °C, which is higher than the crystalline analogue[60,61]. A similar product named LICGC™ is commercialized by the same company, and consists of the melting of Li_2O-Al_2O_3-SiO_2-P_2O_5-TiO_2 to form a NaSICON type membrane[62]. However, one of LATP's main limitations is its instability in contact with Li-metal, due to the reduction of Ti^{4+} cations, which compromises the crystal structure of the material[55,63]. Some solutions have been proposed to address this issue, such as using barrier layers like LAGP, a LATP analogue where titanium is replaced by germanium[64]. Despite this challenge, LATP remains a promising candidate for solid electrolytes in all-solid-state batteries due to its balanced electrochemical properties and the potential for optimizing ionic conductivity through chemical composition modifications.

In conclusion, no single family of solid electrolytes meets all the required characteristics. Polymers suffer from poor ionic conductivity at room temperature, sulphide-based electrolytes have stability issues in ambient air, and depending on the type of oxides, chemical and electrochemical stability problems may arise. Nevertheless, in our study, we focused on LATP, which, although it is not stable against Li-metal, is a promising candidate for use in the composite positive electrode. Moreover, it offers the advantages of easy synthesis, air-stable handling, and a composition made of more readily available, abundant elements[65].

III. Focus on LATP solid electrolyte

III.1. Introduction to NaSICON

The NaSICON (the acronym for Sodium Super-Ionic CONductor) solid electrolyte was firstly reported by Goodenough et al. in 1976[65]. This class of material is characterised by an orthorhombic crystal structure, with the initial formula $NaZr_2(PO_4)_3$[20,66,67].

It was during the early 1990s that their lithium analogues, such as $LiM_2(PO_4)_3$ (with M = Zr, Ti, Hf, Ge), began to be explored[20,59,68,69]. The properties of these materials are similar, with the notable difference that $LiTi_2(PO_4)_3$ exhibits significantly better ionic conductivity compared to the others as it offers the most suitable lattice size for lithium-ion conduction[70]. In contrast, $LiZr_2(PO_4)_3$ demonstrates greater stability with Li-metal[58].

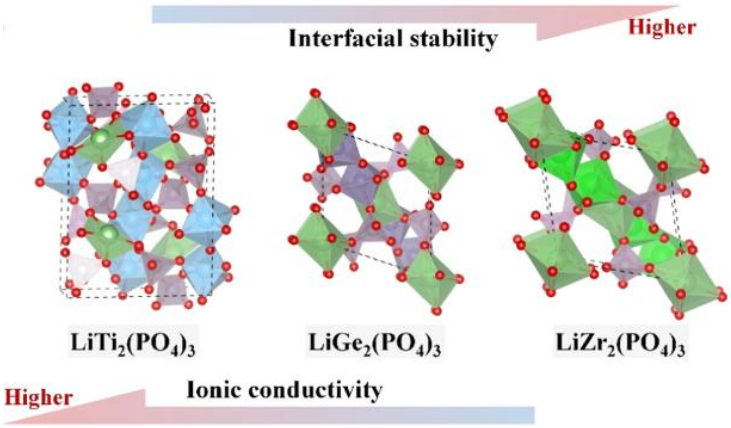

Figure III-1: Comparison of ionic conductivity and interfacial stability for LTP, LGP and LZP. From Xia et al.[58]

Despite this, LTP exhibits poor total ionic conductivity, approximately 10^{-7} S/cm at room temperature, due to the difficulty to densify the material, leading to the presence of high porosity[71]. A strategy documented in the literature to enhance its ionic conductivity is the partial substitution of the tetravalent cation Ti^{4+} with trivalent cations (R = Al^{3+}, Sc^{3+}, Ga^{3+}, Cr^{3+} and others) along with Li^+, following the formula: $Li_{1+x}R_xTi_{2-x}(PO_4)_3$[20]. Among these, the most well-known compound is the $Li_{1.3}Al_{0.3}Ti_{1.7}(PO_4)_3$ (LATP), which was reported for the first time by Aono et al. to have a total ionic conductivity of 7.10^{-4} S/cm at room temperature[59].

III.2. Crystal structure

The structure of LTP/LATP is rhombohedral, belonging to the space group *R*-3*c*. It can be described by an $Al_xTi_{2-x}(PO_4)_3$ skeleton, which consists of PO_4 tetrahedral sites and TiO_6/AlO_6 octahedral sites interconnected by oxygen atoms, as presented in Figure III-2[19]. In LTP, the lithium ions (Li1) exclusively occupy the M1 (Wyckoff position 6b) sites that are surrounded by oxygen atoms. In contrast, for LATP, the incorporation of Al^{3+} to replace some Ti^{4+} comes with the insertion of additional lithium ions (Li2), which theoretically occupy the M2 (Wyckoff position 18e) sites and are located between two M1 positions[72,73]. However, some studies on LATP using Fourier map differences combined with neutron diffraction have shown distinct lithium ion distribution. For LATP, they are more likely to occupy both the M1 and M3 sites, which is another site localised between M1 and M2 (Wyckoff position 36f)[74]. An increase in lithium content in LATP promotes occupancy of the M3 site, reduces electrostatic repulsion between Li1 and Li3 ions, and increases vacancies at the M1 site, leading to enhanced Li^+ conductivity[75,76].

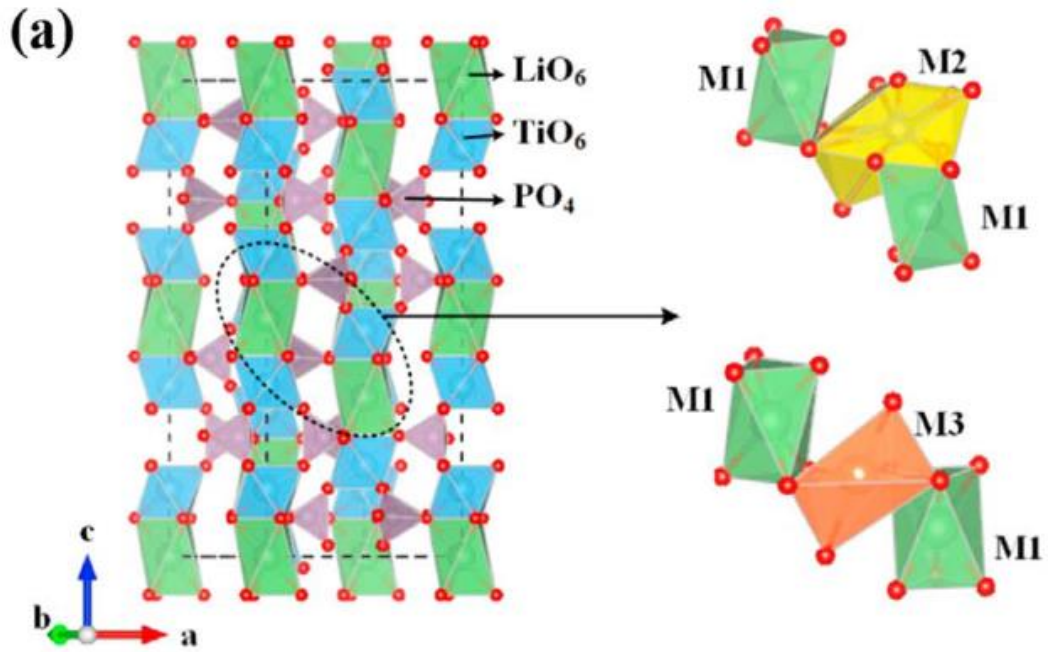

Figure III-2: Crystal structure of a rhombohedral LTP, with the localisation of M1, M2 and M3 sites. From Xiao et al. [75]

According to Monchak et al., who investigated the crystal structure of LATP using neutron diffraction and synchrotron radiation, Li^+ ions may traverse a Z-shaped migration route (M1−M3−M3−M1)[77]. Their theoretical calculations estimated an activation energy of 0.33 eV for Li^+ diffusion, which aligns with most experimental and theoretical findings[25].

III.3. Level of substitution

To summarise, the improvement in ionic conductivity by transitioning from LTP to LATP is attributed to an increase concentration of mobile ions within the framework and the introduction of interstitial migration pathways with lower activation energy, facilitated by the incorporation of trivalent cations[72]. Thus, the proportion of Ti^{4+} substituted by Al^{3+} and Li^{+} modifies the structure and impacts its ionic conductivity. These structural modifications are observable through the variation of lattice parameters as a function of the level of substitution. Indeed, lattice parameters, such as edge lengths and angles of the unit cell, describe the dimensions and symmetry of the crystal lattice. They are essential for understanding structural changes in crystalline materials. In the rhombohedral system, the lattice parameters are defined as follows: $a = b \neq c$, with $\alpha = \beta = 90°$ and $\gamma = 120°$. A large number of studies have determined these lattice parameters for $Li_{x+1}Al_xTi_{2-x}(PO_4)$ with a level of substitution x ranging from 0 to 0.5[76,78–80]. As displayed in Figure III-3, as the substitution rate increases, the lattice parameters *a* and *c* decrease. This diminution can be attributed to the substitution of Ti^{4+}, which has an ionic radius of 0.61 Å, by Al^{3+}, whose ionic radius is smaller (0.54 Å)[81]. Within a substitution range of 0 to 0.5, this decrease is linear, indicating that the substitution is occurring effectively in accordance with Vegard's law[76,78].

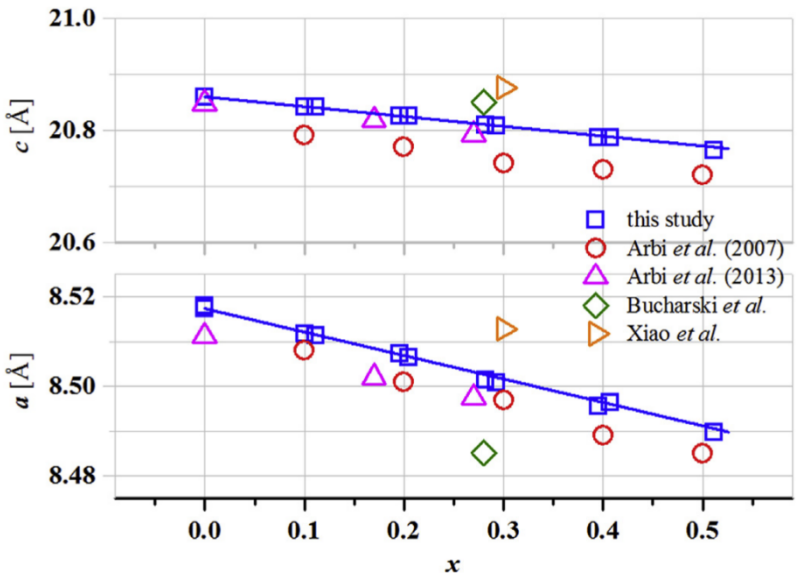

Figure III-3: Variation of lattice parameters in LATP as function of the Al^{3+} substitution level x according to data in the literature. From Redhammer et al.[78]

Pérez-Estébanez et al. synthesised LATP with higher aluminium substitution levels, such as 0.7 and 1. However, the significant presence of impurities raises concerns about the actual level of substitution in these materials and their ionic conductivity[79].

The influence of titanium substitution by different metals on ionic conductivity was investigated by Aono et al., as illustrated in Figure III-4. In the case of substitution by aluminium, a maximum in term of ionic conductivity is reached at 0.3[59].

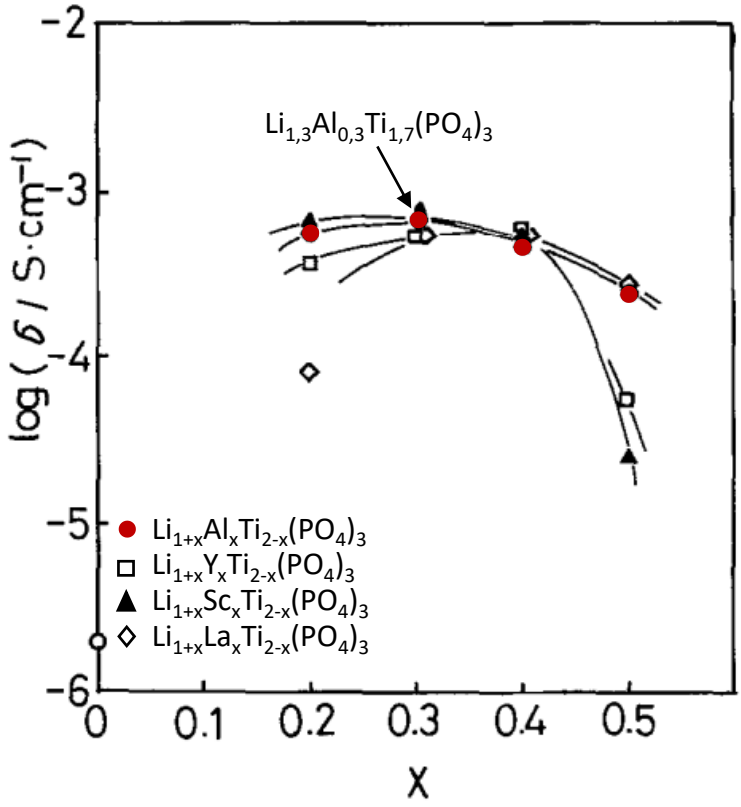

Figure III-4: Ionic conductivities at 25°C of $Li_{1+x}M_xTi_{2-x}(PO_4)_3$ (with M = Al, Y, Sc, La) as a function of the x level substitution of M. Adapted from Aono et al. [59]

This maximum has been confirmed by other studies, notably by Case et al. According to them, the optimal aluminium level of substitution is 0.3, as it maximises ionic conductivity while maintaining a stable rhombohedral crystal structure[82]. Lower or higher the level of substitution tends to decrease conductivity, either due to a lack of mobile ions, the formation of defects in the crystal structure and impurities.

III.4. Synthesis

Numerous synthesis methods have been reported in the literature for the LATP[58,75,83]. First, we will introduce some of the most common methods, including solid-state reaction, melt-quenching, and sol-gel methods.

The first synthesis of the material was carried out via a solid-state reaction, by Aono et al.[59,84] This method involves mixing precursors such as Li_2CO_3, Al_2O_3, TiO_2, and $NH_4H_2PO_4$ in appropriate stoichiometry through manual or automated grinding[58]. Subsequently, a calcination step at temperatures ranging from 900 °C to 1000 °C is required to form LATP[59]. The complete process is illustrated in Figure III-5 and it will be detailed in Chapter II. This approach is advantageous due to its simplicity, involving only two steps, and its capacity to produce large quantities[58,78]. However, the presence of impurities (TiO_2, $AlPO_4$, $LiTiOPO_4$..), often due to lithium loss (Li_2O evaporation) during the calcination step, has been frequently reported in the literature[58,85,86]

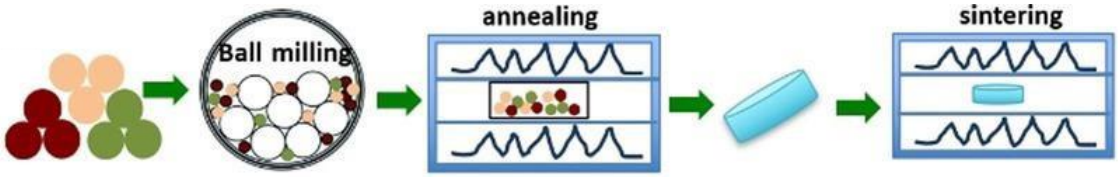

Figure III-5: Schema of Solid-state reaction steps and sintering. From DeWees et al. [83]

The melt-quenching method is another technique used to produce LATP glass-ceramics. This method involves several steps illustrated in Figure III-6: first, the starting reagents are ground, followed by quenching the mixture to room temperature after a thermal treatment at over 1500 °C to melt and react the precursors[83]. LATP materials obtained through this method typically exhibit ionic conductivities on the order of 10^{-3} S/cm at room temperature, primarily due to their low macroscopic porosity and denser microscopic structure, which is related to the densification processes[13,58]. In addition, studies have utilized this method to synthesize LATP films. In that case, the ionic conductivities achieved have not surpassed those obtained by the solid-state reaction method[87,88]. Additionally, the main drawback of this method remains the high thermal treatment temperature, which is too elevated and can also lead to the loss of Li_2O.

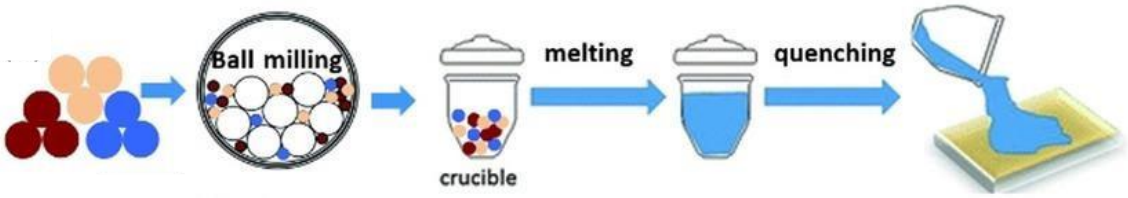

Figure III-6: Schema of melt-quenching method steps and sintering. From DeWees et al. [83]

The sol-gel method involves converting a sol (a colloidal suspension) into a gel (a solid with a three-dimensional structure) by adding gelling agents and controlling parameters such as temperature and pH[75]. The gel is then dried and calcined to produce a powder. The typical process is presented in Figure III-7. For instance, Zhang et al. synthesized pure LATP using propylene glycol-assisted sol-gel processing, achieving a total ionic conductivity of 3.10^{-4} S/cm at 50 °C[89]. This method offers the advantage of producing a pure and homogeneous phase with nano-sized powder[9,90]. However, it is not suitable for large-scale production, and the reagents are relatively expensive compared to those used in the solid-state route[58].

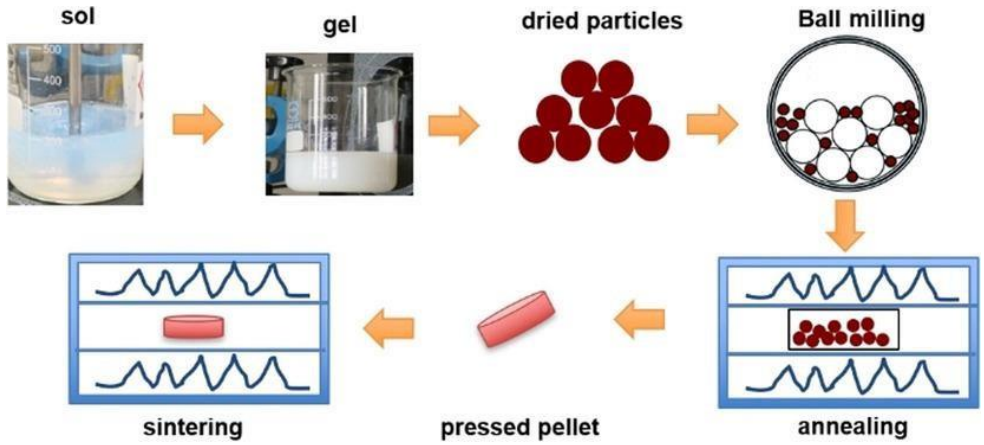

Figure III-7: Schema of a typically sol gel synthesis and sintering. From DeWees et al. [83]

In addition to the previously mentioned synthesis methods, there are other techniques such as liquid-phase synthesis, including co-precipitation[91], hydrothermal[92] and Pechini assisted synthesis[90]. Each of these synthesis methods has its own advantages and disadvantages, as illustrated in Figure III-8.

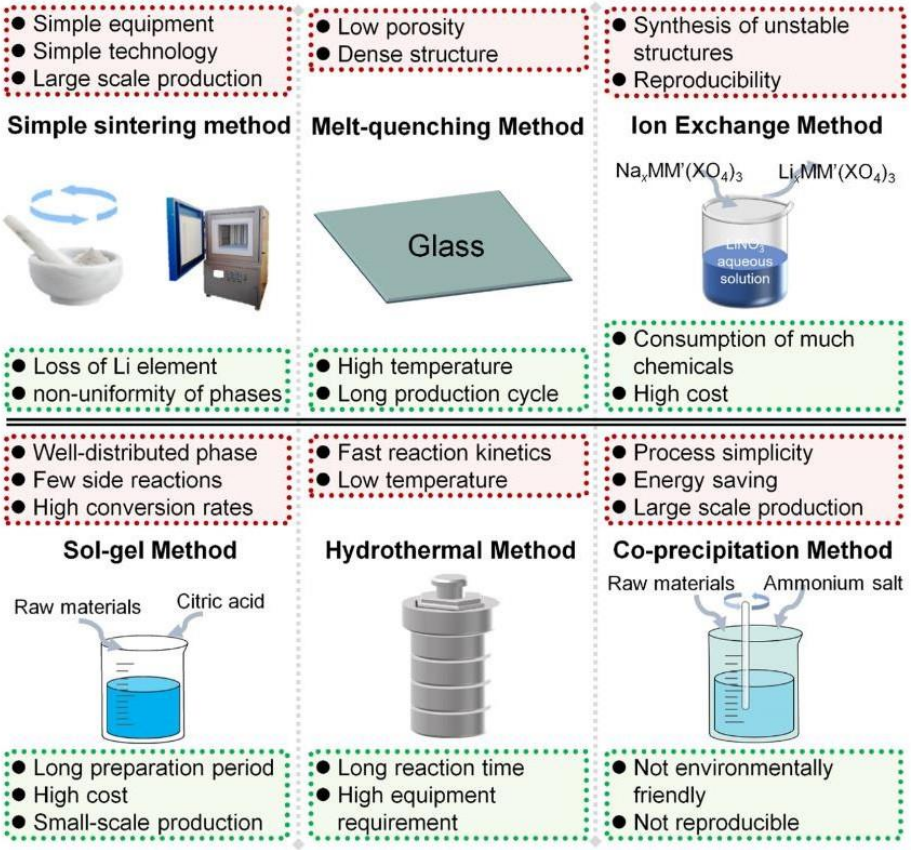

Figure III-8: Summary of the different synthesis route reported from the literature. Red zones present the advantages and the green zones present the disadvantages. From Xiao et al. [58]

IV. Densification and sintering

Once LATP synthesis is complete, it is essential to achieve optimal densification of the material to maximize its ionic conduction and mechanical properties.

First, the total ionic conductivity in a ceramic like LATP consists of the movement of lithium ions which is controlled by diffusion within grains and across grain boundaries. While conductivity within the grains can reach between 10^{-3} and 10^{-4} S/cm at room temperature, the grain boundaries typically exhibit slightly lower conductivity, ranging from 10^{-4} to 10^{-5} S/cm[9,75,93]. Improving conductivity within the grains is largely dependent on the level of substitution, but achieving high conductivity across the entire material also requires minimizing grain boundaries effect by avoiding impurity formation[94]. Sintering, which involves heating the material to promote particle growth and reduce porosity, is an effective method to achieve this by enhancing the connectivity between particles and reducing the number of grain boundaries.

IV.1. Definition and principle

According to Bernache Assolant et al., the sintering step is defined as the transformation of a compacted powder into a coherent material under the influence of a heat source[95]. The sintering step is performed at a temperature below the melting point of the material[95,96] There are several types of sintering, including solid and liquid.

IV.1.1. Solid-state sintering

The process relies on several mechanisms, including atomic diffusion, a phenomenon where atoms move across particles to form solid bonds. This diffusion can occur through various pathways, as presented in Figure IV-1: along the surface of the particles, through grain boundaries, within the grain volume or even by vapor transport. Different sources of material are utilized depending on the diffusion pathway, such as grain boundaries or the surface of the grains, which are cited in the Figure IV-1[95,97].

As the material is heated, the particles draw closer together, and the pores present in the initial structure gradually shrink, leading to a reduction in porosity and an increase in density. As sintering progresses, grain growth also occurs, where smaller grains dissolve in favor of larger ones, resulting in the consolidation of the material's structure[97].

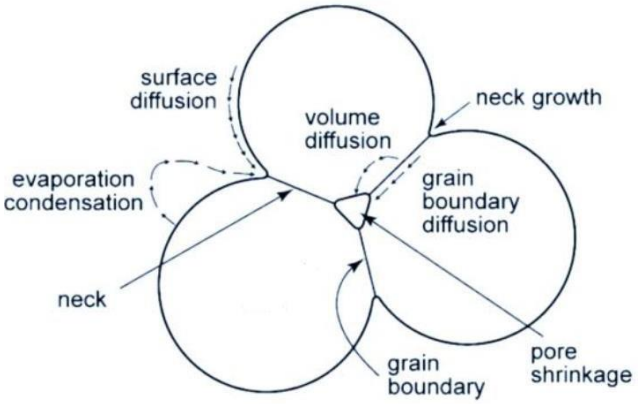

Diffusion pathways	Source of material
Surface diffusion	Surface of particle
Volume diffusion	Surface of particle Grain boundary
Grain boundary diffusion	Grain boundary
Vapor transport	Surface of particle

Figure IV-1: Summary of the different pathways for atomic diffusion in sintering mechanism (to the left). Diffusion pathways with the source of the material (to the right). Adapted from Groover et al. [98]

The sintering process generally occurs in three stages: in the initial stage, particles bond at their contact points, called neck, forming a porous framework. During the intermediate stage, densification accelerates, and the remaining pores begin to shrink, leading to a reduction in open porosity. Finally, in the final stage, the last remaining pores close (closed porosity), and the microstructure theoretically reaches its final state with near-maximum density[97].

The most of the sintering techniques involves compacting a powder into a pellet, which is then subjected to thermal treatment in a muffle furnace or under a controlled atmosphere for a specified duration. The relative density of the pellet, defined as the ratio of its measured density to the crystallographic density (theoretical density) of the sample (see Equation (3)), serves as an indicator of its porosity level. This metric is closely related to the stages of the sintering process, as illustrated in Figure IV-2.

$$\text{Relative Density (RD)} = \frac{Measured\ Density}{Theoretical\ Density} \times 100 \quad (3)$$

The closer this value is to 100%, the lower the porosity of the material. The concept of green density refers to the relative density before thermal treatment. It is determined in the same manner as relative density and is directly related to it since the green density must exceed 40-45 % for effective sintering to occur[99]. The initial stage, where particle bridges form, increases the green density by 3-5 %. The reduction of open porosity can densify the sample up to 92-93 %. The remaining percentage is attributed to the elimination of closed porosity, which is often more challenging to achieve as it requires the evacuation of trapped gases within these pores through diffusion across the solid[95,98].

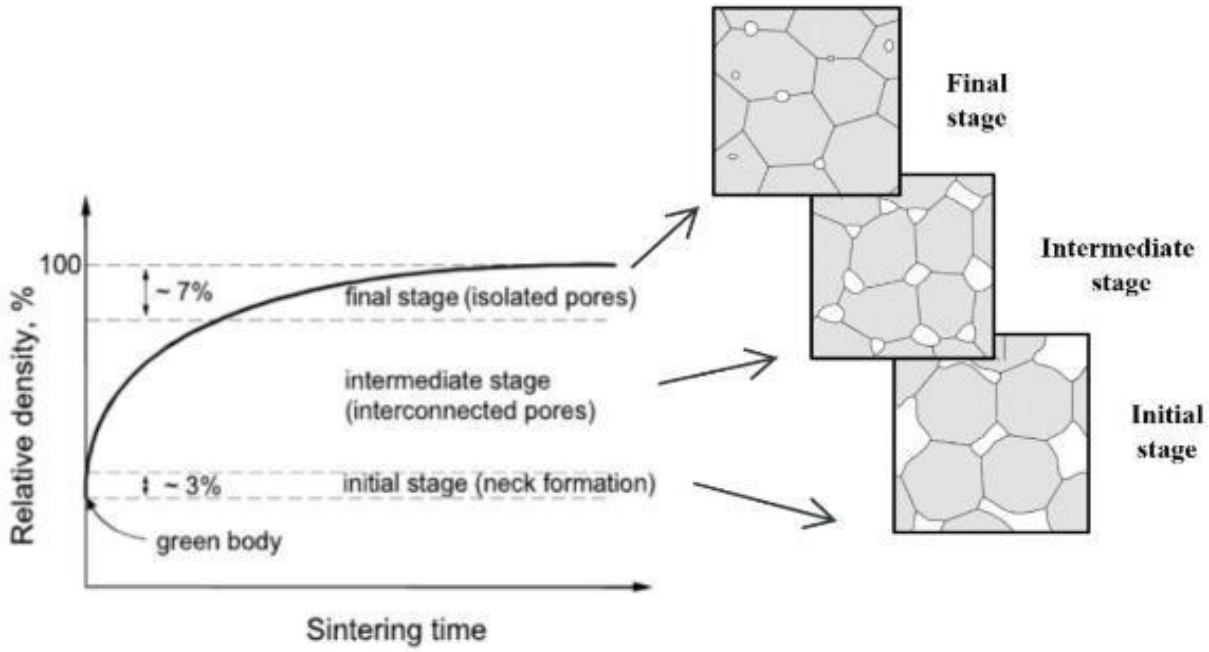

Figure IV-2: Summary of the different sintering stages as a function of the relative density of the sample. From Groover et al. [98]

IV.1.2. Liquid-phase sintering

Liquid-phase sintering differs from solid-state sintering by the presence of a liquid phase during the sintering process. This phase can either be present from the beginning or form during the thermal treatment. This type of sintering involves three stages: particle rearrangement, dissolution-precipitation, and grain coalescence.[96] These three stages are illustrated in the Figure IV-3.

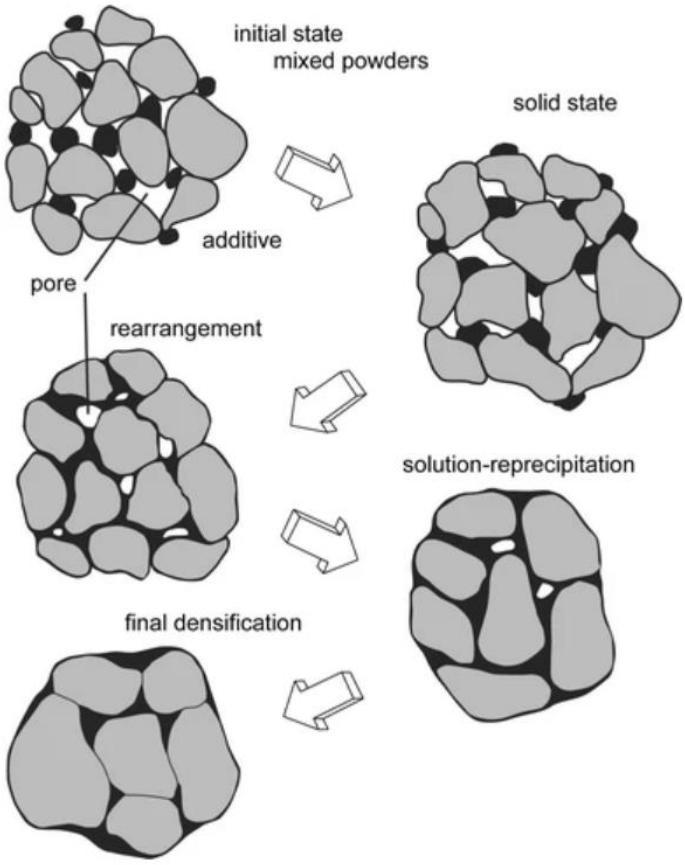

Figure IV-3: Liquid-phase sintering steps. From German et al. [96]

The first stage is the rearrangement stage, where, as the name suggests, the particles rearrange upon the appearance of the liquid. The liquid acts as a lubricant, facilitating the sliding of particles over each other. The forces driving this rearrangement are capillary forces as well as the wettability of the grains by the liquid. High wettability allows the liquid to spread across the surface of the grains, reducing the liquid layer thickness between grains and thereby promoting their proximity[100].

The kinetics of densification associated with this stage are related to the viscosity of the liquid. In fact, low viscosity and high wettability enable a rapid increase in relative density[100].

The second stage, known as dissolution-precipitation, involves the partial dissolution of solid particles into the liquid phase, depending on the solubility of the solid in the liquid. The liquid phase then facilitates the transfer of material from one particle to another, helping to fill the pores. This stage is linked to the final stage, which is grain coalescence and growth, due to the dissolution of smaller particles and their precipitation onto larger ones[97,100].

Thus, this sintering process is governed by the properties of the liquid phase and the temperature at which the phase appears. It enables the densification of materials at lower sintering temperatures compared to those achieved by solid-state sintering[96].

IV.2. Sintering techniques involving solid-state sintering

IV.2.1. Conventional sintering

The traditional method involves forming a pellet of the material and sintering it at high temperatures under a controlled atmosphere for a specified duration. Temperature, sintering time, heating rate, particle morphology, and atmosphere are all parameters that significantly impact the sintering process. In this section, we will explore some of these factors in detail.

According to a study by Hupfer et al., the sintering of LATP begins at 700 °C, and temperatures up to 1100 °C are required to achieve high relative densities (> 95 %)[10]. Other studies have confirmed these observations[76,93,101,102]. For instance, a study by Yan et al. tested various sintering temperatures (950, 1000, 1050, and 1100 °C) on LATP pellets to compare their properties[86]. The relative densities ranged from 94 % at 950 °C to 96 % at 1100 °C. This increase in density was accompanied by an enhancement in ionic properties, with conductivity values rising from 10^{-5} to 10^{-4} S/cm at room temperature.

In contrast, a study by Davasuraan et al. investigated the impact of lower sintering temperature (650-900 °C) on the properties of LATP[103]. They achieved a relative density of approximately 93 % with an ionic conductivity of 2.9×10^{-4} S/cm at room temperature by sintering at 900 °C for 5 hours in air. However, at lower temperatures, the properties were significantly poorer, with pellets reaching only 50 % density at 700 °C and exhibiting an ionic conductivity of 6.1×10^{-7} S/cm at room temperature. This decline in performance is attributed to poor connectivity between grains due to significant porosity, as illustrated in Figure IV-4.

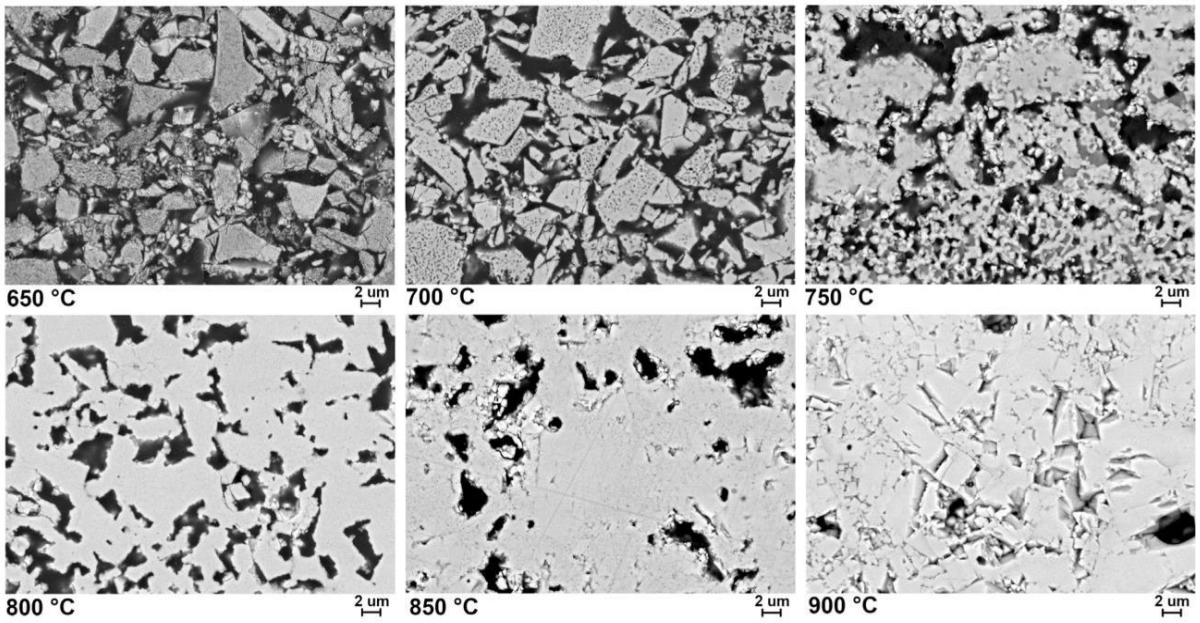

Figure IV-4: SEM images of cross-sectional LATP pellets sintered at different temperatures including 650, 700, 750, 800, 850 and 900 °C. From Davaasuren et al. [95]

Another important factor is the particle size and morphology of the powder to be densified. Numerous studies have demonstrated that decreasing the particle size, particularly transitioning from micron-sized to nano-sized particles, has a beneficial effect on the sintering of LATP. For example, Waetzig et al. showed with dilatometry experiments that densification started 100 °C lower in temperature and was completed at 1020 °C instead of 1050 °C for nano-sized powder compared to micro-sized powder[104]. A similar observation was made in a study by Raj et al., given that the densification of nanoparticles was completed at 850 °C instead of 940 °C for the same heating program as presented in Figure IV-5[105].

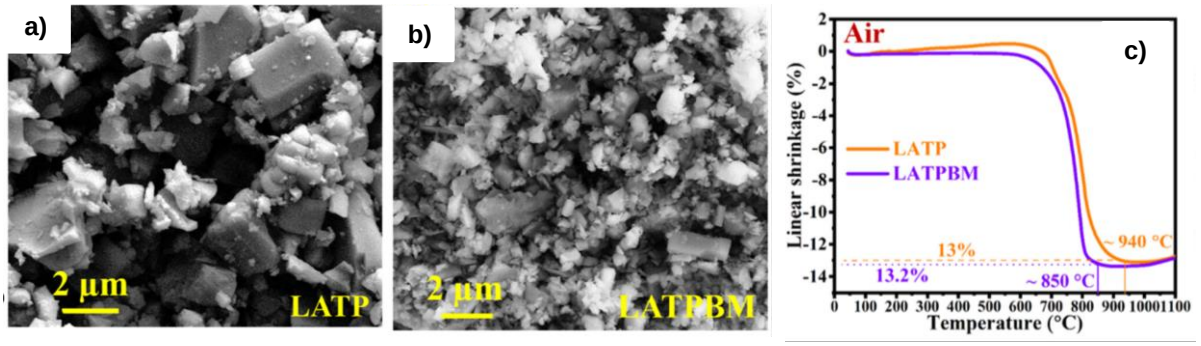

Figure IV-5: SEM images of (a) micrometric LATP particles and (b) nanometric LATP particles. (c) Dilatometry results for the two samples. From Raj et al. [105]

The particle size can be controlled by a milling step or based on the synthesis method used[13,105]. Soft chemistry syntheses, such as sol gel, Pechini method or hydrothermal, tend to produce smaller particles[83]. For example, Ma et al. successfully synthesized LATP particles via a modified sol-gel route, achieving sizes in the range of 60-150 nm, with a sintering temperature

range between 810 °C and 880 °C[90]. They obtained relative densities exceeding 95 % by densifying this powder for 5 hours at 850 °C. The reported ionic conductivity was 6.9 x 10^{-4} S/cm, which is comparable to what is typically achieved at higher sintering temperatures. The impact of particle morphology and size is an aspect that will be further explored in Chapter II.

The densification of LATP through conventional methods requires sintering temperatures above 1000-1100 °C to achieve relative densities greater than 90-95 % and ionic conductivities on the order of 10^{-4} S/cm at room temperature. However, a study by Liu et al. demonstrated that applying temperatures above 1000 °C tends to degrade the ionic conductivity, which decreases from 1.33×10^{-3} S/cm to 5.30×10^{-4} S/cm for a $Li_{1.7}Al_{0.3}Ti_{1.7}Si_{0.4}P_{2.6}O_{12}$ (LATSP) compound[106]. Indeed, after a heat treatment at 1000 °C, they observed the formation of resistive impurities (e.g., $AlPO_4$, $LiTiOPO_4$, TiO_2), likely due to the evaporation of species, such as Li_2O, above 900 °C[13,107]. Additionally, such high temperatures cause cracking within the grains, leading to increase the porosity, as illustrated in Figure IV-6-d. These phenomena have been reported in other studies, with some researchers attributing the cracking to the anisotropic thermal expansion of LATP[10,13,108]. This concept will be discussed in greater detail in Chapter II and III. LATP therefore needs to be densified at lower temperatures to limit the formation of porosity, impurities and cracking[109]. For example, external assistance such as the application of pressure during sintering can be beneficial in achieving the desired material properties.

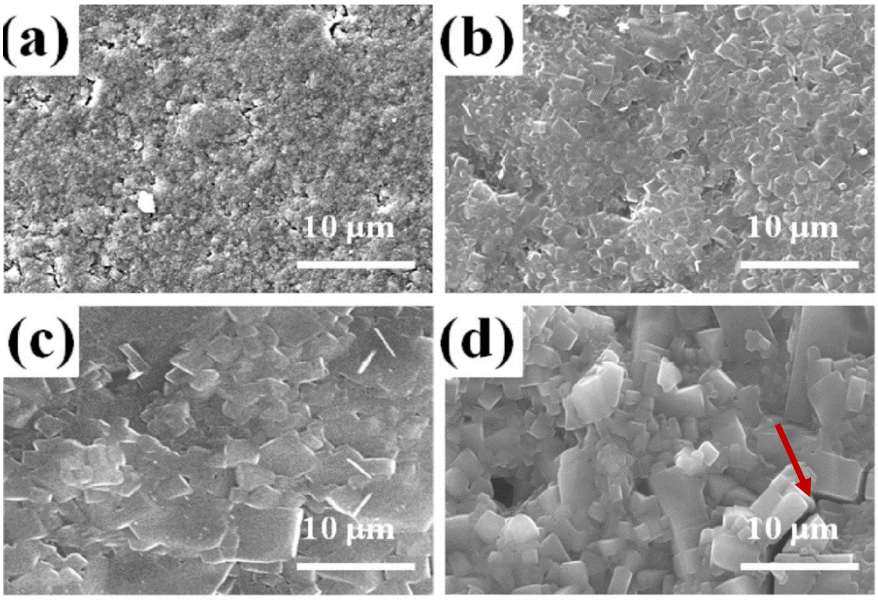

Figure IV-6: SEM images of the surfaces of LATSP pellets after sintering at (a) 900 °C, (b) 1000 °C, (c) 1100 °C and (d) 1200 °C. Red arrow shows crack within the pellet. From Liu et al.[106]

IV.2.2. Hot isostatic pressing (HIP)

One of the initial strategies for improving densification is to apply pressure during the heat treatment process. Indeed, the pressure during sintering promotes pore closure, bringing particles closer together. This proximity intensifies the interactions between particles which enhance the diffusion kinetics that govern the sintering process. As a result, pressure-assisted sintering can reduce the temperatures required to achieve equivalent densification or accelerate the sintering stages at a given temperature[110]. Various techniques exist depending on the temperature and pressure applied, and these can be grouped accordingly in Figure IV-7. For instance, Cold Isostatic Pressing (CIP) combines pressures of approximately 600 MPa with relatively low temperatures (25-100 °C), whereas Hot Isostatic Pressing (HIP) involves temperatures that can reach up to 2000 °C and pressures lower than 200 MPa[111].

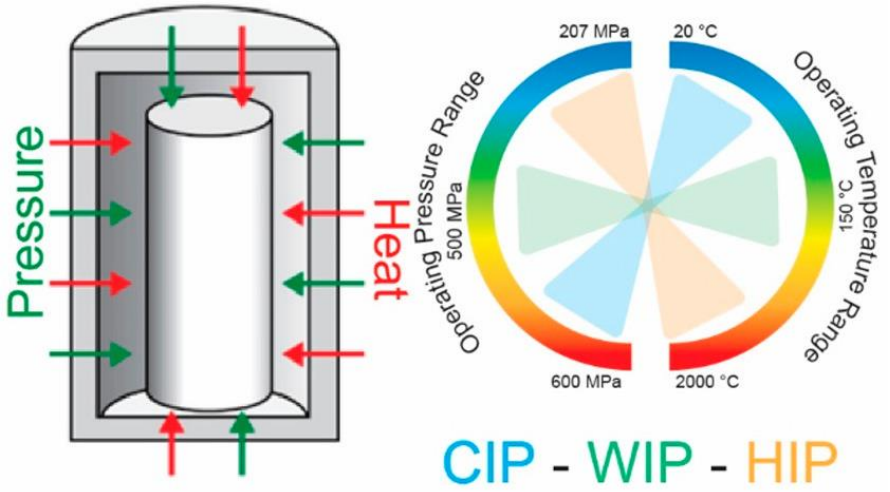

Figure IV-7: Schematic isostatic pressing process and the temperatures and pressure ranges for cold isostatic pressing (CIP), warm isostatic pressing (WIP) and hot isostatic pressing (HIP). From Dixit et al. [111]

Some studies have demonstrated the beneficial effects of HIP in the sintering of LLZO. Under conventional sintering, LLZO typically requires a temperature of 1230 °C for 36 hours[112]. However, a study by Rangasamy et al. achieved 98 % densification of LLZO with a heat treatment at 1000 °C for just 1 hour under a pressure of 40 MPa[113]. Similar results have been reported in the literature: David et al. achieved LLZO pellets with relative densities of 97 % and 99 % through HIP sintering (62 MPa for 1 hour) at 1000 °C and 1100 °C, respectively[114]. Among the studies conducted on NaSICON materials, one notable example is the work by Zhu et al., where $Li_{1.5}Al_{0.5}Ge_{1.5}(PO_4)_3$ (LAGP) was sintered using this method[115]. In their research, the samples were thermally treated at 600 °C for 1 hour under a pressure of 25 MPa. When comparing the densities achieved with conventional sintering, they successfully reduced the

porosity from 12 % to 4 % and lowered the densification temperature by 200 °C. Another study confirmed this improvement in the case of LAGP: Paolella et al. achieved relative densities greater than 99 % by applying a sintering program that reached 650 °C for 1 hour under a pressure of 112 MPa[116]. The resulting microstructure was less porous compared to that obtained through conventional sintering or at lower pressures (Figure IV-8). However, it is crucial to moderate both pressure and temperature to avoid the formation of impurities.

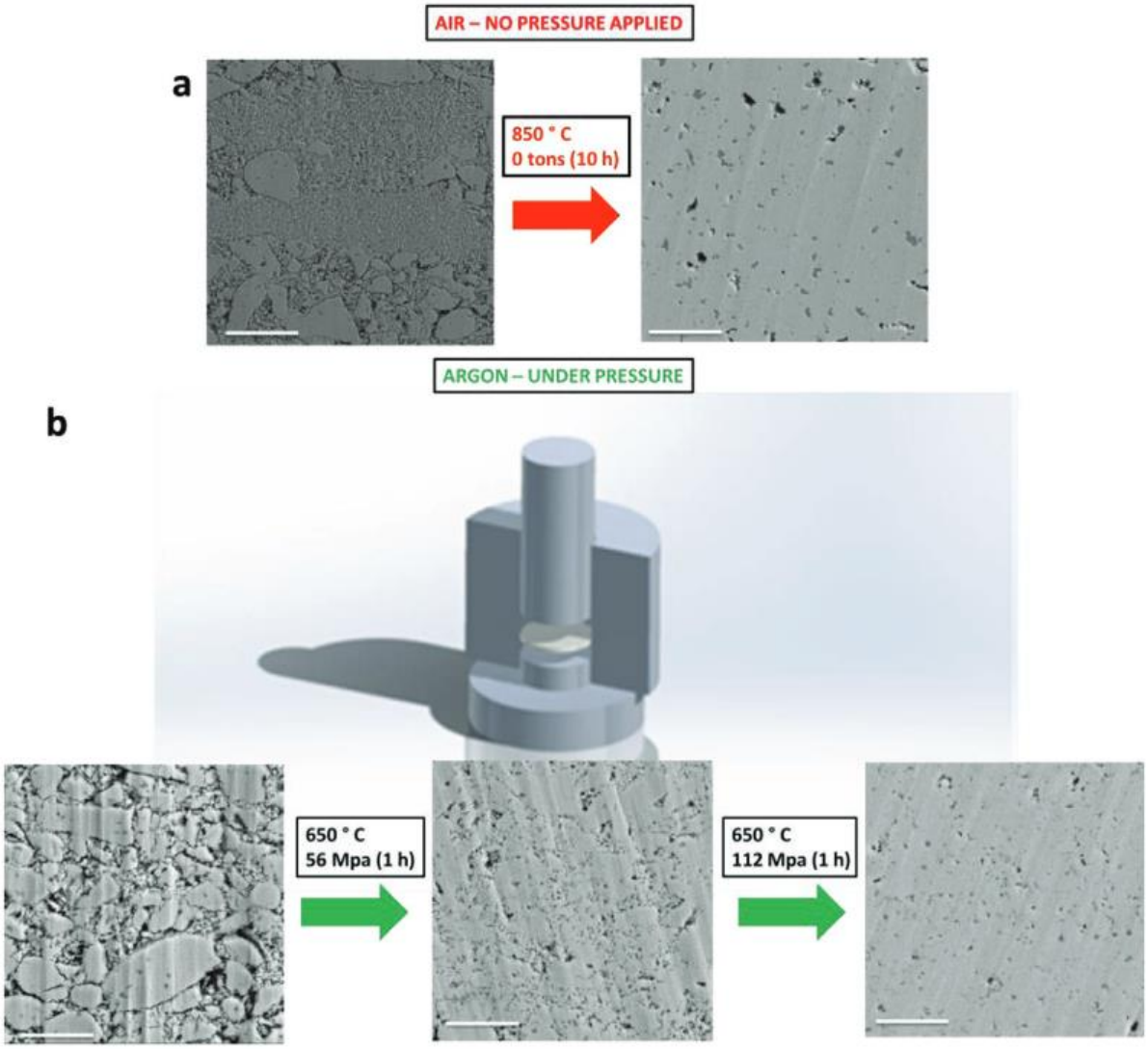

Figure IV-8: SEM images of LAGP pellets after (a) a conventional sintering process at 850 °C for 10 h in air, (b) hot pressed at 650 °C at different pressures including 0, 56 MPa, 112 MPa for 1 h in argon atmosphere. From Paollela et al. [116]

IV.2.3. Spark Plasma Sintering

In contrast, Spark Plasma Sintering (SPS) can densify particles in shorter times (minutes), utilising high heating rates (>100 °C/min), which allows for a faster sintering process completion[83,117]. These performances are possible as the process involves sintering powders by simultaneously applying electric current and uniaxial pressure. Several parameters can be modified to optimise the sintering process by SPS, including the temperature[13,118], holding time, heating rate[119], applied pressure, or atmosphere[120]. Waetzig et al. investigated sintering temperatures for LATP via SPS ranging from 800 °C to 1050 °C and with a applied pressure of 50 MPa[13]. They observed that maximum densification (96.7 %) was achieved at 900 °C for 5 min of holding time, with an ionic conductivity of 1.0 x 10^{-4} S/cm at room temperature. At higher temperatures, the density decreased, dropping from 96.7 % at 900 °C to 93.2 % at 1050 °C, as illustrated in Figure IV-9-a. This trend is explained by the formation of cracks within the microstructure starting at 1000 °C, leading to increased porosity according to the study[10]. Another study by Duluard et al. also examined the influence of temperature (850-1000 °C) and dwell time (5, 10, 20 minutes) on LATP samples synthesised by sol-gel and sintered by SPS (100 MPa)[121]. Similar to Waetzig et al., they observed a maximum relative density (97 %) at 900 °C, with ionic conductivities around 10^{-4} S/cm, but did not observe a decrease in this value at higher temperatures. However, at 1000 °C, the ionic conductivity dropped to 10^{-5} S/cm due to a loss of cohesion between grains in the pellet[122]. The influence of dwell time is presented in Figure IV-9-b, showing that the variations in relative density and conductivity were not significant with the dwelling time[121].

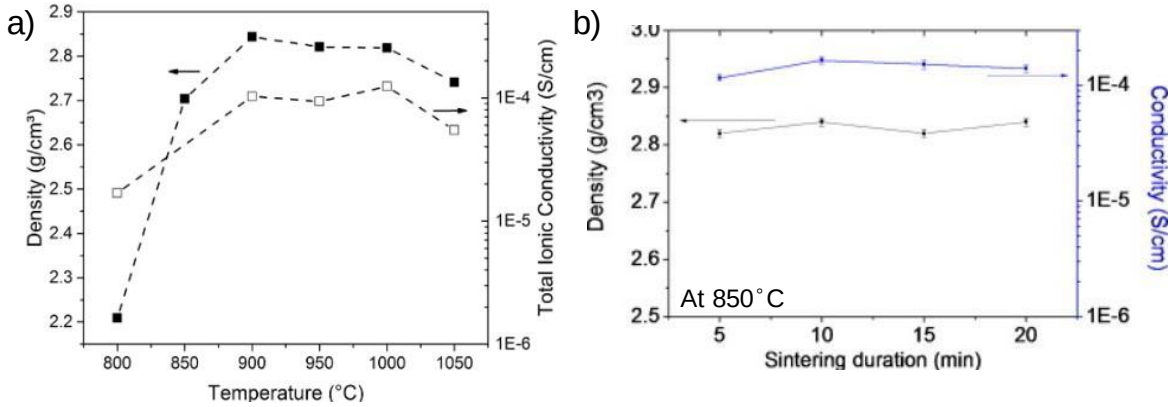

Figure IV-9: (a) Density and total ionic conductivity of LATP pellets as a function of the temperature sintering in SPS. From Waetzig et al. [10] (b) Density and conductivity of LATP pellets as a function of the sintering duration. From Duluard et al.[121]

We can also reference the study by Courbaron et al., which highlighted the influence of the heating rate SPS (50, 73, 100, 200, 300 °C/min) on the relative densities and ionic

conductivities of LATP[119]. At the same temperature of 750 °C, the relative densities reached maximum values of 95 % for heating rates of 50 °C/min and 200 °C/min. Although the ionic conductivities obtained were in the order of 10^{-5} S/cm at room temperature, the activation energy was more favorable in the case of a lower heating rate.

The majority of studies on LATP sintering via SPS achieve relatively high relative densities around 95 % and ionic conductivities on the order of 10^{-4} S/cm at room temperature[13,121]. The thermal treatments applied occur at lower temperatures compared to conventional sintering, specifically 900 °C instead of 1000 °C, with significantly shorter sintering times, typically minutes rather than hours thanks to the application of a pressure and a higher heating rate. However, LATP tends to undergo reduction ($Ti^{4+} \rightarrow Ti^{3+}$), due to the applied current and contact with graphite[119,123]. This reduction, even partial, is problematic as it increases the electronic conductivity of the material. Two possible solutions exist to mitigate this reduction: either limiting the sintering temperature (< 800 °C) or applying a thermal treatment under an oxygenated atmosphere to re-oxidize the material. For example, Courbaron et al. treated their LATP samples at 700 °C for 12 hours under O_2 after sintering via SPS. The complete re-oxidation of Ti^{3+} to Ti^{4+} was confirmed visually by the color transition of the pellet from blue to white, as well as by Electron Spin Resonance (ESR)[119].

IV.3. Sintering techniques involving liquid-phase sintering

IV.3.1. Cold sintering process (CSP)

Cold sintering is a technique that allows the densification of materials at very low temperatures (< 300 °C) by adding a liquid phase, such as a solvent, and applying uniaxial pressure (100-500 MPa)[124]. Typically, the liquid is added in an amount ranging from 1 to 10 vol% and can vary in nature depending on the specific requirements of the sintering process[125]. Conventionally, the densification program for LATP sample is illustrated in Figure IV-10, and it involves a thermal treatment at low temperature, with an applied pressure ranging from 200 to 450 MPa, and eventually followed by a post-treatment at high temperature to enhance the densification and crystallisation[126].

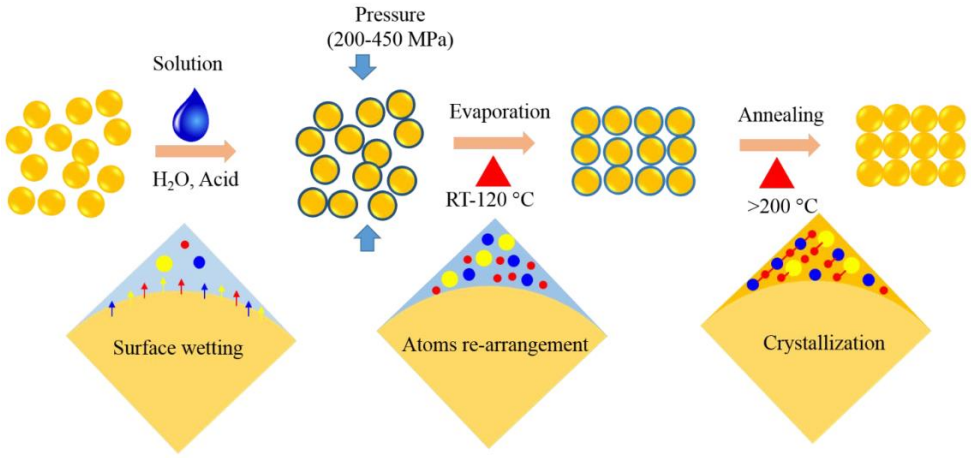

Figure IV-10: Schematic of CSP. From Liu et al.[126]

For example, Liu et al. densified LATP at 120 °C by CSP using two different solvents: water and 1M acid acetic. The CSP step was followed by a heat treatment at 650 °C for 2 h. By comparing these pellets to those sintered by conventional sintering at 1000 °C, they achieved relative densities of 93% with 1 M acetic acid, 79 % with water, and 95 % by conventional sintering. Although the relative density obtained by CSP using 1M acetic acid is comparable to that achieved through conventional sintering, the ionic conductivity after CSP is an order of magnitude lower (10^{-5} S/cm at room temperature) than that obtained with conventional sintering. These values of ionic conductivity and relative density are consistent with other reports in the literature[101,109,127]. This phenomenon may be explained by differences in microstructure. As shown in the Figure IV-11, the grains are smaller (150-300 nm) after CSP treatment compared to conventional sintering (2-5 µm). This indicates that the number of grain boundaries is higher after CSP, which leads to lower ionic conductivity[126,128].

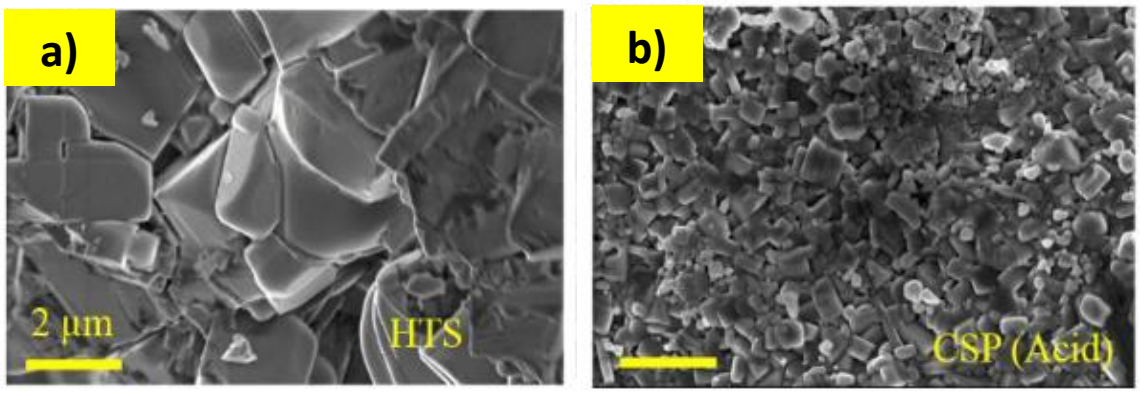

Figure IV-11: SEM images of LATP pellets after (a) conventional sintering at 1000 °C (95 %) and (b) CSP at 120 °C with 1 M acetic acid (93 %). Adapted from Liu et al.[126]

One strategy used to improve ionic conductivity is the dissolution of Li-salts in the solvent. Li-salts such as LiOH, $LiCH_3COO$, $LiNO_3$-LiOH, $LiClO_4$ and LiTFSI have been studied for this purpose[127,129–131]. Indeed, Lee et al. demonstrated that the ionic conductivity of LATP

increased significantly from 2.7 x 10^{-5} S/cm to 1.8 x 10^{-4} S/cm at room temperature with the addition of LiTFSI[129]. We can also refer to the study by Jiang et al., which successfully densified LAGP to 90 % using 10 wt% of $LiClO_4$ under a program of 120 °C for 1 hour and 500 MPa of pressure. This approach led to a slight increase in ionic conductivity, from 3.79 x 10^{-5} S/cm to 6.35 x 10^{-5} S/cm at room temperature[131].

Ultimately, this low ionic conductivity can also be attributed to the amorphization of the material and the precipitation of impurities at grain boundaries. To address these issues, numerous studies have demonstrated the beneficial effects of post-CSP heat treatments at temperatures including 650-1000 °C[124,127,132]. For instance, Cai et al. achieved ionic conductivities on the order of 10^{-4} S/cm at room temperature after a post-treatment at 900 °C for 1 hour, reaching 85 % relative density[133]. This post-treatment significantly improved the ionic conductivity[134], which was two orders of magnitude lower when only CSP was used to achieve a similar density. The process is illustrated in Figure IV-12.

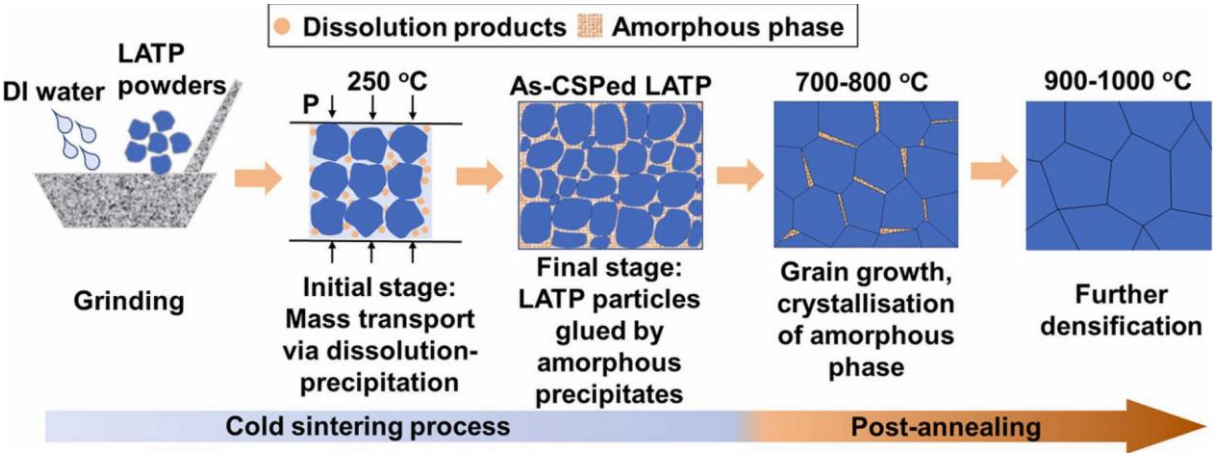

Figure IV-12: Schematic CSP and post-heat treatment. From Cai et al.[133]

CSP does not technically sinter the material but merely densifies it. The need for high-temperature treatment remains crucial to maximize ionic conductivities, as the technique does not promote particle growth and degrades the quality of grain boundaries, due to the uncontrolled precipitation of phases.

IV.3.2. Sintering aids

In parallel, numerous studies have focused on Li-salts as sintering aids for LATP sintering. Unlike other techniques, it does not require any specialized equipment. Indeed, the method is the same as for conventional sintering, except that the sintering aids are initially mixed with the starting powder (see Figure IV-13).

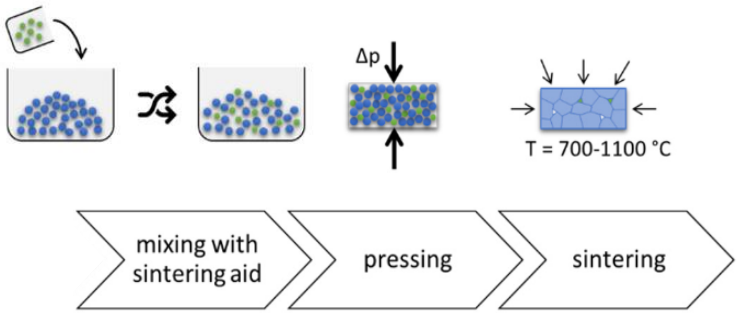

Figure IV-13: Conventional sintering with sintering aids. Adapted from Waetzig et al. [143]

First, a study by Aono et al. demonstrated the effectiveness of this strategy on LTP by adding 2 mol% of Li_3BO_3. They achieved ionic conductivities of 3.0 x 10^{-4} S/cm at room temperature with very low levels of porosity[84]. A study by Rumpel et al. successfully densified LATP at 800 °C by incorporating 5 vol% of Li_3PO_4, while obtaining a good conductivity of 2 x 10^{-4} S/cm at room temperature[135]. This performance was confirmed in the literature, as Shen et al. also managed to densify LATP at 800 °C (94 %) by adding Li_3PO_4[136]. They tested other lithium salts such as $LiBO_2 \cdot 0.3\ H_2O$ and a mixture of 0.32 Li_3PO_4-0.68 $LiBO_2 \cdot 0.3\ H_2O$, but the relative densities were maximized at higher temperatures (900 °C and 850 °C, respectively). The highest ionic conductivity of 5.2 x 10^{-4} S/cm at room temperature was obtained for the compound with Li_3PO_4. Other Li-salts have been tested in the literature, such as Li_2O[137], LiF[138,139], $LiBF_4$[140], $LiBO_2$[141], $LiNO_3$[123,142], LiCl[143], and Li_2CO_3[143], and most show an increase in relative density at lower temperatures while maintaining ionic conductivities around 10^{-4} S/cm. In principle, their addition allows sintering of the material at lower temperatures due to the melting of the salt, which can occur at higher or lower temperatures depending on its nature. The melting of the salt introduces a liquid phase into the system, possibly enabling liquid-phase sintering[96]. However, a study by Waetzig et al. showed that there is no correlation between the maximum sintering temperature of LATP and the melting point of the salts added, as illustrated in Figure IV-14[143]. For example, LiOH, with a melting temperature of 462 °C, enables the densification of LATP around 800 °C, while a salt like $LiBO_2$, with a melting temperature of 849 °C, allows densification of LATP at 775 °C. Although no clear trend is observed, other phenomena occur, such as the systematic formation of impurities like $Li_4P_2O_7$ and $LiTiOPO_4$, regardless of the Li-salts system studied[123,135,139,143,144].

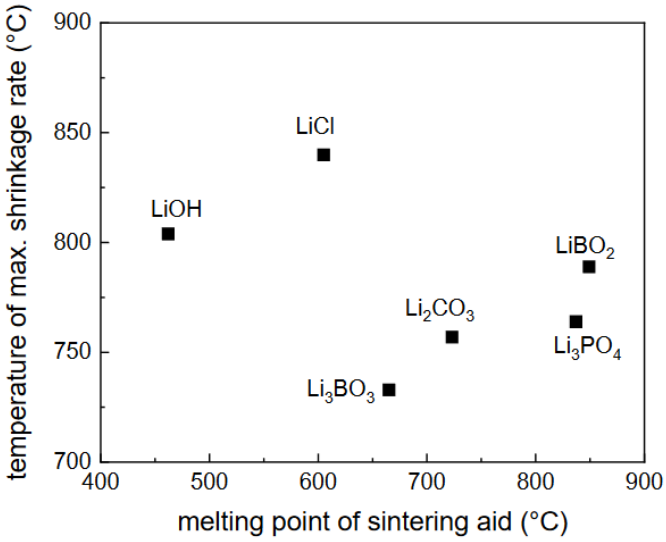

Figure IV-14: Maximum temperature of the shrinkage rate, related to the sintering, of LATP with 15 mol% of sintering aid as a function of the melting temperature of the aids. From Waetzig et al. [143]

Although this method seems very promising, as it combines low sintering temperatures (700-900 °C) with good ionic conductivity (10^{-4} S/cm), the underlying mechanism remains unknown and needs to be further explored to potentially decrease the sintering temperatures of LATP even further.

V. Co-sintering

We have seen that densifying LATP is important for maximising its ionic conductivity and that sintering temperatures can vary from 800 °C to 1100 °C depending on the techniques used. The need for densification also stems from the goal of improving solid-solid contacts, as in the case of the separator (solid electrolytes), but also in the case of the composite positive electrode which contains the solid electrolyte, active material, and conductive additives[145]. In the latter case, we refer to co-sintering, which involves densifying all the components at high temperatures to maximise contact at the interfaces as illustrated in Figure V-1.

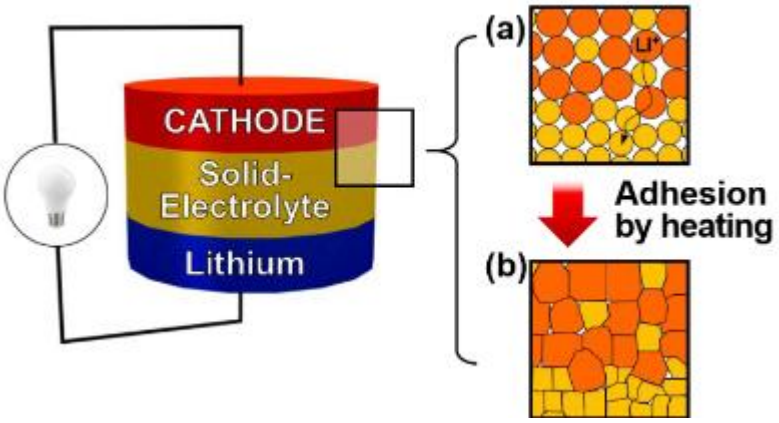

Figure V-1: Schema of a mixture of active material and solid electrolyte (a) before and (b) after co-sintering. From Yu et al. [145]

The co-sintering is problematic since several studies have shown that LATP reacts with most active materials at temperatures lower than those required for its sintering. For example, Yu et al. studied the chemical stability of LATP with the active materials $LiNi_{0.5}Mn_{1.5}O_4$ (LNMO), $LiNi_xMn_yCo_{1-x-y}O_2$ (NMC), $LiFePO_4$ (LFP), $LiCoO_2$ (LCO), and $LiNiO_2$ (LNO) in temperature ranges between 500-900 °C[145]. Using 1:1 molar ratio mixture of LATP and active material, thermally treated and analysed by X-ray diffraction, they determined the reactivity temperatures for each system as well as the decomposition products. These temperatures vary depending on the nature of the active material, as shown in Figure V-2. For instance, LATP-LNMO system reactivity begins at 700 °C, whereas for LATP-LFP, it starts as low as 500 °C. Most of the decomposition products take the form of $LiMPO_4$ (M = Mn, Ni, Co, etc.).

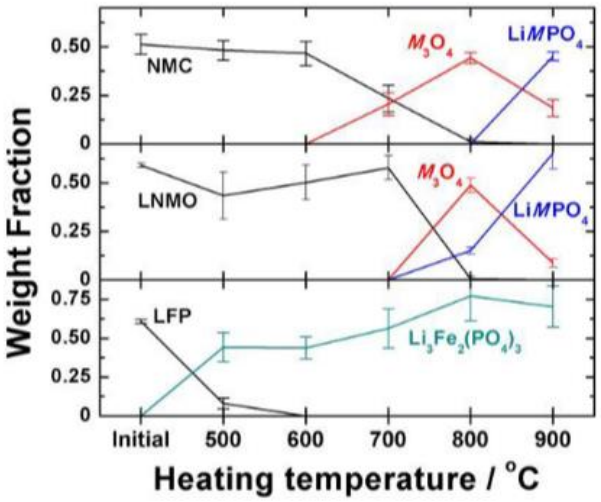

Figure V-2: Simplified diagram of the weight fraction of the different compounds formed and consumed for three mixtures of LATP and active material (1:1) as a function of the temperature. From Yu et al. [145]

In the case of the active material LCO, a study by Ichihara et al. identified three reaction stages with LATP, the first of which begins as early as 300 °C[146]. Another study by Miara et al. also confirmed this incompatibility between LATP and active materials with spinel structures ($Li_2NiMn_3O_8$, $Li_2FeMn_3O_8$, $LiCoMnO_4$) at high temperatures: degradation occurs as early as 600 °C, accompanied by the formation of impurities such as Li_3PO_4, TiO_2, and $LiMPO_4$[147].

These impurities are evidence of the decomposition of the solid electrolyte and the active material, leading to a decrease in the electrochemical properties of the system. Similarly, insufficient densification of the solid electrolyte would result in reduced contacts and, consequently, lower performance[145].

It is therefore essential to find strategies to lower the temperature at which LATP densifies to avoid these issues.

VI. Conclusions of Chapter I

Chapter I established the fundamental knowledge of all-solid-state battery technology and the necessity of transitioning from Li-ion technology to these advanced batteries. This shift is driven by the need to enhance both safety and performance. However, a major challenge in this technology is the selection of the electrolyte, as each type presents its own set of challenges. For instance, polymer electrolytes exhibit low ionic conductivity at room temperature, while sulphide-based electrolytes decompose upon exposure to air, releasing toxic gases.

Given these issues, our focus has shifted to solid oxide electrolytes, which generally exhibit favourable properties but require high-temperature processes, such as sintering, to maximise their ionic conductivity and compatibility with other battery components (solid electrolyte particle and active material). These thermal treatments are energy-consuming, often requiring temperature above 1000 °C to achieve relative densities over 95 % for conventional LATP sintering. Alternative methods, such as Hot Isostatic Pressing (HIP) or Spark Plasma Sintering (SPS), can reduce the sintering temperature and/or duration, but they involve expensive equipment and still operate around 900 °C. The Cold Sintering Process (CSP) allows densification at much lower temperatures (120-200 °C); however, the resulting ionic conductivities are too low (10^{-5} S/cm), necessitating a high-temperature post-treatment.

The addition of Li-salts has emerged as a promising approach, enabling densification at lower temperatures (around 800 °C) while maintaining adequate ionic conductivities (10^{-4} S/cm). However, the underlying mechanism of this method needs further investigation to potentially decrease sintering temperatures even more.

Densifying LATP presents an additional challenge because, despite being an excellent candidate for forming composite positive electrodes, the sintering process can degrade both the electrolyte and the active material.

To address this, this thesis explores several strategies aimed at reducing the sintering temperature of LATP. These include studying the effects of particle size and morphology on conventional sintering, investigating the mechanisms that enable densification at lower temperatures with the addition of Li-salts, and exploring the combination of SPS with Li-salts.

Chapter II: Solid-state sintering, impact of size particle and morphology

I. Introduction

In Chapter I, we presented that the densification of LATP requires a sintering step at temperatures typically exceeding 1000 °C to achieve maximum relative densities[85,148]. This densification temperature is crucial for enhancing ionic conductivity and ensuring good interfaces within the material.

Decreasing particle size is widely recognised in the literature for its beneficial effects on the densification temperature. For instance, Waetzig et al. demonstrated through dilatometry that the onset of LATP densification occurred 100 °C earlier for nanoparticles compared to micro-particles, with maximum densification observed at 1020 °C instead of 1050 °C, respectively[13]. In a study by Raj et al., densification of LATP nanoparticles was completed at 850 °C, whereas it required 940 °C for micro-particles under the same sintering process[105]. Ma et al. found that LATP synthesised with nanometer-sized primary particles (60-150 nm) densified within a temperature range of 810 °C to 880 °C[149].

Based on these studies, we first investigated the effect of particle size by comparing the densification temperatures and behaviour of synthesised LATP with micrometre-sized primary particles to those of commercial $LATP_{0.3}$ with nanometre-sized primary particles. This initial study also aims to define the various characteristics of $LATP_{0.3}$.

In the second part, the impact of secondary particle size on densification will be examined, particularly using spray drying, known for producing spherical particles with controlled sizes. Finally, the ionic properties of the most promising materials, in terms of densification, will be studied.

II. Impact of particle size on $LATP_{0.3}$ densification

II.1. Synthesis of micron-sized particles and introduction to commercial nanoscale $LATP_{0.3}$

II.1.1. Material synthesis

For the micron-sized LATP particles, one of the most commonly used synthesis methods for $Li_{1.3}Al_{0.3}Ti_{1.7}(PO_4)_3$ ($LATP_{0.3}$) in the literature is the solid-state reaction synthesis. This method is widely used due to its ease of execution and the high purity of the synthesised product[59,150,151]. The synthesis involves two steps including grinding and homogeneously mixing the starting precursors in stoichiometric proportions, followed by a high temperature heat treatment[59].

Initially, the synthesis was adapted from Aono et al.[59] and Liang et al.[152]. It was conducted using Li_2CO_3 (Sigma-Aldrich), Al_2O_3 (Sigma-Aldrich), TiO_2 anatase (Sigma-Aldrich, 99.9%) and $NH_4H_2PO_4$ (Sigma-Aldrich, > 98%). All starting material were mixed in stoichiometric proportions by ball-milling in a Retsch PM-100 planetary mill, with 1/2/10 mass ratios of sample powder/ isopropanol/ Ø5 mm Zirconia beads in a 250 mL zirconia grinding jar and in order to synthesise 30 g of $LATP_{0.3}$. The milling process was carried out at a speed of 450 rpm for 2 h (10 min grinding cycle with 10 min pause). The solvent was then removed under air atmosphere for 12 h, and the dried powder mixture was placed in an alumina crucible. The powder was calcined at 900 °C for 2 h, with a heating ramp of 5 °C/min in a muffle furnace. The overall synthesis reaction is summarised by Equation (1):

$$0.65\ Li_2CO_3 + 0.15\ Al_2O_3 + 1.7\ TiO_2 + 3\ NH_4H_2PO_4 \rightarrow Li_{1.3}Al_{0.3}Ti_{1.7}(PO_4)_3 + 0.65\ CO_2 + 4.5\ H_2O + 3\ NH_3 \quad (1)$$

At the end of the synthesis, a grinding step using a mortar followed by ball milling was performed to break up the aggregates and obtain a fine powder. The powder was placed in 250 mL grinding jar, and the following milling program was used: 400 rpm for 30 minutes with Ø5 mm Zirconia beads. The milling process was carried out without solvent and with 1/10 mass ratios of sample/ Ø5 mm Zirconia beads.

In parallel, $LATP_{0.3}$ commercial (Ampcera) with a monodisperse particle size diameter of 300 nm was used as a comparison with synthesised LATP.

II.1.2. Nature and powder morphology

Both products were subsequently characterised by X-ray diffraction (XRD) to confirm their nature and composition. The analyses were conducted using the following acquisition parameters, which are considered standard: 2θ = 10-80 °, with 0.02 ° steps and a time of 0.2 s/step. They were carried out with a fixed slit of 0.18 cm and with a Cu anode ($\lambda K_{\alpha1}$ = 1.54056 Å, $\lambda K_{\alpha2}$ = 1.54439 Å). The results presented in Figure II-1 show the presence of characteristic diffraction peaks of $LATP_{0.3}$, which has a rhombohedral structure with *R*-3*c* space group for both products. However, the commercial $LATP_{0.3}$ is not pure, as the main diffraction peak of $AlPO_4$ phase ($C222_1$) at 21.8 ° is visible. Although only a single diffraction peak is observed, this impurity has been frequently reported in the literature, as it is commonly formed during synthesis[13,153,154] or after a sintering step at high temperature[85]. This formation could suggest that the aluminium content of the LATP phase may not be exactly 0.3.

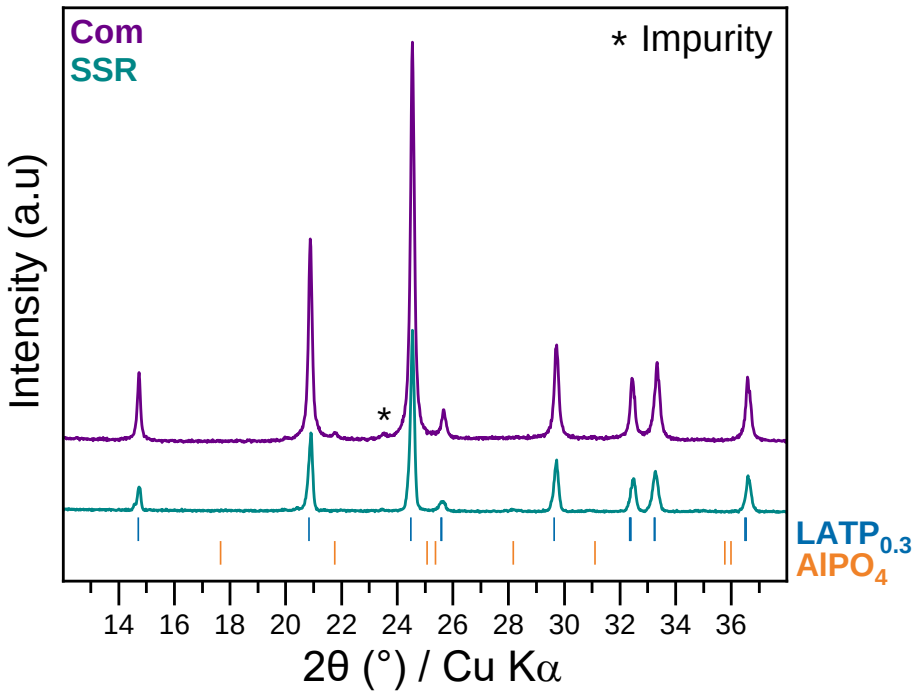

Figure II-1: XRD patterns of $LATP_{0.3}$ synthesised by solid-state reaction after heat treatment at 900 °C during 2 h (SSR) (—) and $LATP_{0.3}$ commercial (Com) (—).

Next, the patterns were refined using Le Bail refinements to determine the lattice parameters. The fits presented in Figure II-2 appear to be accurate, with χ^2 values close to and slightly above 1. In the same figure, the lattice parameters extracted from the refinements are also presented. As a reminder, the material presents an orthorhombic symmetry with a *R*-3*c* space group, where $a = b \neq c$ and $\alpha = \beta = 90$ ° and $\gamma = 180$ °[93,155]. The resulting lattice parameters are similar for both LATP, and the values are in good agreement with those in the literature for this level of

substitution[13,76,78,156]. Nevertheless, interpreting the aluminium content using this technique is an approximation, as several lattice parameter values have been reported in the literature for the same aluminium content.

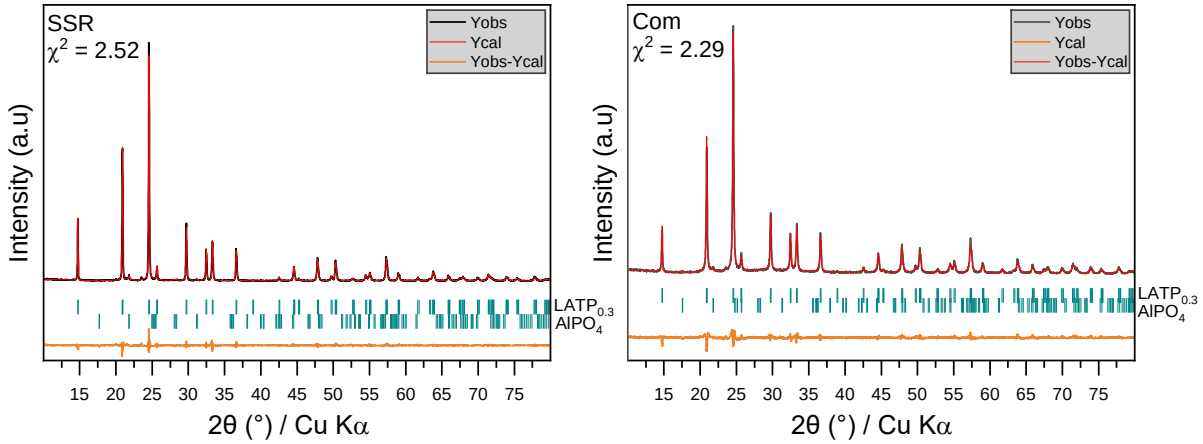

Samples	*a* = *b* (Å)	*c* (Å)	Reference
SSR	**8.4969(1)**	**20.8341(3)**	Our work
Com	**8.4975(2)**	**20.8288(7)**	Our work
$LATP_{0.3}$	8.4987(7)	20.8316(3)	[157]
$LATP_{0.3}$	8.5063(9)	20.8325(4)	[158]

Figure II-2: Le Bail refinement patterns of $LATP_{0.3}$ SSR and $LATP_{0.3}$ Com powders sample. Experimental plots are shown in black lines, calculated in red lines, Bragg reflection peaks by blue vertical lines and difference plot by orange line. Based on these fits, values of lattice parameters were extracted for both products.

Next, the particle size was determined using two methods: laser granulometry and scanning electron microscopy (SEM). The laser granulometry analysis reveals the particle size distribution for the sample, spanning a range between 0.5 and 400 µm. The analysis was conducted on 30 ml solution of pure ethanol containing a few milligrams of powder under stirring. The results are represented as cumulative number distributions relative to particle size, allowing us to extract the D10, D50, and D90 values. The results are shown in Figure II-3. For the SSR sample, the D90 is ~15 µm, meaning that 90 % of the particles have diameters less than or equal to this value. This D90 is three times larger than that of the commercial $LATP_{0.3}$ sample, which has a D90 of approximately 5 µm. On average, the particles in the $LATP_{0.3}$ SSR sample are larger than those in the commercial $LATP_{0.3}$ sample. The size distribution is broader for the SSR sample compared to the commercial $LATP_{0.3}$. In contrast, the $LATP_{0.3}$ com is characterised by a majority of small particles, with some large aggregates that are also present. However, it is important to point out that particles smaller than 0.5 µm are not considered, which can impact the results obtained, particularity with $LATP_{0.3}$ com.

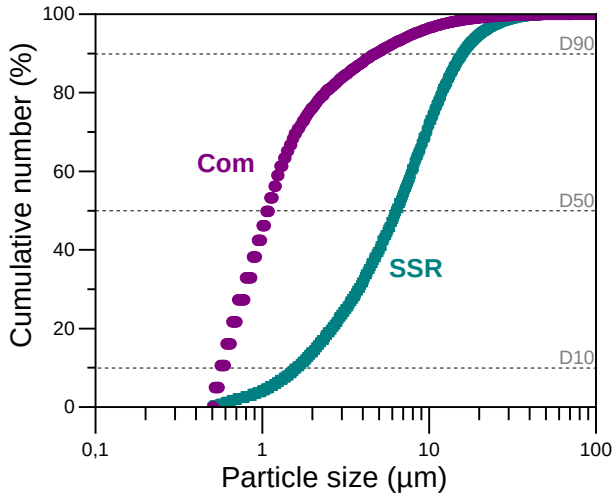

	SSR	Com
D10	1.6	0.5
D50	6	1
D90	15	5

Figure II-3: Laser granulometry results for SSR (■) and Com (■) samples dispersed in pure ethanol solution.

On the other hand, the scanning electron microscopy (SEM) was conducted to study the morphology and the size of the primary particle of the two samples. The size of the primary particles was determined graphically using the software ImageJ. As displayed on Figure II-4, the $LATP_{0.3}$ SSR is composed of irregular-shaped primary particles with an average size of 1 µm whereas the $LATP_{0.3}$ Com sample consists of irregular-shaped particles of 0.3 µm.

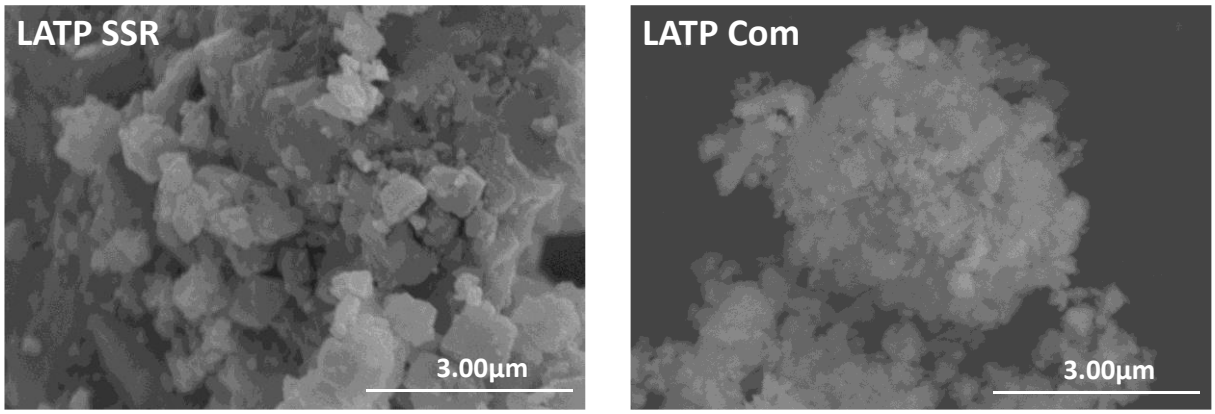

Figure II-4: SEM images of LATP SSR (to the left) and LATP com (to the right).

These analyses confirm that the particles of commercial $LATP_{0.3}$ (LATP Com) are generally smaller than those of $LATP_{0.3}$ synthesised via the solid-state reaction (LATP SSR). In the case of $LATP_{0.3}$ Com, the SEM analyses shows that particles predominantly consist of micron-sized aggregates, which are composed of primary nanometric particles. Therefore, for the remainder of this study, we will refer to the size of the primary particles of the powders: $LATP_{0.3}$ com as nanometres particles and LATP SSR as micrometric particles.

II.2. $LATP_{0.3}$ densification

II.2.1. Stability at high temperature

The previous section allowed us to confirm both the nature and the particle size for the two samples. However, before studying the sintering of the materials, their stability at high temperature was investigated using thermogravimetric analysis (TG). The experiments were conducted from 30 °C to 1000 °C, with a heating ramp of 10 °C/min and an air flow rate of 25 ml/min. The results are displayed on Figure II-5. The TG curve for the $LATP_{0.3}$ SSR sample shows that the material loses a total mass of approximately 2 %, whereas this loss is twice as significant for $LATP_{0.3}$ Com. This difference can be explained by a higher water adsorption in the case of $LATP_{0.3}$ Com, as the smaller particles are more reactive. However, the mass losses observed are continuous throughout the thermal treatment, suggesting that some residual organic species from the precursors may be decomposed. Given that the total mass losses are minimal (< 5%), the materials are considered stable at high temperatures. According to the literature, the decomposition temperature of $LATP_{0.3}$ is around 1200 °C[147], although lithium losses (Li_2O evaporation) can occur as early as 900 °C[13,85,86,159].

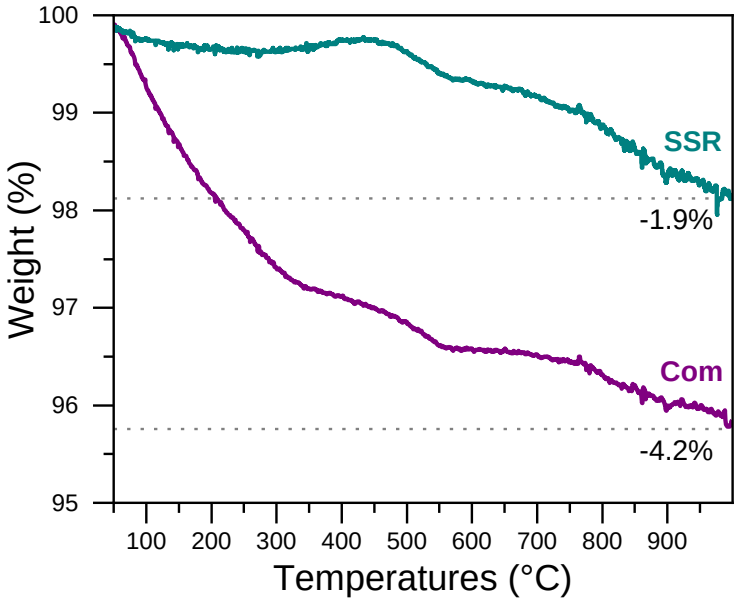

Figure II-5: TG curves of LATP SSR powder (—) and LATP Com powder (—).

II.2.2. Impact of the size of primary particles on the densification processes

Many factors can impact the sintering of a ceramic such as the heating ramp, the dwelling time or the temperature of the heat treatment[97]. The latter one is the key factor: according to the literature, $LATP_{0.3}$ sintering begins around 700 °C, but temperatures exceeding 1000 °C are necessary to maximise relative densities[13,102,150]. This temperature range is broad, and the optimal temperature for densification varies from one sample to another, depending on the morphology and therefore by the method used to synthesise the material[75,94,149,160]. The ideal technique for determining the densification temperature is the dilatometry, as this is a technique that measures the dimensional changes of a material as a function of temperature. Usually, the process involves gradually heating a pellet of the material and recording the changes in thickness (ΔL) in real-time. This value is then compared to the initial thickness (L_0) of the pellet to obtain a shrinkage curve as a function of temperature.

In our study, $LATP_{0.3}$ SSR and Com samples were analysed using dilatometry to confirm the beneficial impact of smaller particle size on the densification temperature of $LATP_{0.3}$. The analysis was conducted on 8 mm diameter pellets, pressed at 1.5 ton for approximately 1 minute. The experiments were carried out from 25 °C to 1000 °C under air, with a heating rate of 5 °C/min. The results are shown in Figure II-6. Initially, a slight expansion of the pellet is observed in both cases until shrinkage begins around 650-700 °C. This volume increase is explained by the effect of thermal dilatation of the grains as the temperature rises[95]. Subsequently, shrinkage continues beyond 1000 °C in the $LATP_{0.3}$ SSR curve. This stage corresponds to the sintering process, which involves the initial formation of bridges between particles, followed by a reduction in both open and closed porosity within the pellet[95,97]. The derivative of the curve reveals a plateau between 900 °C and 1000 °C, indicating that the process reaches its maximum within this temperature range. In comparison, the maximum densification occurs at 781 °C for the commercial sample with nanometre-sized primary particles, showing that the densification temperature is lower for nanometric particles compared to micrometric ones. For the same heat treatment program, a greater relative shrinkage is observed for the commercial $LATP_{0.3}$ (16 %) compared to the SSR $LATP_{0.3}$ (7 %).

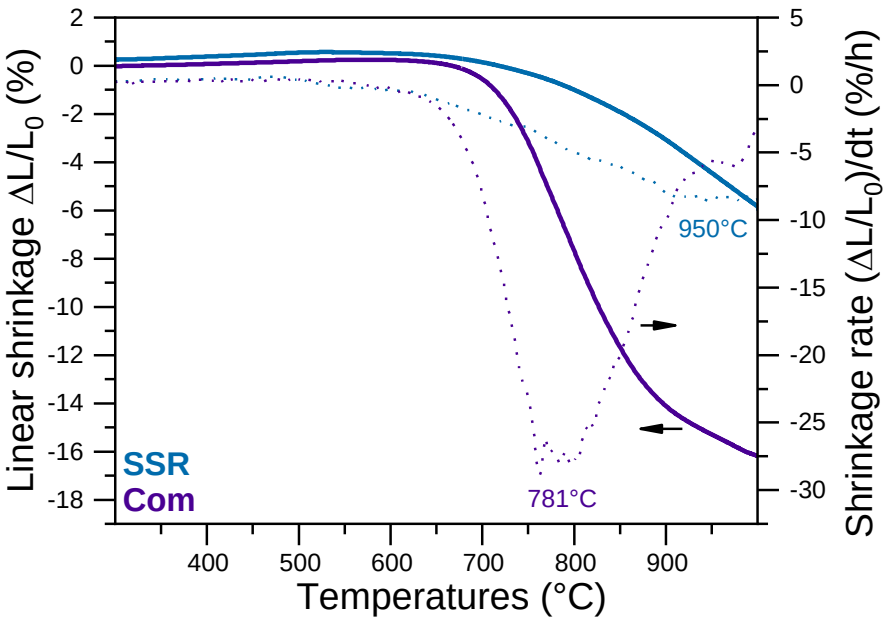

Figure II-6: Dilatometry experiments of pellet of $LATP_{0.3}$ SSR (—) and $LATP_{0.3}$ Com (—). The dashed lines represent the derivatives of the dilatometry curves.

These results confirm that decreasing the particle size of $LATP_{0.3}$ enhances the densification process at lower temperatures. To explain this observation, a reminder of the solid-state sintering mechanism is necessary. As previously discussed in Chapter I, the first step in sintering involves the formation of bridges between particles through various diffusion processes within the materials. According to the Herring's scaling law[161], the rate of material transport during sintering depends on the particle size. Indeed, when the particles are smaller, they have a larger specific surface area and increased capillary pressure, which accelerates the sintering process. This results in faster sintering at lower temperatures or over a shorter period of time for smaller granulometry[162,163].

Nevertheless, this improvement is not as significant as reported in the literature, where temperatures typically shift by only 50 or 100 °C when transitioning from micron-sized to nano-sized particles[13,105].

In parallel with dilatometry analysis, conventional sintering experiments were conducted. This method involves applying heat treatment to pellets of the material for a specified duration in a controlled atmosphere. Three pellets per sample (SSR and Com), each with a diameter of 13 mm and weighing approximately 300 mg, were prepared by applying a pressure of 3.5 ton. A heat treatment followed this program: the pellets were placed in alumina crucibles and heated to 900 °C for 6 hours, with a heating rate of 5 °C/min in a muffle furnace. The cooling process occurred passively as the furnace cooled down.

The relative densities of the pellets before and after sintering were determined using Equation 2:

$$\text{Relative Density (RD)} = \frac{Measured\ Density}{Theoretical\ Density} \times 100 \quad (2)$$

The theoretical density of $LATP_{0.3}$ is 2.92 g/cm³[108]. The measured density (g/cm³) for each pellet was determined using geometric measurements and according to Equation 3[86]:

$$\text{Measured density} = \frac{m}{\pi \times r^2 \times h} \quad (3)$$

where m, r and h correspond to the mass (g), the radius (cm) and the thickness of the pellet (cm) respectively. All the values for the green densities (before sintering) and relative densities (after sintering) are compiled in Figure II-7. First, we can observe better compaction before sintering for the $LATP_{0.3}$ SSR pellets, with green density values around 70 %, whereas for the $LATP_{0.3}$ com pellets, the green densities are around 60 %. This improved packing in the SSR case can be explained by the broader particle size distribution observed in Figure II-3, where smaller particles tend to fill the gaps between the larger particles during pressing[164]. By comparing these green densities with the obtained relative densities, we can observe that the powders were successfully sintered, with relative densities reaching up to 90 %.

Although smaller particle size accelerates sintering at lower temperatures, at an equal sintering temperature of 900 °C, the relative densities are similar in both cases. This can be explained by the significantly higher initial compaction observed with the micron-sized powder.

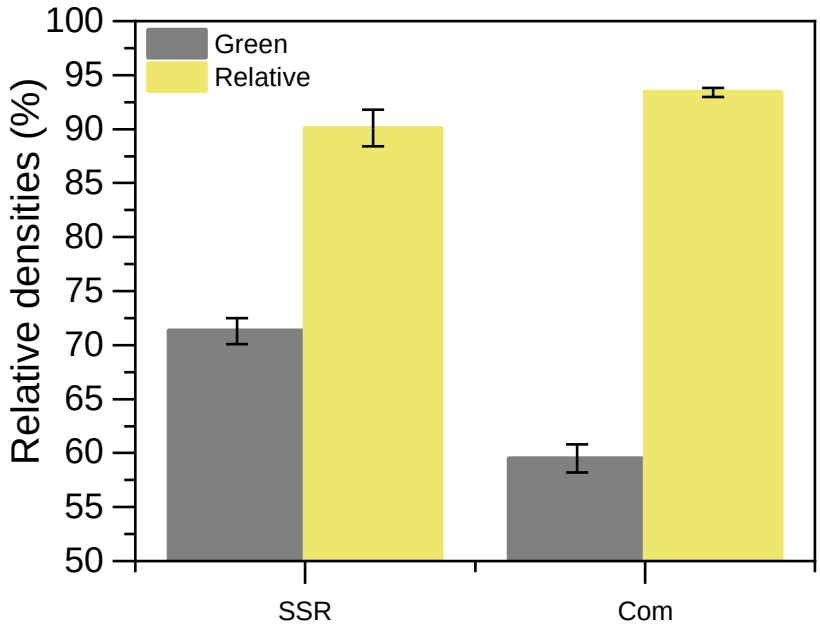

Figure II-7: Comparison of the green relative densities and the relative densities of $LATP_{0.3}$ SSR and Com pellets after heat treatments at 900 °C for 6 h.

II.2.3. Impact of the size of primary particles on the grain morphology after densification

The microstructure of these pellets was studied using scanning electron microscopy (SEM). To achieve this, the pellets were broken before analysis in order to visualise the core of the samples. The results are presented in Figure II-8. First, the sample composed of $LATP_{0.3}$ SSR (Figure II-4-a) shows grains with a cubic shape and a fairly monodisperse size of around 1.2 µm.
Then, for the Com sample, the grain size is polydisperse: small particles in the range of 0.1 to 1 µm are accompanied by larger grains exceeding 5 µm due to abnormal grain growth (AGG). This phenomenon occurs when some grains grow disproportionally larger than the surrounding grains, disrupting the microstructural homogeneity[165]. This is problematic as it leads to micro-cracking (indicated by red arrows in Figure II-8-a), which, according to the literature, tends to decrease mechanical and ionic conductivity properties[108,121,128]. Micro-cracks typically appear when the grain size exceeds 1.6-1.9 µm, as noted by Jackman et al. and Waetzig et al[13,108]. This suggests that it is crucial to adjust the initial primary particle size, particularly by selecting particles smaller than 1.6 µm, to prevent the formation of micro-cracks. However, unlike what is reported in the literature[13,105,121,149], we observed that this phenomenon occurred in the nanometre-sized sample but not in the micrometre-sized one.

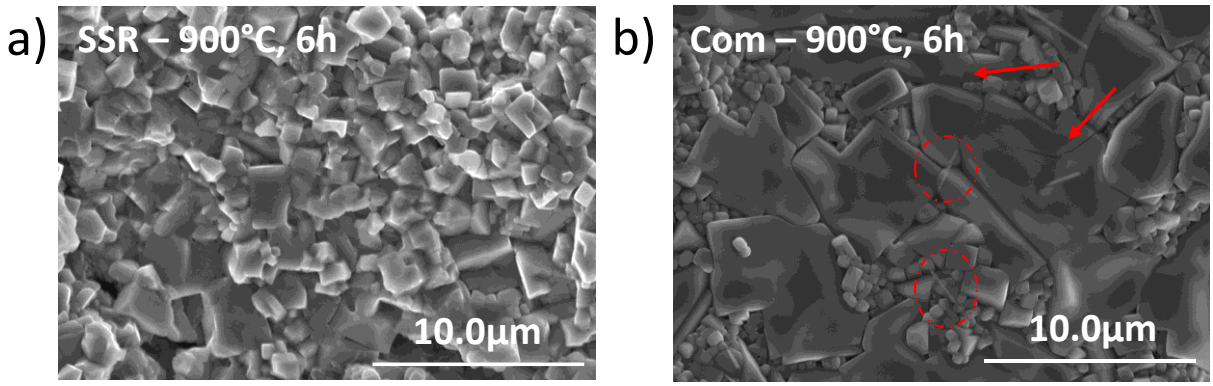

Figure II-8: SEM images of broken pellets of (a) $LATP_{0.3}$ SSR and (b) $LATP_{0.3}$ com after a heat treatment at 900 °C for 6 h under air atmosphere. The red arrows indicate microcracking, and the red dashed circles highlight filaments whose origin remains unidentified.

Two hypotheses can be proposed: the first is that the presence of large aggregates, with a higher local green density compared to other particles, leads to faster densification kinetics in some spots of the sample. This creates an imbalance in the overall progress of densification. The second could be linked to the presence of some filaments (red dashed circles) of indeterminate origin which are observed for the $LATP_{0.3}$ Com sample in Figure II-8-b. This observation, coupled with the 4 % of mass loss in TG (Figure II-5) and the significant improvement in

densification rate at lower temperature (Figure II-6) lead us to question the composition of the Com sample and the possible presence of additives that could alter the growth of the grains.

II.2.4. Investigation of AGG origin for $LATP_{0.3}$ commercial

Therefore, we decided to perform a 2-hour heat treatment on the commercial sample, under air atmosphere at 300 °C and 600 °C to remove any potential additives. The initial powder is white, but it turned grey after treatment at 300 °C. However, it returned to white after thermal treatment at 600 °C, suggesting that organic compounds were present in the initial commercial powder.

A sintering step was performed on the sample heat treated at 600 °C, called Com treated, under the same conditions as those presented in Figure II-7: the powder was pressed into pellets and subjected to thermal treatment in air for 6 hours at 900 °C, with a heating ramp of 5 °C/min. The relative densities of these pellets were measured and compared to the other samples, as shown in Figure II-9. The green densities of the treated commercial pellets are in the same range, around 60 %, as the untreated commercial sample. However, the relative densities only reached 80 % for the treated sample, which is lower than those of both the SSR and the original commercial samples. One of the treated and sintered pellets was fractured for SEM analysis, with the results shown in Figure II-9. Compared to the untreated commercial $LATP_{0.3}$ pellet (Figure II-8-b), the sample exhibits a more uniform grain size, predominantly consisting of larger grains. Some smaller particles are also present, which could explain why the pellet only achieved 80 % relative density.

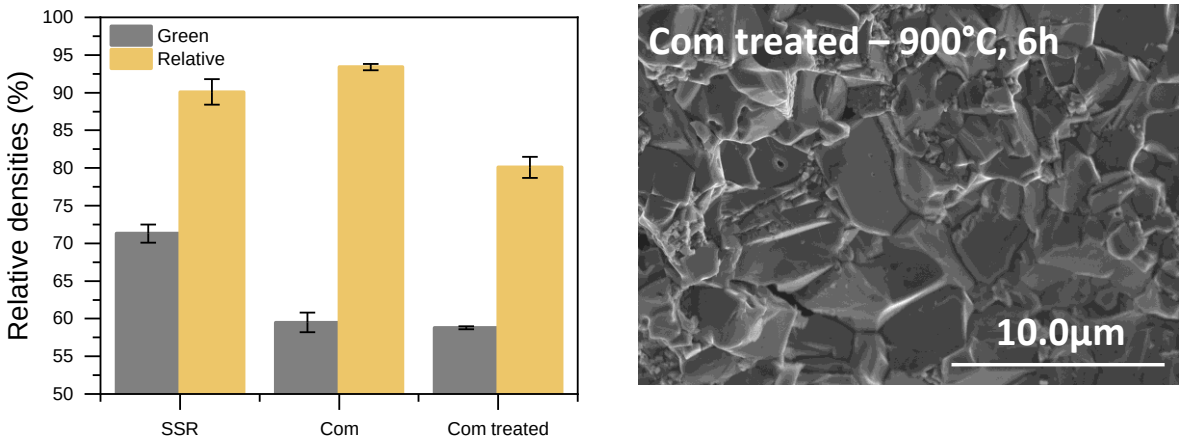

Figure II-9: Comparison of relative densities and green densities of pellets of $LATP_{0.3}$ SSR, Com, and Com treated at 600 °C for 2 h, after a sintering step at 900 °C for 6 h under air atmosphere (to the left). SEM image of a broken pellet of LATP0.3 Com treated, after a sintering step at 900 °C for 2 h (to the right).

This result does not allow us to confirm either hypothesis because the heat treatment before the sintering step may have altered the particle morphology, potentially leading to the formation of more aggregates or causing partial sintering between particles. Nevertheless, this heat treatment successfully removed the filaments, as they are no longer observed in Figure II-9. In order to determine the origin of these residues, some characterisations were performed on the commercial powder treated. First, it was characterised by XRD, but it showed no difference from the initial commercial power. The chemical composition of the two samples was also compared after analysis by Wavelength Dispersive X-ray Fluorescence Spectroscopy (WDXRF). For this end, each sample was compacted at 8 ton during 2 min using a uniaxial press. The results are summarised in the Table 1, wherein the mass content of each atom (Ti, O, Al) was normalised to the phosphorus content.

Samples	Ti/P	O/P	Al/P
Theoretical	0.87	2.06	0.08
Commercial	0.88 (± 0.001)	2.22 (± 0.09)	0.08 (± 0.01)
Commercial treated	0.88 (± 0.01)	2.20 (± 0.04)	0.08 (± 0.005)

Table 1: WDXRF data of $LATP_{0.3}$ commercial and $LATP_{0.3}$ commercial treated at 600 °C for 2 h in air.

The theoretical mass ratios were calculated based on the formula of the $LATP_{0.3}$. The Al/P and Ti/P ratios are identical for both samples and align with the theoretical expectations. The O/P ratios are also similar between the two samples, but a slight excess of oxygen is observed compared to the theoretical values. This discrepancy could be attributed to absorbed water on the surface of the particles, as no other atoms in significant quantities were detected during the analysis. Further characterisation is required to better identify this additive. For example, we could consider thermogravimetric analysis (TG) coupled with mass spectrometry (MS), infrared spectroscopy analysis, or perform energy-dispersive X-ray spectroscopy (EDX) to determine the nature of the filaments shown in Figure II-8-c.

II.3. Conclusion

Decreasing particle size has a well-documented beneficial impact in the literature, as numerous studies have demonstrated a decrease in densification temperature when moving from the micron scale to the nanometres scale[13,75,105,121,149]. However, the use of nanometric particles does not bring beneficial effects. In our case, AGG is observed after sintering, leading to micro-cracking and consequently increased porosity. This phenomenon is not commonly observed in the literature for this particle size and it could be explained by the potentially presence of unidentified additives or large aggregates.

Although we have not presented any ionic conduction properties in this section, it is noteworthy that a study by Li et al. demonstrated that the microstructure obtained from sample composed of particles smaller than 400 nm exhibited a greater number of grain boundaries compared to that achieved from initial micron-sized particles[128]. Consequently, this results in a decrease of ionic conductivity properties compared to samples made from micron-sized initial particles.

In other words, it is necessary to use primary particles with a size smaller than 1.6 µm to achieve densification and avoid the formation of pores due to micro-cracking[108], but they should not be smaller than 400 nm to maximise the ionic conductivity properties of $LATP_{0.3}$[64].

III. Control of the particle morphology of $LATP_{0.3}$

Other synthesis methods are described in the literature, which can be grouped under liquid-phase synthesis. Within this category, we can cite the sol-gel synthesis[85,118,149,150,156,166], modified Pechini methods[167], co-precipitation[91,168], spray drying[160,169,170], and others[92,171]. Compared to solid-state synthesis, these methods offer better homogeneity of reactions at the molecular level, which allows for precise adjustment of morphology and microstructure. According to the literature, this control can notably improve ionic conductivity and decrease synthesis temperatures[75].

In this section, we focused specifically on the spray drying route, which is notable for producing spherical particles with sizes that can be easily controlled. The spray drying processing parameters will be adjusted to examine their impact on secondary particle size and its effect on densification. We expect that these modifications, along with the advantages of liquid-phase synthesis methods, will result in $LATP_{0.3}$ with improved densification properties and enhanced ionic conductivity.

III.1. $LATP_{0.3}$ synthesis

We adapted a three-step synthesis process described by Schroeder et al.[169], which involves the preparation of an $LATP_{0.3}$ precursor solution through the precipitation of reactants, followed by drying or rather atomisation of the solution using spray drying, and finally the crystallisation of the $LATP_{0.3}$ by a high temperature heat treatment.

III.1.1. Solution preparation by the precipitation route

The synthesis was conducted from the starting material lithium acetate (Sigma, $Li(CH_3COO)$), basic aluminium acetate (Sigma, $Al(CH_3COO)_2OH$), titanium butoxide (Sigma, $Ti(OCH_2(CH_2)_2CH_3)_4$) and ammonium dihydrogen phosphate (Sigma-Aldrich, > 98%, $NH_4H_2PO_4$). All starting material were weighed according to the following molar ratio: 1.3:0.3:1.7:3 respectively. First, the lithium acetate was dissolved in a solution mixture of pure ethanol and acetic acid in a 1:1 volume ratio. In parallel, the basic aluminium acetate was dissolved in a solution mixture of pure ethanol and distilled water in a 1:1 volume ratio. The two solutions were then mixed together under stirring. The titanium butoxide, which was previously mixed with pure ethanol, was added to the solution containing the dissolved Li and Al precursors under stirring. Subsequently, the ammonium dihydrogen phosphate was

dissolved in distilled water and slowly added to the reaction mixture under stirring. By the end of the addition, the translucent solution had turned into a white gel-like solution. The various steps of the synthesis pre-Spray Drying are summarised in Figure III-1.

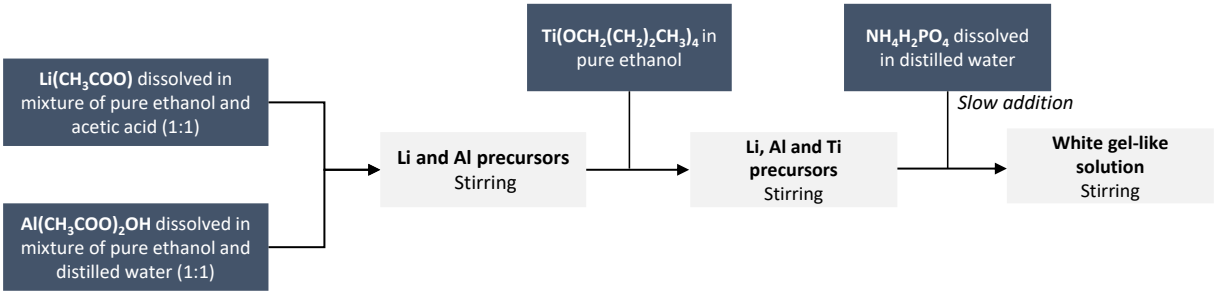

Figure III-1: Schematic of the solution of $LATP_{0.3}$ precursors via the precipitation route. Adapted from Schroeder et al. [169]

The final concentration of the reactants in the solution mixture is a key parameter that impacts the particle size distribution of the powder obtained through spray drying. Therefore, these concentrations will be detailed later.

III.1.2. Spray Drying

III.1.2.1. Principle

Spray drying is a dehydration process used mainly to transform liquid solutions into dry powders, taking advantage of a hot and gaseous drying medium[172]. Generally, this technique is used for pharmaceutical technology and food industry[173].

The process is composed of three main step: the atomization of the solution called feed solution, the droplet-to-particle conversion and the particle collection[174,175]. The device and the different component of the Spray Dryer are illustrated in Figure III-2.

The first step, which corresponds to the atomization of the solution, is crucial because it is during this stage that the liquid is converted into a mist of droplets by using a device called atomizer. This transformation is driven by decreasing the liquid's surface tension, a phenomenon influenced by external forces such as gravity or pressure[176,177]. In our study, we used a two-fluid nozzle as atomizer, where the liquid is pumped at a specific flow rate and combined with a stream of compressed gas, typically air[172,174,178]. The interaction between the liquid and the high-velocity gas creates intense shear forces, which break the liquid into tiny droplets. The size and uniformity of these droplets are influenced by the properties of the liquid feed, the flow rates of both the liquid (Peristatic pump rate) and the gas (inlet gas), as well as the design of the nozzle[175].

The second step is the droplet-to-particle conversion, which involves removing the solvent from the droplets to obtain dried particles. This drying process occurs when the droplets come into contact with the flow of hot drying gas (air, in our case) in the drying chamber. The efficiency of this process depends on factors such as the temperature (drying temperature) and flow rate of the hot gas, the size of the droplets, and the nature of the solvent[175].

Finally, the dried particles are collected using a cyclone. This device is based on centrifugal force that allows to separate the particle-gas stream separation[174].

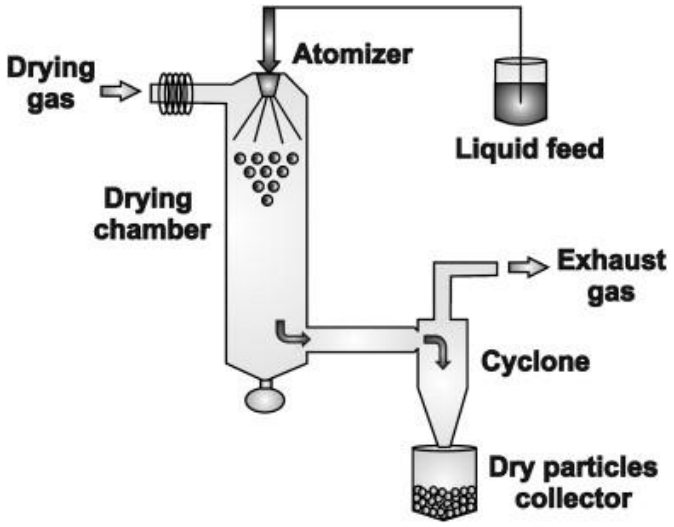

Figure III-2: Schematic of a Spray Drying device. From Sosnik et al. [173]

III.1.2.2. $LATP_{0.3}$ solution atomization

Several parameters influence particle size during the spray drying process[179]. In our study, two particle size populations were targeted, and certain parameters were adjusted accordingly. The parameters chosen for each sample are summarised in Table 2.

For the first sample, called SD_1, we selected some standard parameters to produce small secondary particles by specifically adjusting the inlet gas (1744 L/h) and the concentration of the feed solution at 10 % to generate finer droplets. For SD_2, the strategy involved concentrating the solution while keeping the pump rate at 15 mL/min, the same as for SD_1, to increase the material available for atomization and consequently encourage the formation of larger particles. Additionally, by decreasing the flow rate of inlet gas, the dispersive force on the droplets is decreased, allowing the droplets to remain larger before drying[173]. Both experiments were conducted using a two-fluid nozzle with a diameter of 2 mm.

During the droplet-to-particle conversion step, we selected a drying temperature of 100 °C for SD_1 sample, as reported in the study of Schroeder et al[169]. As bigger droplets were expected in the case of SD_2, the drying temperature was slightly increased, ranging from 100 °C to 120 °C, in order to ensure that the particles were thoroughly dried. Finally, the aspiration flow rate was also adjusted based on the sample. This parameter reflects the level of ventilation within the system, which affects the drying efficiency. Specifically, it influences how quickly the gas is removed from the chamber. A higher aspiration rate, as used for SD_1, promotes faster drying, leading to the formation of smaller particles.

Parameters	SD_1	SD_2
Mass concentration in feed solution (%)	10	20
Drying temperature (°C)	100	120
Aspiration flow rate (%) *	75	50
Peristatic pump rate (mL/min)	15	15
Inlet gas (L/h)	1744	667

**For a maximum aspiration flow rate of 35 m^3/h.*

Table 2: Summary of the processing parameters used in Spray Drying for samples SD_1 and SD_2.

The particle morphology and size were determined using laser granulometry and scanning electron microscopy (SEM). First, the SEM images are shown in Figure III-3-a and Figure III-3-b for samples SD_1 and SD_2 respectively. Typically, spherical particles are produced using spray routes, which is the case for both SD_1 and SD_2. Concerning the size of the secondary particles, SD_2 particles are visually larger than those for SD_1, as intended. In parallel, the granulometry analysis was performed following the same protocol described earlier. The results are presented in Figure III-3-c. The D10 value is smaller for SD_2, whereas its D90 is greater than that of SD_1, indicating that the SD_2 sample has a broader size distribution, comprising both large particles around 20 µm and smaller ones around 0.6 µm. At this stage, $LATP_{0.3}$ is not yet formed, so a high-temperature heat treatment step is necessary to crystallise it.

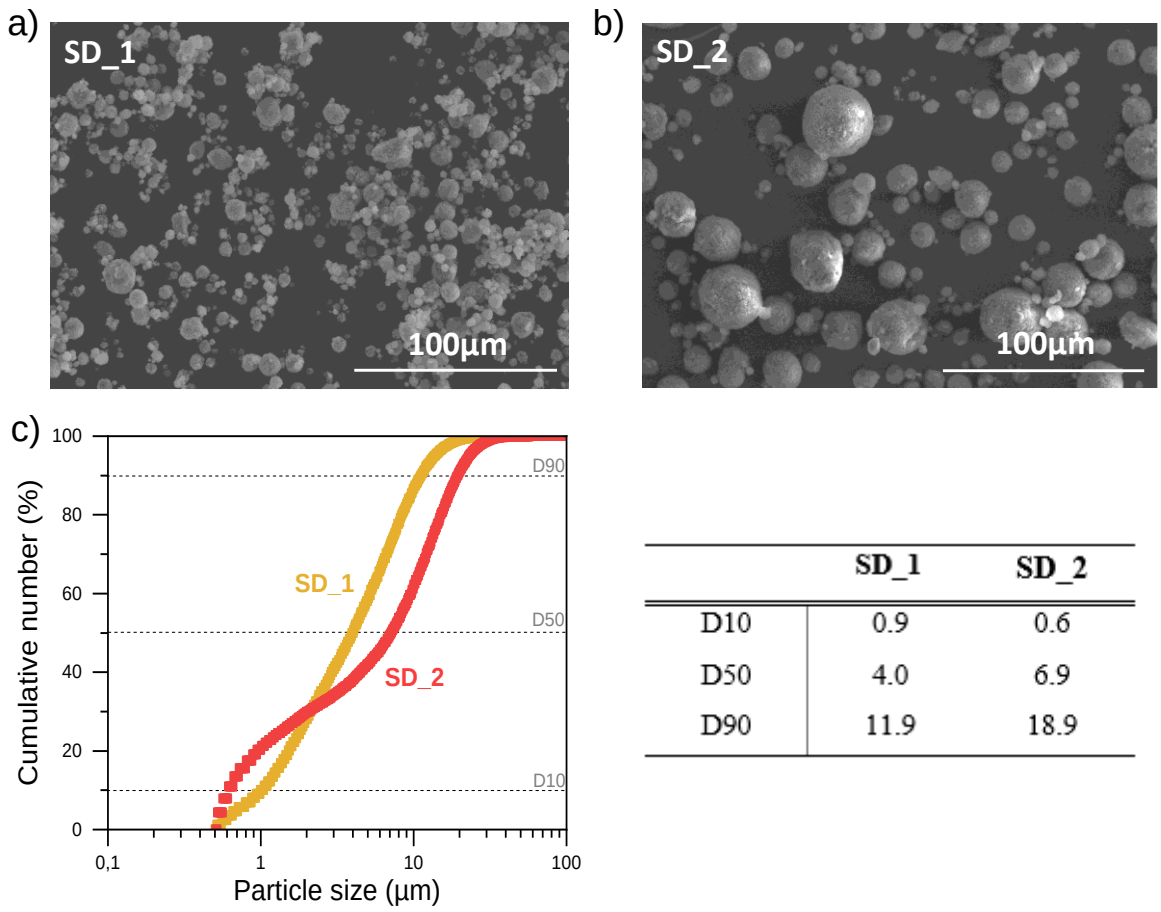

	SD_1	SD_2
D10	0.9	0.6
D50	4.0	6.9
D90	11.9	18.9

Figure III-3: SEM images of (a) SD_1 and (b) SD_2 after atomisation by Spray Drying. (c) Laser granulometry results for SD_1 (■) and SD_2 (■).

III.1.3. Calcination step

The two samples, SD_1 (small particles) and SD_2 (large particles), must be calcined in order to remove organic compounds and also crystallise the $LATP_{0.3}$. According to Schell et al., the minimum crystallization temperature for LATP is approximately 750°C[118]. However, we opted for a higher temperature, specifically 850°C, to enhance its crystallinity and to better identify any potential impurities. For this purpose, each powder was placed in an alumina crucible and they were heated at 850 °C, with a heating ramp of 5 °C/min, for 30 min, in a muffle furnace. First, SD_1 and SD_2 were characterised by XRD in order to confirm $LATP_{0.3}$ crystallisation. The scans presented in Figure III-4 were acquired in the range 2θ = 10-80 °, with 0.02 ° steps and a time of 0.2 s/step. As expected, the main diffraction peaks of $LATP_{0.3}$ are observed in both cases, confirming successful synthesis of the phase. This crystallization is accompanied by the formation of the $AlPO_4$ phase, as well as the TiP_2O_7 impurity is the SD_1

case. The presence of TiP_2O_7 is typically observed when there is an excess phosphate. However, its absence in SD_2 indicates that it is possible to achieve a purer phase.

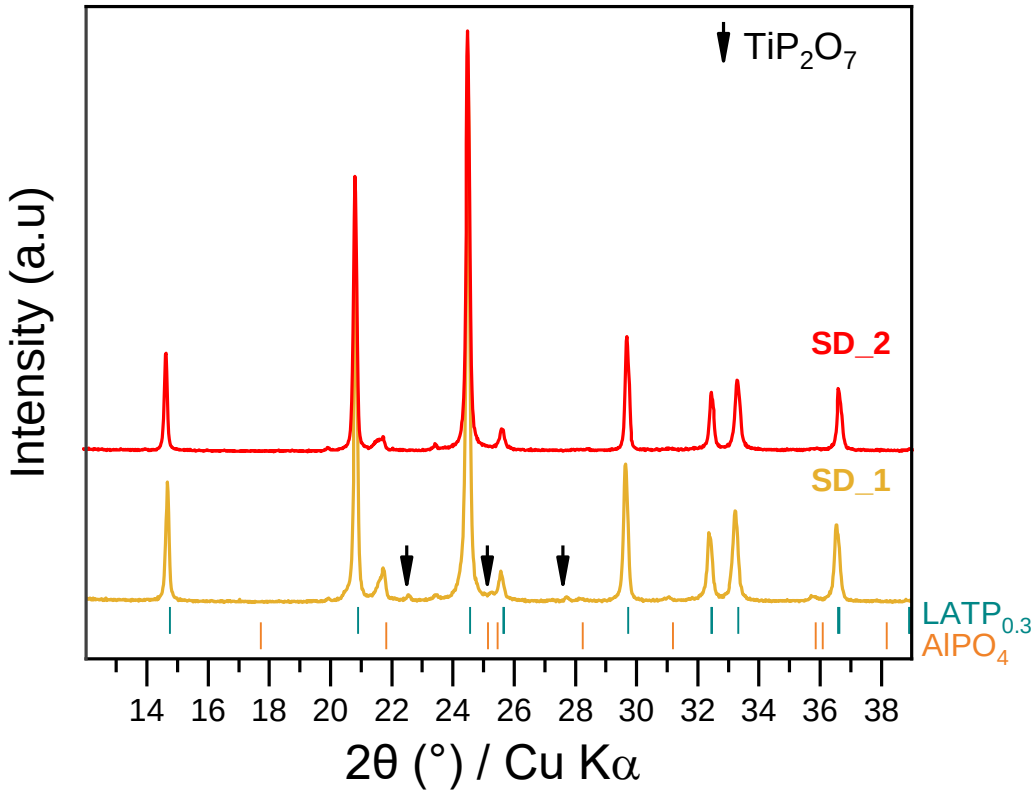

Figure III-4: XRD pattern of SD_1 (—) and SD_2 (—) samples calcined at 850 °C for 30 min in muffle furnace.

Additionally, the powders were analysed by SEM to confirm that the morphologies remained unchanged after the heat treatment. The Figure III-5-a and the Figure III-5-b presents the SEM images for SD_1 and SD_2 calcined respectively. In both cases, it can be observed that the particles partially disintegrated as the temperature increased, indicating that the granulometry results presented in Figure III-3 are not the same. Additionally, there is evidence of particle aggregation, particularly in the case of SD_1. Finally, a close-up of the primary particles constituting the secondary particles reveals that they have started to sinter together due to the intimate contact facilitated by the spray drying process. This final observation impacts the densification process and will be discussed in further detail later.

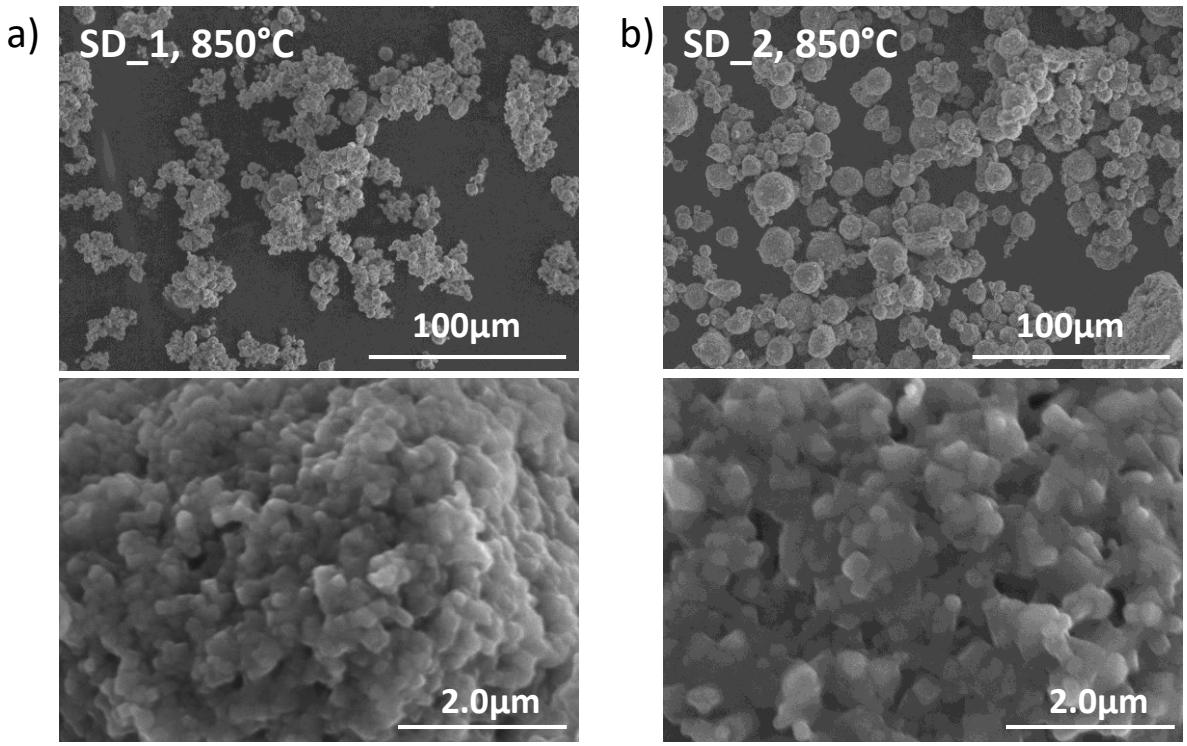

Figure III-5: SEM images of (a) SD_1 and (b) SD_2 after calcination step at 850 °C for 30 min in a muffle furnace.

III.2. Densification and ionic conductivities

III.2.1. Impact of the size of secondary particle in densification

The two resulting powders were pressed into 13 mm diameter pellets after applying 3.5 ton of pressure for 2 min. The pellets were then sintered using conventional sintering, which involved a 6-hour heat treatment at 900 °C, with a heating rate of 5 °C/min in a muffle furnace. The green densities and relative densities were determined from the geometric dimensions of the pellets, as explained by equations (1) and (2) in previous section. All of these density values are presented in Figure III-6. The densities obtained for the SSR synthesis before and after sintering are also shown for comparison. Initially, the average green density of the SD_2 samples (62 %) is slightly higher than that of SD_1 (57 %). However, both averages remain lower than those obtained for SSR samples, indicating a certain difficulty in compacting powders obtained via spray drying. Next, examining the relative densities, we observe that densities reach up to 90 % in the case of SD_1 (small particles), which is similar to what was achieved for SSR samples. For SD_1 sample, the initial compaction is low, but the final relative density is high, mimicking the behaviour observed for $LATP_{0.3}$ com. This suggests a faster densification process at lower temperatures compared to SSR. In contrast, the relative densities for SD_2 are lower, reaching around 75 %, suggesting that a significant amount of open porosity remains, unlike in the other samples. In other words, sintering was effective only for SD_1, which consisted of small particles.

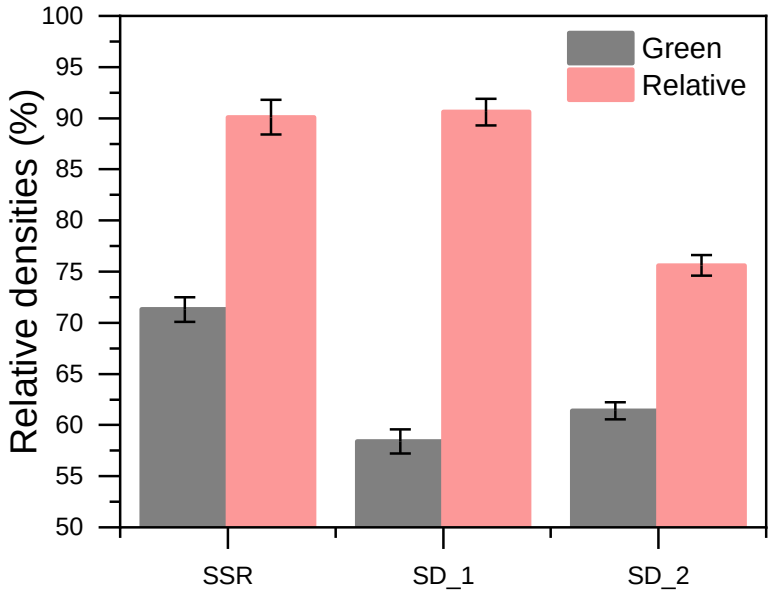

Figure III-6: Comparison of the green relative densities and the relative densities of $LATP_{0.3}$ SSR, SD_1 and SD_2 pellets after heat treatments at 900 °C for 6 h.

Then, the pellets were fractured to study the cross-sections using SEM. The images are presented in Figure III-7. In the case of SD_1, the particles are fairly well sintered together despite the presence of porosity. In contrast, for SD_2, we can confirm that the thermal treatment was insufficient to sinter the particles together, as the original particle shapes are still visible. This phenomenon may be attributed to pre-sintering that occurs during the calcination step at 850 °C, as observed in Figure III-5. During the crystallisation step, the powder is calcined while still in its powdered form, rather than as pellets. Consequently, secondary particles are less in contact with one another compared to primary particles. As a result, when the temperature of 850 °C is applied, sintering initiates primarily among the primary particles. This pre-sintering makes it more challenging for secondary particles to undergo sintering during the subsequent pellet-forming stage. This phenomenon appears to have less impact on the densification of SD_1, likely because the smaller secondary particles facilitate more effective sintering, as no such effect is observed. To avoid this issue in the case of SD_2, one possible solution could be to decrease the calcination temperature to 600-700 °C, which is the minimum temperature required to remove organic phases. Although this approach may compromise the purity and crystallinity of $LATP_{0.3}$, the formation can be completed during the sintering step.

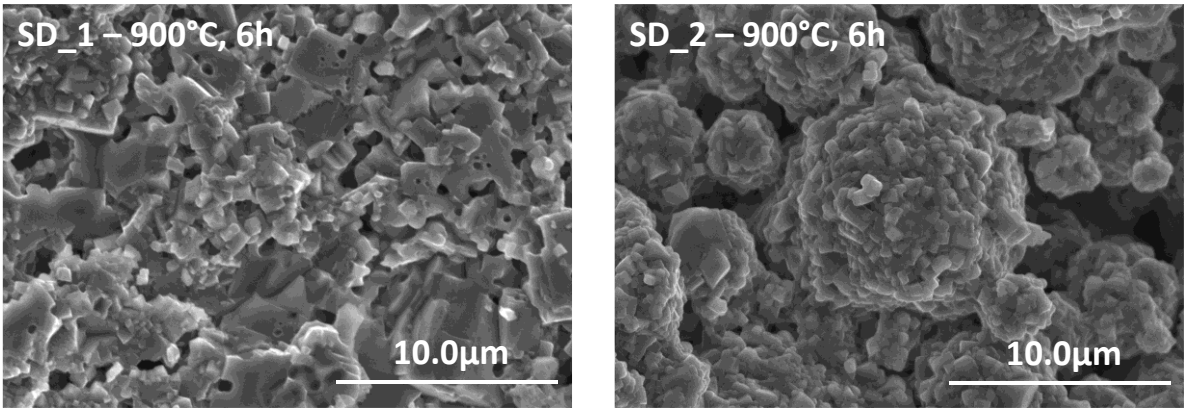

Figure III-7: SEM images of broken pellets of $LATP_{0.3}$ SD_1 (to the left) and $LATP_{0.3}$ SD_2 (to the right) after a heat treatment at 900 °C for 6 h under air atmosphere.

Based on these densification experiments, only the SD_1 sample could be effectively sintered at 900 °C. The formation of excessively large secondary particles, as seen with SD_2, demonstrates the difficulty in achieving effective sintering between particles. In our study, this challenge was further exacerbated by the occurrence of pre-sintering during the calcination stage. Consequently, new experiments are underway with multiple objectives. First, we plan to adjust the spray drying parameters to produce even smaller particles. These smaller particles could be densified on their own or mixed with SD_1 and/or SD_2 to investigate the effects of

a broad particle size distribution on densification. Additionally, the calcination step needs to be optimised to balance pre-sintering and LATP crystallisation.

III.2.2. Ionic conductivity properties for the most densified systems

Finally, the ionic conductivities of SD_1 and SSR were determined using Electrochemical Impedance Spectroscopy (EIS) as they reached the same high relative densities (~90%). The SD_2 sample was not analysed due to the low relative densities obtained. The principle is based on applying a low-amplitude alternating electrical potential across the pellet while measuring the resulting current response. This response allows for modelling the electrical impedance of the material at different frequencies. By analysing the obtained data, particularly through a Nyquist plot, information about the resistance can be extracted, enabling the determination of the ionic conductivity of the tested material. The measurements were carried out in a range of frequencies between 10^7 Hz and 10^{-1} Hz, with a perturbation of 10 mV at the open circuit voltage, recording 11 points per decade. Before analysis, the pellets were covered with a 20 nm layers of gold, serving as a blocking electrode. The pellets were assembled in a Swagelok-type cell using two stainless-steel current collectors. A spring was used in order to maintain the contact pressure.

The Nyquist Plots were acquired at 25 °C and they are presented in Figure III-8. This type of diagram is represented by plotting the imaginary part of the impedance as a function of the real part, which means reactance versus resistance of the system. For the characterised samples, we observe a semicircle, where the value at the low-frequency intersection with the x-axis corresponds to the total resistance of the system[180–182]. In ceramics like LATP, the total resistance is often dominated by the grain boundary resistance, as these boundaries can present barriers to ionic conduction[10,156]. However, obtaining a single semicircle does not mean that the contribution of grain resistance is absent, but rather that both contributions are not easily distinguishable at room temperature. The axes were normalised by the surface area and thickness of each pellet to allow for a visual comparison of the resistances of the samples: the sample obtained by Spray Drying is less resistant than the sample obtained by SSR. The associated ionic conductivities were determined by fitting the data with the Debye equivalent circuit[183], which is also presented in Figure III-8.

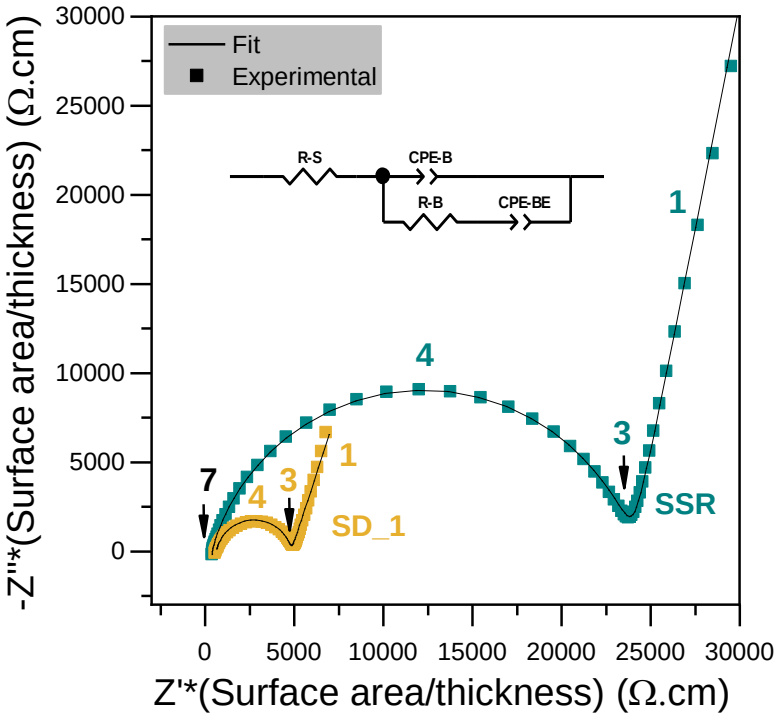

Figure III-8: The Nyquist plots at 25 °C of pellets of $LATP_{0.3}$ SD_1 (RD 90 %) (■) and SSR (RD 91 %) (■) sintered at 900 °C during 6 h in air. The EIS data were fitted with the Debye equivalent circuit. The numbers represent the power of frequencies.

The model is composed of the resistance associated to the contribution of the setup (R-S), the capacitive behaviour and the resistance of the sample (CPE-B and R-B respectively) and the capacitive response of the blocking electrodes (CPE-BE). Based on the values of the resistivity obtained, the ionic conductivities can be determined according the following equation (3):

$$\sigma = \frac{1}{R_B} \times \frac{e}{S} \quad (3)$$

Where σ is the ionic conductivity ($S.cm^{-1}$), R-B (Ω) is the resistivity of the system, e and S are the thickness (cm) and the surface area (cm^{-2}) of the pellets respectively. The ionic conductivity values are on the order of 2.10^{-4} (± 0.2) S/cm for SD_1 and 4.10^{-5} (± 0.3) S/cm for SSR at room temperature. These values are consistent with those reported in the literature. As previously explained, most liquid-phase synthesis methods tend to enhance ionic conductivities, with values reaching 10^{-3} to 10^{-4} S/cm at room temperature[58]. On other hand those obtained via solid-state routes suffer from lower ionic conductivities, sometimes as low as 10^{-7} S/cm for comparable relative density (90 %)[184]. Our study follows this trend, as we observe that at similar relative densities, the use of spray drying leads to improved ionic conductivity as we improved the densification and the microstructure. These results in terms of density and ionic conductivity are, therefore, encouraging

IV. Conclusion of Chapter II

In this second Chapter, we demonstrated that particle size plays a crucial role in densification and the resulting microstructure after sintering. As reported in the literature, decreasing particle size enhances densification at lower temperatures and prevents the abnormal formation of large grains, which are prone cracking. However, this reduction in particle size must be carefully controlled, as excessively small particles can degrade ionic conductivity properties.
In a second part, we explored another strategy: determining the impact of spherical secondary particles of varying sizes on densification. Tests conducted using spray drying produced samples with different particle sizes. Similar to primary particles, smaller secondary particles exhibited better densification properties. However, several aspects of $LATP_{0.3}$ synthesis using this method still require optimisation.

While adjusting the particle size distribution can improve the densification process at a fixed temperature, this strategy has limitations in significantly lowering the densification temperature. To overcome these challenges, other strategies discussed in the literature include the use of additives or alternative sintering techniques. These strategies will be discussed in the following chapters.

All experiments conducted in these chapters will use $LATP_{0.3}$ synthesised by solid-state reaction, as we are capable of producing significant quantities of pure powder. Additionally, it exhibits lower densification and ionic conduction properties compared to other samples, which will allow us to better visualise the effects on these properties obtained by the other strategies.

Chapter III: Reactive Sintering

I. Introduction

In the previous Chapter, we found that heat treatment at temperatures above 900 °C is necessary to achieve relative density values exceeding 90 % for pure $LATP_{0.3}$. Another method discussed in the literature for decreasing the sintering or densification temperature is the use of sintering aids. For LATP (x = 0-0.3), the most commonly used sintering aids are Li-salts. For instance, Rumpel et al. successfully reduced the sintering temperature of LATP from 950 °C to 800 °C by adding 5 vol% of Li_3PO_4[135]. Dai et al. achieved a relative density of 98 % at 800 °C for LATP by incorporating 5 wt% of $LiBF_4$[140]. Numerous other studies have investigated the use of Li-salts as sintering aids, including Li_3BO_3[144,185], $LiBO_2$[141], Li_3PO_4[135,185,186], LiF[139,187], $LiNO_3$[188] and $LiBF_4$[140].

One hypothesis for achieving densification at lower temperatures suggests that the salt melts below the sintering temperature of the ceramic, facilitating liquid phase sintering. This liquid phase aids in particle rearrangement of the particles and grain growth at lower temperature. However, Waetzig et al. investigated the effect of several Li-salts (e.g. Li_3BO_3, Li_3PO_4, Li_2CO_3, LiCl, LiOH, $LiBO_2$) on the densification of LATP by optical dilatometry. They found no correlation between the shrinkage temperature of the LATP pellet and the melting temperature of the corresponding Li-salts[189]. This indicates that densification at lower temperatures with Li-salts cannot be solely attributed to the formation of a liquid phase upon melting.

Furthermore, the systematic formation of impurities $LiTiOPO_4$ and/or $Li_4P_2O_7$ after heat treatment with Li-salts suggests that chemical reactivity might also play a significant role in LATP densification.

Therefore, the main goal of this chapter is to understand the impact of chemical reactivity on the sintering or densification temperature of LATP. To this end, the chemical reactivity mechanism between LATP and Li-salts was first analysed. The link between this reactivity and densification was then established to optimise the parameters that enhance densification. As a result of this study, we achieved a relative density of 85 % at 760 °C, and an ionic conductivity of 2.10^{-4} $S.cm^{-1}$ at room temperature for a pellet of $LATP_{0.3}$ with 5 wt% of $Li_4P_2O_7$.

II. High temperature reactivity between lithium salts and $LATP_{0.3}$

II.1. Screening of chemical reactivity between various lithium salts and $LATP_{0.3}$

A wide range of Li-salts were chosen to investigate their chemical reactivity at high temperatures with $LATP_{0.3}$. The Li-salts used, listed in the Table 3, cover a broad range in terms of chemical nature and melting temperature.

Compounds	Melting temperatures (°C)	References
$LiNO_3$	253	[142]
$LiBF_4$	309	[190]
LiBr	551	Our work
LiCl	605	[142]
Li_3BO_3	706	[191,192]
Li_2CO_3	723	[142]
LiF	848	[193]
Li_3PO_4	1205	[194]

Table 3: All the Li-salts used to study the chemical reactivity with $LATP_{0.3}$ and their melting temperature (°C).

Chemical reactivity was studied by conducting heat treatment on pellets made from mixtures of $LATP_{0.3}$ and Li-salts. The mixtures were prepared with a fixed lithium molar ratio of 1.3:1 for $LATP_{0.3}$ to Li-salts in order to maximise the chemical reactivity. This corresponds to a 1:1 molar ratio for a mixture of $LATP_{0.3}$ and LiBr, and to a molar ratio of 1:0.5 for a mixture of $LATP_{0.3}$ and Li_2CO_3. All the mixtures were prepared by grinding each reactant with a mortar inside a glovebox. As a reference, a pellet composed of pure $LATP_{0.3}$ was studied as a control test. The Figure II-1 displays the XRD patterns obtained for each mixture after a 2 h heat treatment at 900 °C, with a heating ramp of 5 °C/min in a muffle furnace. The acquisitions were carried out in the range 2θ = 10-80°, with 0.02° steps and a time of 0.2 s/step.

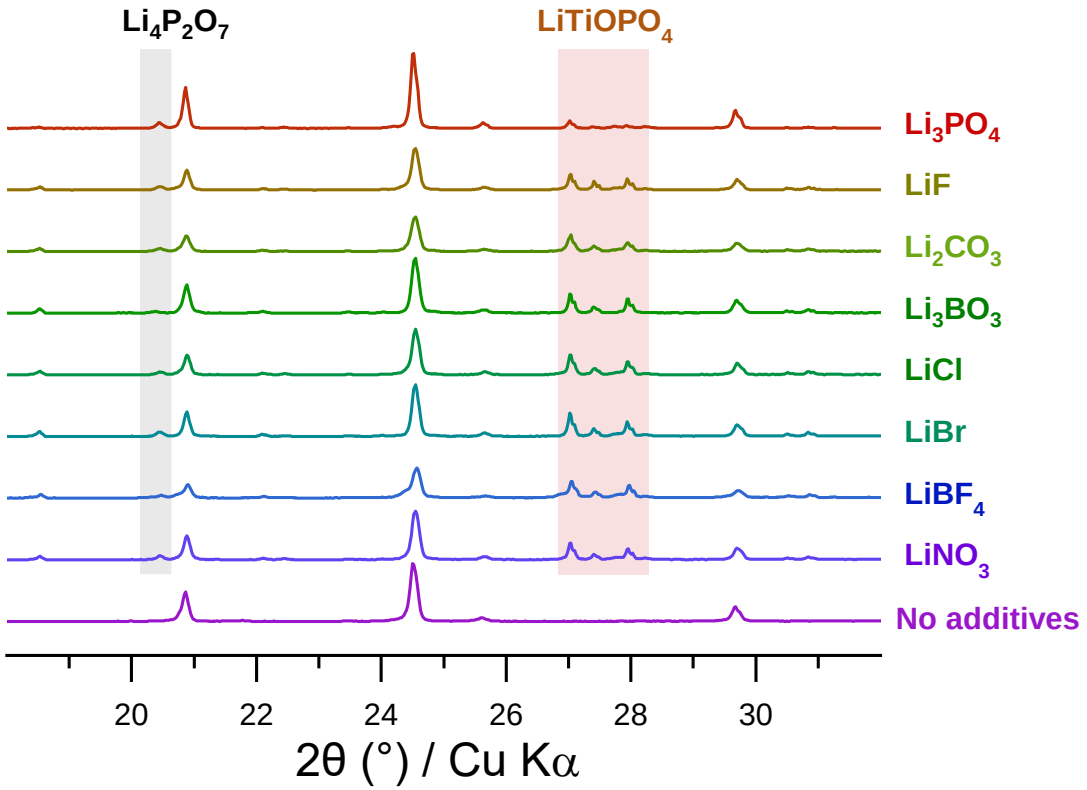

Figure II-1: Diffraction data of $LATP_{0.3}$ (*R*-3*c*) and mixtures of $LATP_{0.3}$ and various lithium salts heat-treated at 900 °C during 2 h under air atmosphere. Main diffraction peaks of impurities $LiTiOPO_4$ (*Pnma*) and $Li_4P_2O_7$ (*P*-1) are present, as highlighted by the orange and grey rectangles respectively.

Based on these experiments, the heat treatment applied to samples containing Li-salts results in the disappearance of the initial Li-salts and the formation of the same impurities: $LiTiOPO_4$ (Orthorhombic, *Pnma*) and $Li_4P_2O_7$ (Triclinic, *P*-1). This result is consistent with the literature, as the formation of $LiTiOPO_4$ is inevitable when significant amount of Li-salts is added to $LATP_{0.3}$[135,139,140,188,195,196]. In contrast, the formation of $Li_4P_2O_7$ is not systematic but it has been observed for similar systems[139,141,188,195]. These impurities are not formed when applying the same heat treatment on pure $LATP_{0.3}$, indicating that they are due to the reactivity between Li-salts and the solid electrolyte.

As a first approach, we made the hypothesis that $LiTiOPO_4$ and $Li_4P_2O_7$ are produced by adding an excess of lithium to LATP, which is supplied by Li-salts. This hypothesis can be summarised by equation (1), where $LATP_{0.3}$ is replaced by LTP to simplify the reaction:

$$1\ LiTi_2(PO_4)_3 + 3/2\ Li_2O \rightarrow 2\ LiTiOPO_4 + ½\ Li_4P_2O_7 \quad (1)$$

However, the ternary phase diagram of Li_2O, TiO_2 and P_2O_5 shown in Figure II-2 indicates that there is no equilibrium between these impurities and LTP/LATP. This implies that the mechanism involves the formation of other phases to reach the final impurities.

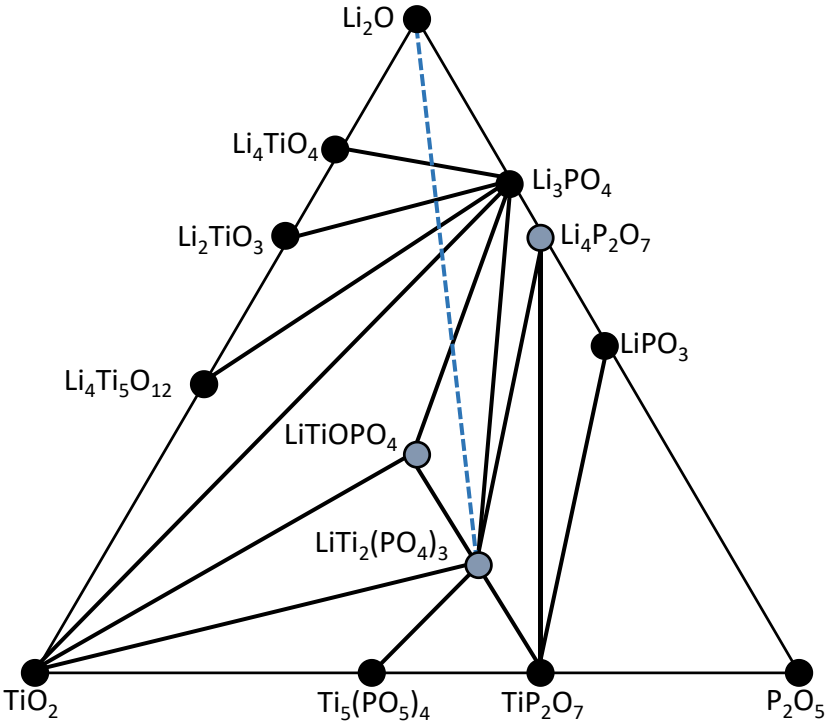

Figure II-2: Ternary phase diagram of TiO_2-P_2O_5-Li_2O reproduced from the study of Hupfer et al[197]. The blue line represents the addition of Li_2O to LTP while the grey points represent the interest phases.

Moreover, the mechanism is simplified compared to the studied systems as it circumvents the diversity of Li-salts and the impact of the aluminium level substitution in the case of $LATP_{0.3}$.

II.2. Chemical reactivity between $LATP_{0.3}$ and LiBr

II.2.1. Reactivity mechanism by high-temperature X-ray diffraction

Since the chemical reactivity remains similar regardless of the salt used, we looked specifically at how LiBr interacts with $LATP_{0.3}$ to form $LiTiOPO_4$ and $Li_4P_2O_7$ using high-temperature X-ray diffraction (HTXRD). The experiment was conducted on a pellet made from a mixture of $LATP_{0.3}$ and LiBr with the same lithium molar ratio of 1.3:1. The pellet was made by placing powder in a 13 mm diameter die and applying a pressure of 4.5 tons. During the experiment, the pellet was heat-treated from 30 °C to 900 °C under an air flow of 50 mL/min, with a temperature ramp of 10 °C/min. The XRD patterns were acquired using two types of measurements during the same experiment. The first type, called **P1**, involves short scans (around 5 min) in the range 2θ = (10-60) ° with 0.02 ° steps and a time of 0.1 s/step, each 10 °C from 30 °C to 900 °C. The last one, named **P2**, consists of long scans (around 1 h) every 100 °C from 100 °C to 900 °C in the range 2θ = (10-80) ° with 0.02 ° steps and a time of 1 s/step. All the diffraction patterns acquired by **P1** are presented in Figure II-3, allowing us to qualitatively follow the formation and disappearance of chemical species.

- At room temperature, LiBr is not visible because it is so hydrated that it is amorphous, which means that only the diffraction peaks of $LATP_{0.3}$ (*R*-3*c*) and $AlPO_4$ ($C222_1$) are observed.
- The dehydration of LiBr starts at 50 °C by the transition from the amorphous phase to hydrated structure of LiBr (*Cmcm*), followed by the transition from the hydrated structure to the cubic structure of non-hydrated LiBr (*Fm*-3*m*) at 110 °C.
- A phase transition from the orthorhombic to the cubic structure is observed around 240 °C for $AlPO_4$[198].
- The next change occurs at around 410 °C, when the diffraction peaks of LiBr (*Fm*-3*m*) disappear as Li_3PO_4 (*Pnma*) begins to form.
- At 710 °C, $AlPO_4$ disappears, and a diffraction peak at approximately 25 ° could indicate TiO_2 anatase ($I4_1/amd$) but additional characterisation is necessary to validate its formation. In parallel, $LiTiOPO_4$ (*Pnma*) starts to form, followed by $Li_4P_2O_7$ ($P12_1/n1$) at 810 °C. These formations correspond to the total consumption of Li_3PO_4 at this last temperature.

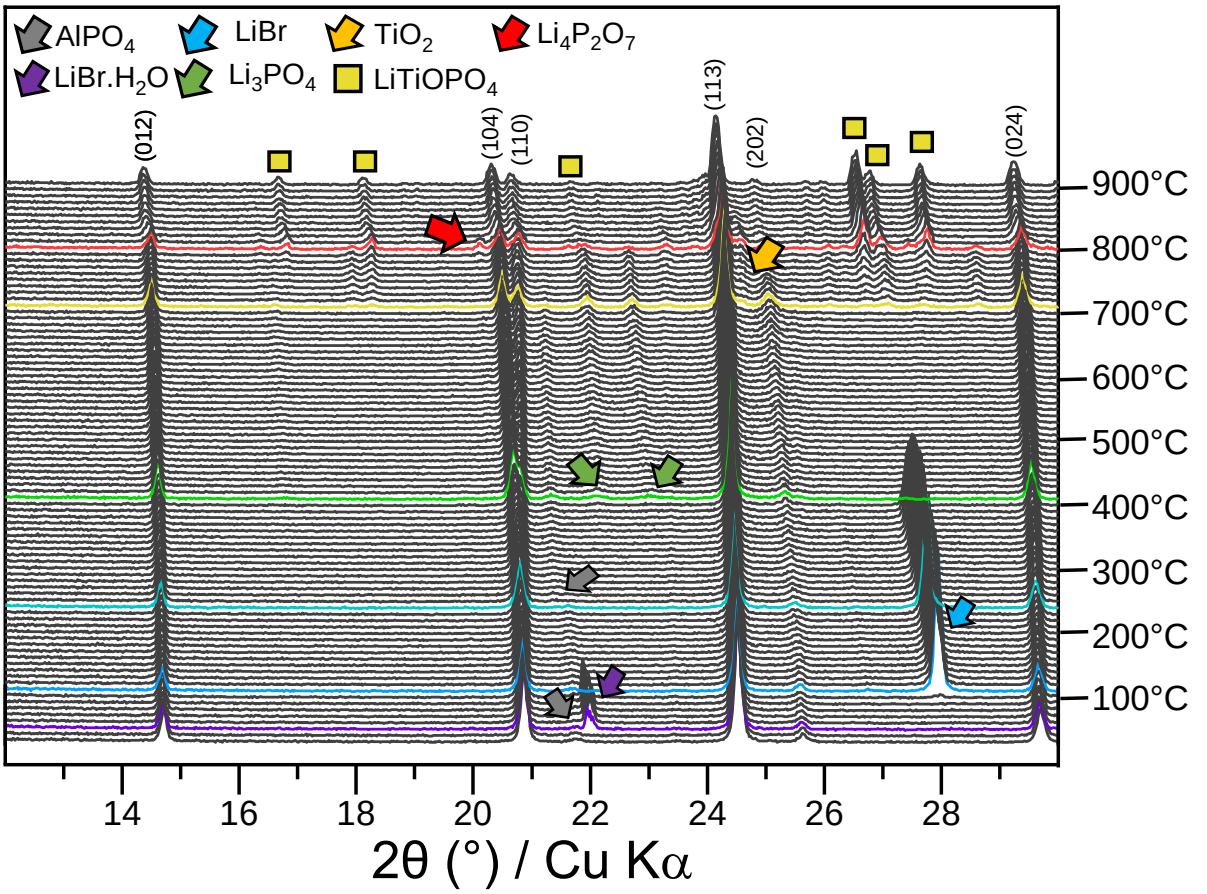

Figure II-3: High-temperature X-ray diffraction data of a pellet of $LATP_{0.3}$ and LiBr (1:1) in a temperature range from 30 to 900 °C in air flow. Diffraction peaks of $LATP_{0.3}$ (*R-3c*) are indexed by hkl indices. Temperatures at which important changes take place, such as species formation/disappearance, are marked by colour: 50 °C (—), 110 °C (—), 240 °C (—), 410 °C (—), 710 °C (—) and 810 °C (—).

Then, the HTXRD data obtained using the type of measurement **P2,** which consists of long scans, were analysed using Rietveld refinements. This analysis allows us to quantify each species (wt%) present every 100 °C, from 100 °C to 900 °C, as well as the XRD pattern upon returning to ambient temperature. The Figure II-4 presents the results obtained by Rietveld refinements. This provides a clearer visualisation of the appearance and disappearance of each phase, enhancing understanding of the key steps in the mechanism.

The initial stage between room temperature to 400 °C, involves the conversion of LiBr to Li_3PO_4 in the presence of $LATP_{0.3}$, as LiBr disappears once Li_3PO_4 forms. Then, the second step occurs between 500 °C and 800 °C and it involves the formation of TiO_2 and the disappearance of $AlPO_4$. These two steps are associated with an artificial increase in the mass percentage of $LATP_{0.3}$. This increase could indicate the formation of an amorphous phase which is not quantified by Rietveld analysis. The final step between 800 °C and 900 °C is illustrated by the formation of $Li_4P_2O_7$ and $LiTiOPO_4$ at the temperature at which Li_3PO_4, $AlPO_4$ and TiO_2

disappears, and the mass percentage of $LATP_{0.3}$ decreased. It reflects the formation of $Li_4P_2O_7$ and $LiTiOPO_4$ from the reactivity of these phases. Finally, $Li_4P_2O_7$ disappears before 900 °C, as expected from its melting temperature of 875 °C[199]. Upon returning to ambient temperature, we find the final impurities $LiTiOPO_4$ and $Li_4P_2O_7$, correlating with results in Figure II-1.

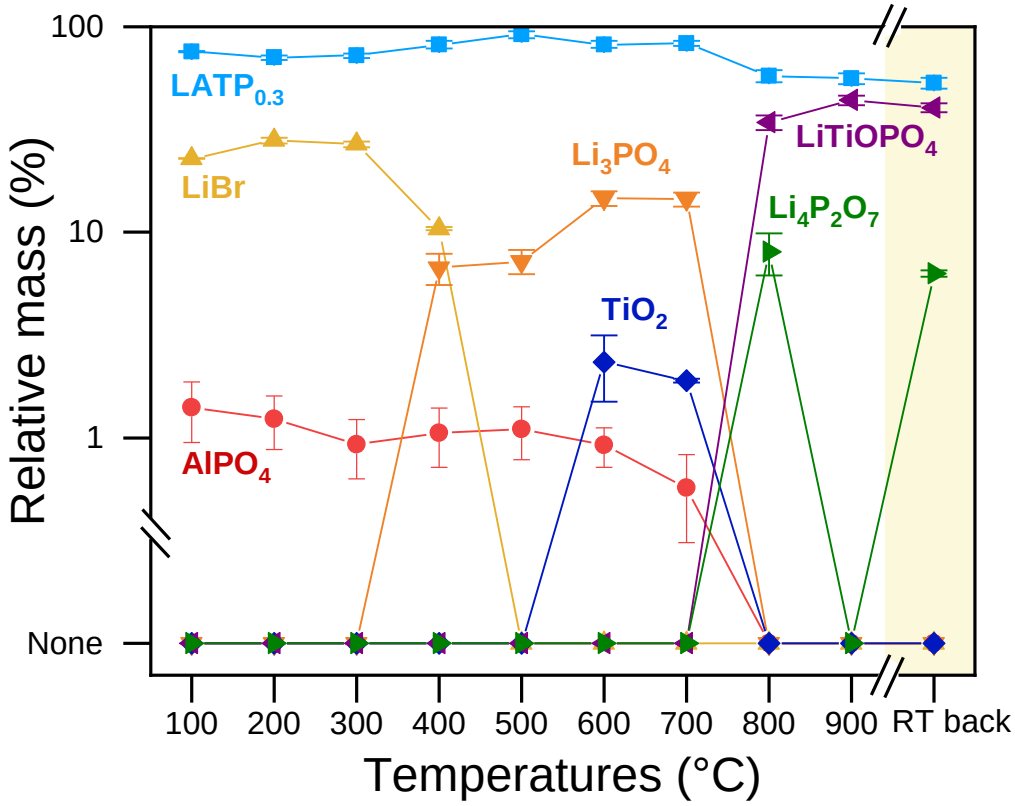

Figure II-4: Relative mass of each species (%) determined by Rietveld refinements, as a function of temperatures. The results are represented in log scale in order to highlight species with small mass percentages.

Although Rietveld refinements allow for the determination of the relative mass percentages of species present at each temperature, the error bars associated with the results are larger than those presented in Figure II-4. The first point to consider is that the duration of an acquisition is 75 minutes, which is long compared to the kinetics of the various observed reactions. In other words, some reactions occur simultaneously with the acquisition.

An example is shown in Figure II-5, which presents diffraction patterns acquired quickly using a short measurement program **P1** before and after a long measurement acquired using program **P2** at 100°C. In this specific case, the short acquisition performed before the long acquisition shows LiBr in its hydrated form, whereas the short acquisition performed after the long one shows LiBr in its anhydrous form. In the case of the long acquisition, it presents a mixture of hydrated and anhydrous LiBr. However, by focusing on the diffraction peaks of hydrated LiBr with the same intensity at 21.8 ° and 38.4 °, it can be noted that only the diffraction peak at

21.8 ° is present in the scan acquired over a long time. This highlights that the dehydration of LiBr occurs simultaneously with the acquisition. Consequently, this results in inconsistencies in peak intensities between low and high angles, leading to inaccuracies in the mass quantity of the chemical species determined by refinement.

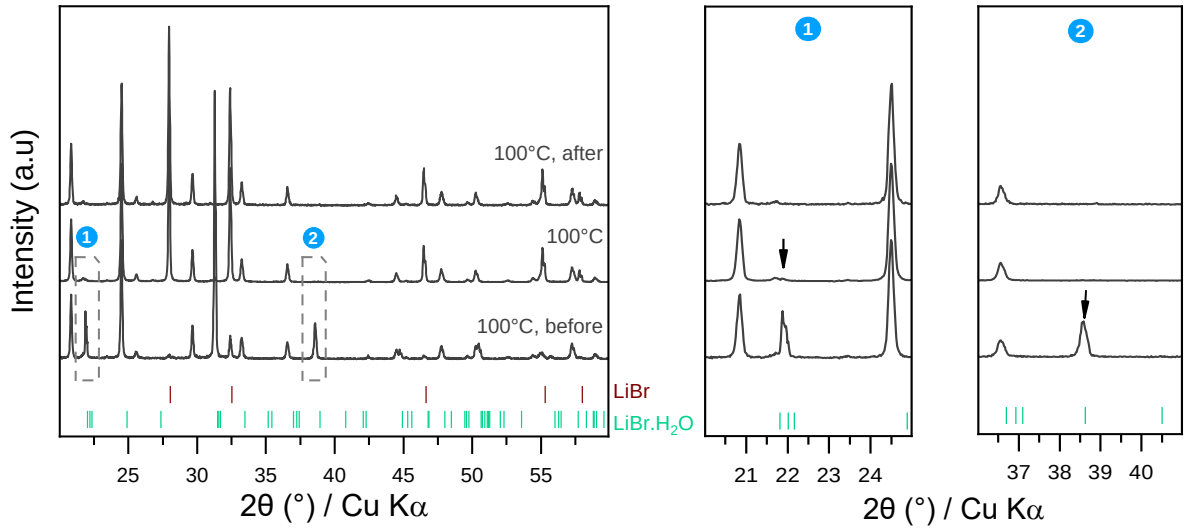

Figure II-5: High-temperature X-ray diffraction data of mixture of $LATP_{0.3}$ and LiBr (1:1) acquired at 100 °C. The line named "100 °C, before" corresponds to a scan acquired quickly with P1 measurement before the long scan; the line called "100 °C" corresponds to a scan acquired with a longer type of measurement (P2); and the line named "100 °C, after" corresponds to a scan acquired quickly with P1 measurement after the long scan. The black arrows indicate the two diffraction peaks at 21.8 ° and 38.4 ° of equal intensity from hydrated LiBr.

One way to limit this phenomenon would have been to perform faster acquisitions, but this would have resulted in a loss of quality in the raw experimental data represented by wrong Rietveld discrepancy values. Indeed, even in our case, all refinements exhibit χ^2 values lower than 1, which is unusual since a good fit typically results in a χ^2 value close to and larger than 1. However, this can be attributed to the inconsistencies in peak intensities discussed previously and insufficient data quality, as indicated by an R-factor (R_{exp}) greater than R_{wp}. Moreover, some phases are not identified at high temperatures, impacting the quantification of certain phases and consequently affecting the R-factor. Thus, the quality of the Rietveld fits was determined by graphically viewing the difference between the observed and calculated patterns, after verifying that the model is chemically correct[200].

Finally, the behaviour of lattice parameters of $LATP_{0.3}$ in temperature was determined by Rietveld refinements. The material presents an orthorhombic system with a *R*-3*c* space group, where $a = b \neq c$ and $\alpha = \beta = 90$ ° and $\gamma = 120$ °[93,155]. The lattice parameters of a sample of pure $LATP_{0.3}$ were first measured upon heating and the results are presented in Figure II-6. In this case, the *a* and *b* parameters vary little throughout the experiment, with corresponding values

of 8.5007(4) Å and 8.5008(3) Å at 30 °C and 900 °C respectively. For the *c* cell parameter, the variation is more significant as it is corresponding to 20.825(2) Å at 30 °C and 21.346(1) Å at 900 °C. These variations can be better illustrated by the linear thermal expansion coefficient (LTEC) which is expressed by the equation (2)[201]:

$$LTEC = (2\alpha_a + \alpha_c)/3 \quad (2)$$

The factors α_a and α_c are defined by the linear thermal expansion coefficient measured along the *a* and *c* axis respectively. They are expressed by the equations (3)[202] :

$$|\alpha_a| = \frac{1}{a_1} \times \left[\frac{a_2 - a_1}{T_2 - T_2}\right] \text{ and } |\alpha_c| = \frac{1}{c_1} \times \left[\frac{c_2 - c_1}{T_2 - T_2}\right] \quad (3)$$

Where a_1 and a_2 indicate the values of the *a* lattice parameter at temperatures T_1 and T_2, respectively. The same logic applies to the *c* lattice parameter.

In our case, the α_a corresponds to a value of $1.3.10^{-8}$ K^{-1} and the α_c is described by a value of $2.8.10^{-5}$ K^{-1}, which is in good agreement with the literature[133,195,202,203]. These results indicate a strong anisotropy along the *c*-axis, which is a typical behaviour observed in some materials of the NaSICON family[204–206]. With the addition of LiBr, the *a* and *c* parameters correspond to 8.4982(5) Å and 20.841(2) Å at 30 °C, while the values reach 8.4959(5) Å and 21.327(2) Å at 900 °C. In that case, the linear thermal expansions of *a* and *c* remains similar to pure $LATP_{0.3}$ with $\alpha_a = 2.7.10^{-8}$ K^{-1} and $\alpha_c = 2.6.10^{-5}$ K^{-1}. Upon returning to room temperature, the parameters *a* and *c* correspond to 8.49(1) Å and 20.87(2) Å respectively for both samples. This analysis indicates that the $LATP_{0.3}$ that is not consumed during the reaction does not undergo any change in terms of composition, such as lithium insertion, for example.

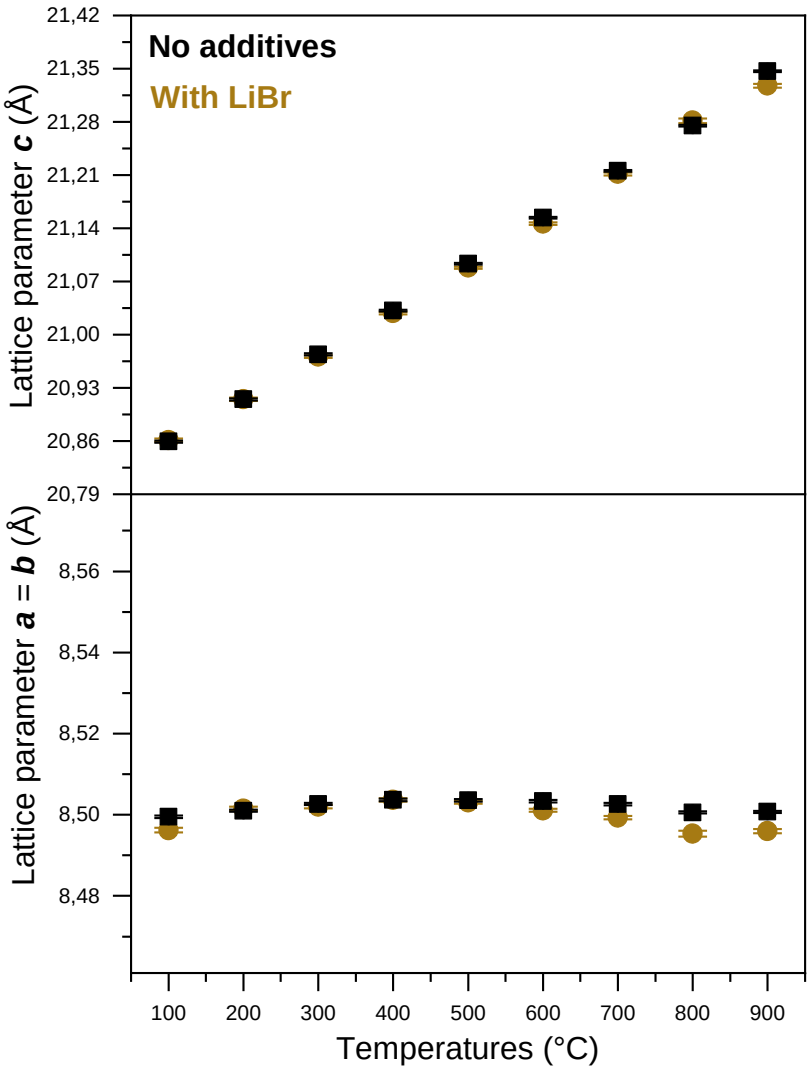

Figure II-6: Monitoring the lattice parameters of $LATP_{0.3}$, where *a* = *b* and differs from *c*, as a function of temperature. Black squares denote lattice parameters of pure $LATP_{0.3}$ sample, while yellow circles denote $LATP_{0.3}$ sample in the presence of LiBr.

Based on these initial results, the reactivity mechanism seems to involve two steps:

1. The consumption of LiBr and $LATP_{0.3}$ to form Li_3PO_4 and TiO_2.
2. The reaction of Li_3PO_4, $AlPO_4$ and TiO_2 with $LATP_{0.3}$ to form $LiTiOPO_4$ and $Li_4P_2O_7$.

However, these steps need to be confirmed by additional analyses.

II.2.2. Investigation of the behaviour of LiBr

To explore further the reactivity of LiBr with $LATP_{0.3}$, Differential Scanning Calorimetry (DSC) measurements were performed on a pure LiBr sample and on a mixture of $LATP_{0.3}$ and LiBr with the same composition as in the HTXRD experiment (Section II.2.1). The two samples were not analysed under the same conditions: the DSC of the mixture was performed in air to maintain the same atmosphere as the HTXDR experiment, while pure LiBr sample was analysed under argon to prevent hydration. The two experiments were conducted with a heating ramp of 10 °C/min. In the case of pure LiBr, the result in Figure II-7-a shows an endothermic peak at 553 °C during heating, and an exothermic peak at 554 °C during cooling. These two peaks correspond to the melting and solidification temperature of LiBr. The Figure II-7-b displays the result for the mixture. Only the heating was analysed and, in this case, two endothermic peaks are observed at 55 °C and 115 °C, which correspond to the transition from the hydrated forms of LiBr, i.e. the amorphous one and the $LiBr.H_2O$, to the non-hydrated form, respectively. At higher temperatures, an exothermic peak is observed at 551 °C, corresponding to the melting temperature of LiBr. However, since the melting of the salt is an endothermic process, this suggests that the peak at 551 °C is not solely due to the melting of LiBr.

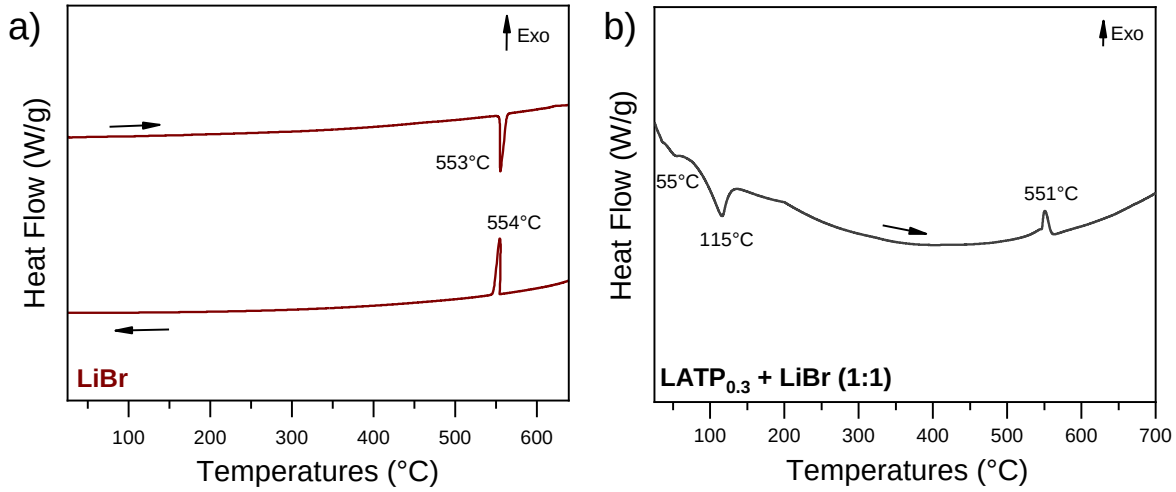

Figure II-7: DSC curves of (a) pure LiBr and (b) mixture of $LATP_{0.3}$ and LiBr (1:1). The measurements were performed under argon conditions for the pure LiBr whereas it was under air conditions for the mixture.

In comparison, the HTXRD data (Figure II-3 and Figure II-4) show that LiBr is no longer visible above 410 °C, which is well before its melting temperature. To understand the disappearance of LiBr, a thermogravimetric analysis (TG) coupled with Mass Spectroscopy (MS) was conducted on a sample composed of $LATP_{0.3}$ + LiBr (1:1). The experiment was performed at 700 °C, with a heating ramp of 10 °C/min, under air flow. The Figure II-8-a presents only the

TG curve obtained: three mass losses are observed at 54 °C, 116 °C and 548 °C. Based on Figure II-8-(b), where the MS results are presented, two H_2O^+ emissions (m/z = 18) are detected within a temperature range corresponding to mass losses at 54 °C and 116 °C. This observation is in correlation with the dehydration of the two hydrated LiBr polymorphs observed in HTXRD and DSC. Then, it was assumed that if LiBr degraded during the experiment, the analysis would detect bromine fragments: the analysis shows traces of Br^+ emissions (m/z = 79; 81 and 160) at approximately 150 °C and 550 °C, confirming our hypothesis. However, there is a concern regarding the low sensitivity of the bromine detection method, which might affect the accuracy of the results.

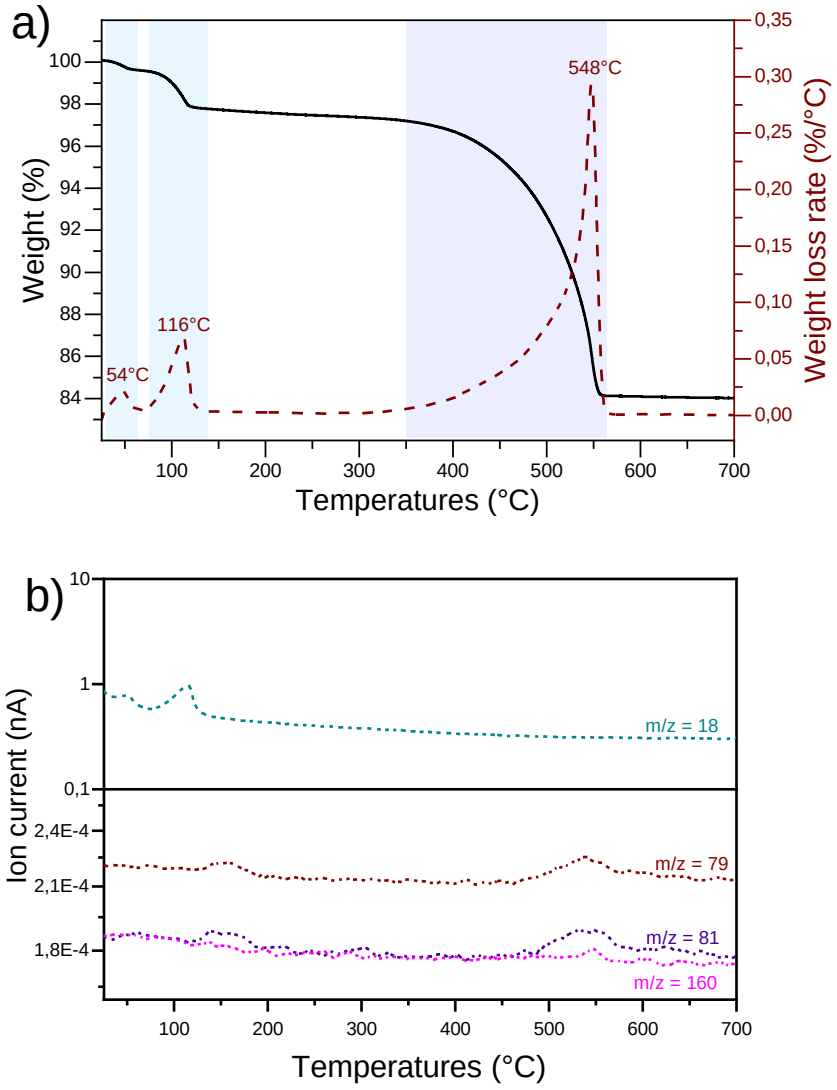

Figure II-8: (a) TG (—), DTG (- - -) curves of a mixture of $LATP_{0.3}$ and LiBr (1:1) in a temperature range from 30 to 700 °C, with a heating ramp of 10 °C/min, under air flow. The blue areas correspond to the dehydration of LiBr while the purple area shows the release of bromine species. (b) MS profiles of mixture of $LATP_{0,3}$ and LiBr (1:1).

To address this, Wavelength Dispersive X-Ray Fluorescence Spectroscopy (WDXRF) measurements were conducted to monitor the evolution of sample's chemical composition during thermal treatment. The measurements were taken after thermal treatments at temperatures corresponding to those before and after the mass losses observed in Figure II-8. For this purpose, pellets of mixture of $LATP_{0.3}$ and LiBr (1:1) were quenched at various heat treatment temperatures, including 350, 600, and 900 °C in air atmosphere and with a heating ramp of 10 °C/min. Each pellet was then ground using an agate mortar and re-compacted at 8 tons during 2 min using a uniaxial press for analysis. Results are summarised in the Table 4, wherein the mass content of each atom (Ti, O, Al, Br) was normalised to the phosphorus mass content.

Temperatures (°C)	Ti/P	O/P	Al/P	Br/P
25 (calculated)	0.87	2.06	0.08	0.93
350	1.06 (±0.15)	2.56 (±0.09)	0.11 (±0.03)	0.94 (±0.02)
600	0.88 (±0.02)	2.45 (±0.08)	0.08 (±0.03)	0.007 (±0.008)
900	0.91 (±0.04)	2.33 (±0.19)	0.08 (±0.01)	0 (±0.000)

Table 4: WDXRF data of a of $LATP_{0.3}$ and LiBr (1:1) samples quenched at various temperatures including 350, 600, 900 °C in air. The data obtained for a temperature of 25 °C were calculated theoretically from the equivalents for a mixture of $LATP_{0.3}$ and LiBr.

The values at 25 °C are calculated, as the sample is too sensitive towards air humidity for accurate analysis. For the Br/P ratio, its value decreases after heat treatment at 600 °C, dropping from ~0.9 at 350 °C to 0 at 600 °C, while no significant variations are observed for the other ratios. Considering the total mass loss after a heat treatment at 900°C (14 %), all the results suggest that a significant portion, if not all, of what is released during the heat treatment is only bromine, i.e. Br_2.

Although all experiments were conducted under the same program, the decomposition of LiBr is faster in the HTXRD experiment compared to the TG and DSC experiments. Indeed, the sample remains at elevated temperatures for a longer period in the HTXRD experiment than in the DSC and TG, due to the duration of each acquisition. This suggests that the rate at which temperature is increased may impact the mechanism. In order to understand the discrepancy concerning the decomposition of LiBr, TG at different heating ramp temperatures were carried out on a mixture of $LATP_{0.3}$ and LiBr (1:1). The measurements were conducted up to 900 °C, with heating ramps of 10, 5 and 2 °C/min under an air flow. The TG curves obtained and their first derivative curves are presented in Figure II-9. For all curves, two mass losses are observed in the temperature ranges of 45-65 °C and 100-130 °C, corresponding to water evaporation due

the transition from the hydrated forms of LiBr to the non-hydrated form (see Figure II-8). For the heating ramp of 10 °C/min, the curves in Figure II-9-a show a significant mass loss of 15 %, starting at 400 °C and peaking at 555 °C (as also presented in Figure II-8-a). In comparison, with a heating ramp of 5 °C/min (Figure II-9-b), the significant mass loss of 15 % is also observed but it is starting at 350 °C with a maximum peak at 559 °C. Finally, with a heating ramp is 2 °C/min, the previous significant mass loss of 14 % is split into two mass losses starting at ~300 °C and peaking at 365 °C for the first one, and starting at ~400 °C with a maximum peak at 555 °C for the second one.

For all the curves, the total percentage of mass loss observed between 300 °C and 555 ± 3 °C is 14 ± 1 %, confirming that it corresponds to release of Br_2, but the kinetics vary depending on the temperature ramp. Indeed, the slower the heating rate, the lower the temperature at which the mass loss is observed. In the case of a very slow heating rate, i.e., 2 °C/min, this mass loss corresponds to two processes: the reactivity of LiBr with $LATP_{0.3}$ that starts at a lower temperature (as observed in the HTXRD experiment) and the reactivity of LiBr accelerated by its melting (as observed in the DSC and TG experiments). This phenomenon is also evident when observing the mass loss rate at 555 °C ± 3 °C relative to the temperature ramp: the rate changes from -6 %/min, to -0.7 %/min, and then to -0.25 %/min for temperature ramps of 10, 5, and 2 °C/min, respectively.

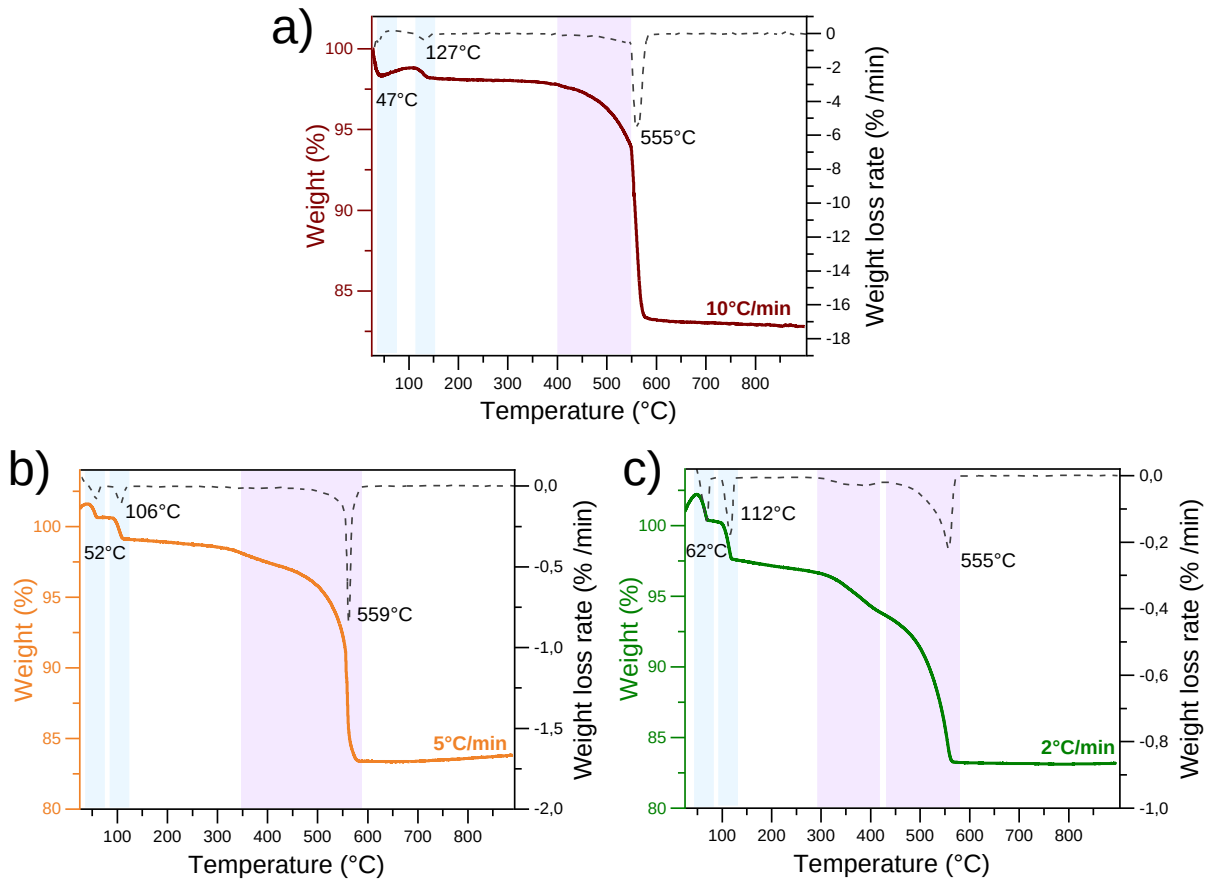

Figure II-9: TG curves of sample of $LATP_{0.3}$ and LiBr (1:1) analysed under air, with different heating ramp: (a) 10°C/min (—), (b) 5°C/min (—) and (c) 2°C/min (—).

However, it is necessary to determine whether this decomposition is directly related to its reactivity with $LATP_{0.3}$ or to its instability in air atmosphere.

For that purpose, samples consisting $LATP_{0.3}$ and LiBr (1:1) were treated at 850 °C for 30 min, with a heating ramp of 10 °C/min, under air or argon flow. The experiment involved analysing the composition of the outgoing flux using a colour indicator that reacts in the presence of bromine (Fluorescein Test). In the case of the test under air condition, the test showed a positive result for bromine, as the initial yellow colour (Figure II-10-a) turned in pink (Figure II-10-b). For the experiment under argon flow (Figure II-10-c), the colour of the indicator remained predominantly yellow, with some pink spots, indicating that less Br_2 was released under this atmosphere. This low intensity can be explained by system leaks or impure argon.

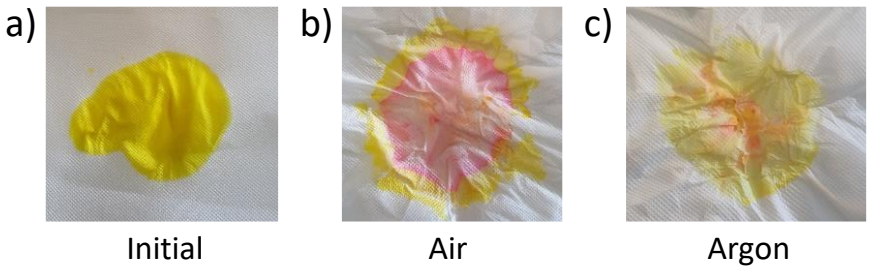

Figure II-10: Fluorescein test results, where (a) corresponds to the initial colour of the indicator, (b) and (c) the colour of the indicator after a heat treatment under air and argon conditions respectively.

Finally, a sample of pure LiBr were thermally treated in air with the same program than the mixture. In that case, the test also yielded a positive result for pure LiBr, highlighting its instability in an oxidising atmosphere. Thus, the decomposition of LiBr can be summarised by equation (4):

$$1\ LiBr + ¼\ O_2 \rightarrow ½\ Li_2O + ½\ Br_2 \qquad (4)$$

The formation of Li_2O is difficult to observe in the system with the characterisation methods used, but we can make the hypothesis that it directly reacted with $LATP_{0.3}$ to form other species such as Li_3PO_4.

II.2.3. Formation of transient chemical species

To confirm the Li_3PO_4 formation from Li_2O, a pellet from a mixture of $LATP_{0.3}$ and Li_2O (1:0.5) was prepared and thermally treated at 500 °C in air atmosphere. The chosen temperature corresponds to the disappearance of LiBr and the formation of Li_3PO_4 in Figure II-3. The XRD pattern is presented in Figure II-11. In this figure, the intensities were plotted in log scale to better observe the less intense diffraction peaks.

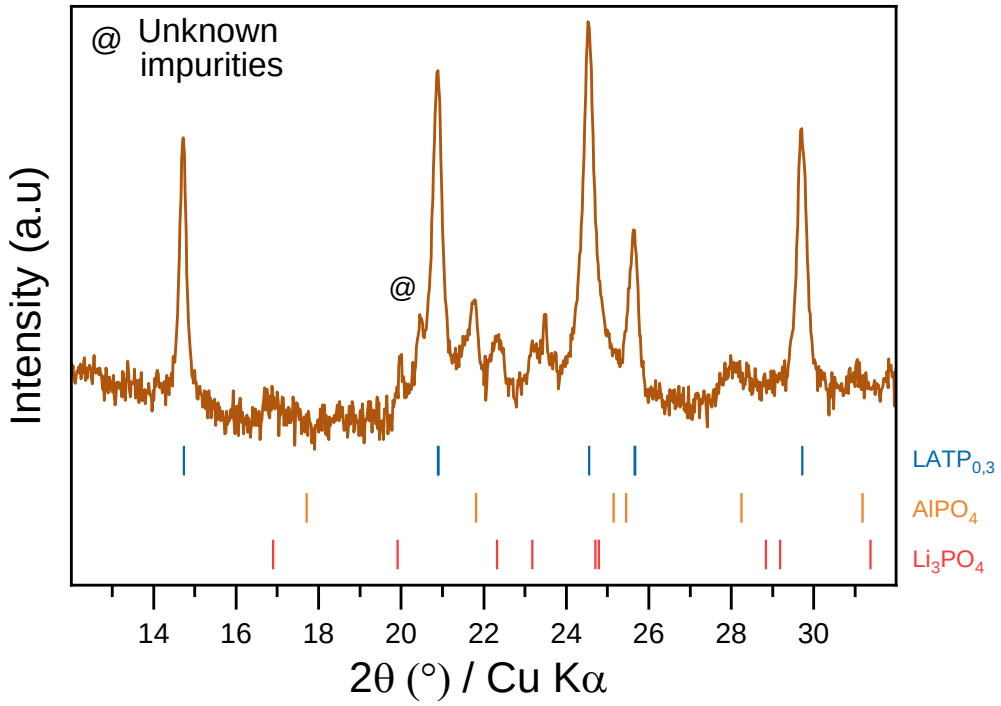

Figure II-11: XRD pattern of a mixture of $LATP_{0.3}$ and Li_2O (1:0.5) heat treated at 500 °C for 2 h under air atmosphere. The results are represented as a log of the intensity as a function of 2theta in order to improve the detection of low-intensity phases.

The results clearly show the formation of the Li_3PO_4 phase at this temperature. This confirms the hypothesis that the initial lithium salt reacts to form Li_2O, and thus Li_3PO_4. In parallel, new phases composed of titanium/aluminium atoms are expected. Based on the Figure II-3, no phases composed of aluminium are observable (excepted $AlPO_4$), but a TiO_2 phase is probably formed. However, it is mostly detected by diffraction at higher temperature compared to that of Li_3PO_4, and the detection of one diffraction peak is not sufficient to confirm its nature.

The formation of TiO_2 was investigated using Raman spectroscopy, as this technique is more sensitive to TiO_2. First, pure $LATP_{0.3}$ and pure TiO_2 anatase were analysed in order to determine their characteristic bands. In the case of pure $LATP_{0.3}$ presented in Figure II-12-a, the typical pattern is composed of bands between 100 and 1200 cm^{-1}. The bands between 100 and 350 cm^{-1} correspond to external modes which consisting of different types of atomic motions as Ti^{4+}

and PO_4^{3+} for example; bands at 400-500 cm^{-1} are attributed to O – P – O bending; bands at 500-700 correspond to the vibrations of Li-O and TiO_6; and finally, bands between 900-1100 cm^{-1} represent PO_4 symmetrical et asymmetrical vibrations[207–211]. As shown in Figure II-12-b, TiO_2 is characterised by five bands: three assigned to the E_g modes at 141, 195 and 636 cm^{-1}, one to the $B1_g$ mode at 394 cm^{-1}, and a final band at 517 cm^{-1} corresponding to the $A1_g$ and $B1_g$ modes[212,213].

Then, pellets of mixture of $LATP_{0.3}$ and LiBr (1:1) heat treated and quenched at different temperature including 200 °C, 400 °C, 600 °C and 800 °C in air, were analysed. Each pellet was then ground using an agate mortar in a glovebox and sealed in glass tubes for analysis. All the Raman spectra were normalised using the most intense band of $LATP_{0.3}$ around 1005 cm^{-1} in order to better visualise potential variations in intensities. Results are presented in Figure II-12-c. A sample composed of the mixture at 25 °C was also analysed as a reference. It presents only the characteristic bands of $LATP_{0.3}$, since LiBr is more difficult to observe using Raman spectroscopy. At 200 °C, no modifications are observed, but the band initially at 139 cm^{-1} shifts to 143 and 141 cm^{-1} at 400 °C and 600 °C respectively. Furthermore, the shift observed is accompanied by a slight variation in the intensity, which seems to be higher at 400 °C. At higher temperature, the characteristic bands of $LATP_{0.3}$ are greatly modified, and the impurity $LiTiOPO_4$ is observed at 781 cm^{-1}[60,214].

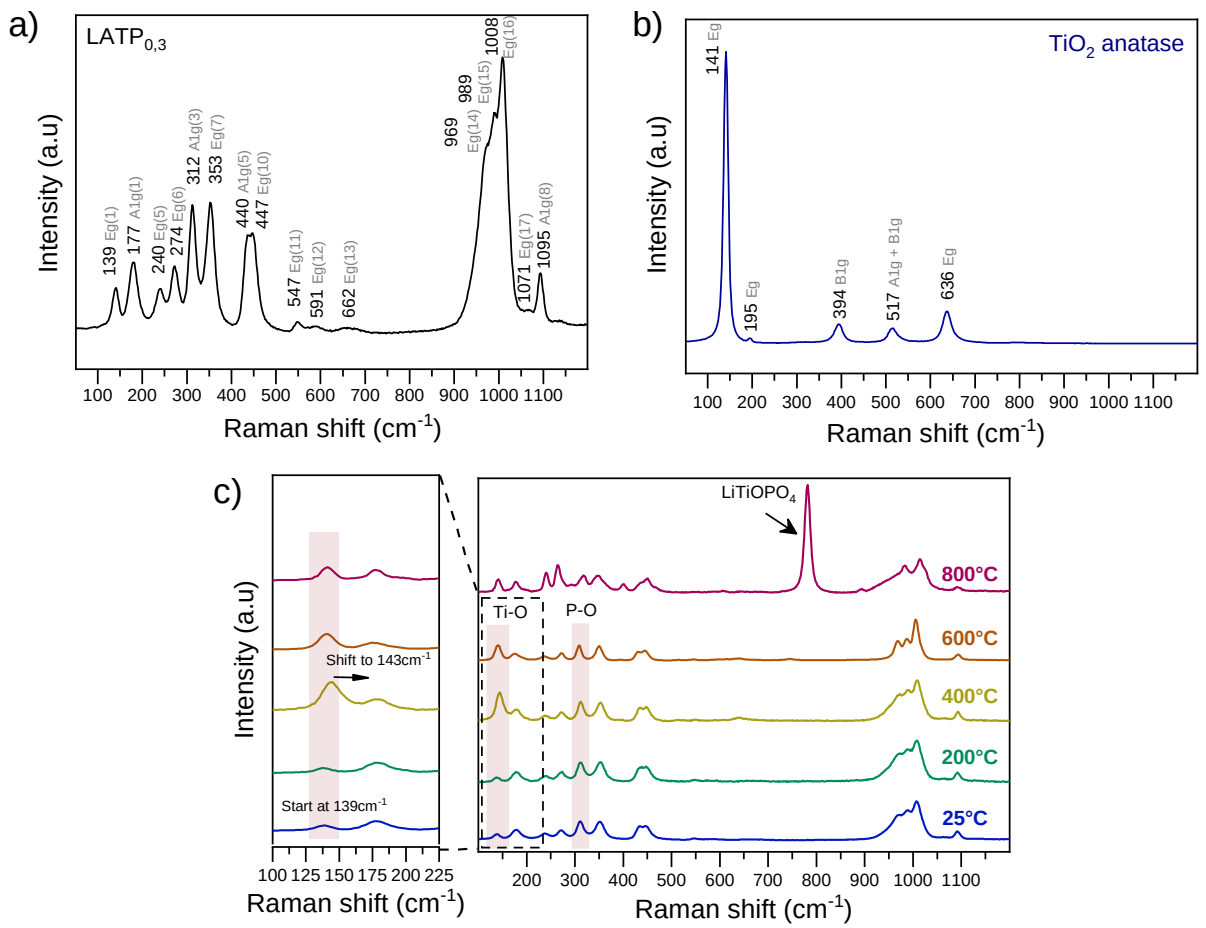

Figure II-12: Raman spectra of (a) pure $LATP_{0.3}$, (b) pure TiO_2 anatase and (c) mixture of $LATP_{0.3}$ and LiBr (1:1) at room temperature and quenched at different temperatures including 200°C, 400 °C, 600 °C and 800 °C.

In the literature, the band at 139 cm^{-1} corresponds to translational vibrations of Ti^{4+} from $LATP_{0.3}$[209], but according to our hypothesis, it may also be superimposed with the band at 141-143 cm^{-1}, associated with the Ti-O bond from TiO_2 anatase[213]. The variations in the integration ratio of the range of band between 139 and 141 cm^{-1} (associated with $LATP_{0.3}$ and TiO_2) relatives to the band at 312 cm^{-1} (associated with P-O vibrational modes of $LATP_{0.3}$) were monitored and summarised in Table 5. All values are averaged over two to three spectra per sample.

Temperatures (°C)	Mean of Ti-O/ P-O
25	0.26 (±0.03)
200	0.17 (±0.03)
400	0.96 (±0.80)
600	1.00 (±0.20)

Table 5: Average integration values for the Ti-O band at ~ 139-143 cm^{-1} (associated with $LATP_{0.3}$ and TiO_2) versus the P-O band at 309 cm^{-1} (associated with P-O vibrational modes of $LATP_{0.3}$) as a function of heat treatment temperatures.

These results show an increase in the intensity of the range at 139-141 cm^{-1} relatives to the band at 309 cm^{-1} between 400 and 600 °C, highlighting the formation of TiO_2 at theses temperatures. The significant standard deviation determined for the values at 400 °C is explained in Figure II-13, where three spectra acquired at different points of the sample heat treated at 400 °C are presented. The values corresponding to the Ti-O/P-O ratio vary from one spectrum to another, highlighting the non-uniformity of the reactivity. Indeed, the experiment involves quenching the sample 5-10 minutes after reaching the target temperature, which means that the reaction can be more or less advanced in different parts of the sample.

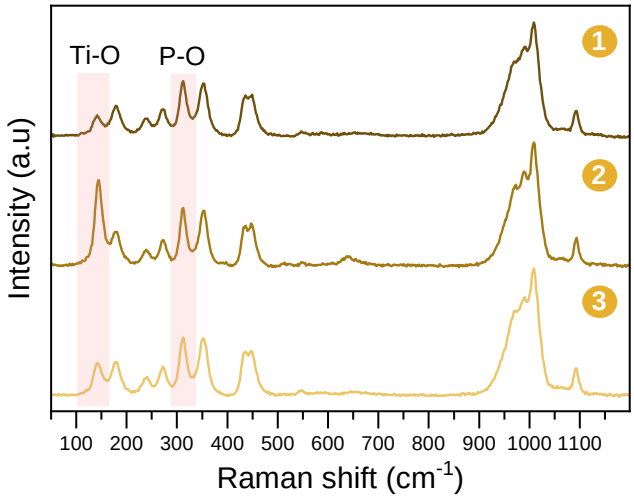

N° spectra	Ti-O/ P-O
1	0.35
2	1.86
3	0.65

Figure II-13: Raman spectra of the mixture of $LATP_{0.3}$ and LiBr heat treated at 400 °C acquired at different points in sample. The table corresponds to the integration values for the Ti-O band versus the P-O band.

Finally, as TiO_2 is observed from 400 °C according to this technique, it suggests that the formation of TiO_2 could be correlated with the formation of Li_3PO_4.

II.2.4. Formation of final impurities

In order to confirm how final impurities are formed, an *ex-situ* high temperature test of a mixture of Li_3PO_4 and $LATP_{0.3}$ was carried out. The molar ratio between the two compounds was chosen to convert all the $LATP_{0.3}$ into $Li_4P_2O_7$ and $LiTiOPO_4$. This reaction can be expressed according to equation (6), where LATP is replaced by LTP to simplify the reaction:

$$1/3\ LiTi_2(PO_4)_3 + Li_3PO_4 \rightarrow 2/3\ LiTiOPO_4 + 2/3\ Li_4P_2O_7 \quad (6)$$

Two temperatures were tested, namely 700 °C and 800 °C, which correspond to the temperature range where impurities are formed. The Figure II-14 displays the XRD pattern of each sample. At 700 °C, only diffraction peaks of Li_3PO_4 and $LATP_{0.3}$ are observed, while at 800 °C, $Li_4P_2O_7$ and $LiTiOPO_4$ are formed. This experiment confirms the final reaction seen by HTXRD: $LiTiOPO_4$ and $Li_4P_2O_7$ are formed by the reaction of Li_3PO_4 with $LATP_{0.3}$ up to 800 °C.

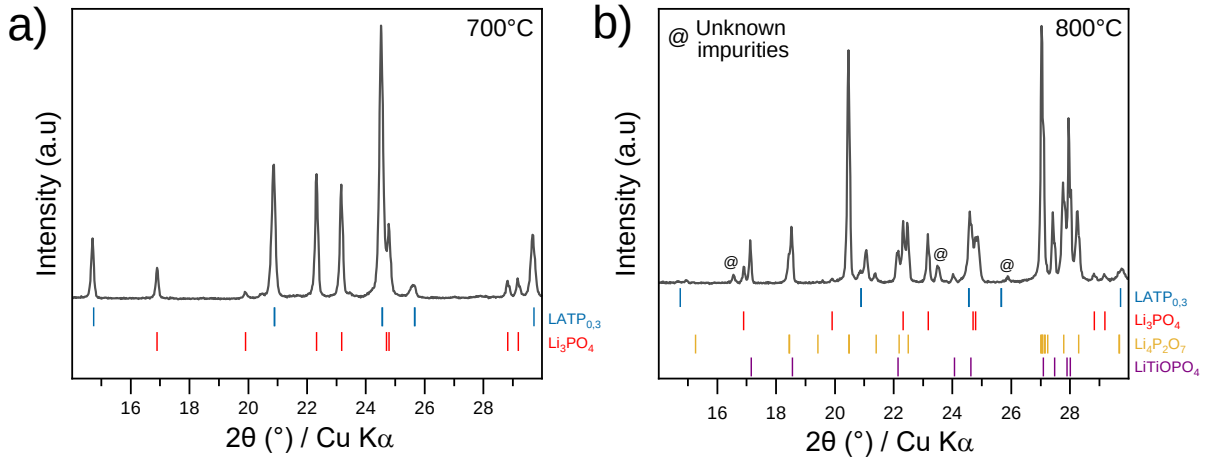

Figure II-14: *Ex-situ* XRD patterns of mixture of $LATP_{0.3}$ and Li_3PO_4 (1:3) heat treated at (a) 700 °C and (b) 800 °C during 2 h, in air.

In the case of TiO_2, it is suggested by the literature[215] and the ternary diagram Li_2O-TiO_2-P_2O_5 (Figure II-2) that it reacts also with the $LATP_{0.3}$ to form $LiTiOPO_4$. The reaction is expressed by the equation (7):

$$LiTi_2(PO_4)_3 + Li_3PO_4 + 2\ TiO_2 \rightarrow 4\ LiTiOPO_4 \quad (7)$$

Finally, the only remaining questions concern what happens to the $AlPO_4$ impurity and the aluminium atoms from the $LATP_{0.3}$ consumed in the previous reactions.

II.2.5. Aluminium exchange

The reaction mechanism previously studied (Figure II-4) shows that a part of the initial $LATP_{0.3}$ has been consumed, and that the $AlPO_4$ phase reacts at the same temperature as the formation of the final impurities. However, no other phases containing aluminium could be identified. In this section, we are exploring two hypotheses concerning the behaviour of aluminium in the mechanism by using Magic Angle Spin Nuclear Magnetic Resonance (MAS NMR) spectroscopy and Density Functional Theory (DFT) calculations. These analyses were performed with the collaboration of Christel Gervais and Cristina Coelho-Diogo (LCMCP, SU).

II.2.5.1. Increasing the Al^{3+} substitution level

One possibility discussed by Kwatek et al[139,216], is the increase of the level of substitution of Ti^{4+} by Al^{3+} and Li^+ in $LATP_{0.3}$ thanks to the decomposition of the LiBr during the mechanism. This substitution should be visible via a modification of lattice parameters of $LATP_{0.3}$, as the substitution of Ti^{4+} by Al^{3+} and Li^+ decreases these parameter values[155,217,218]. In our case, a variation is observed for the *c* value based on results from Figure II-6, when comparing the lattice parameters of $LATP_{0.3}$ before and after the thermal treatment. However, this variation is also observed for a pure $LATP_{0.3}$ sample. The XRD results alone are insufficient to confirm a variation of the substitution level of $LATP_{0.3}$, as lattice parameter values are averaged and vary significantly in the literature for the same level of Al^{3+} substitution[155]. In the literature, this substitution level can be monitored by MAS NMR spectroscopy, as some studies have investigated several Al^{3+} substitution level for $Li_{1+x}Al_xTi_{2-x}(PO_4)_3$ (x = 0-0.7)[218,219]. Thus, we decided to use this technique to confirm, or infirm, this first hypothesis. The ^7Li, ^{27}Al and ^{31}P MAS NMR experiments were carried out on pellets composed of mixtures of $LATP_{0.3}$ and LiBr (1:1), quenched in air at different temperatures including 200, 400, 600 and 800 °C. The heat treatments were conducted with a heating ramp of 10 °C/min.

First, ^{31}P (spin I = 1/2) and ^7Li (spin I = 3/2) MAS NMR spectra of samples are presented in Figure II-15-a and Figure II-15-b respectively. The ^{31}P MAS NMR spectra of a sample kept at room temperature and heated at 200°C show an asymmetric broad signal centred at -27 ppm. It can be assigned to the $P(OTi)_{4-n}(OAl)_n$ phosphate groups (with n = 0-4) of $LATP_{0.3}$ and is observed in all spectra[93,216]. This signal may be superimposed to the signal of $AlPO_4$. At 400 °C and 600 °C, new signals are observed at 10.8 ppm, -3.5 ppm and -5.6 ppm. The individual spectra of known impurities Li_3PO_4, $LiTiOPO_4$ and $Li_4P_2O_7$ are also presented, and the signal at 10.8 ppm indicates the presence of Li_3PO_4 whereas the two smaller signals

correspond to $Li_4P_2O_7$ (2 phosphorous crystallographic sites). At 800°C, the signal centred at -27 ppm related to the phosphate groups of $LATP_{0.3}$ is broader: this phenomenon could indicate Al^{3+} diffusion in $LATP_{0.3}$ by a conversion from small quantity of n in $P(OTi)_{4-n}(OAl)_n$ to a greater quantity. Indeed, the higher the number n of $P(OTi)_{4-n}(OAl)_n$ groups, the more positive the signal[139,218–220]. Furthermore, the distribution of all these groups broadens the $LATP_{0.3}$ signal. However, the spectrum is composed of several other signals: two signals at -3.5 and -5.6 ppm corresponding to $Li_4P_2O_7$; one at -9.8 ppm indicating the formation of $LiTiOPO_4$; and another one at -29.7 ppm which remains unidentified. This indicates that the broader signal of $LATP_{0.3}$ at 800 °C could also be due to the overlap of signals from other unidentified species.

Pure samples of $LATP_{0.3}$ and LiBr were analysed by ^{7}Li MAS NMR: two signals are observed at 0.49 ppm and -0.94 ppm for the $LATP_{0.3}$ sample, whereas only one is observed at -1.75 ppm for LiBr. The narrow signal at -0.94 ppm is characteristic of $LATP_{0.3}$ with a level of substitution of Al^{3+} equal to 0.3[219], which considered both lithium sites Li1 and Li2. However, the broad signal at 0.49 ppm remains unidentified and is not present in the other spectra. Only the contributions of LiBr and $LATP_{0.3}$ are visible at 200 °C, whereas the signal related to LiBr disappears at 400 °C and above. It is accompanied by the appearance of a new signal at 0.08 ppm that could be Li_3PO_4 according to the ^{31}P MAS NMR. At 800 °C, this signal disappears and another one appears at 0.21 ppm, corresponding to $Li_4P_2O_7$. The $LiTiOPO_4$ impurity is not clearly visible as its signal is overlapped with that of $LATP_{0.3}$ but it is well defined in Figure II-15-a. According to the literature, a higher substitution level implies a broader signal corresponding to Li sites from $LATP_{0.3}$ as the substitution of Ti^{4+} by Al^{3+} involves the insertion of additional Li^+ to be neutral. The signal is shifted only when the substitution level x exceeds 0.5 in $Li_{1+x}Al_xTi_{2-x}(PO_4)_3$[219].

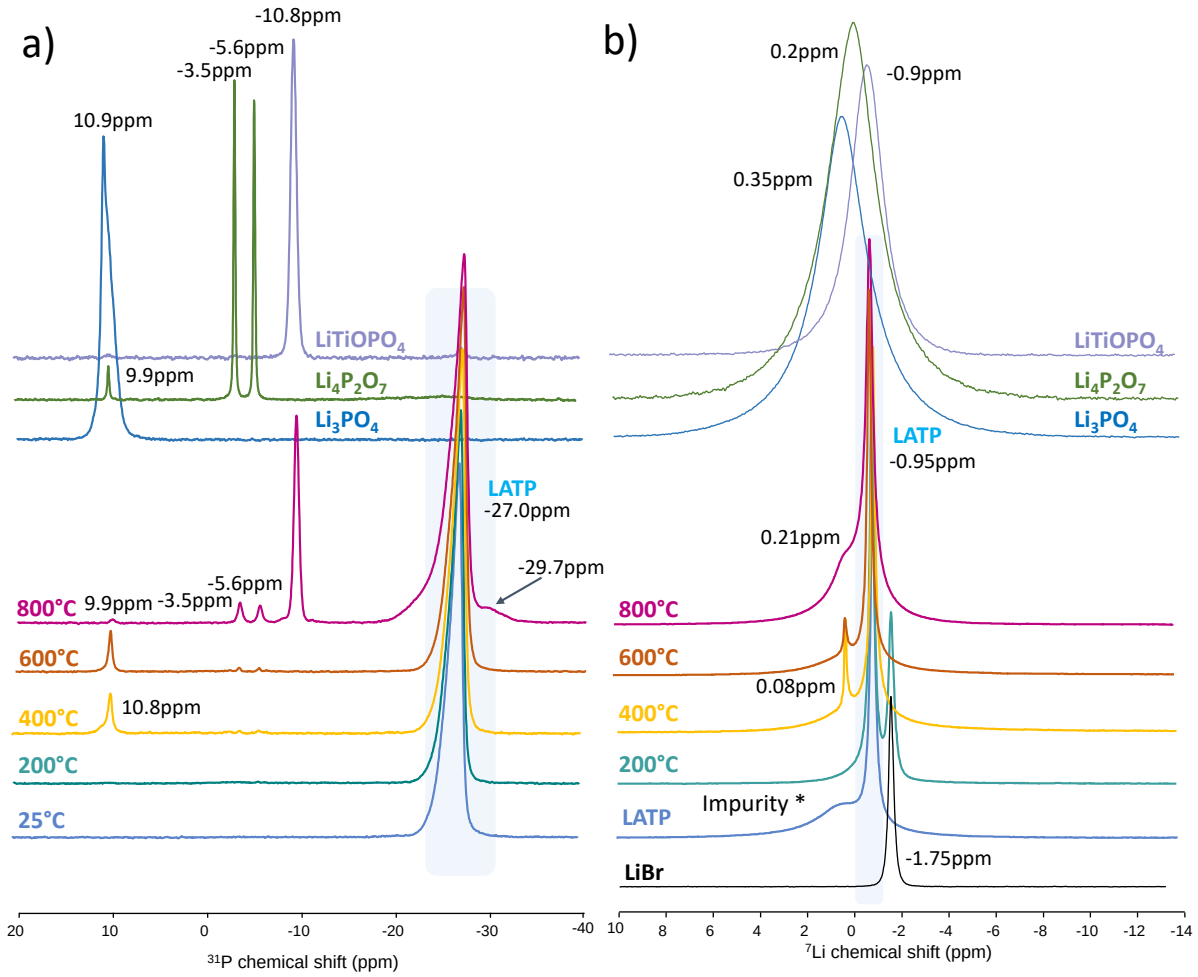

Figure II-15: (a) ^{31}P MAS NMR spectra of $LATP_{0.3}$ and LiBr (1:1) samples quenched at different temperature, including 200 °C, 400 °C, 600 °C and 800 °C and one at 25 °C and spectra of impurities such as $LiTiOPO_4$, Li_3PO_4 and $Li_4P_2O_7$. (b) ^{7}Li MAS NMR spectra of $LATP_{0.3}$ and LiBr (1:1) samples quenched at different temperature, including 200 °C, 400 °C, 600 °C and 800 °C; and spectra of impurities such as $LiTiOPO_4$, Li_3PO_4 and $Li_4P_2O_7$.

Finally, all ^{27}Al (spin I = 5/2) MAS NMR spectra of the samples are presented in Figure II-16-a. According to the literature, a signal is expected around -15 ppm in the case of pure LATP, corresponding to Al in octahedral coordination (Al^{VI}), which substitutes for Ti in the TiO_6 group[139,219]. The signal is present across all spectra at -14 ppm, and is accompanied by other signals around 40 ppm. The latter corresponds to Al sites in tetrahedral environments (Al^{IV}), which indicates the presence of $AlPO_4$[93,221]. For the spectrum of pure $LATP_{0.3}$ and for the mixture at 25 °C, this signal is split at 41.1 and 39 ppm, probably indicating the presence of two $AlPO_4$ with slightly different structures. Starting at 200 °C, a single signal is present at 40.9 ppm, which eventually disappears at 800 °C.

At the same temperature, a new signal appears at -17.2 ppm, next to that of LATP at -14 ppm. Considering the proximity between the two peaks we performed a 2D Multiple Quantum Magic Angle Spinning (2D MQMAS) experiment on the sample thermally treated at 800 °C. The

result of this analysis is presented in Figure II-16-b, in which two sites are observable. This indicates that the signals at -14 ppm and -17.2 ppm originate from two sites that exhibit small quadrupolar coupling constants C_Q with different environments. In the literature, the presence of two signals has already been observed when the level of Al^{3+} substitution is greater than x = 0.5 in $Li_{1+x}Ti_{1-x}Al_x(PO_4)_3$, and the authors proposed the formation of a new amorphous phase containing Al in octahedral site to explain it, without further investigation[218,219].

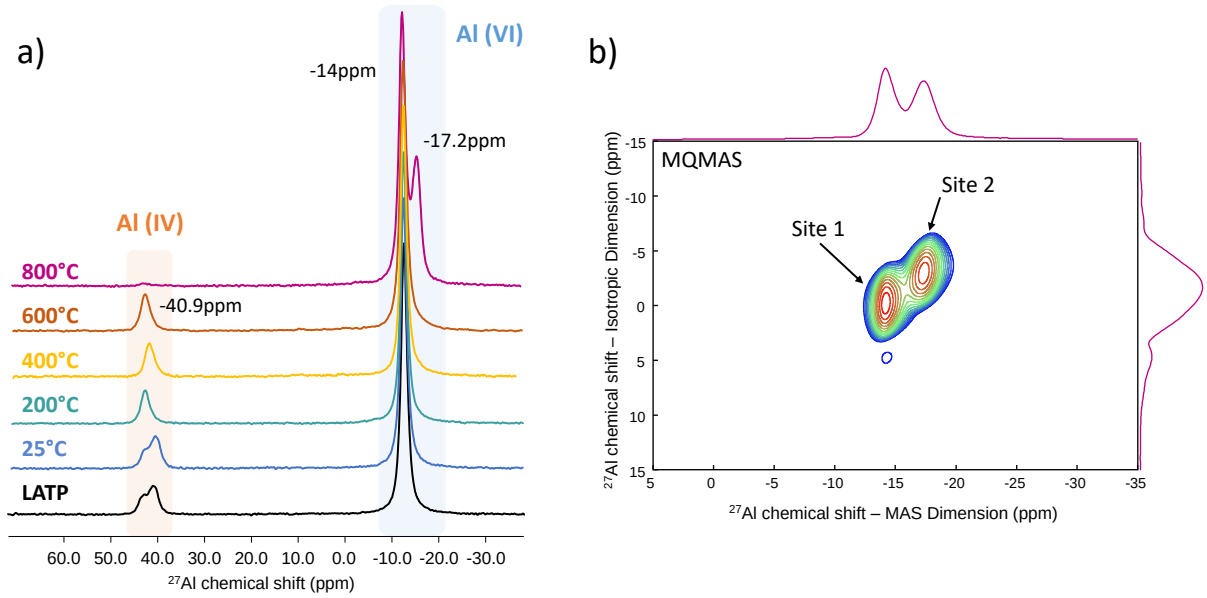

Figure II-16: (a) ^{27}Al MAS NMR spectra of pure $LATP_{0.3}$ without heat treatment and of a mixture of $LATP_{0.3}$ and LiBr (1:1) quenched at different temperature, including 200 °C, 400 °C, 600 °C and 800 °C and one at 25 °C. (b) ^{27}Al 2DMQMAS of the mixture of $LATP_{0.3}$ and LiBr (1:1) quenched at 800 °C.

Based on these results, both hypotheses are possible: the appearance of new peaks in ^{31}P and ^{27}Al MAS NMR can be attributed either to the formation of a new phase or to the substitution of Ti^{4+} by Al^{3+} and Li^+.

In the case of the second hypothesis, it is assumed in literature that a greater level of Al substitution does not imply any shift of LATP signals from ^{27}Al and ^{31}P MAS NMR spectra. However, the impact of the Li and Al distributions within the structure has not been studied. Thus, we decided to conduct some DFT calculations in order to understand the impact of these distributions on the ^{27}Al and ^{31}P chemical shifts of the signals related to $LATP_{0.3}$.

For this purpose, different models (Figure II-17) were obtained starting from the crystalline structure of $Li_{1-x}Al_xTi_{2-x}(PO_4)_3$[155] and using 1×1×1 and 2×1×1 supercells in which Al atoms substitute some of the Ti positions with addition of Li atoms (in crystallographic positions of Li2-type) to keep the structure neutrally charged.

- Models named **Model 1** and **Model 5** consist in a 1x1x1 cell with two Al substituting two Ti. In the first case, one Li is added in the vicinity of each Al while in the second case, the two additional Li are placed close to one of the Al. The global composition of the cell is **$Ti_{10}Al_2P_{18}O_{72}Li1_6Li2_2$**.
- Models named **Model 2**, **Model 3** and **Model 7** consist in a 2x1x1 supercell with five Al substituting five Ti with a global composition **$Ti_{19}Al_5P_{36}O_{144}Li1_2Li2_5$.** In these models, aluminium atoms are isolated in the sense that there are only Ti octahedral in their second shell of neighbouring atoms. Differences between them stand in the position of the five additional Li: one in the vicinity of each Al in **Model 2**, two in the vicinity of one Al in **Model 3** (meaning that one of the Al has no additional Li in its coordination sphere), and three in the vicinity of one Al in **Model 6**. In the case of **Model 7**, three additional Li2 atoms are in the vicinity of one Al but they are accompanied by a Li1.
- **Model 6** consists in a 2x1x1 supercell with four Al substituting four Ti with a global composition **$Ti_{19}Al_4P_{36}O_{144}Li1_2Li2_4$** in which three of the additional Li2 atoms are in the vicinity of one of the Al.
- Finally, model named **Model 4** also consists in a 2x1x1 supercell with five Al substituting five Ti with a global composition **$Ti_{19}Al_5P_{36}O_{144}Li1_2Li2_5$**. This model resembles to **Model 2** but with a clusterisation of Al in the sense that there is systematically an Al octahedral in the second shell of a given Al site.

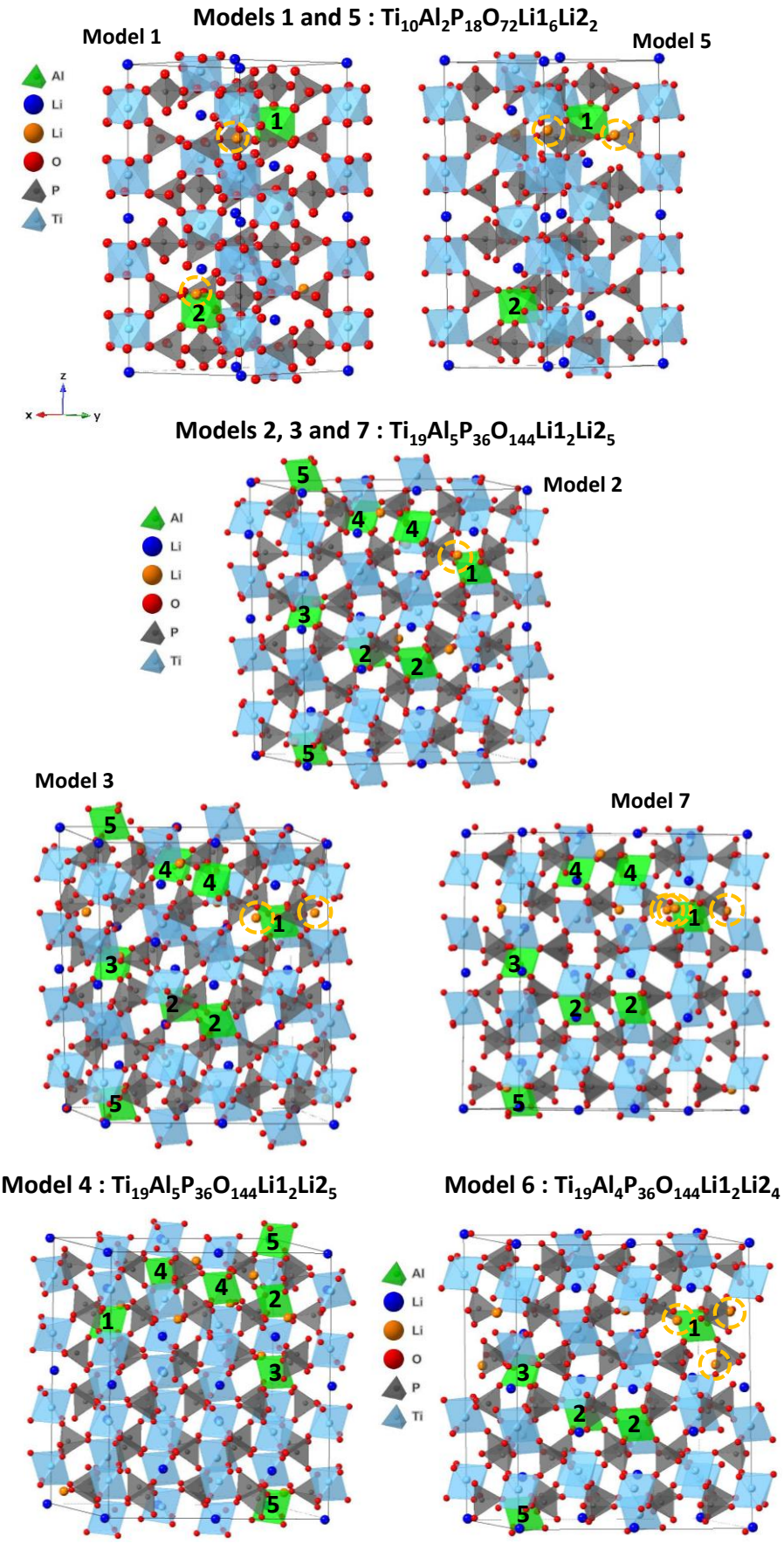

Figure II-17: Crystal structures of models used for DFT calculations. The numbers represent the different Al environments.

All atomic positions were then relaxed with the VASP (Vienna Ab-initio Simulation Package) code[222] based on the Kohn-Sham Density Functional Theory (DFT) and using a plane-wave pseudopotential approach. The cells parameters were fixed to X-ray diffraction parameters during geometry optimizations. The NMR parameters were then calculated within Kohn-Sham DFT using the QUANTUM-ESPRESSO code[223], keeping the atomic positions equal to the values previously calculated with VASP. The PBE generalized gradient approximation[224] was used and the valence electrons were described by norm conserving pseudopotentials[225] in the Kleinman Bylander form[226]. The shielding tensor was computed using the Gauge Including Projector Augmented Wave (GIPAW) approach[227], which enables the reproduction of the results of a fully converged all electron calculation. The isotropic chemical shift δ_{iso} is defined as $\delta_{iso} = -[\sigma - \sigma_{ref}]$ where σ is the isotropic shielding and σ_{ref} is the isotropic shielding of the same nucleus in a reference system. In the present case, we used the comparison between the experimental δ_{iso} and calculated δ_{iso} ^{31}P chemical shift values for Li_3PO_4 and ^{27}Al for a-Al_2O_3.

Based on these models, ^{31}P and ^{27}Al NMR spectra were calculated to compare them with the spectra obtained from the experiments conducted at 800 °C (see Figure II-18). The **Model 1** corresponds to a perfect schematic theoretical structure where all the Al are accompanied by one Li in their vicinity. In that case, two Ti atoms are substituted by two Al atoms in the Ti sites. Thus, the two signals corresponding to these environments are observed at close chemical shifts but with different quadrupolar parameters. Based on results from **Model 5**, by enriching one of the two sites with lithium at the expense of the other, a shift in the signal corresponding to the lithium-enriched environment towards positive values can be observed. This shift is accompanied by a greater C_Q. This observation is also verified by comparing results from **Model 2, 3, 6 and 7**: the more an Al site local environment is enriched in Li, the more its δ_{iso} (^{27}Al) is shifted towards positive values and the more its C_Q is important. In our case, the new signal appears at more negative values, indicating that the lithium enrichment of one of the aluminium sites is not the cause. The **Model 4** exhibits a structure where all the Al and Li (Li2) atoms are clustered, but in that case, the global signal calculated is narrower than that experimentally observed. Examining the calculated ^{31}P NMR spectra, we find that **Models 3**, **7**, **4**, and **6** could potentially correspond to the experimental observations. However, only **Model 6** aligns most closely with both the ^{27}Al and ^{31}P NMR experimental results, though it does not fully reproduce the experimental data. These experiments demonstrate that the distribution of aluminium and lithium impacts the ^{31}P and ^{27}Al signals associated with $LATP_{0.3}$. This suggests

that the hypothesis of aluminium and lithium substitution as the origin of the peak at -17.2 ppm cannot be ruled out and requires further investigation.

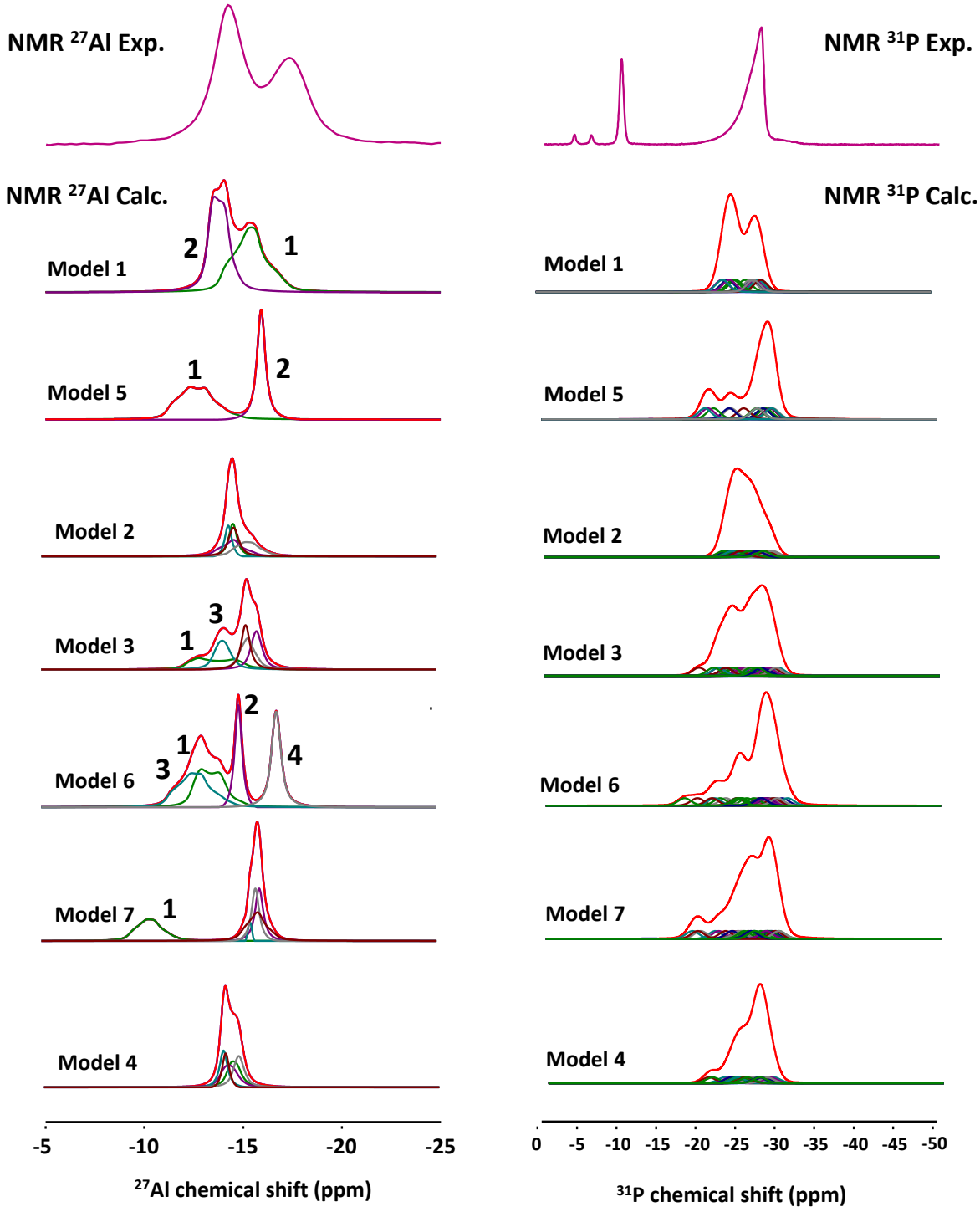

Figure II-18: ^{27}Al and ^{31}P NMR spectra calculated from DFT calculations. Each coloured curve in a spectrum represents a different environment for the atom being probed. In the case of ^{27}Al NMR spectra, some of these curves are labelled with numbers, correlating with specific environments in the crystal structure models.

II.2.5.2. New phases Al-containing

On the other hand, the formation of aluminium-containing phases cannot be excluded. Although literature reports made mentions of a possible amorphous phase, in our experiments unidentified crystalline impurities have been observed by XRD. To help identify these impurities, the phases formed after a heat treatment at 800 °C were compared as function of the Al substitution level of LATP (x = 0; 0.3). For that, mixtures of $LATP_{0.3}$ + LiBr (1:1) and of LTP + LiBr (1:1) were quenched at 800 °C, and the heat treatment was conducted in air with a heating ramp of 10 °C/min. The resulting powders were analysed by XRD and the results are presented in Figure II-19. As first observation, the reactivity is similar for $LATP_{0.3}$ and LTP with LiBr: the major impurities $LiTiOPO_4$ and $Li_4P_2O_7$ are formed. Interestingly, some additional peaks appear in the case of $LATP_{0.3}$, which may indicate that these peaks are due to the presence of one or multiple phases containing aluminium. Unfortunately, no matches were found on structural databases, and these phases remain unidentified.

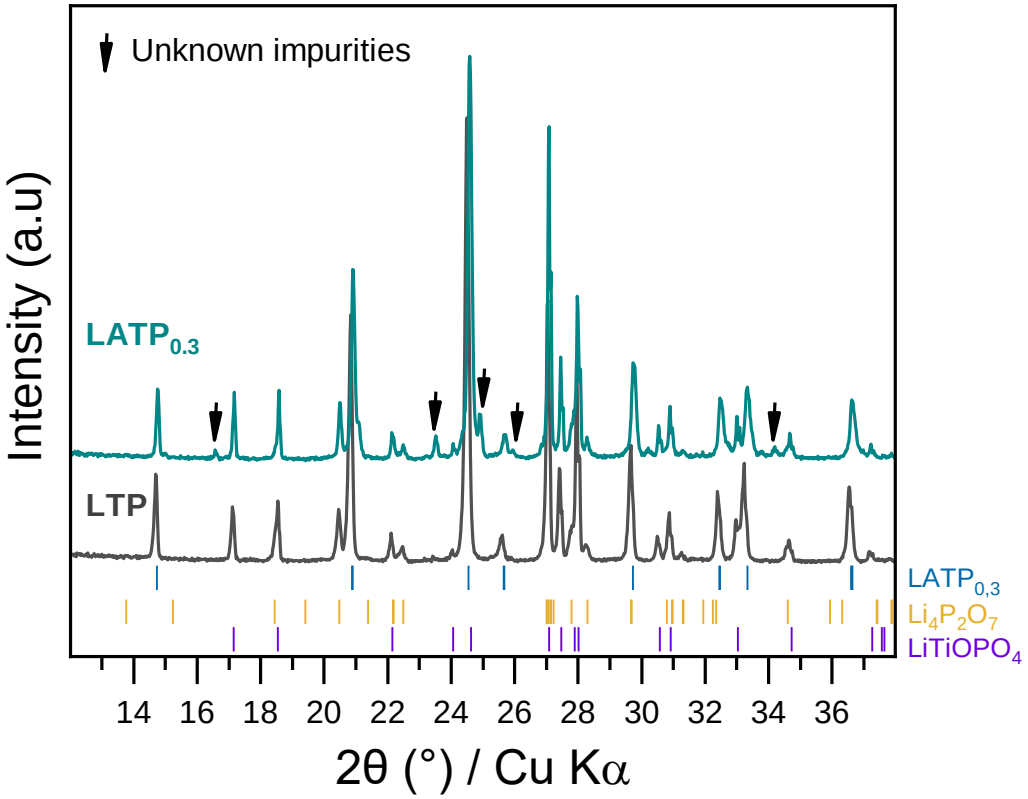

Figure II-19: XRD patterns of mixtures of $LATP_{0.3}$ + LiBr (1:1) (—) and LTP + LiBr (1:1) (—) quenched at 800 °C. The black arrows show the unknown impurities which indicate the formation of Al-containing phases.

A LATP phase with a higher level of Al substitution (x = 0.5) was also investigated, but the same unidentified impurities were observed, and this did not aid in their identification.

In the literature, Waetzig et al[189], presented the possibility of a similar phase of $LiTiOPO_4$ but with a substitution of some Ti atoms by Al atoms. This substitution must be accompanied by the insertion of Li^+ in order to keep the neutrality of the structure. No crystallographic data for this phase has been reported in the literature to our knowledge, but we decided anyway to explore this possibility in more details.

As a first approach, we made the hypothesis that the new phase $Li_{1+x}Ti_{1-x}Al_xOPO_4$ retains the same orthorhombic system with the same space group *Pnma* as $LiTiOPO_4$. Then, the Bond Valence Sum (BVS) method was used in order to identify potential preferential site where an additional lithium atom could be placed in this structure. This method is built upon Pauling's rules, and it is based on structural information such as bond lengths and atomic valence. According to BVS, one atomic position for the insertion of an additional lithium (Li2) is possible, as described in Figure II-20. All other atomic positions for the remaining atoms come from the crystalline structure of $LiTiOPO_4$[228].

Atoms	x	y	z
Ti	0.3220	0.7500	0.2190
P	0.3740	0.2500	0.1270
O1	0.1120	0.7500	0.1500
O2	0.7910	0.7500	-0.0010
O3	0.0470	0.2500	0.4840
O4	0.8710	0.4460	0.2470
Li1	0.0000	0.0000	0.0000
Li2	**0.6200**	**0.0000**	**0.1500**

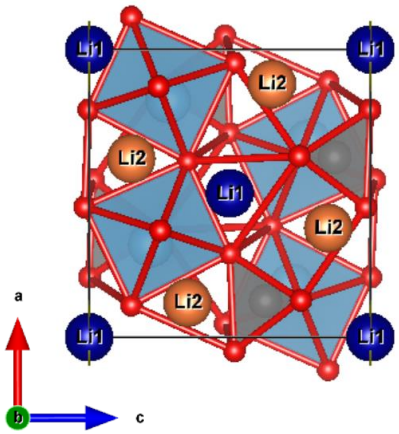

Figure II-20: Atomic positions for atoms in $LiTiOPO_4$, accompanied by the additional insertion site for Li atom (Li2). These positions are represented by a crystal structure where Ti atoms are described by blue octahedral, P atoms by grey tetrahedral, O atoms by small red spheres. Li atoms are represented by blue spheres (Li1) while additional Li atoms are represented by orange spheres (Li2).

Finally, DFT calculations was conducted based on a model obtained from the crystalline structure presented in Figure II-20. We used a 2×2×2 supercell in which two Al atoms substitute two Ti atoms in Ti position with the addition of two additional Li atoms in Li2 sites, for a global composition of $\mathbf{Li_{34}Ti_{32}Al_2O_{32}(PO_4)_{32}}$. Based on these calculations, calculated ^{27}Al and ^{31}P NMR spectra were determined to compare with experimental spectra of the previous mixture quenched at 800 °C. The results presented in Figure II-21 show an incompatibility between the calculated and experimental signals. Thus, the phase $Li_{1+x}Ti_{1-x}Al_xOPO_4$ with the previously determined crystal structure is not formed during the mechanism.

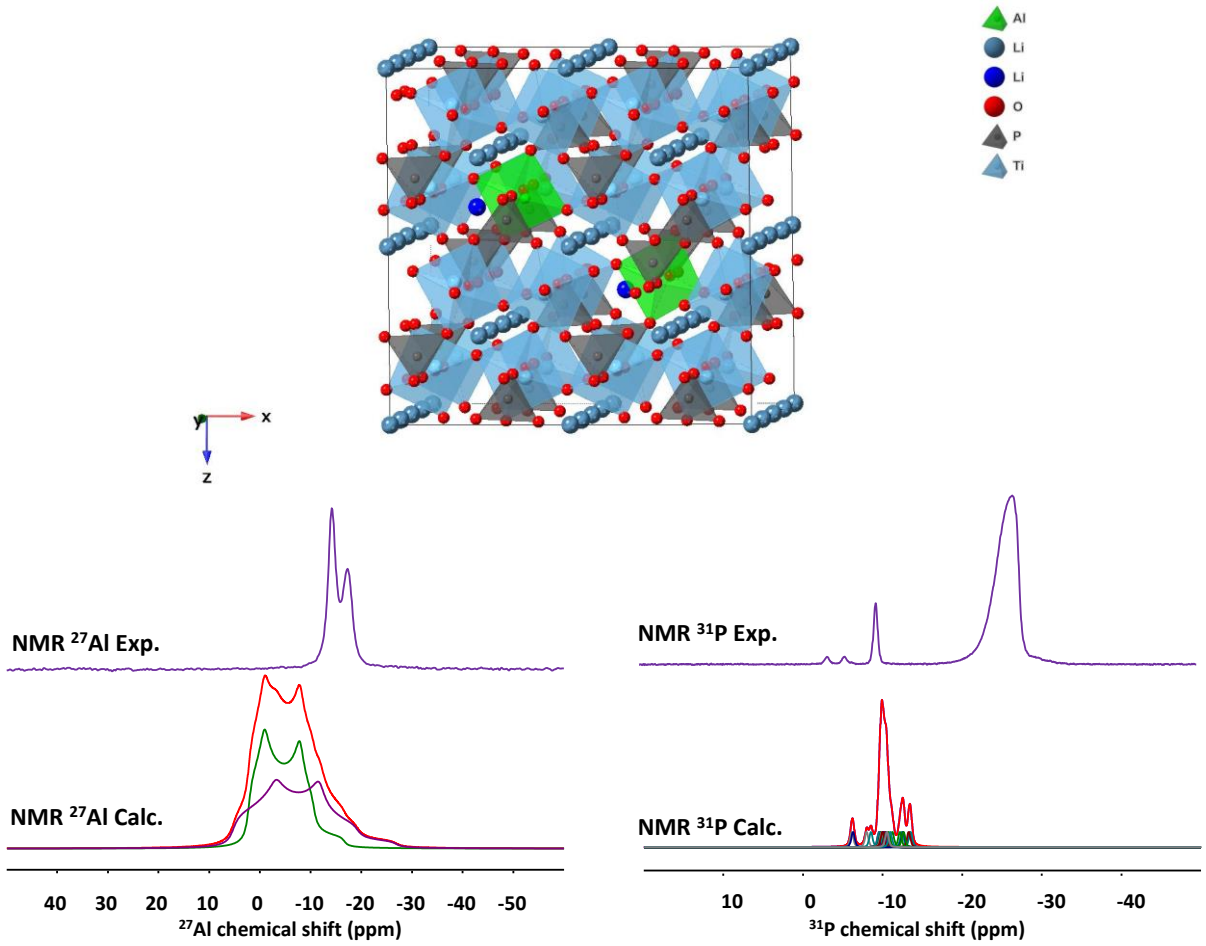

Figure II-21: Crystal structure of the model used for DFT calculations and comparison of calculated and experimental ^{27}Al and ^{31}P NMR spectra.

The simulations conducted in this section indicate that a modification of the Al doping level in the material is possible. However, insights from XRD and solid-state NMR suggest that the formation of an unreported crystalline phase containing Li and Al in octahedral site is very likely. Nonetheless, these phases do not appear to influence the overall mechanism significantly, as it remains similar to LTP. Further synthesis efforts to isolate this new phase in the Li-Al-Ti-P-O phase diagram are ongoing.

II.3. Generalisation of the mechanism

II.3.1. Decomposition of the lithium salts

We have previously seen that the reactivity involved the decomposition of the salt in the case of LiBr. For the other salts, the verification of gas release was determined by calculating the percentage of mass lost after thermal treatment at 900 °C for 2 hours in air. The experiment was conducted with a molar ratio fixed at 1:1 for all samples like those used in the first experiment conducted in section II.1. The results are presented in Figure II-22, where the experimental

masses lost are compared to theoretical masses lost. These theoretical masses were determined based on hypotheses of gas released which are also presented in Figure II-22.

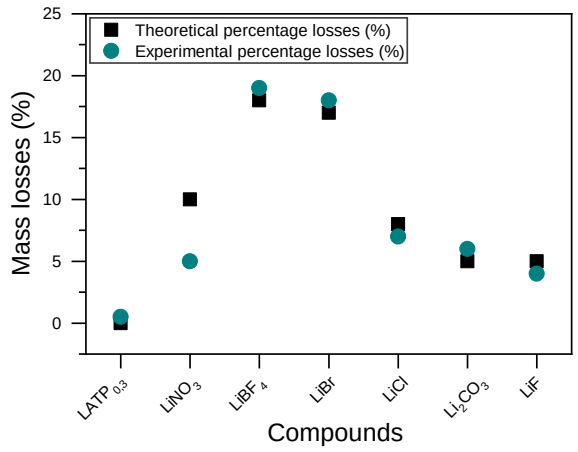

Compounds	Nature (Hypothesis)
$LATP_{0.3}$	H_2O traces
$LATP_{0.3}$ + $LiNO_3$	NO_2 + ¼ O_2
$LATP_{0.3}$ + $LiBF_4$	BF_3 + HF
$LATP_{0.3}$ + LiBr	Br_2
$LATP_{0.3}$ + LiCl	Cl_2
$LATP_{0.3}$ + Li_2CO_3	CO_2
$LATP_{0.3}$ + LiF	HF

Figure II-22: Comparison of experimental versus theoretical masses (%) for $LATP_{0.3}$ and mixtures of $LATP_{0.3}$ and Li-salts in a 1:1 lithium molar ratio after a heat treatment à 900 °C, under air. The theoretical masses were calculated based on the hypotheses presented in the table

All mixtures, except the one containing $LiNO_3$, exhibit an experimental mass loss similar to the expected values. The observed differences are ±1 %, which can be considered within the margin of error. For the mixture with $LiNO_3$, the origin of the deviation has not been found. According to these results, all the Li-salts studied involve gas release, suggesting their decomposition at elevated temperatures due to their reactivity with $LATP_{0.3}$.

II.3.2. Formation of transient species in the case of others lithium salts

According to previous results, we know that all Li-salts studied form $LiTiOPO_4$ and $Li_4P_2O_7$ (Figure II-1) and decompose at elevated temperatures (Figure II-22). However, it is necessary to confirm if this reactivity leads to the formation of transient species, i.e. Li_3PO_4 or TiO_2. For this purpose, pellets of three mixtures composed of others salts were studied by HTXRD. The heat treatments were conducted from 30 °C to 900 °C, with a heating ramp of 10 °C/min, under vacuum. The Li-salts were selected to cover a wide range of melting temperatures: $LiBF_4$ (296 °C), Li_2CO_3 (723 °C), and LiF (848 °C). The mixtures were prepared with a lithium molar ratio of 1.3:1, The scans were acquired according the type of measurement **P1**, as the main goal of the experiment is to qualitatively monitor the phases. Based on the experimental data obtained using this technique, a scan at 600 °C was selected for each of these three samples and they are presented in Figure II-23. Li_3PO_4 is observed in all samples, confirming the transition through this phase to form the final impurities. TiO_2 is not observed, but as previously discussed, additional characterisation methods are necessary to confirm its formation. When LiF is added, the salt is no longer present at 600 °C, highlighting that it has decomposed before

reaching its melting temperature. In the case of $LiBF_4$, it has decomposed to form LiF for which a diffraction peak is still observed at 600 °C. But like the addition of LiF, it decomposes before reaching its melting temperature. Finally, some Li_2CO_3 is also remaining at 600 °C but it has started reacting to form Li_3PO_4.

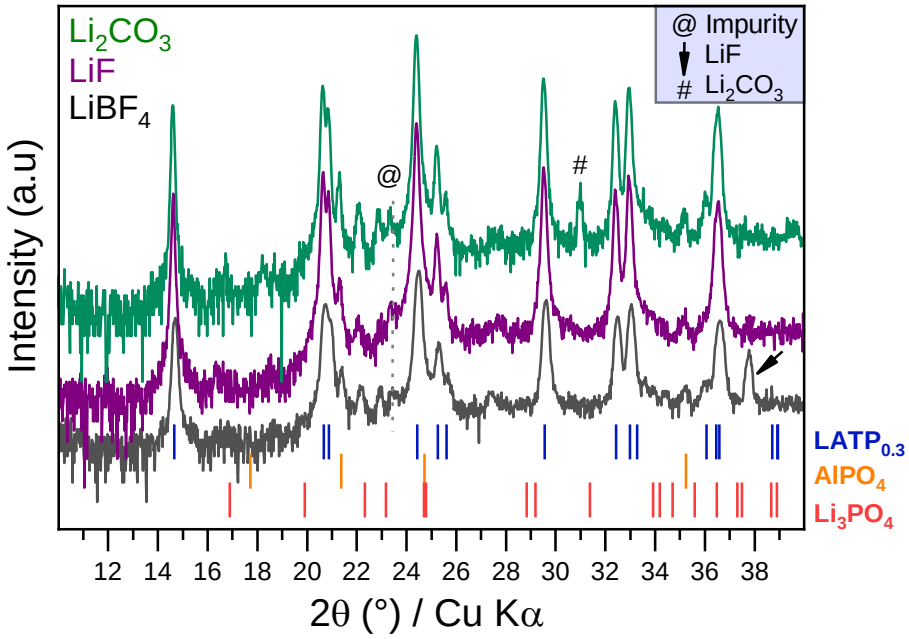

Figure II-23: XRD patterns at 600 °C of pellets composed of mixtures of $LATP_{0.3}$ + LiF (1:1) (—), $LATP_{0.3}$ + $LiBF_4$ (1:1) (—) and $LATP_{0.3}$ + Li_2CO_3 (1:1) (—) obtained during HTXRD.

These experiments indicate a similar chemical reactivity mechanism for all the Li-salts studied. Some differences may exist concerning the decomposition temperatures and the reaction of the salts with $LATP_{0.3}$, but the major steps of the mechanism have been observed across all cases:

1. The consumption of LiBr and $LATP_{0.3}$ to form Li_3PO_4 and TiO_2. The temperature associated with this stage depends on the reactivity of the LATP-lithium salt system being studied. In the case of the mixture LATP-LiBr, Li_3PO_4 and TiO_2 have been observed as early as 400°C and up to 700°C through Solid-state NMR (Figure II-15) and Raman spectroscopy (Figure II-12), respectively, in addition to XRD experiments (Figure II-4).
2. The reaction of Li_3PO_4, $AlPO_4$ and TiO_2 with $LATP_{0.3}$ to form $LiTiOPO_4$, $Li_4P_2O_7$ and an unidentified impurity. This reaction occurs around 800°C according to Solid-state NMR and XRD experiments in Figure II-15 and Figure II-14 respectively.

Now that most of the major steps of the mechanism have been identified and confirmed through various characterisation methods, the relationship between this reactivity and the densification of $LATP_{0.3}$ will be discussed in the next section.

III. Chemical reactivity controls the sintering process in $LATP_{0.3}$

Most hypotheses in the literature rely on the melting of the added salt to explain the improvement in densification and sintering of $LATP_{0.3}$ at lower temperatures. Indeed, the melting of the salt enables liquid-phase sintering[135,140,141,185]. This process involves three main steps: particle rearrangement, followed by dissolution and re-precipitation of the material, and finally grain growth phenomena when the appropriate criteria for wettability, viscosity, and solubility are met[97].

III.1. Impact of decreasing additive quantity on chemical reactivity

However, the chemical reactivity mechanism studied previously revealed that the initial lithium salt decomposes and reacts in a temperature range below its melting temperature. Furthermore, the melting of the salt accelerates its decomposition and reactivity. The system previously studied to investigate the reactivity, with a 1:1 molar ratio of $LATP_{0.3}$ and LiBr is not representative of those studied for densification in the literature. It is equivalent to 15 wt% of LiBr, whereas most studies work with proportions ranging from 1 to 10 wt% of Li salt. Thus, we conducted a TG analysis on a mixture of $LATP_{0.3}$ and 10 wt% LiBr to study the decomposition of the salt in these conditions. The analysis was performed under an air flow from 25 to 900 °C with a heating ramp of 10 °C/min. The resulting TG curve and its first derivative are presented in Figure III-1. A first mass loss is observed between 50 and 150 °C, corresponding to water loss. However, since the mixture was prepared in a glove box, this water must have been adsorbed by the mixture before the analysis. A second mass loss of 9 wt% is observed at 457 °C. This percentage corresponds to a complete loss of Br_2, highlighting the decomposition of LiBr well before reaching its melting temperature, i.e. 555 °C. Thus, this result shows that a smaller quantity of the salt reacts before melting and does not induce liquid-phase sintering. This indicates that other mechanisms contribute to the improvement of $LATP_{0.3}$ densification at lower temperatures.

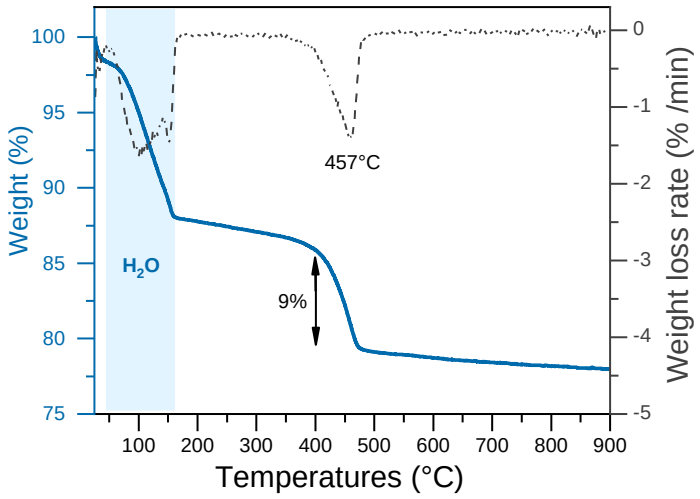

Figure III-1: TG and DTG curves of a mixture of $LATP_{0.3}$ and 10 wt% of LiBr.

To study these mechanisms, we decided to start with mixtures of $LATP_{0.3}$ and Li_3PO_4 in proportions similar to those reported in the literature for densification studies, i.e. 1, 5 and 10 wt%. However, since we are working with smaller quantities of salts compared to the previous section, the chemical reactivity was verified on a sample of LATP with 1 wt% Li_3PO_4. The sample was thermally treated in air at 830°C for 6 hours, which are typically conditions for a sintering step. Based on the XRD pattern in Figure III-2-a, acquired under standard conditions, only the diffraction peaks of $LATP_{0.3}$ are visible. However, ^{31}P NMR analyses in Figure III-2-b confirm the formation of $Li_4P_2O_4$ due to the reaction between Li_3PO_4 and $LATP_{0.3}$.

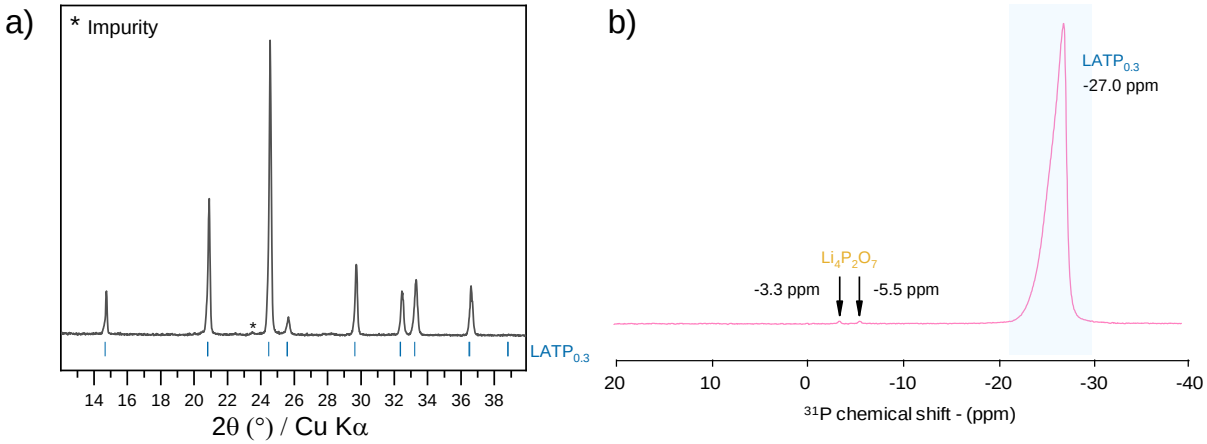

Figure III-2: (a) XRD pattern and (b) ^{31}P NMR spectra of a mixture of $LATP_{0.3}$ and 1 wt% of Li_3PO_4 after a heat treatment at 830 °C during 6 h under air atmosphere.

These analyses confirm the formation of impurities even at small quantities of salts, allowing us to study the connection between chemical reactivity and densification in the following sections. Since the lithium salt Li_3PO_4 is responsible for the formation of the final impurities, it will be used as the starting salt to mimic the overall chemical reactivity.

III.2. Melting of impurities

As a first approach, mixtures of $LATP_{0.3}$ and Li_3PO_4 at 1, 5 and 10 wt% were studied by DTA. The experiments were conducted under an air flow of 25 ml/min, from 25 °C to 900 °C with a temperature ramp of 5 °C/min. Only curves with 5 wt% and 10 wt% of Li_3PO_4 are displayed in Figure III-3-a as no signal is observed in the case of an addition of 1 wt%.

During heating, an endothermic peak at 795 °C is observed for the curve with 5 wt%, whereas two signals are observed at 791 °C and 816 °C for the curve with 10 wt% of salt. During cooling, two exothermic peaks are observed at 774 °C and 621 °C in the case of 5 wt%, and at 770 °C and 622 °C in the case of an addition of 10 wt%. These results suggest that a compound is melting between 770 °C and 820 °C, but it is not the starting salt, as Li_3PO_4 melts at 1206 °C[194].

In section II.2.4, we showed the formation of $Li_4P_2O_7$ from the reactivity of Li_3PO_4 with $LATP_{0.3}$ in this range of temperature. The compound has a melting temperature of 876 °C ± 10 °C[194,228,229], which has been previously confirmed experimentally by DTA analysis.

To investigate the impact of the formation of $Li_4P_2O_7$ in the presence of $LATP_{0.3}$, a DTA measurement was performed on a mixture of $LATP_{0.3}$ and $Li_4P_2O_7$ (molar ratio 1:0.25). It was performed under the same conditions as the experiment with the mixtures at 5 and 10wt% of Li_3PO_4. The results are presented in Figure III-3-b. During heating, three endothermic peaks are observed at 632 °C, 773 °C and 805 °C, and two exothermic peaks are present at 618 °C and 768 °C during cooling. No peak is observed at the temperature at which $Li_4P_2O_7$ melts. The reversible peak in a temperature range of 610-635 °C corresponds to a structural phase transition, which is also observed in the case of pure $Li_4P_2O_7$[194]. For the other signals observed in the temperature range of 750-810 °C, they are close to those of the mixtures of $LATP_{0.3}$ and Li_3PO_4.

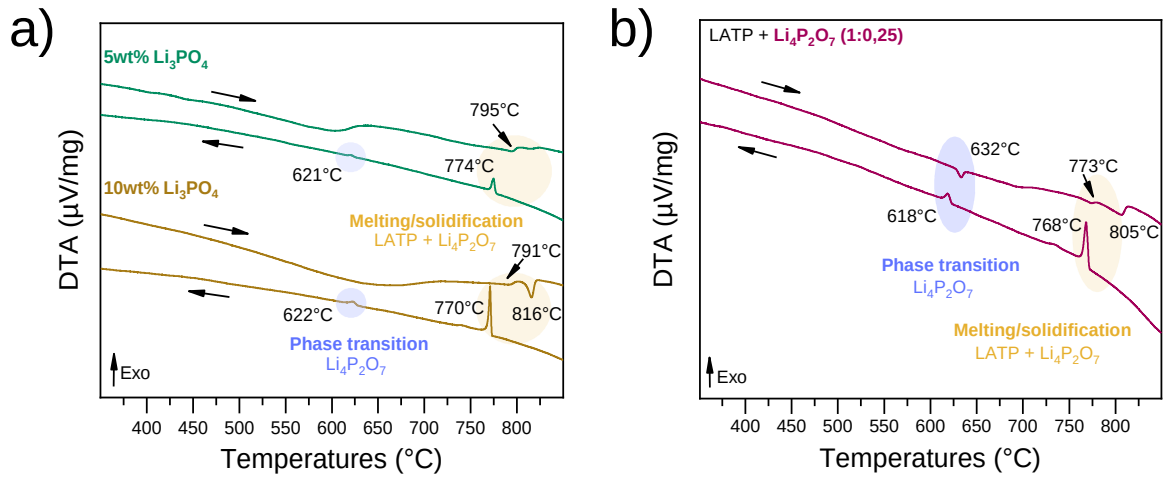

Figure III-3: (a) DTA curves of mixtures of $LATP_{0.3}$ with 5 wt% (—) and 10 wt% (—) of Li_3PO_4. (b) DTA curves of mixture of $LATP_{0.3}$ and $Li_4P_2O_7$ (—) with a molar ratio of 1:0.25.

In the literature, only one study has observed these DTA signals around 770 °C, from a system consisting of LTP and $LiNO_3$. The authors identified it as the melting/solidification of a mixture made up of the solid electrolyte and $Li_4P_2O_7$, formed in situ by the reaction of $LiNO_3$ with LTP[188]. The partial solubility of LTP in $Li_4P_2O_7$ explains the decrease in melting temperature of $Li_4P_2O_7$. Although their system is slightly different due to the use of LTP, the reactivity of the Li-salts is similar to that with LATP at an aluminium level of x = 0.3. In other words, these peaks are associated with the melting of a $LATP_{0.3}$-$Li_4P_2O_7$ mixture in our system.

This experiment allows us to identify the signals observed in the case of mixtures of $LATP_{0.3}$ and Li_3PO_4 as the melting of the $LATP_{0.3}$-$Li_4P_2O_7$ mixture. $Li_4P_2O_7$ is therefore formed during the heat treatment, although no signal associated with this reaction is observed. However, the exothermic peak at 621-622 °C during cooling in Figure III-3-a, unambiguously confirms the formation of $Li_4P_2O_7$.

III.3. Impact of the formed phases on densification

DTA measurements have highlighted the partial melting of the $LATP_{0.3}$-$Li_4P_2O_7$ in the case of a mixture of $LATP_{0.3}$ and $Li_4P_2O_7$, as well as in mixtures of $LATP_{0.3}$ and Li_3PO_4. According to our hypothesis, this melting is responsible for the densification of $LATP_{0.3}$ at lower temperatures. To confirm this, dilatometry measurements were first performed on pellets of pure $LATP_{0.3}$ and mixtures of $LATP_{0.3}$ with various proportions of Li_3PO_4, i.e. 1, 5 and 10 wt%. The pellets were made by placing powder in an 8 mm diameter die and applying a pressure of 2 tons. All experiments were conducted in air, with a thermal treatment ranging from 25 °C to 1000 °C and with a heating ramp of 5 °C/min. The results are shown in Figure III-4, and they

are illustrated by the linear shrinkage as a function of temperature (a and c) and the shrinkage rate as a function of temperature (b and d) respectively.

The results from the dilatometry experiment on $LATP_{0.3}$ synthetized by solid-state reaction were reused in Figure III-4 to compare them with those obtained from the mixtures. The pure $LATP_{0.3}$ shows minimal shrinkage up to 1000 °C and treatment temperatures exceeding 1000 °C are necessary to obtain better sintering performance. This is consistent with literature reports[195,230].

In comparison, the shape of $LATP_{0.3}$ shrinkage curve is altered with the addition of the Li_3PO_4. With 1 wt%, the behaviour of the curve remains similar to that of pure $LATP_{0.3}$, but the densification process occurs at a faster rate, as indicated by the change in the slope of the curve. The derivative in Figure III-4-b shows a new contribution at 783 °C, which is responsible for the change in rate. Adding larger amounts of salts, such as 5 wt% and 10 wt%, further enhances this effect, which can be explained by several phenomena. Firstly, the onset of shrinkage is slightly shifted to lower temperatures. Then, the curves in Figure III-4-b tend toward lower temperature, i.e. 800 °C, than the sample with 1 wt%, suggesting that the densification is more efficient. This behaviour is illustrated in Figure III-4-d, where new contributions are observed at 806 °C for 5 wt%; at 805 °C, 817 °C and 826 °C for 10 wt%. This temperature range corresponds to the melting temperature of the LATP-$Li_4P_2O_7$ mixture as observed in the DTA analysis (Figure III-3). Based on these results, the addition of Li_3PO_4 leads to densification at a temperature range around 800 °C, thanks to the in-situ formation and melting of $Li_4P_2O_7$.

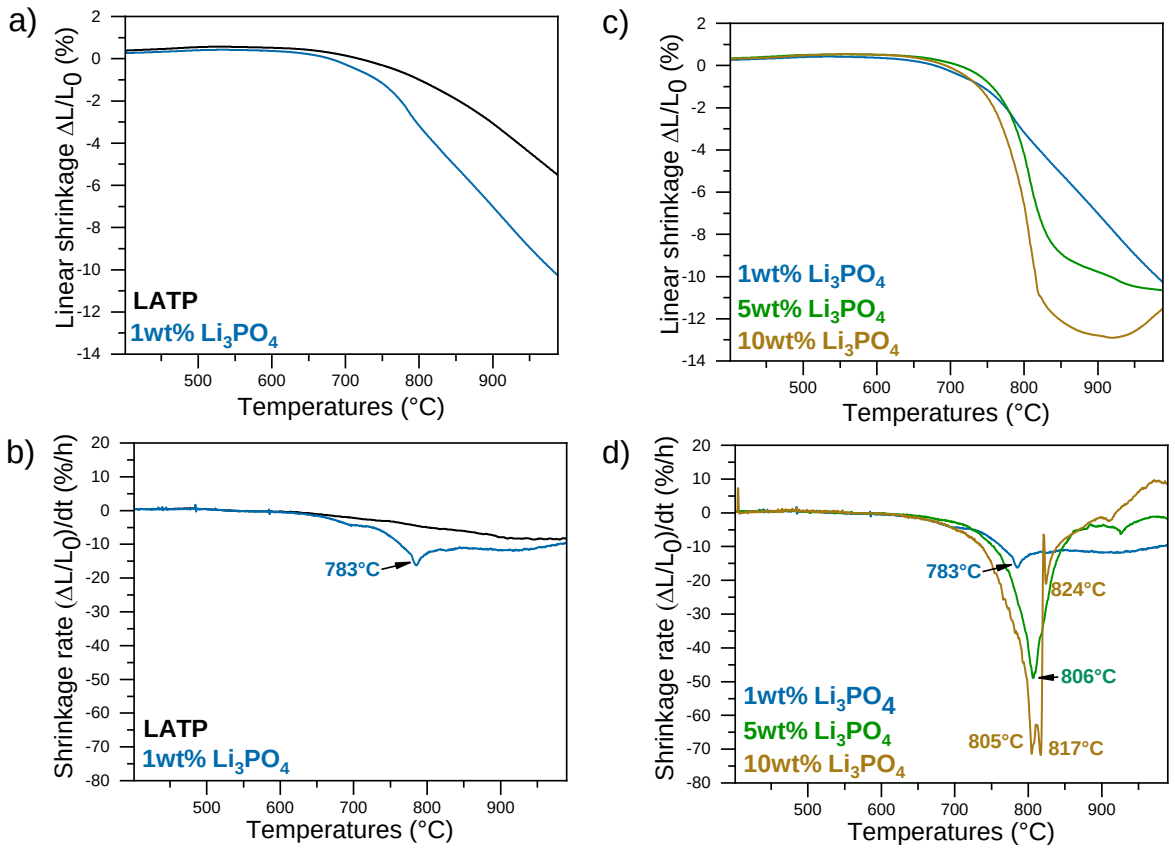

Figure III-4: Dilatometry experiments of pure pellet of $LATP_{0.3}$ synthetized by solid state reaction, pellet made from mixtures composed of $LATP_{0.3}$ and various proportion of Li_3PO_4, i.e. 1 wt%, 5 wt% and 10 wt%. Results are presented in two formats: (a-c) linear shrinkage as a function of temperature and (b-d) the shrinkage rate as a function of temperature.

Furthermore, the quantity of the salts added is an important factor as it is necessary to add at least 5 wt% of Li_3PO_4 to lead to a significant improvement. On the other hand, the addition of 10 wt% is too high: the shrinkage curve exhibits a phenomenon that could be associated with sample expansion above 940 °C. This phenomenon is in correlation with the phosphate quantity and it could be due to gas release.

We also conducted the same dilatometry experiment on a sample of $LATP_{0.3}$ with 5wt% $Li_4P_2O_7$. If the hypothesis that the decrease in $LATP_{0.3}$ shrinkage temperature is due to the presence of $Li_4P_2O_7$ is correct, then, we should observe the same shrinkage temperatures as those observed with the addition of Li_3PO_4. The resulting curves are presented in Figure III-5. Focusing on the derivative, two phenomena are observed at 779 °C and 813 °C, contributing to a shrinkage peak shifting towards 800 °C. These temperatures correspond well to the melting temperature of the mixture $LATP_{0.3}$-$Li_4P_2O_7$ and are similar to what is observed with Li_3PO_4. As for the samples with Li_3PO_4, the onset of shrinkage occurs at a lower temperature compared to pure $LATP_{0.3}$.

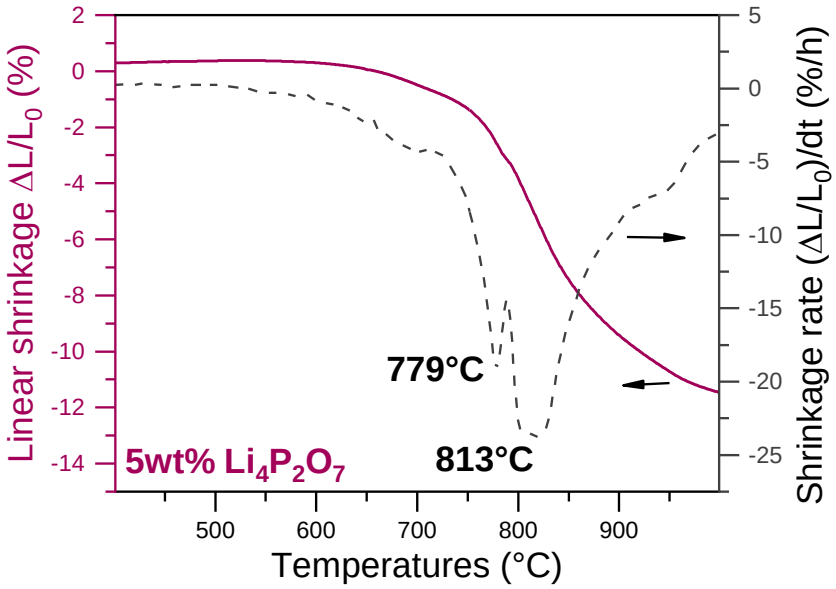

Figure III-5: Dilatometry experiment of pellet made from a mixture composed of $LATP_{0.3}$ and 5 wt% of $Li_4P_2O_7$.

Comparing the relative densities (RD) of each pellet provides a more accurate determination of which case involves better improvement in terms of final densification. As a reminder, the values can be expressed according the equation (8):

$$\text{Relative Density (RD)} = \frac{Measured\ Density}{Theoritical\ Density} \times 100 \qquad (8)$$

The measured density (g/cm^3) corresponds to the geometrical measurements of the pellet, while the theoretical density (g/cm^3) corresponds to the crystallographic density of the material. The theoretical densities differ between the two systems: $Li_4P_2O_7$ has a theoretical density of 2.35 g/cm^3 and Li_3PO_4 has a theoretical density of 2.44 g/cm^3[199]. This results in a total theoretical density of 2.89 g/cm^3 for a pellet of $LATP_{0.3}$ with the addition of 5 wt% of $Li_4P_2O_7$ and 2.90 g/cm^3 with the addition of 5 wt% of Li_3PO_4. Although the theoretical density remains unchanged during the heat treatment for the pellet with $Li_4P_2O_7$, it is altered for the pellet with Li_3PO_4. Indeed, Li_3PO_4 (2.35 g/cm^3) and some $LATP_{0.3}$ (2.92 g/cm^3) are converted into $Li_4P_2O_7$ (2.44 g/cm^3) and $LiTiOPO_4$ (3.26 g/cm^3) during the heat treatment. However, the change in chemical composition has a negligible effect on the relative density values (less than 1%), as there is an equilibrium in the theoretical densities between the consumed and newly formed phases. In both cases, the mechanism responsible for the densification is the dissolution of $LATP_{0.3}$ in $Li_4P_2O_7$, leading to a similar final shrinkage of 10-11 %.

Finally, it is worth mentioning that in a study conducted by Hupfer et al., the effect of $LiTiOPO_4$ on the densification of $LATP_{0.3}$ was investigated. According to their findings, the addition of

5 wt% $LiTiOPO_4$ to LATP does not lead to a significant improvement in the shrinkage onset temperature. However, increasing the amount of $LiTiOPO_4$ beyond this concentration can even result in a higher shrinkage onset temperature[197]. This phenomenon is likely indirectly related to the amount of $AlPO_4$ present in the sample. $AlPO_4$ improves the densification of LATP by limiting the abnormal growth of grains and lowering the densification temperature[231,232]. However, when an excess of $LiTiOPO_4$ is added, $AlPO_4$ would react with this phase to form LATP[197]. In our study, this reaction does not occur because $AlPO_4$ reacts before that the $LiTiOPO_4$ formation.

IV. Comparison of $LATP_{0.3}$ properties as a function of the additives

Previous experiments in dilatometry and DTA have demonstrated that the decrease of the densification temperature of $LATP_{0.3}$ is due to the melting of the $LATP_{0.3}$-$Li_4P_2O_7$ mixture around 800 °C. The formation of $Li_4P_2O_7$ is caused by the reactivity of Li_3PO_4 with $LATP_{0.3}$, and Li_3PO_4 itself is formed by the decomposition and reactivity of the starting salt, such as LiBr, with $LATP_{0.3}$. The aim of this section is to compare the impact of the addition of these three salts to $LATP_{0.3}$ on its properties as a function of the nature, the quantities of additives and the temperatures.

IV.1. Relative densities and microstructures

IV.1.1. Impact of the temperature on the densification of $LATP_{0.3}$

First, the densification of pure $LATP_{0.3}$ was investigated by conducting a conventional sintering step. As a reminder, this step involves making pellets from the material and applying heat treatment for a chosen dwelling time. For this experiment, the pellets were made by placing ~ 250-300 mg of powder in a 13 mm diameter die and applying a pressure of 4.5 tons. The heat treatments were conducted at three different temperatures: 760 °C, 830 °C and 900 °C, each for 6 h, with a heating ramp of 5 °C/min, and under an air atmosphere. The green relative densities (before heat treatment) and the relative densities (after heat treatment) were determined from geometrical measurements. Three samples per heat treatment temperature were made in order to check the repeatability. The results are presented in Figure IV-1, where the relative densities of the pellets of pure $LATP_{0.3}$ are compared as a function of temperature alongside the green relative densities. At 760 °C, the relative densities (78 %) are close to the green densities (~72 %), indicating that the temperature is not sufficient to densify pure $LATP_{0.3}$. The relative densities at 830 °C (~83 %) are higher than those obtained at 760 °C, but it is only at 900 °C that $LATP_{0.3}$ reaches relative density values above 90 %. These results confirm that increasing the sintering temperature positively impacts the densification of $LATP_{0.3}$, and are consistent with the literature[90,230,233].

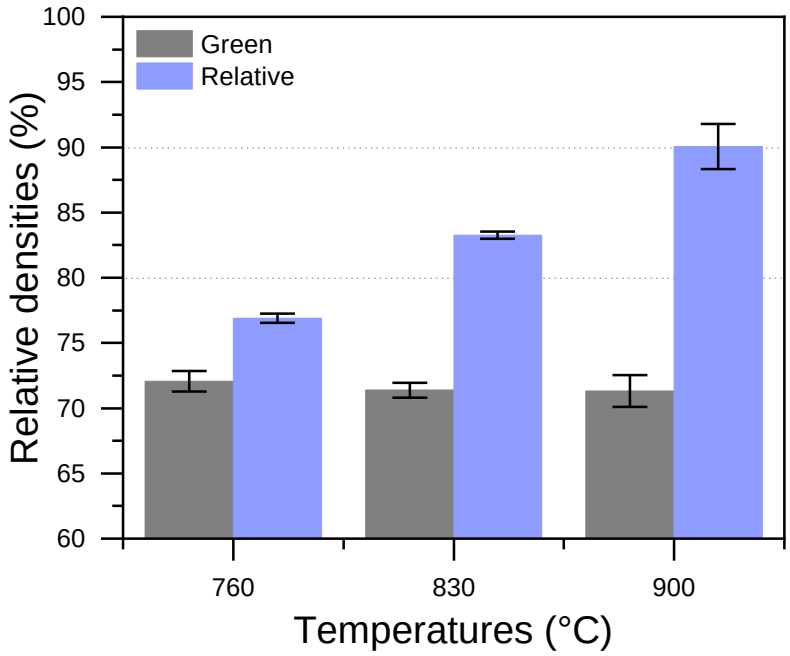

Figure IV-1: Comparison of the green relative densities and the relative densities of pure $LATP_{0.3}$ pellets after heat treatments at different temperatures including 760 °C, 830 °C and 900 °C.

IV.1.2. Impact of the addition of lithium salts on the densification of $LATP_{0.3}$

Then, the impact of adding LiBr, Li_3PO_4, and $Li_4P_2O_7$ in different proportions on the densification of $LATP_{0.3}$ was studied. For this purpose, the same experiments were conducted as previously: pellets of mixtures of $LATP_{0.3}$ and additives were heat-treated according to the same heat treatments program as for pure $LATP_{0.3}$ pellets. Three proportions of additives were chosen, including 1, 5, and 10 wt% and each mixture was prepared by grinding manually in a mortar. The relative densities after heat treatments were determined from geometrical measurements.

IV.1.2.1. Addition of reacting salts LiBr and Li_3PO_4

First, let's examine the relative densities in the case of adding the reactive Li-salts LiBr and Li_3PO_4. In this case, we expected an improvement in the densification after that the salts react with $LATP_{0.3}$ to form $Li_4P_2O_7$. The results are presented in Figure IV-2, where the relative densities are shown as a function of the proportion of Li-salts, alongside the temperature of the heat treatment. For a heat treatment at 760 °C, the LiBr added is converted to Li_3PO_4, but it is not converted to $Li_4P_2O_7$. This results in values of relative density close to those obtained for pure $LATP_{0.3}$ at this temperature ranging between 75-80 %. However, with the addition of Li_3PO_4, the relative densities are greater, ranging between 80 % and 85 %, even though $Li_4P_2O_7$ has not been formed. At temperatures of 830 °C and 900 °C, $Li_4P_2O_7$ and $LiTiOPO_4$ are formed, but the reaction is more advanced at 900 °C. Furthermore, $Li_4P_2O_7$ is molten at both

temperatures, leading to an increase in relative densities, with values ranging between 85 % and 92 %. By comparing these results with those obtained for $LATP_{0.3}$, the addition of LiBr shows an improvement in densification starting at 830 °C. This improvement is more significant from 760 °C in the case of Li_3PO_4, with an optimum at 830 °C. We also observe that the relative densities are lower at 900 °C compared to those at 830 °C.

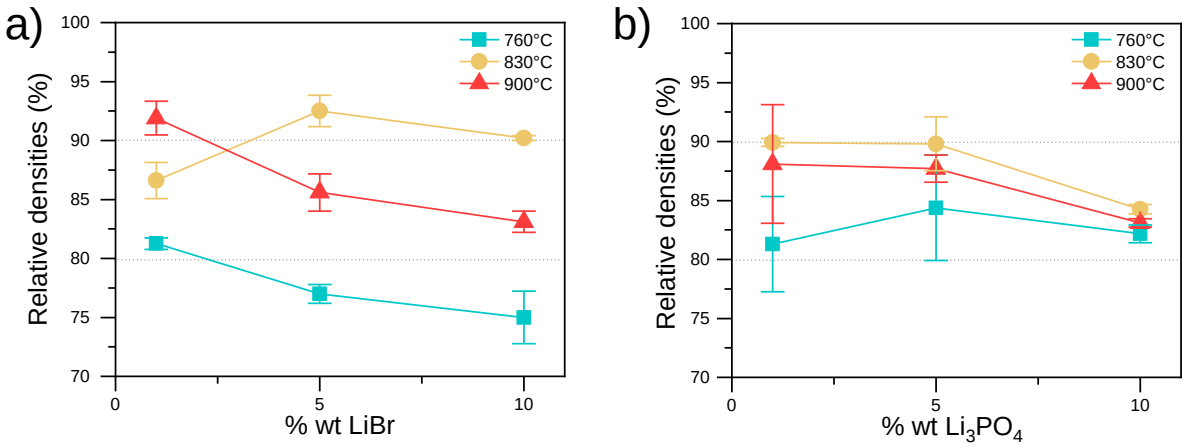

Figure IV-2: Relative densities of $LATP_{0.3}$ and 1, 5, 10 wt% of (a) LiBr; and (b) Li_3PO_4 after heat treatments at 760, 830 and 900 °C for 6 h under air atmosphere.

Then, the microstructure of the pellets of pure $LATP_{0.3}$ and the pellets containing LiBr and Li_3PO_4 were analysed by Scanning Electron Microscopy (SEM) in order to investigate the lower relative densities observed at 900 °C. We focused on the pellets with 10 wt% salt additives as the relative densities are comparable for each system. The pellets were broken before analysis in order to visualise the core of the samples. As presented in Figure IV-3, some differences are observed between the sample of pure $LATP_{0.3}$ and those with salts. The particles are larger in the two samples with salts, but small pores are observed. This indicates that, even though the sintering process is more advanced, the additions of salt leads to the formation of porosity. The size of the pores was determined visually using the software ImageJ: they are larger in the case of Li_3PO_4 (~21.5 µm) than LiBr (~9 µm). The origin of this porosity will be discussed later.

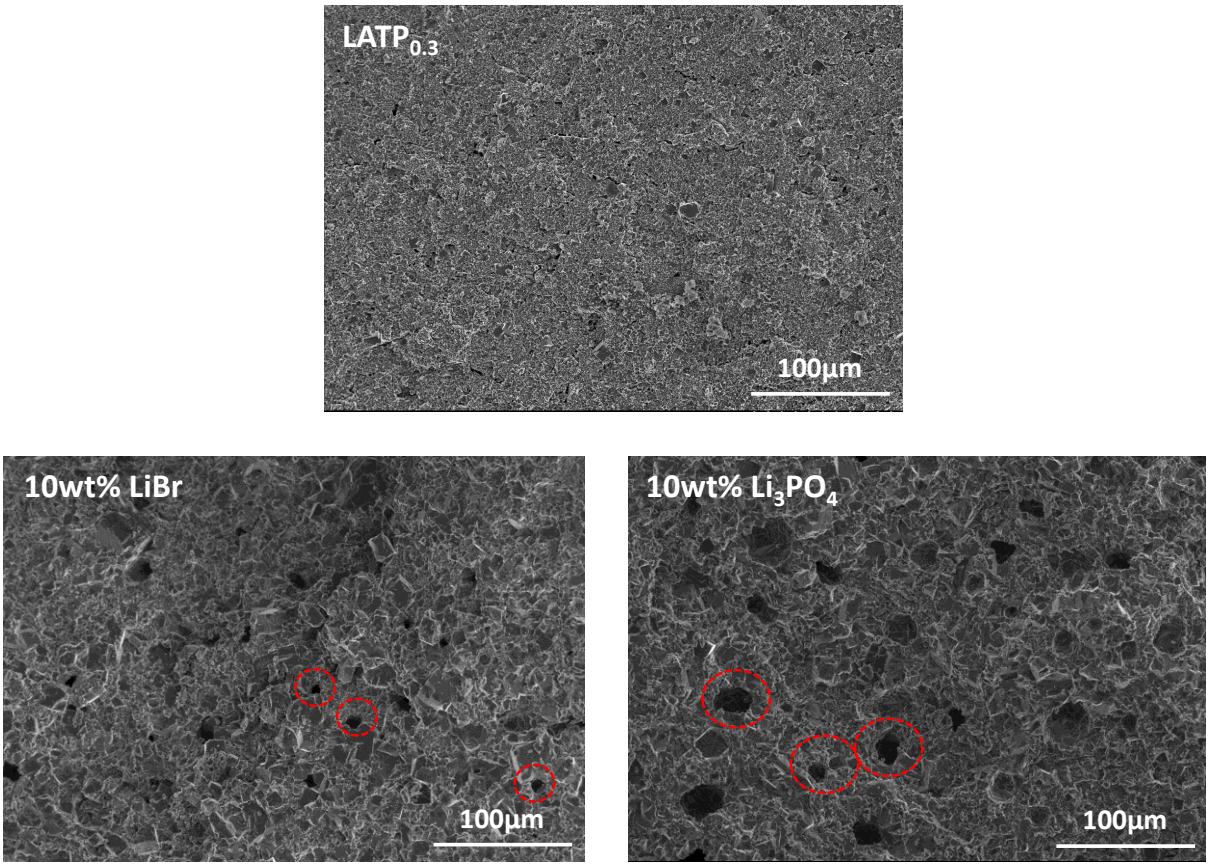

Figure IV-3: SEM images of broken pellets of $LATP_{0.3}$, $LATP_{0.3}$ and 10 wt% of LiBr, and $LATP_{0.3}$ and 10 wt% of Li_3PO_4 after a heat treatment at 900 °C for 6 h under air atmosphere. Red circles show the pores.

IV.1.2.2. Addition of non-reacting salt $Li_4P_2O_7$

We then focus on mixtures composed of the lithium salt $Li_4P_2O_7$. In comparison with LiBr and Li_3PO_4, $Li_4P_2O_7$ does not react with $LATP_{0.3}$ and melts between 770 °C and 800 °C in presence of $LATP_{0.3}$. Most of the relative densities presented in Figure IV-3, for all heat treatment temperatures combined, range between 80-90 %, which is greater than in the case of pure $LATP_{0.3}$. However, the quantity of additive impacts the densification of $LATP_{0.3}$, as increasing the amount of additive decreases the value of the relative densities. The only exception is observed for 1 wt% of $Li_4P_2O_7$ at 760 °C. Contrary to LiBr and Li_3PO_4, the temperature of the heat treatment influences negatively the densification.

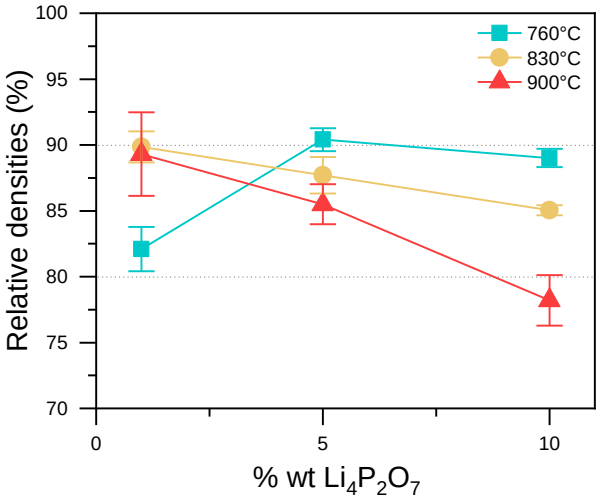

Figure IV-4: Relative densities of $LATP_{0.3}$ and 1, 5, 10 wt% of $Li_4P_2O_7$ after heat treatments at 760, 830 and 900 °C for 6 h under air atmosphere.

In order to understand these tendencies, the microstructures of the pellets at 10 wt% of $Li_4P_2O_7$ at 760 °C and 900 °C were analysed using SEM and the results are presented in Figure IV-5. As for LiBr and Li_3PO_4 pellets previously studied, the samples were broken prior to analysis. After a heat treatment at 760 °C, the sample exhibits small pores that are mostly filled by another species that shows a different microstructure. This can be associated to the salt that has begun to melt and then recrystallised after returning to room temperature. At 900 °C, the pieces of salt disappeared, as they diffused into the sample, giving way to larger pore sizes averaged at ~50 µm. It is assumed that the quantity of these pores increases with a significant addition such as 10 wt%, which can explain why the relative densities decrease with the quantity of salt. Conversely, the pores are not formed at 760 °C, since the salt has not yet melted, resulting in higher relative densities with a higher quantity of $Li_4P_2O_7$.

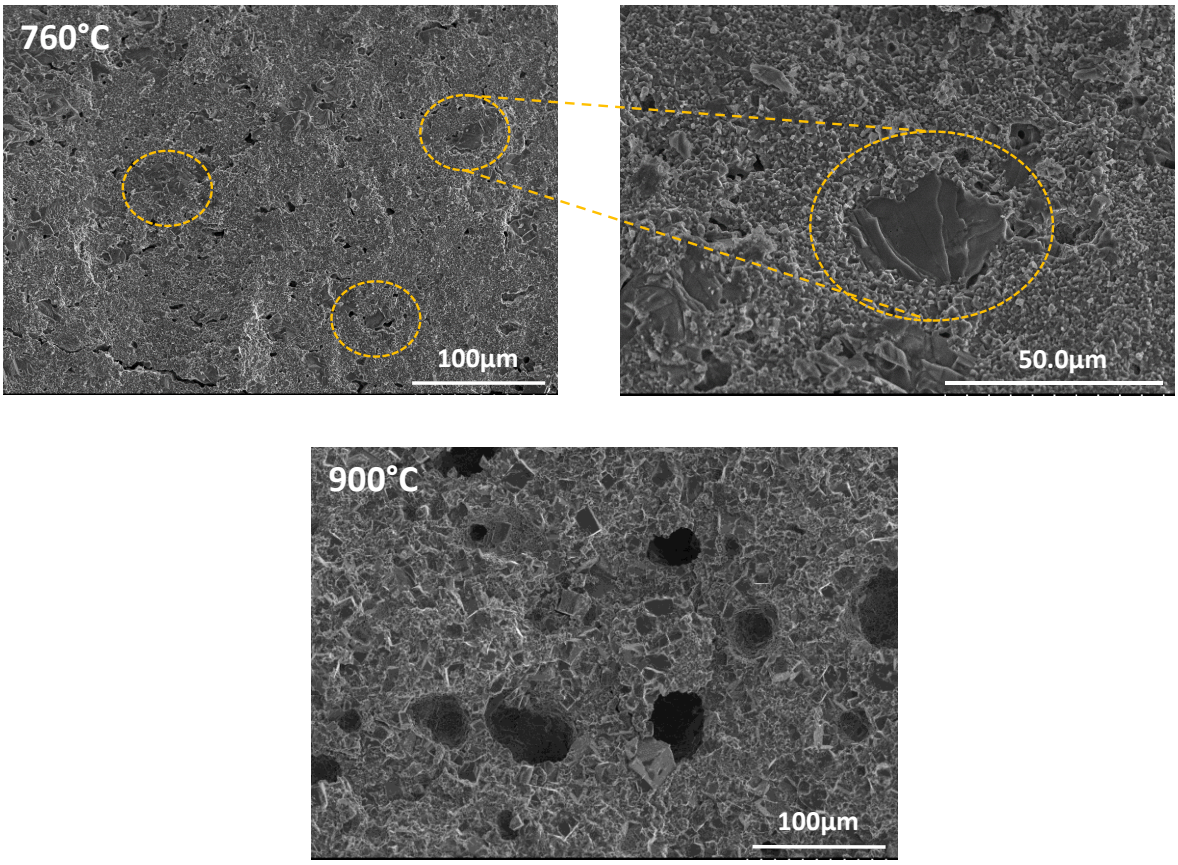

Figure IV-5: SEM images of broken pellets of $LATP_{0.3}$ and 10 wt% of $Li_4P_2O_7$ after a heat treatment at 760 °C and 900 °C for 6 h under air atmosphere.

To summarise the overall results obtained from these experiments, the addition of additives such as LiBr, Li_3PO_4, and $Li_4P_2O_7$ improves the densification of $LATP_{0.3}$ at lower temperatures. For LiBr, this improvement is only significant starting from 830 °C, as it is necessary for the salt to be converted into Li_3PO_4, and then into a sufficient quantity of $Li_4P_2O_7$. By eliminating this initial conversion step, the addition of Li_3PO_4 enhances the densification of $LATP_{0.3}$ at 760 °C. Finally, by completely removing these reactive steps, significant densification can be achieved at 760 °C with $Li_4P_2O_7$, reaching relative densities of around 90 %. Under the same temperature program, $LATP_{0.3}$ alone only densifies to approximately 78 %. Nevertheless, the improvement in relative densities is accompanied by the formation of porosity, with the size of the pores becoming increasingly larger as the reactive steps are eliminated. Several explanations are possible:

- The first one is the release of gas, particularly for samples with LiBr, as the release of Br_2 is expected during the heat treatment. However, no release occurs for the samples with Li_3PO_4 and $Li_4P_2O_7$.

- The second one implies an inadequate solubility. Indeed, a good solubility of particles of $LATP_{0.3}$ in the liquid is expected for effective liquid phase sintering, but a good solubility of the liquid in the $LATP_{0.3}$ can lead to a different process called transient liquid phase sintering[234]. In that case, the liquid diffuses along solid-solid contacts, causing swelling of the compact and generation of pores[96]. However, more characterisation methods are needed in order to confirm this hypothesis.

Interestingly, the size of the pores is smaller in the case of the salts that react with $LATP_{0.3}$, suggesting that reactivity can help to prevent the formation of large pores. However, it is assumed that this phenomenon is exacerbated by a high quantity of the additive (10wt%) and is less observed at lower quantities. The size, quantity, and method of adding the additive are factors that can impact the final microstructure of $LATP_{0.3}$.

IV.2. Ionic conductivity properties of $LATP_{0.3}$ with additives

The microstructure of $LATP_{0.3}$ affects its total ionic conductivity; the denser and more compact the pellet, the higher the ionic conductivity. This is generally explained by an improvement in lithium ion conduction through the structure in the absence of porosity and by the formation of larger particles[235,236]. In our case, the addition of additives implies more porosity and the formation of impurities. These two phenomena can affect the properties of ionic conductivity of $LATP_{0.3}$. In the literature, the presence of $LiTiOPO_4$ in small quantity is reported not to affect the properties of $LATP_{0.3}$ but an excess (more than 10 wt%) is not beneficial[188,197]. On the other hand, the presence of $Li_4P_2O_7$ has been shown to improve the ionic conductivity of LATP[188]. However, the question is whether this improvement is due to better densification or to the presence of the salt. Thus, the objective of this section is to understand how the additives affect the ionic conductivity performances of $LATP_{0.3}$.

To achieve this, the ionic conductivity of samples with similar relative densities was determined using Electrochemical Impedance Spectroscopy (EIS) to better visualise the contribution of the salts on the LATP properties. The measurements were conducted on samples sintered at 760 °C and 900 °C, corresponding to a temperature without $LiTiOPO_4$ formation for the former and with a much more advanced reactivity for the latter.

IV.2.1. Ionic conductivity properties of $LATP_{0.3}$ before the chemical reactivity

First, samples with 1 wt% of additive at 760 °C were chosen as they exhibit a similar relative density of ~82 % (see Figure IV-2 and Figure IV-4). At this temperature, the $LiTiOPO_4$ and $Li_4P_2O_7$ are not formed or are present in small amounts in the case of LiBr and Li_3PO_4. A pellet of pure $LATP_{0.3}$ at this temperature was also analysed as a blank. The Nyquist Plots obtained for pure $LATP_{0.3}$ and for the mixtures are presented in Figure IV-6-a and b, respectively. All the data show only a single semi-circle, the right intercept of which with the Z' axis corresponds to the total resistivity of the system. As each impedance data point was normalised to the thickness and surface area of the respective pellets, the following tendency can be observed: $R_{LATP}>R_{Li3PO4}>R_{Li4P2O7}>R_{LiBr}$. However, the exact values are needed in order to determine the ionic conductivity in each sample.

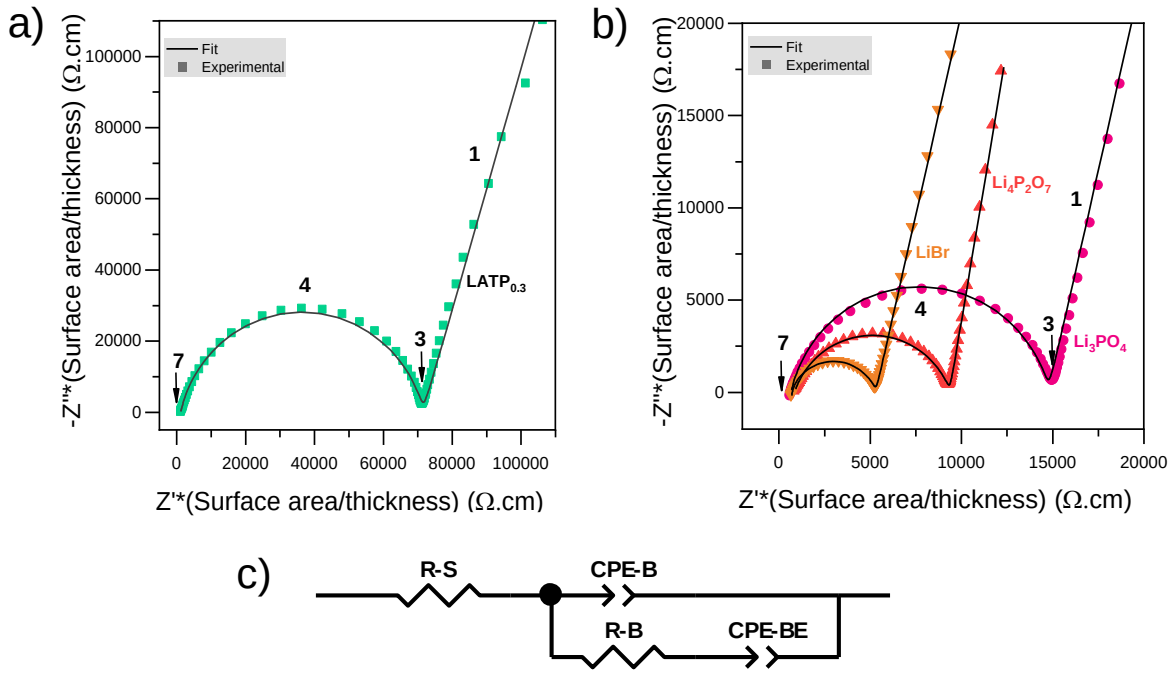

Figure IV-6: The Nyquist plots at 25 °C of pellets of (a) $LATP_{0.3}$ and (b) mixtures of 1 wt% of LiBr, Li_3PO_4 and $Li_4P_2O_7$. All the pellets were heat treated at 760 °C for 6 h. The numbers on the data indicate the power of frequency. The pellets exhibit a relative density of ~82 % in the case of the mixtures and ~77 % for pure $LATP_{0.3}$. The EIS data were fitted with the Debye equivalent circuit presented in (c).

Since all the data show a semi-circle, they were fitted with a conventional equivalent circuit[183] shown in Figure IV-6-c. As a reminder, this model is composed of the resistance associated to the contribution of the setup (R-S), the capacitive behaviour and the resistance of the sample (CPE-B and R-B respectively) and the capacitive response of the blocking electrodes (CPE-BE). Based on the values of the resistivity obtained, the ionic conductivities can be determined according the following equation (9):

$$\sigma = \frac{1}{R_B} \times \frac{e}{S} \quad (9)$$

Where σ is the ionic conductivity ($S.cm^{-1}$), R-B (Ω) is the resistivity of the sample, e and S are the thickness (cm) and the surface area (cm^{-2}) of the pellets, respectively. The results are presented in Table 6.

Samples	Relative densities (%)	χ^2	σ at 25°C ($S.cm^{-1}$)
$LATP_{0.3}$	76.9 (± 0.3)	6.10^{-4}	1.10^{-5} (± 0.1)
1wt% Li_3PO_4	81.2 (± 0.5)	4.10^{-3}	7.10^{-5} (± 0.6)
1wt% $Li_4P_2O_7$	82.1 (± 1.6)	5.10^{-4}	1.10^{-4} (± 0.3)
1wt% LiBr	81.3 (± 4.0)	8.10^{-5}	2.10^{-4} (± 0.9)

Table 6: Conductivity results of pellets heat treated at 760°C and obtained from fitting the Nyquist plots using the conventional equivalent circuit. The relative densities are also presented.

The χ^2, also named the goodness of fit, shows values that are lower than 10^{-3}. It suggests that the fit correctly matches the data. Based on these results, the ionic conductivity increases from 10^{-5} $S.cm^{-1}$ to 10^{-4} $S.cm^{-1}$ at 25 °C with the addition of LiBr or $Li_4P_2O_7$. However, this improvement is surprising in the case of LiBr, as it has been completely converted into Li_3PO_4, and the ionic conductivity of the sample with the addition of Li_3PO_4 is of the same order of magnitude as that of pure $LATP_{0.3}$. Indeed, the ionic conductivity of Li_3PO_4 is around 10^{-9}-10^{-10} $S.cm^{-1}$ at 30 °C[237], which means that even if the microstructure is improved, the ionic conductivity remains in the same range as that of $LATP_{0.3}$. A possible explanation for the greater ionic conductivity in the sample with the initial addition of LiBr is that the LiBr generates less than 1 wt% of Li_3PO_4. In the case of the addition of $Li_4P_2O_7$, the ionic conductivity of the pure salt is around 10^{-6}-10^{-7} $S.cm^{-1}$ at 30 °C[238], which is more conductive than Li_3PO_4. However, quantity is not the only factor that can impact ionic conductivity; the distribution of porosity and impurities also play a significant role. Agglomerates are less likely to degrade lithium conduction pathways compared to well-distributed pores or impurities.

IV.2.2. Ionic conductivity properties of $LATP_{0.3}$ after the chemical reactivity

On the other hand, the same analyses were conducted on samples with 5 wt% of additives at 900 °C, as the pellets at this temperature present a more advanced reaction. As previously, all the pellets have relative densities of 85-87 % and a pellet of pure $LATP_{0.3}$ densified at this temperature was chosen as a blank (~90 %). The Nyquist Plots are presented in Figure IV-7, a single semi-circle is observed for all samples except for the one with the initial addition of LiBr. Indeed, a new contribution appears at low frequencies. Initially, these data were fitted with the equivalent model shown in Figure IV-6-c to extract the resistances. Visually, the fits work quite

well for the pure $LATP_{0.3}$ sample, as well as those with the additions of $Li_4P_2O_7$ and Li_3PO_4. However, the conventional equivalent circuit is not sufficient in the case of the LiBr addition, as the impedance points at low frequencies do not match.

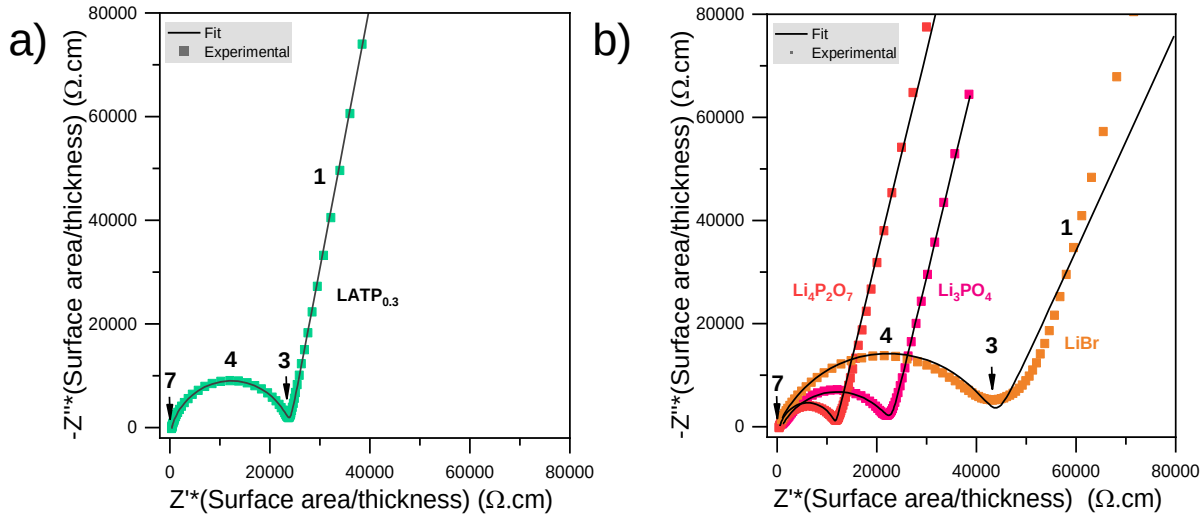

Figure IV-7: The Nyquist plots at 25 °C of pellets of (a) $LATP_{0.3}$ and (b) mixtures of 5 wt% of LiBr, Li_3PO_4 and $Li_4P_2O_7$. All the pellets were heat treated at 900 °C for 6 h. The pellets exhibit a relative density of ~85-87 % in the case of the mixtures and ~90 % for pure $LATP_{0.3}$. The EIS data were fitted with the Debye equivalent circuit. The numbers on the data indicate the power of frequency.

Thus, the data for this sample were fitted with a modified Debye model (Figure IV-8-c), which involves adding a new resistance, R2, and a capacitance, CPE2, to account for this new contribution. As shown in the Figure IV-8-a, the new model visually fits the data for this sample more accurately. This new contribution could arise from the formation of an excessive amount of $LiTiOPO_4$ at the grain boundaries. However, it was expected that the same contribution would appear for the Li_3PO_4 sample, which is not the case.

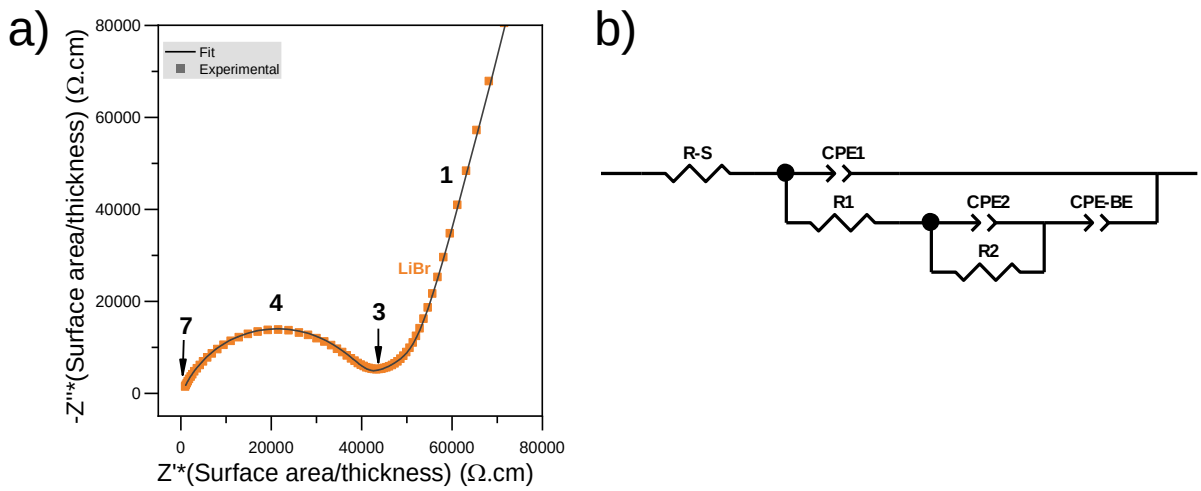

Figure IV-8: (a) The Nyquist plots at 25 °C of pellets of mixture of 5 wt% of LiBr. The numbers on the data indicate the power of frequency. The EIS data was fitted with the modified Debye model presented in (b). The numbers on the data indicate the power of frequency.

Based on the results from the fits, the total ionic conductivities were determined according to equation (9). All the results are presented in Table 7.

Samples	Model	Relative densities (%)	χ^2	σ at 25 °C (S.cm^{-1})
$LATP_{0.3}$	Debye	90.0 (± 1.7)	6.10^{-5}	4.10^{-5} (± 0.3)
5wt% Li_3PO_4	Debye	85.7 (± 1.6)	6.10^{-4}	5.10^{-5} (± 3)
5wt% $Li_4P_2O_7$	Debye	85.5 (± 1.5)	6.10^{-3}	9.10^{-5} (± 0.6)
5wt% LiBr	Modified Debye	87.7 (± 1.1)	3.10^{-4}	2.10^{-5} (± 2)

Table 7: Results of pellets heat treated at 900 °C obtained from fitting the Nyquist plots.

The ionic conductivities obtained from the EIS measurements are of the same order of magnitude whether Li-salts are added or a pure sample is used. This suggests that the presence of Li-salts does not significantly affect the ionic conductivity properties of $LATP_{0.3}$, even after the formation of porosity or $LiTiOPO_4$. However, it is assumed that the quantity of impurities and porosity, which are related to the amount of added salts, could negatively impact the ionic conductivity of $LATP_{0.3}$.

All experiments conducted on ionic conductivities show that the addition of Li-salts does not appear to degrade the ionic properties of $LATP_{0.3}$. Before the reaction of the salt, it could even be beneficial at an optimised quantity, as evidenced by the increase in conductivity from 10^{-5} to 10^{-4} S/cm at a similar relative density of pure $LATP_{0.3}$ (see Table 6). With the formation of $LiTiOPO_4$ and pores within the microstructure, the ionic conductivity remains in the same order of magnitude as that of pure $LATP_{0.3}$, indicating that it is not degraded.

IV.3. Optimised system with the addition of $Li_4P_2O_7$

Based on the insights gained in the previous section, the optimal combination of relative density and ionic conductivity is achieved with a mixture containing 5 wt% $Li_4P_2O_7$, sintered at 760 °C for 6 hours. In this section, we adjusted the incorporation of the lithium salt by decreasing its particle size to try to improve both the relative density and ionic conductivity.

For this purpose, the initial $Li_4P_2O_7$ powder was ball milled according the followed program: 450 rpm, 10 min of grinding for 10 min of break during 2 hours and with Zirconia balls of 5 mm of diameter. The ground powder, called BM, and the initial powder were analysed by SEM to qualitatively observe the decreasing in particle size. As presented in Figure IV-9, the initial particle size ranges between 100 µm and 50 µm (Figure IV-9-a), whereas after grinding, the aggregate size is decreased, with maximum values around 50 µm (Figure IV-9-b).

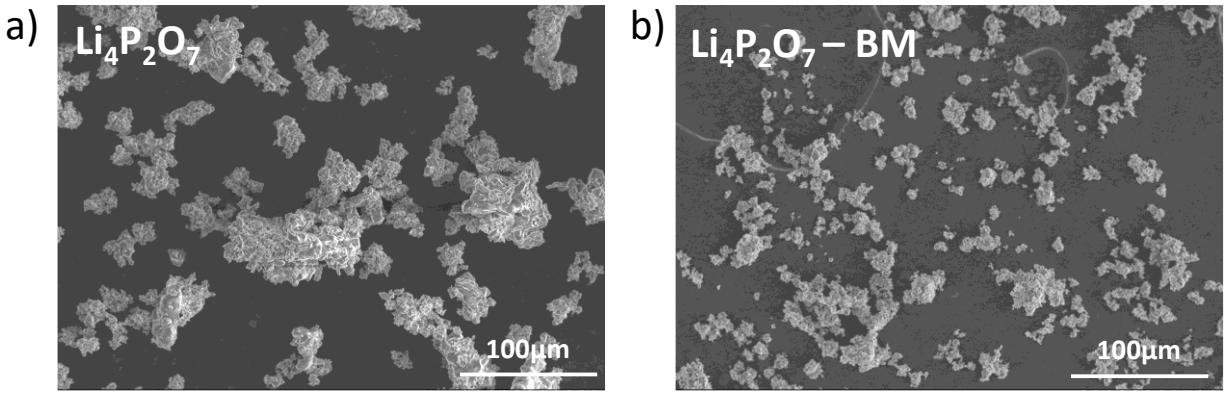

Figure IV-9: SEM images of (a) $Li_4P_2O_7$ powder and (b) $Li_4P_2O_7$ powder after ball milled.

Then, 5 wt% of ball-milled $Li_4P_2O_7$ was added to the $LATP_{0.3}$ via manual mixing to form pellets. These pellets were subsequently heat-treated at 760 °C for 6 hours. The relative densities were determined through geometric measurements. The average relative density obtained from these three pellets is 84 ± 1 %, which is lower than what was observed with the unground $Li_4P_2O_7$. The microstructures of the pellets for these two systems were also examined by SEM, and the images are shown in Figure IV-10. As discussed in section IV.1.2.2, the salt particles form pores, resulting in increased porosity.

However, by decreasing the particle size of $Li_4P_2O_7$, it can be observed that the porosity in the $LATP_{0.3}$ microstructures is decreased because the particles occupy smaller volumes.

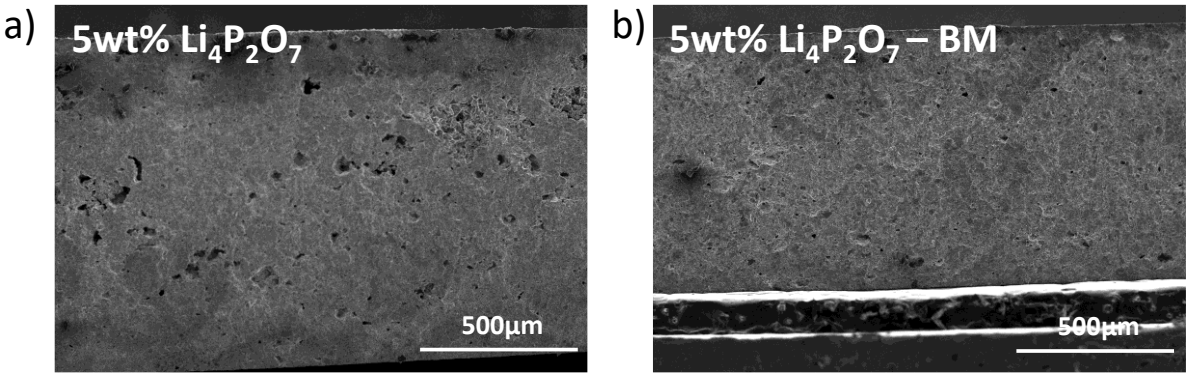

Figure IV-10: SEM images of (a) pellets composed of 5 wt% of $Li_4P_2O_7$ and $LATP_{0.3}$; (b) pellets composed of 5 wt% of $Li_4P_2O_7$ BM and $LATP_{0.3}$. These pellets were analysed after a heat treatment at 760 °C for 6 h.

Finally, an EIS measurement was conducted on a pellet containing 5 wt% of ground $Li_4P_2O_7$ heat-treated at 760 °C. From this analysis, an ionic conductivity of 2.10^{-4} $S.cm^{-1}$ at 25 °C was obtained. In comparison with the literature, most studies achieve ionic conductivities of 10^{-4} $S.cm^{-1}$ with relative densities of around 90 %, but it is at higher heat treatment temperatures (> 800 °C)[139,140,189]. One study reached a relative density of 92 % at 740 °C with a system containing 15 mol% of Li_3PO_4, but the ionic conductivity remains in the order of 10^{-5} $S.cm^{-1}$[189].

V. Conclusion of the Chapter III

To understand the relationship between $LATP_{0.3}$ densification using Li-salts and their reactivity, the first part of the chapter focused on studying the chemical reactivity mechanism between certain Li-salts and $LATP_{0.3}$.

To begin with, we started from a general observation: the formation of the same impurities, $LiTiOPO_4$ and $Li_4P_2O_7$. Using a reference lithium salt, LiBr, we were able to identify the key steps involved in forming these impurities: the decomposition and reaction of the initial salt with $LATP_{0.3}$, before reaching its melting temperature, to form Li_3PO_4 and TiO_2; and the reaction of these three species to form the final impurities, $Li_4P_2O_7$ and $LiTiOPO_4$.

The combination of $Li_4P_2O_7$ and $LATP_{0.3}$ enhances densification at lower temperatures through liquid-phase sintering at the melting temperature of the mixture. This indicates that the reactivity between Li-salts and $LATP_{0.3}$ is crucial for forming this phase. However, this reactivity leads to the formation of $LiTiOPO_4$ and consumes part of the $LATP_{0.3}$.

Thus, we focused on how the Li-salts and the reactivity impacts the microstructure and ionic conductivity properties of $LATP_{0.3}$ in the final part of the chapter. Although the addition of Li-salts improves the relative densities (> 85 %) at lower temperatures (760°C-830 °C) compared to pure $LATP_{0.3}$, the microstructures are affected by the formation of porosity. Initial studies have shown that this porosity can be limited by adjusting the particle size of the additive. Ultimately, adding Li-salts can enhance the ionic properties of $LATP_{0.3}$, but the formation of impurities diminishes this effect, leaving the overall properties largely unchanged.

By reacting Li-salts with $LATP_{0.3}$, we were able to lower the densification temperature of $LATP_{0.3}$ to 760 °C, thanks to the formation of $Li_4P_2O_7$. However, this approach has limitations, as it is governed by the melting behaviour of $Li_4P_2O_7$ in the presence of $LATP_{0.3}$. This indicates that alternative strategies must be explored to achieve $LATP_{0.3}$ densification at even lower temperatures. Therefore, in the next chapter, we will focus on lithium salt mixtures that melt at lower temperatures without reacting. Additionally, we will explore a sintering method known as Spark Plasma Sintering (SPS) combined with the addition of salts, as an alternative to conventional sintering techniques

Chapter IV: Non-Reactive Sintering

I. Introduction

The study conducted in Chapter III demonstrated that the addition of Li-salts indeed enhances the densification of $LATP_{0.3}$ at lower temperatures. However, this improvement is limited to the melting of $Li_4P_2O_7$, resulting from the reactivity of $LATP_{0.3}$ with the Li-salts.

In this final chapter, we explore the use of lithium salt mixtures that do not react and have lower melting temperatures than $Li_4P_2O_7$ to induce liquid phase sintering at reduced temperature. We selected two phosphate mixtures: $LiPO_3$-Li_3PO_4 and $LiPO_3$-$Li_4P_2O_7$ in their eutectic compositions, with melting points of 604 °C[194,239]. To the best of our knowledge, the effect of these mixtures on the densification of $LATP_{0.3}$ has not been previously investigated in the literature.

To achieve this, two strategies were explored. The first method involves densification through a conventional sintering process, where a pellet is heat-treated in air using a muffle furnace. The second approach utilised Spark Plasma Sintering (SPS), which is a process that involves sintering powders by simultaneously applying electric current and uniaxial pressure during an extremely fast heat treatment. This section will discuss the densification of $LATP_{0.3}$ with the addition of eutectic mixtures using both methods. Additionally, the ionic conductivity of the pellets demonstrating the best density and microstructure will be evaluated.

II. Eutectic mixtures

Most Li-salts tend to decompose and react at high temperatures before they reach their melting temperature. To mitigate this reactivity, it is effective to use Li-salts that either do not react with LATP or melt before any reaction occurs. As a first approach, we focused on lithium phosphates such as Li_3PO_4, $LiPO_3$, and $Li_4P_2O_7$, mixing them in proportions that correspond to the reported eutectic, which melts around 604 °C ± 1 °C[194]. We selected two precursors' mixtures to study this eutectic, with an average composition of $Li_{1.28}PO_{3.14}$ (Figure II-1). The first one, referred to Eut1, consists of $LiPO_3$ and Li_3PO_4 in a mole percentage of 86 % and 14 %, respectively. The second one, referred to Eut2, is composed of 84.5 mole% $LiPO_3$ and 15.5 mole% $Li_4P_2O_7$[239]. Initially, all mixtures were prepared by grinding each reactant together using a mortar, in specific proportions.

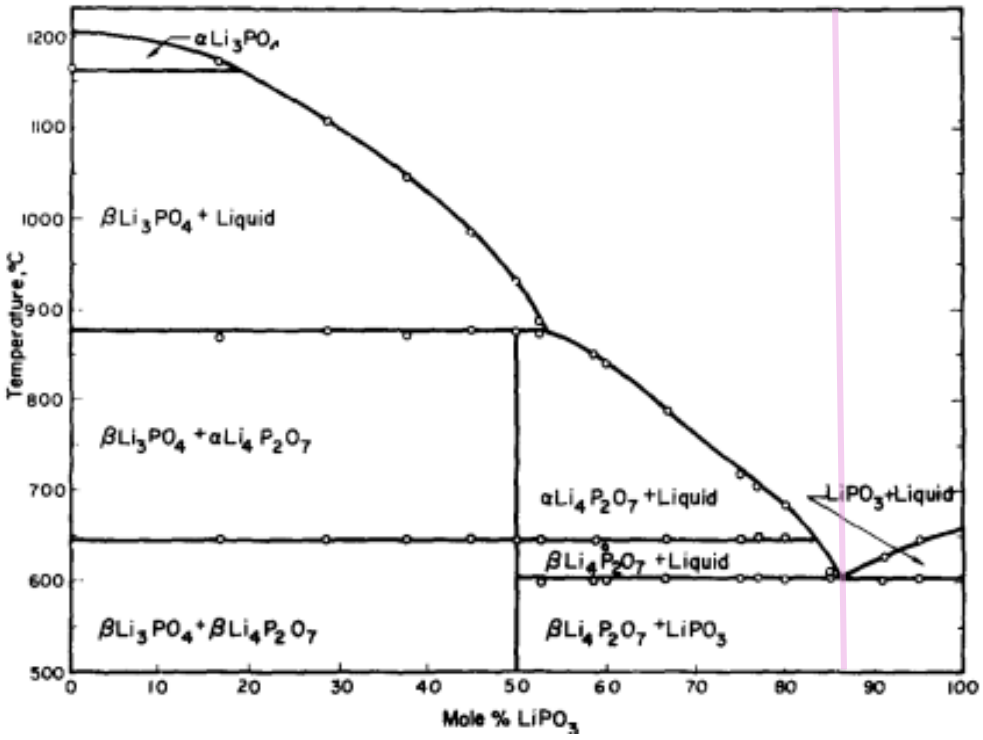

Figure II-1: Binary diagram of $LiPO_3$-Li_3PO_4 system from Osterheld et al study.[194]

The first step of the study was to investigate the chemical reactivity of $LATP_{0.3}$ and these mixtures in order ensure that their melting temperature corresponds to the eutectic.

II.1. Chemical reactivity

The reactivity of $LiPO_3$, Eut1 and Eut2 with $LATP_{0.3}$ was studied by X-Ray Diffraction measurements after heat treatments at 200 °C, 400 °C, 600 °C and 800 °C. The pellets were prepared from mixtures composed of a molar ratio of 1:1 in order to exacerbate the chemical reactivity. The heat treatments were conducted under an air atmosphere, with a heating ramp of 10 °C/min, and mixtures were quenched after reaching the desired temperature. The acquisitions were carried out in the range 2θ = 10-80 °, with 0.02 ° steps and a time of 0.2 s/step.

In the case of an addition of $LiPO_3$, the XRD pattern at room temperature (Figure II-2-a) presents the main diffraction peaks of $LATP_{0.3}$ (*R*-3*c*), $AlPO_4$ ($C222_1$) and $LiPO_3$ (*P*12/*n*1). Only these peaks are observed at 200 °C, 400 °C and 600 °C, indicating no apparent reactivity. The intensities of the $LiPO_3$ diffraction peaks vary from one sample to another, which can be explained by insufficient homogenisation of the initial mixture. At 800 °C, the diffraction peaks of $LiPO_3$ are not visible anymore as $LiPO_3$ melts at 656 °C ± 3 °C[194,240,241]. The absence of the $AlPO_4$ impurity suggests that it has likely been dissolved by the salt melts. These findings indicate that $LiPO_3$ does not react with $LATP_{0.3}$ to form any additional species.

On the other hand, results from XRD experiments for the mixture of $LATP_{0.3}$ and Eut2 are presented in Figure II-2-b. The main diffraction peaks of $LATP_{0.3}$ (*R*-3*c*) are mainly observed while the diffraction peaks of $AlPO_4$ ($C222_1$), $LiPO_3$ (*P*12/*n*1) and $Li_4P_2O_7$ (*P*-1) are less intense. No changes are observed up to 600 °C, with only LATP diffraction peaks appearing at 800 °C. This confirms that the salt mixture melts before reaching 800 °C. These results suggest that there is no significant chemical reactivity before or after melting.

Finally, the XRD results of the mixture of Eut1 and $LATP_{0.3}$ are presented in Figure II-2-c. At room temperature, only the diffraction peaks of $LiPO_3$, $LATP_{0.3}$ and $AlPO_4$ are observed. The diffraction peaks of Li_3PO_4 (*Pnma*) are difficult to observe because the mass proportion of Li_3PO_4 is smaller compared to $LiPO_3$ (*P*12/*n*1), being 18 wt% and 82 wt% respectively. As in the $LiPO_3$ and Eut2 addition experiments, no additional peaks are observed at 200 °C and 400 °C. Nevertheless, a diffraction peak of $Li_4P_2O_7$ appears at 600 °C, in addition to the peaks of the initial species. Two hypotheses can be proposed to explain this formation. The first one involves chemical reactivity between $LATP_{0.3}$ and one or the two compounds of Eut1. However, previous results from Figure II-2-a show that $LiPO_3$ does not react with $LATP_{0.3}$, whereas Li_3PO_4 starts reacting at 800 °C to form $Li_4P_2O_7$ and $LiTiOPO_4$, which is not observed. On the other hand, the temperature of the thermal treatment is close to the melting temperature of the

eutectic mixture, i.e. 604 °C ± 3 °C, which means that melting may have already begun. According to Figure II-1, its melting temperature is incongruent, resulting in the formation of two phases upon cooling to ambient temperature, i.e. $LiPO_3$ and $Li_4P_2O_7$. In other words, if the quenching is not rapid enough, $Li_4P_2O_7$ may form during cooling. At the final stage, only the diffraction peaks of $LATP_{0.3}$ are observed at 800 °C, indicating that Eut1 has fully melted at this temperature.

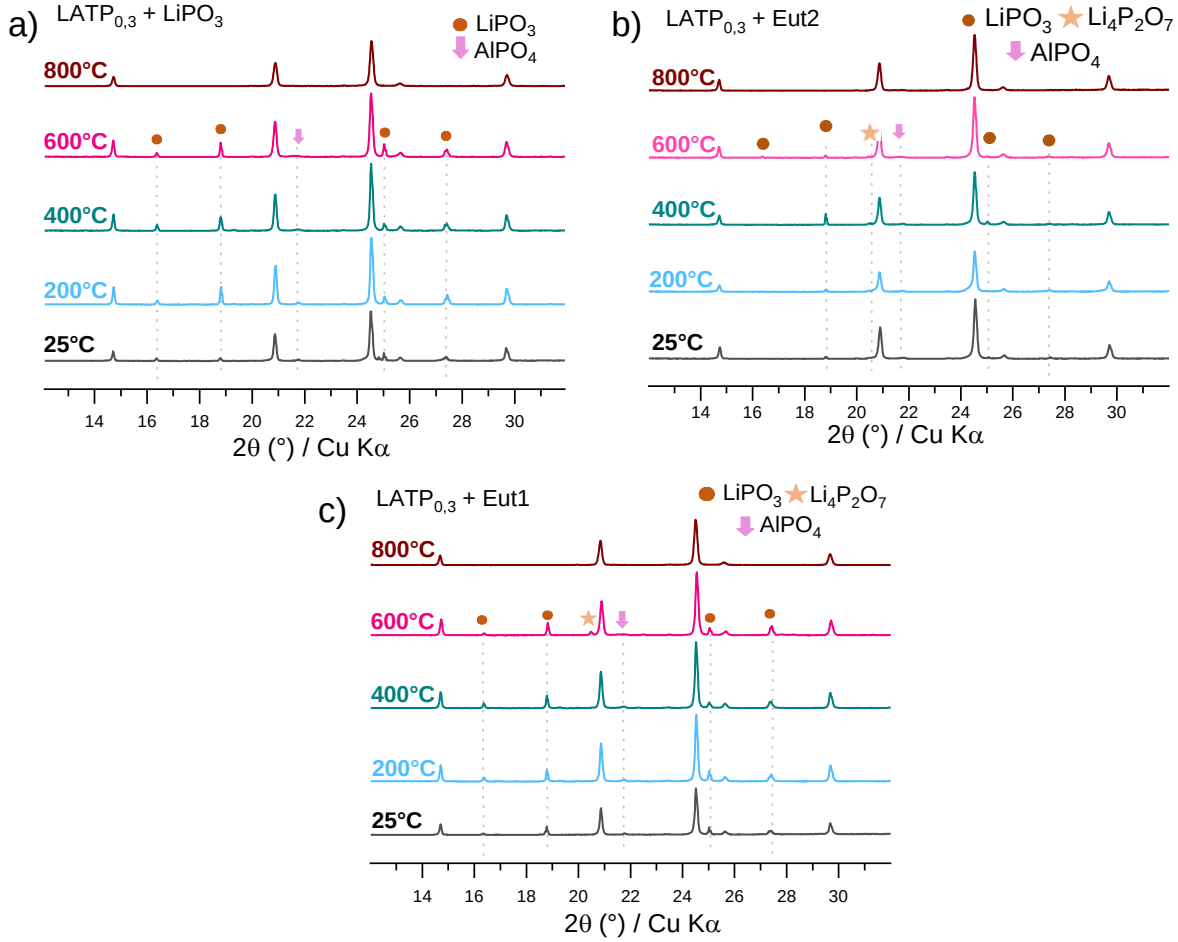

Figure II-2: XRD results of mixtures of (a) $LATP_{0.3}$ and $LiPO_3$ (1:1), (b) $LATP_{0.3}$ and Eut2 (1:1), and (c) $LATP_{0.3}$ and Eut1 (1:1) quenched at different temperatures including 200 °C (—), 400 °C (—), 600 °C (—) and 800 °C (—).

No apparent chemical reactivity is observed for the mixtures of $LATP_{0.3}$ and $LiPO_3$, and $LATP_{0.3}$ and Eut2. However, additional characterisations are needed in the case of $LATP_{0.3}$ and Eut1. Therefore, *in-situ* XRD was performed on a sample of $LATP_{0.3}$ and Eut1 (1:1) to compare with *ex-situ* XRD and investigate the formation of $Li_4P_2O_7$. The heat treatment was conducted from 30 °C to 900 °C with a heating ramp of 10 °C/min and under air with a flow rate of 50 ml/min. The measurements were carried out according to the **P1** program (2θ = 10-60 ° with 0.02° steps and a time of 0.1 s/step), involving rapid scans every 10 °C from 30 °C to 900 °C. Results are presented in Figure II-3. At the beginning of the experiment, the main diffraction

peaks of $LiPO_3$, $AlPO_4$ and $LATP_{0.3}$ are well defined, whereas those of Li_3PO_4 are more difficult to observe. The phase transition of $AlPO_4$ from orthorhombic to cubic structure is observed around 240 °C[242]. No changes occur until 540 °C, where the $Li_4P_2O_7$ phase forms. This observation confirms that the formation of $Li_4P_2O_7$ is not due to the incongruence of the melting temperature but could be related to the reactivity of Li_3PO_4 and $LATP_{0.3}$. Finally, all present phases, except $LATP_{0.3}$, disappear at 650-660 °C. This phenomenon could be associated with the melting of the eutectic mixture, but the melting temperature corresponds to that of $LiPO_3$[194,239,241].

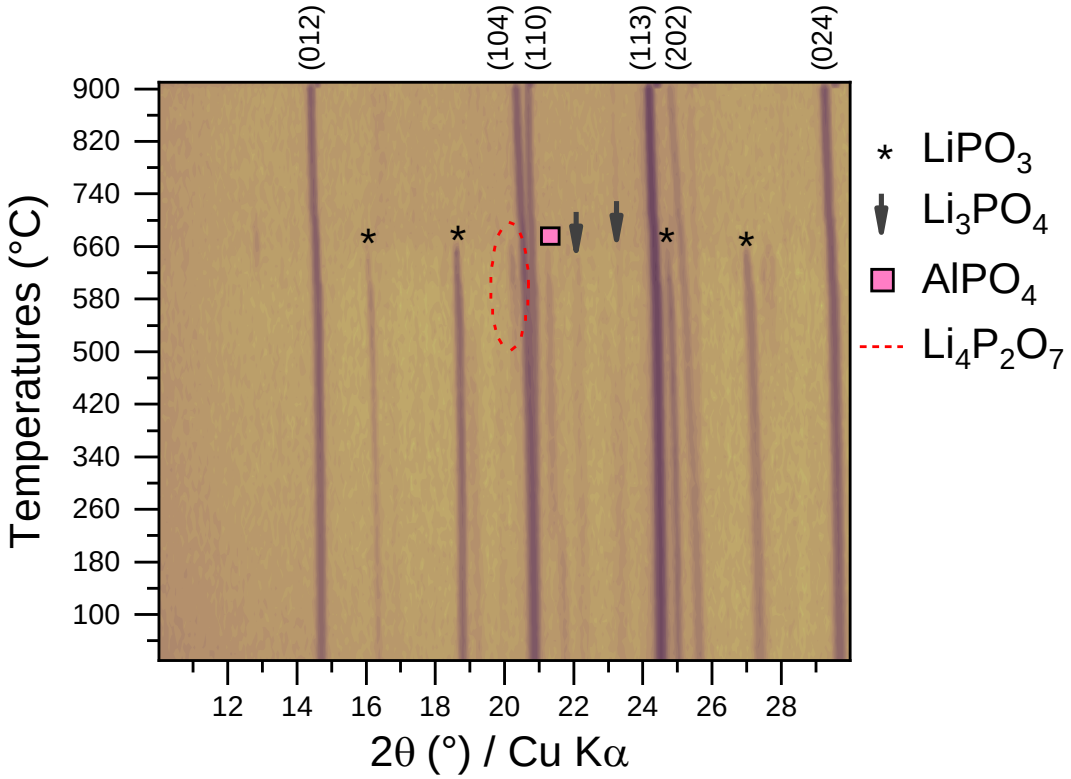

Figure II-3: High-temperature X-ray diffraction data of a pellet of a mixture of $LATP_{0.3}$ and Eut1 (1:1) in a temperature range from 30 to 900 °C in air flow (50 mL/min).

Then, we analysed the mixtures Eut1 and Eut2 with $LATP_{0.3}$, in the same molar proportion as previous experiments, by DTA in order to determine at which temperature the salts or the mixtures of salts melt. The experiments were conducted from 30 to 900 °C, with a heating ramp of 5 °C/min in an air flow rate of 25 ml/min. In the case of the mixture with Eut1, the DTA curve (Figure II-4-a) exhibits two endothermic peaks at 590 °C and 640 °C, corresponding to the melting temperature of Eut1 and $LiPO_3$ respectively. This indicates that a portion of Li_3PO_4 reacts to form $Li_4P_2O_7$, while the remaining portion melts with $LiPO_3$ at the eutectic melting temperature. Thus, the remaining $LiPO_3$ melts at around 650 °C. We hypothesized that improving the contact between the two salts might reduce the formation of $Li_4P_2O_7$, encouraging

the entire mixture to melt at the eutectic temperature. The result for the Eut2 mixture in Figure II-4-b reveal a single endothermic peak at 636 °C, corresponding to the melting of $LiPO_3$. This suggests that better homogenisation of the $Li_4P_2O_7$-$LiPO_3$ mixture is necessary to reach the eutectic melting.

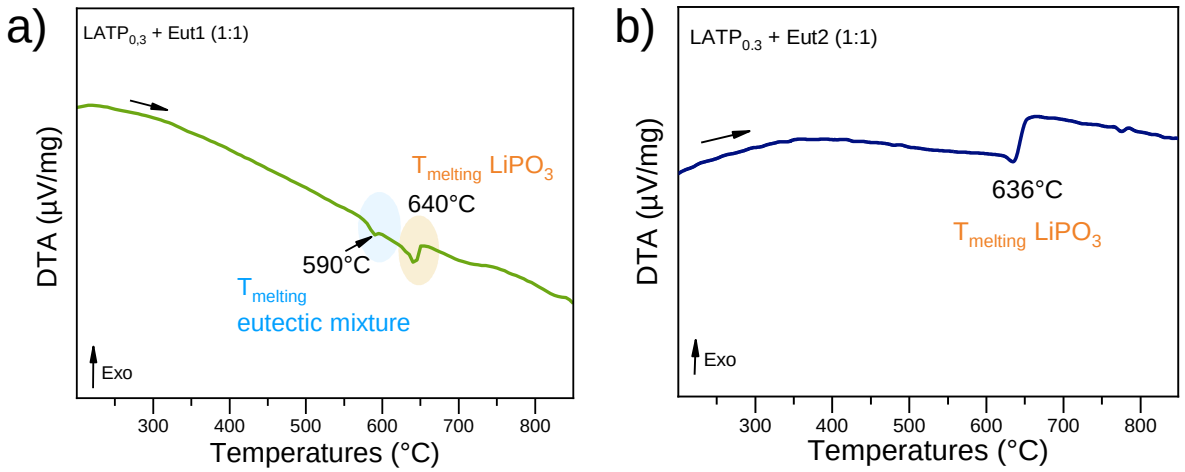

Figure II-4: DTA curves of (a) a mixture of $LATP_{0.3}$ and Eut1 in equimolar proportions (—) and (b) a mixture of $LATP_{0.3}$ and Eut2 in equimolar proportions (—).

Based on the results in the first section, Eut1 seems to react with $LATP_{0.3}$ through Li_3PO_4 to form $Li_4P_2O_7$. This chemical reactivity was observed in *in-situ* and *ex-situ* XRD experiments, which also showed multiple melting temperatures in DTA. Despite Eut2 not reacting with $LATP_{0.3}$, only the melting of $LiPO_3$ was observed, suggesting inhomogeneity in the mixture. To address this, we focused on improving the homogenization of Eut1 and Eut2 before adding them into $LATP_{0.3}$.

II.2. Homogenisation of the eutectic mixtures

One way to homogenise the mixtures is to melt them before mixing them with $LATP_{0.3}$. For this purpose, each reactant in the eutectic proportions was ground using a mortar and placed in a sealed tube under air. In the case of Eut1, the tube was heated to 750 °C during 1 h, which is above the melting temperature of the mixture, and with a heating rate of 5 °C/min. The program was similar for Eut2 but the heat treatment was conducted at a temperature of 650 °C. The tubes were then quenched to prevent separation of the parent species at ambient temperature. The quartz tubes were subsequently broken to recover the powder. This material was ground into a powder using a planetary mill prior to X-ray diffraction analysis. The XRD results of Eut1 and Eut2 after the quenching are presented in Figure II-5-a and Figure II-5-b respectively. The acquisitions were carried out in the range 2θ = 10-80 °, with 0.02 ° steps and a time of 0.2 s/step.

First, the results for Eut1 are discussed: after quenching the mixture at 750°C, the phases $LiPO_3$ (*P*12/*n*1) and $Li_4P_2O_7$ (*P*-1) are observed. As previously explained, the incongruent melting results in the observation of $Li_4P_2O_7$ and $LiPO_3$. These results suggest that the quenching process was insufficiently rapid, as indicated by the presence of species and the change in the mixture's appearance from a white powder to a glassy material that lacks full transparency. To improve this, a more aggressive quenching method could be employed, such as immersing the material in liquid nitrogen immediately after removal from the muffle furnace or quenching from a higher temperature.

On the other hand, the XRD results after quenching the second mixture (Figure II-5-b) show that the main diffraction peaks of $LiPO_3$ and $Li_4P_2O_7$ have disappeared. Some unknown impurities are present but they may be due to the quartz tube. The appearance of the powder also changed, from a white powder to a glassy and transparent material. These results suggest that the quenching process successfully prevented crystallization of the parent phases in the mixture during cooling. Henceforth, the quenched Eut2 will be referred to as Eut2M or Eut2 Melted.

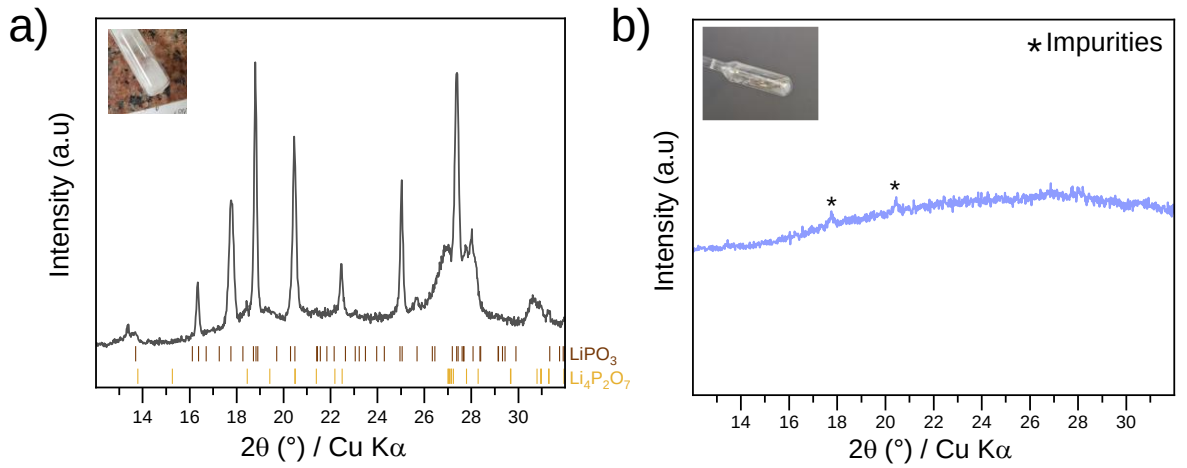

Figure II-5: XRD results of (a) the eutectic mixture $LiPO_3$-Li_3PO_4 before (—) and after quenching at 750 °C (—), and (b) the eutectic mixture $LiPO_3$-$Li_4P_2O_7$ after quenching at 650 °C (—).

Then, DTA analysis was performed on a mixture of $LATP_{0.3}$ and Eut2 Melted in equimolar proportions, using the same program as for mixtures containing Eut1 and Eut2. The result in Figure II-6 shows a single exothermic peak at 590 °C, corresponding to the melting of the eutectic. This result confirms that quenching successfully homogenised the mixture, ensuring it melts at its eutectic temperature. Without this step, the mixture remains heterogeneous, resulting only in the melting of $LiPO_3$.

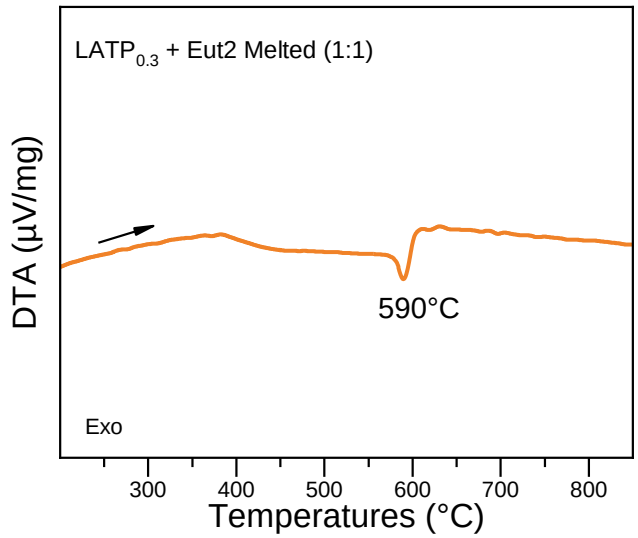

Figure II-6: DTA curves of mixtures of $LATP_{0.3}$ + Eut2 melted (—) in equimolar proportions. The experiments were conducted in air, with a heating ramp of 5 °C/min.

Based on these results, we have chosen to investigate the effect of Eut2M on the densification temperature of $LATP_{0.3}$. Unlike Eut1, Eut2M does not show noticeable chemical reactivity with $LATP_{0.3}$ and has melted at the eutectic temperature.

III. Conventional densification by liquid phase sintering

III.1. Densification with the addition of eutectic mixture melted

In order to investigate the impact of the addition of Eut2M on the densification of $LATP_{0.3}$, we sintered pellets of $LATP_{0.3}$ with 5wt% of Eut2M at different temperatures including 600 °C, 700 °C and 800 °C. The heat treatments were performed for 6h under an air atmosphere and with a heating rate of 5 °C/min. The green relative densities and the relative densities of the pellets after the heat treatments were determined by geometrical measurements. These values are compared in Figure III-1. The green relative densities of all the pellets range between 68 % and 76 %, which is sufficient for sintering pellets by heat treatment. After a heat treatment at 600 °C, corresponding to the melting temperature of Eut2, the pellets exhibit an average relative density of ~73 %. This value is close to the green relative densities of the pellets, indicating that densification did not occur despite the melting of the salt mixture. At 700 °C, a slight increase in relative density values is observed (~76 %) compared to those at 600 °C and the green relative densities. Finally, heat treatment at 800 °C resulted in a significant increase in relative density (~83 %) compared to those obtained at 600 °C and 700 °C. However, experiments conducted on pure $LATP_{0.3}$ pellets sintered at 830 °C for 6 hours (Chapter III) show relative densities similar to those achieved with the addition of Eut2M at 800 °C for 6 hours. This suggests that Eut2M does not significantly improve relative density at lower temperatures, as similar outcomes are achieved without its addition within the same temperature range.

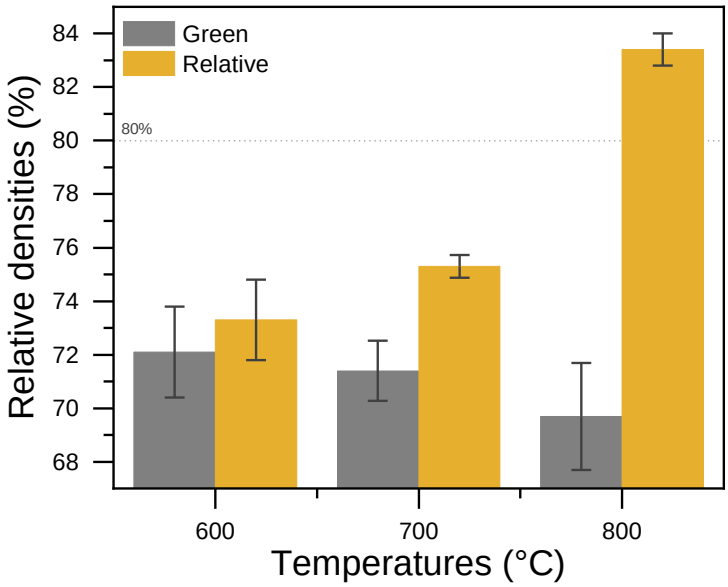

Figure III-1: Green relative densities and relative densities of pellets of mixtures of $LATP_{0.3}$ + 5 wt% Eut2M at 600 °C, 700 °C and 800 °C for 6 h.

In parallel with the study of relative densities, a dilatometry experiment was performed on samples made with the same composition as before. The applied heat treatment was from 25 °C to 1000 °C, with a heating ramp of 5 °C/min, in air. The results are presented as linear shrinkage as a function of temperature (Figure III-2-a), and as shrinkage rate as a function of temperature (Figure III-2-b). Based on Figure III-2-a, by comparing the results to those of pure $LATP_{0.3}$ pellet, the curve of the mixture has the same shape as the curve of $LATP_{0.3}$, indicating the same regime of densification. However, the curve corresponding to the mixture is shifted to a lower temperature with a shrinkage onset temperature occurring at ~550 °C instead of ~700 °C as observed without additives. At the end of the heat treatment, the curve of the mixture exhibits a value of linear shrinkage of 8 %, which is close to that obtained in the case of $LATP_{0.3}$ (7 %). The shift to lower temperature is also observed when comparing the derivatives (Figure III-2-b), as the plateau corresponding to the signal of the mixture is at 875 °C, while that of $LATP_{0.3}$ is greater than 950 °C. Since the end of the plateau is visible in the case of the mixture, it indicates that the densification step is almost completed at this temperature unlike the case of pure $LATP_{0.3}$. However, this signal does not correspond to the eutectic melting temperature of the mixture, which explains the lack of improvement in relative densities at 600°C.

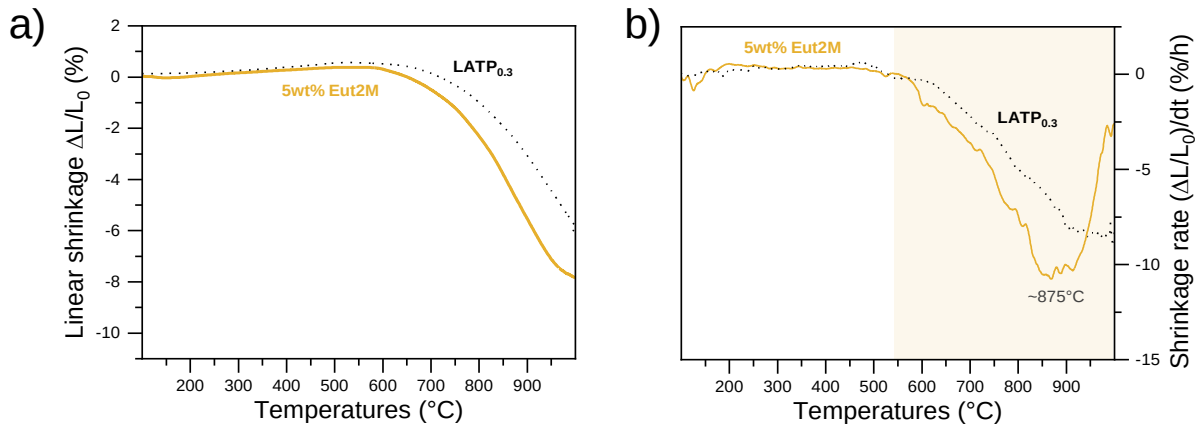

Figure III-2: Dilatometry experiments of pellet of $LATP_{0.3}$ (- - -) and mixture of $LATP_{0.3}$ + 5 wt% Eut2M (—). The experiments were conducted in air, with a heating rate of 5 °C/min. Results are presented in two formats: (a) linear shrinkage as a function of temperature and (b) the shrinkage rate as a function of temperature. The yellow part shows the temperature at which densification starts.

In comparison with an addition of 5 wt% of $Li_4P_2O_7$ (Chapter III), the addition of Eut2M does not appear to significantly impact the densification of $LATP_{0.3}$ to decrease its densification temperature. Indeed, the nature and the quantity of the additive play an important role for the liquid phase sintering. The additive Eut2M is composed of $Li_4P_2O_7$ and $LiPO_3$: in the case of $Li_4P_2O_7$, the experiments conducted in Chapter III have shown that it leads to better densification of $LATP_{0.3}$. However, in the case of $LiPO_3$, this capacity remains to be determined.

III.2. Compatibility of $LATP_{0.3}$ with $LiPO_3$ in densification process

In order to investigate the capacity of $LiPO_3$ to densify $LATP_{0.3}$, a dilatometry experiment was first conducted under the same conditions as for Eut2M, but on a mixture of $LATP_{0.3}$ and 5 wt% of $LiPO_3$. The result presented in Figure III-3 shows that the shrinkage onset temperature occurs at ~575 °C, which is close to that obtained with 5 wt% of Eut2M. Moreover, the curve representing the linear shrinkage as a function of the temperature is not centred on the melting temperature of $LiPO_3$ (650 °C), as its shape is similar to that obtained in the case of $LATP_{0.3}$. No improvement in the final linear shrinkage is observed, as similar results were obtained with the addition of Eut2M. The final observation relates to the derivative, where the plateau corresponding to the LiPO3 signal occurs at 950 °C, higher than that observed with Eut2M.

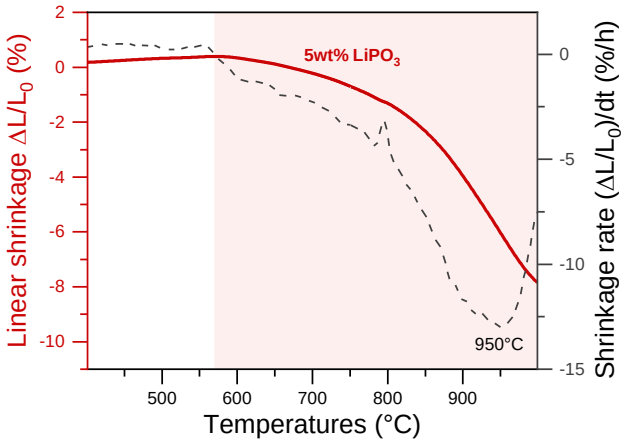

Figure III-3: Dilatometry experiments of pellet of mixture of $LATP_{0.3}$ + 5 wt% $LiPO_3$. The experiments were conducted in air, with a heating rate of 5 °C/min. The red part shows the temperature at which densification starts.

Based on these results, it appears that $LiPO_3$ does not enhance the densification of $LATP_{0.3}$ at lower temperatures. Given that Eut2M comprises 69 wt% $LiPO_3$, this explains why it does not significantly improve $LATP_{0.3}$ densification.

The poor densification with $LiPO_3$ can be explained by two hypotheses: the first one involves a low wettability and a high viscosity of the melted salt. If $LiPO_3$ does not wet $LATP_{0.3}$ particles well, it could hinder the rearrangement of particles during the densification process. This step is crucial because, once completed, all $LATP_{0.3}$ particles may become coated with a thin liquid film, which facilitates the transition to the second stage of liquid-phase sintering.[97] The viscosity parameter is relevant only during the particle rearrangement stage, as it influences the kinetic aspects [95].

The second hypothesis pertains to the second stage of $LATP_{0.3}$ sintering, where the solubility of $LATP_{0.3}$ in the salt is crucial. It suggests that low solubility of $LATP_{0.3}$ in the salt could

hinder the dissolution and re-precipitation process, making effective densification more difficult to achieve.

In the literature, particle rearrangement during this stage is characterised by a significant increase in relative density[97] as the liquid phase acts as a lubricant to rearrange the particles and eliminate porosity. However, despite the additives melting, no improvement in relative densities was observed in our experiments. This suggests that the limiting factor lies in the initial stage of liquid- phase sintering.

This limitation can be addressed by mechanically forcing particle rearrangement using alternative sintering techniques. Methods like hot pressing and spark plasma sintering (SPS), where powders are pressed throughout the thermal treatment process, are examples of such techniques. In our study, we opted to focus on SPS, for reasons that we will detail in the next section.

IV. Spark Plasma Sintering

Spark Plasma Sintering (SPS) is an advanced sintering technique used to consolidate metallic, ceramic, or composite powders into solid pieces. Compared to conventional methods, SPS can densify particles at lower temperatures and in shorter times, utilising high heating rates (>100 °C/min), which allows for a faster sintering process completion[52,83].

IV.1. Principle

The SPS process involves sintering powders by simultaneously applying electric current and uniaxial pressure. The system, described in Figure IV-1, is composed of several components: first, the die, typically made of graphite, is placed between graphite spacers. Steel cylinders are then placed on each side of the spacers to connect with the hydraulic press[243]. The die is usually covered with a graphite layer (Papyex®) before the powder is added to limit contamination and facilitate demoulding. Heating occurs by passing a pulsed direct current (DC) through the die and the sample if it is conductive[244]. Temperature is controlled by a thermocouple, although there is some discrepancy between the applied temperature and the temperature experienced by the sample. The monitoring of shrinkage during sintering is performed by tracking the displacement of the bottom part of the system. The process can be conducted under primary/secondary vacuum or a neutral atmosphere such as N_2 or Argon[245]. Finally, the system is cooled by a water-cooling system.

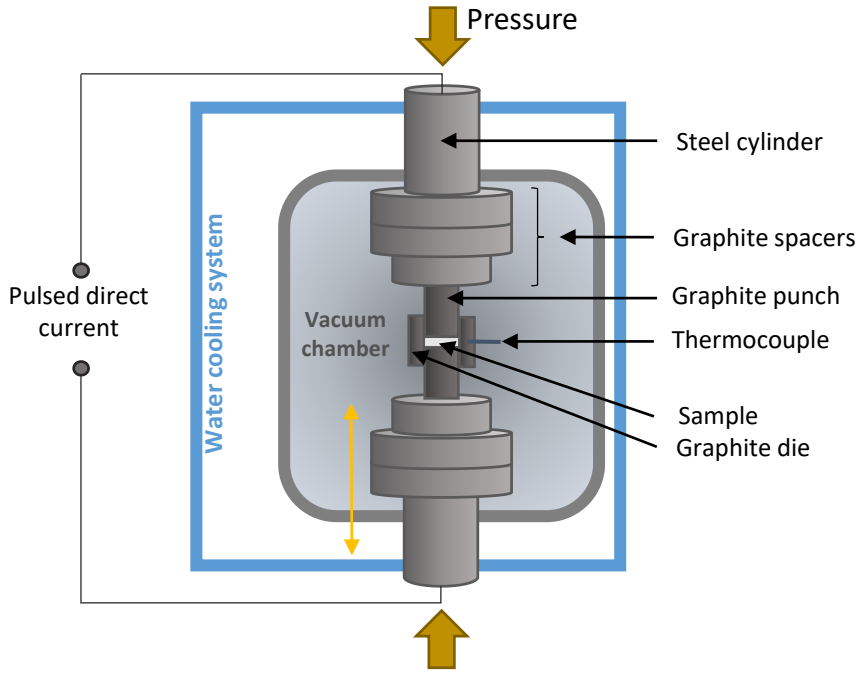

Figure IV-1: Schematic of SPS system. Reproduced and adapted from Y.Le Godec et al. [243]

The sintering mechanism occurring during the process is composed of several steps, including the formation of spark, followed by plasma between the powder particles, and finally by Joules heating[246]. However, the formation of plasma is still debated in the literature[246,247]. In the case of $LATP_{0.3}$, which is an electrical insulator, densification is achieved through rapid heating of the die via the Joule effect.

Several parameters can be modified to optimise the sintering process by SPS, including the temperature[118,195], holding time, heating rate[119], applied pressure, or atmosphere[244].

IV.2. Screening of the impact of additives on the densification of $LATP_{0.3}$

The aim of this section is to study the impact of additives on the densification processes of $LATP_{0.3}$ at high temperature, using SPS. Therefore, before investigating the eutectic salt mixtures such as Eut1 ($LiPO_3$-Li_3PO_4), Eut2 ($LiPO_3$-$Li_4P_2O_7$), and Eut2M ($LiPO_3$-$Li_4P_2O_7$ melted), we examined the constituent salts, namely Li_3PO_4, $Li_4P_2O_7$, and $LiPO_3$, to extract their characteristic fingerprint in the $LATP_{0.3}$ densification processes.

IV.2.1. Method

To achieve this, a mixture was prepared for each type of salt, with a fixed additive percentage of 5 wt% added to $LATP_{0.3}$. Each mixture was manually ground using a mortar and then placed in a ø15 mm graphite die. Unlike conventional sintering, determining the initial relative densities is not possible, as the pellet only forms when the experiment begins. Thus, pure $LATP_{0.3}$ samples were also sintered using SPS to determine the impact of additive on the densification of $LATP_{0.3}$. Given that several parameters can be modified to optimise the densification processes in SPS, we initially fixed a common program, shown in Figure IV-2, for all these experiments. The program involves applying pressure up to 50 MPa (0.9 tons), a standard value reported in the literature[195,248], during the first two minutes while maintaining room temperature. This step is followed by heating up to 900 °C with a heating rate of 50 °C/min. Unlike what is commonly done in the literature, this ramp rate is slower to allow the lithium salt to melt at its melting temperature. This temperature is maintained for 1 min, and the applied pressure is kept constant up to this stage. Cooling is performed more rapidly, and the pressure is released until the end of the experiment. All the experiment was conducted under primary vacuum. At the end, the pellets were collected and polished to remove the Papyex®.

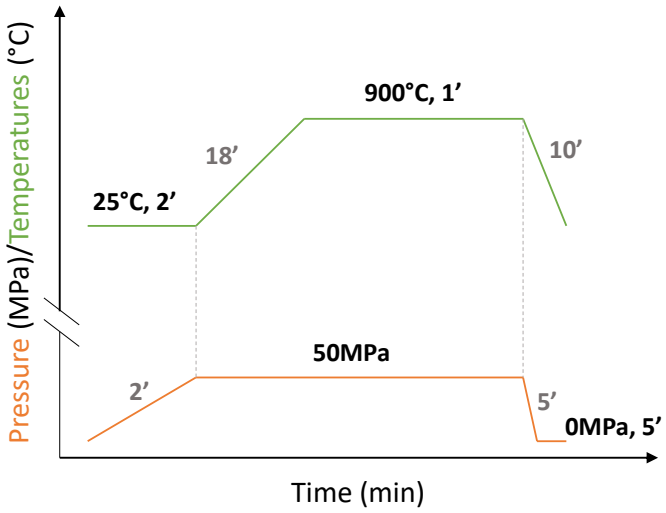

Figure IV-2: Program used for SPS experiments in Section IV.2. The green line represents the temperature parameter, and the orange line corresponds to the pressure parameter.

IV.2.2. Densification of pure $LATP_{0.3}$

First, the experiment was conducted on pure $LATP_{0.3}$ powder synthesised by solid-state reaction (Chapter II). As a reminder, the densification of the pellet is monitored by the displacement of the lower piston, as the pressure must be maintained at 50 MPa during the experiment. Thus, the displacement as a function of temperature for a pure $LATP_{0.3}$ pellet is presented in Figure IV-3. Densification of $LATP_{0.3}$ begins at 500 °C and continues up to 900 °C, as also observed by the derivative of this curve. A plateau is reached at 850 °C, highlighting that the densification process can be achieved by staying at this temperature for a longer duration. The final relative density is around 97.6 %, which is comparable to values reported in the literature for this temperature range[118,121,195,249]. This value is significantly higher than what is achieved through conventional sintering, but the powder, initially white, emerged as a blue pellet after polishing (Figure IV-3). This is caused by the partial reduction of Ti^{4+} to Ti^{3+} due to the applied electric current and contact with graphite paper during the experiment. This reduction occurs when the thermal treatment temperature exceeds 800 °C[188], indicating the need to either decrease the temperature or increase the heating rate[119]. Moreover, post-SPS heat treatments under oxygen are often performed, which leads to the re-oxidation of Ti^{3+} to Ti^{4+}.

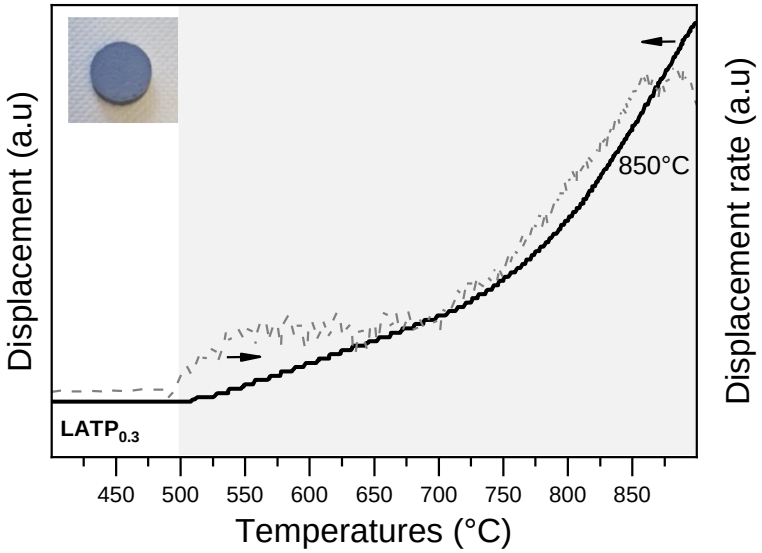

Figure IV-3: Displacement of the lower piston as a function of temperature for a pure $LATP_{0.3}$ powder. The first derivative of this curve is also presented, representing the displacement rate as a function of temperature. A picture of the pellet after SPS and after polishing is displayed. The pellet exhibits a relative density of 97.6 %. The heat treatment was conducted up to 900 °C, with a heating ramp of 50 °C/min, under primary vacuum. The grey zone represents the temperature range during which densification occurs.

IV.2.3. Contribution of $Li_4P_2O_7$, Li_3PO_4 and $LiPO_3$ on densification of $LATP_{0.3}$

Next, the samples were prepared from a mixture of $LATP_{0.3}$ and simple salts such as Li_3PO_4, $LiPO_3$, and $Li_4P_2O_7$. Each mixture consists of 5 wt% lithium salt and 95 wt% $LATP_{0.3}$, with a total powder mass of 2 g. All the pellets turned in blue at the end of the heat treatment as presented in Figure IV-3.

The results obtained for a powder consisting of 5 wt% $Li_4P_2O_7$ are presented in Figure IV-4-a. The temperature at which densification begins is the same as in the case of pure $LATP_{0.3}$, (~500°C), but the curve corresponding to the displacement rate shows a maximum that is reached at 783 °C. This temperature may correspond to the melting temperature of the $Li_4P_2O_7$-LATP mixture (Chapter III), considering there may be discrepancies between the temperature sensed by the thermocouple and the actual temperature of the sample. The curve representing the piston displacement as a function of temperature reaches a plateau at 800 °C, suggesting that all the porosity has been removed at this temperature. However, the observed temperatures may differ from the actual temperatures experienced by the sample due to the rapid heating rate. Next, in the case of a mixture of Li_3PO_4 and $LATP_{0.3}$ (Figure IV-4-b), the temperature at which densification begins is higher than for the mixture with $Li_4P_2O_7$ or pure $LATP_{0.3}$. However, the derivative shows that the maximum densification rate occurs at 720 °C, which is lower than with the addition of $Li_4P_2O_7$. This suggests the melting of a species present at this temperature, which is not Li_3PO_4, but rather $Li_4P_2O_7$ formed by the reactivity of Li_3PO_4 with $LATP_{0.3}$.

Although this reactivity mechanism was revealed through our various studies, we made the hypothesis that applying a heating ramp 10 times faster than conventional sintering would limit this chemical reactivity.

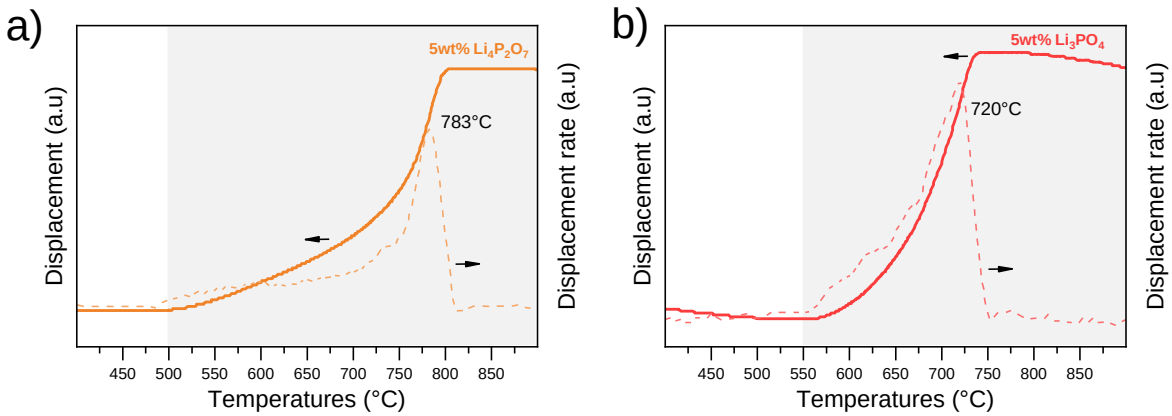

Figure IV-4: Displacement of the lower piston as a function of temperature for (a) $LATP_{0.3}$ + 5 wt% $Li_4P_2O_7$ and (b) $LATP_{0.3}$ + 5 wt% Li_3PO_4. The first derivative of the curves is also presented, in dashed line, representing the displacement rate as a function of temperature. The heat treatment was conducted up to 900 °C, with a heating ramp of 50 °C/min, under primary vacuum. The grey zones represent the temperature range during which densification occurs.

Finally, the results obtained for the powder composed of 5 wt% $LiPO_3$ are presented in Figure IV-5. The temperature at which densification begins is around 550 °C, which is similar to the addition of Li_3PO_4. An initial phenomenon is observed on the curve representing the piston displacement around 600-650 °C. By examining the derivative, this phenomenon is due to a faster densification kinetics in this temperature range, with a peak at 612 °C. This temperature range corresponds to the melting of $LiPO_3$, which is approximately 650 °C. This initial observation indicates that by applying pressure during the thermal treatment, it is possible to facilitate the initial stage of liquid-phase sintering, specifically the rearrangement of particles. Unlike the addition of Li_3PO_4 and $Li_4P_2O_7$, a second densification process occurs after the melting of $LiPO_3$, with a maximum at 850 °C. This suggests that the melting of $LiPO_3$ was insufficient to densify the $LATP_{0.3}$ fully, leading us to make the hypothesis that the second stage is governed by a solid-state densification mechanism.

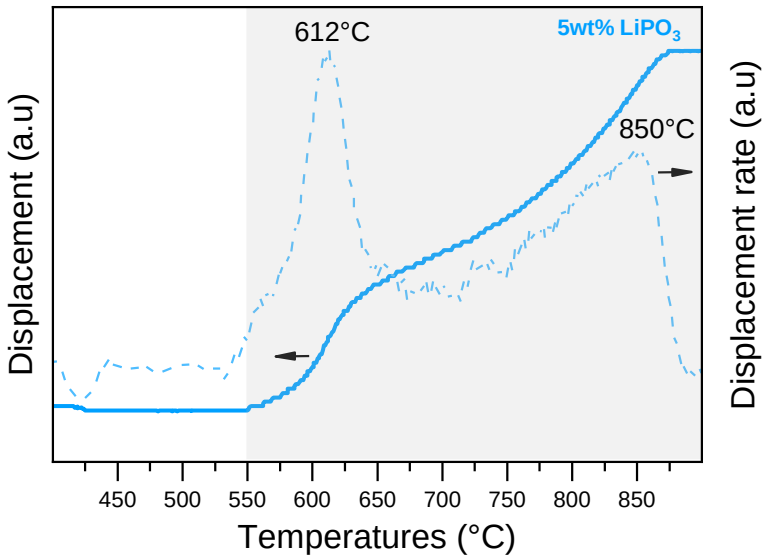

Figure IV-5: Displacement of the lower piston as a function of temperature for $LATP_{0.3}$ + 5 wt% $LiPO_3$. The first derivative of the curves is also presented in dashed line, representing the displacement rate as a function of temperature. The heat treatment was conducted up to 900 °C, with a heating ramp of 50 °C/min, under primary vacuum. The grey zones represent the temperature range during which densification occurs.

Now that the contributions of each lithium salt to the densification process of $LATP_{0.3}$ by SPS have been identified, the contribution of adding the eutectic mixtures Eut1, Eut2, and Eut2M will be discussed in the next section.

IV.2.4. Contribution of Eut1, Eut2 and Eut2M on densification of $LATP_{0.3}$

As with the addition of simple salts, the salt mixtures were added to $LATP_{0.3}$ at 5 wt% for a total powder mass of 2 g. All results are presented in Figure IV-6 and all the pellets turned blue at the end of the heat treatment. First, the behaviour of the piston displacement as a function of temperature for each sample is compared in Figure IV-6-a: the temperatures at which densification begins are similar for Eut1 and Eut2, with temperatures ranging between 515 and 550 °C. For Eut2M, densification starts earlier, at around 400 °C. Multiple phenomena are observed for each curve, leading to a final plateau at 800 °C for Eut1 and Eut2M, and 850 °C for Eut2.

These phenomena are explained by analysing the first derivative of each curve: for the sample containing Eut1 (Figure IV-6-b), two contributions are observed at 608 °C and 741 °C. Each contribution is identified by comparing them to those obtained with the addition of simple salts. The signal at 608 °C corresponds to the melting of $LiPO_3$, while the signal at 741 °C corresponds to $Li_4P_2O_7$ formed by the reaction of Li_3PO_4 with $LATP_{0.3}$. The amount of $Li_4P_2O_7$ formed is not the same as in the case of the addition of pure Li_3PO_4, leading to a slight difference

in temperature. This underscores once again the importance of the amount of $Li_4P_2O_7$ added/formed. The same pattern is observed for the mixture consisting of Eut2 (Figure IV-6): two contributions are observed at 592 °C and 779 °C, corresponding to the melting of $LiPO_3$ and $Li_4P_2O_7$, respectively. Just as observed in conventional sintering, adding a mixture of salts which is not perfectly homogeneous, does not allow melting at the temperature of the eutectic composition. This is even more significant, as no contribution at the eutectic melting temperature is observed. Given the discrepancies between the melting temperatures of the salts and those observed, the contribution of the eutectic should appear around 550°C-570 °C.

Finally, the derivative of Eut2M shows three contributions: one at 466 °C, another at 550 °C, and the last at 760 °C. We can make the hypothesis that the signal at 760 °C corresponds to the melting of $Li_4P_2O_7$, the one at 550 °C to the melting of the eutectic mixture, but the last signal remains unidentified. Although we do not know exactly why densification occurs at a lower temperature in the case of Eut2M, especially at 466 °C, this mixture seems more promising compared to the other two.

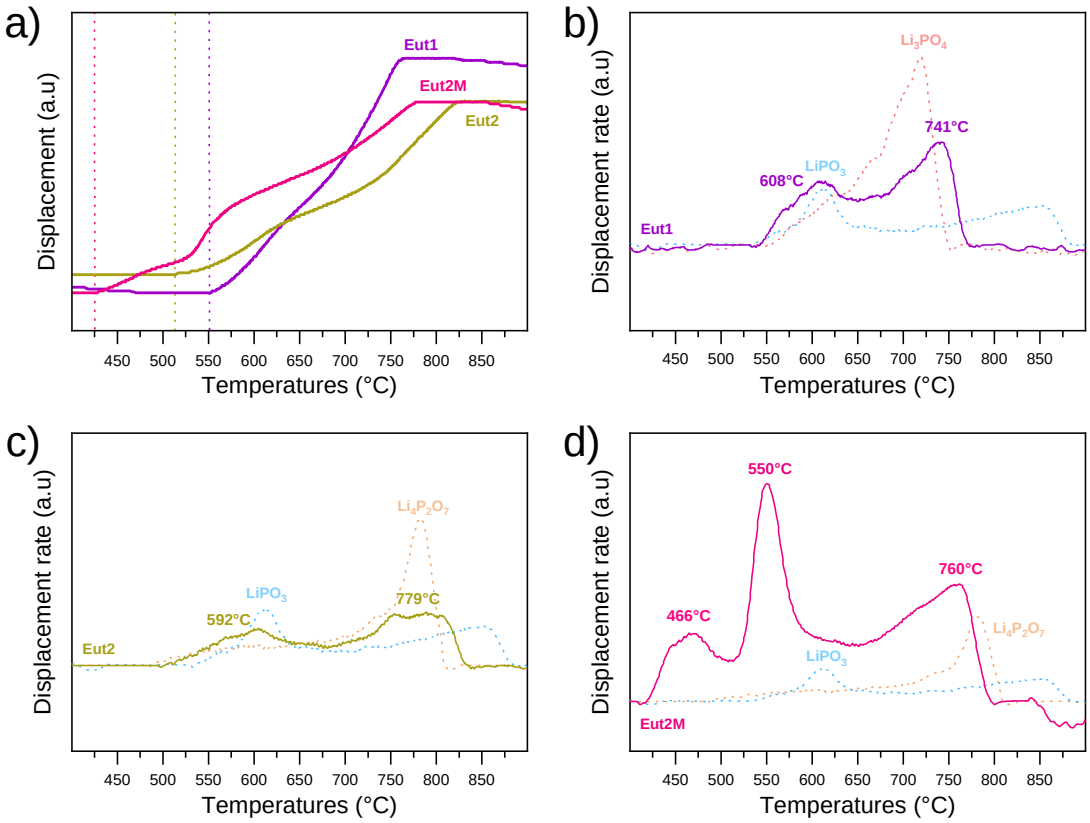

Figure IV-6: (a) Displacement of the lower piston as a function of temperature for $LATP_{0.3}$ + 5 wt% Eut1 (—), $LATP_{0.3}$ + 5 wt% Eut2 (—) and $LATP_{0.3}$ + 5 wt% Eut2M (—). The dashed lines represent the temperature range during which densification occurs. The first derivative of the curves is also presented for (b) $LATP_{0.3}$ + 5 wt% Eut1, (c) $LATP_{0.3}$ + 5 wt% Eut2 and (d) $LATP_{0.3}$ + 5 wt% Eut2M. The heat treatment was conducted up to 900 °C, with a heating ramp of 50 °C/min, under primary vacuum.

IV.2.5. Phases purity

All the pellets were broken, and a portion was ground in a mortar for XRD analysis in order to check chemical reactivity. The scans presented in Figure IV-7 were acquired in the range 2θ = 10-80 °, with 0.02 ° steps and a time of 0.2 s/step. Due to the difficulty in grinding the pellets, only small quantities of powder were obtained. As a result, special silicon-based supports were used for the analyses, but this tends to amplify the noise in the measurements. The main diffraction peaks of $LATP_{0.3}$ are identified for all the samples. Moreover, the main peak of $Li_4P_2O_7$ at 20.4 ° is identified for the samples consisting 5 wt% of $Li_4P_2O_7$, Li_3PO_4 and Eut2. It confirms that Li_3PO_4 reacted to form $Li_4P_2O_7$, even in these experimental conditions (fast heating and reducing atmosphere). However, no traces of $LiPO_3$ are detected in samples consisting of 5 wt% of $LiPO_3$, Eut1 and Eut2. Even prior to SPS, the $LiPO_3$ was not observed, indicating that the quantity added is insufficient for detection via XRD. The sample with Eut2M is not presented as the mixture of salts is amorphous (see Figure II-5-b), meaning that only $LATP_{0.3}$ is visible.

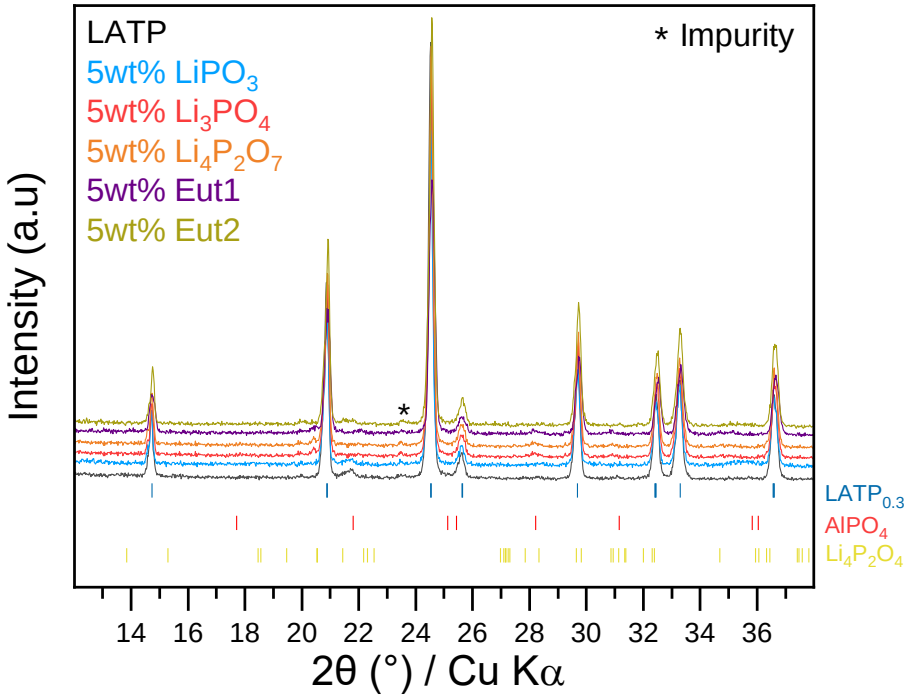

Figure IV-7: XRD patterns of $LATP_{0.3}$ and mixtures of $LATP_{0.3}$ and 5wt% of $LiPO_3$, Li_3PO_4, $Li_4P_2O_7$, Eut1 and Eut2 after SPS at 900 °C during 1 min, with a heating ramp of 50 °C/min.

Finally, it is noteworthy that $AlPO_4$ is only detectable in the pure $LATP_{0.3}$ and $LATP_{0.3}$ + 5wt% $LiPO_3$ samples. Its absence in other systems can likely be attributed to the solubilisation of the phase when the salt melts. Further characterization is necessary to confirm this hypothesis.

IV.2.6. Impact of the additives on the densification

Finally, the relative densities of the pellets are discussed. They were determined based on the Archimedes principle, rather than geometric measurements, due to the high density of the obtained pellets. The theoretical, calculated densities and the relative densities of each pellets are presented in Table 8.

Samples	Theoretical density ($g.cm^{-1}$)	Calculated density ($g.cm^{-1}$)	Relative density (%)
Pure $LATP_{0.3}$	2.92	2.85	**97.6**
5wt% $Li_4P_2O_7$	2.88	2.86	**99.2**
5wt% Li_3PO_4	2.90	2.84	**98.0**
5wt% $LiPO_3$	2.89	2.74	**94.6**
5wt% Eut1	2.91	2.86	**97.9**
5wt% Eut2	2.89	2.83	**97.9**
5wt% Eut2M	2.89	2.82	**97.4**

Table 8: Theoretical and calculated densities for all samples. The relative densities determined after SPS at 900 °C are also presented.

At 900 °C, the pure $LATP_{0.3}$ pellet is already very dense (> 95 %), similar to all the pellets with additives. This indicates that the contribution of the salt is negligible, as SPS already significantly improves the densification of pure $LATP_{0.3}$ at this temperature. However, differences can be made by applying lower thermal treatment temperatures. Indeed, this first part has shown us at which temperatures the salts contribute to the densification of $LATP_{0.3}$. Thus, we focused particularly on the Eut2M additive, as densification processes begin at lower temperatures (~450 °C) compared to other samples. Similar to the pure LATP pellet, the initially white powders turned blue at the end of the treatment at 900 °C. Therefore, the addition of Eut2M could address the reduction problem by combining low temperature (< 800 °C) with high density.

IV.3. Optimization of parameters applied in SPS to improve $LATP_{0.3}$ densification with additive at lower temperatures

Based on the results from the previous section, we observed that the contribution of Li-salts to improve the densification of $LATP_{0.3}$ is negligible at 900 °C, as SPS already achieved densification above 95 %. In this section, the objective is to decrease the temperature applied during SPS to study the impact of Li-salts on densification. To this end, we focused on the Eut2M mixture, where densification occurs at temperatures below 750 °C (Figure IV-6-c). The parameters of temperature and the duration of the hold time at this temperature will be studied. Samples that demonstrate the best performance in terms of relative densities and microstructures will ultimately be analysed through impedance measurement.

IV.3.1. Impact of the parameters during SPS on the microstructure of $LATP_{0.3}$

The SPS program applied in the previous section (see Figure IV-2) was slightly modified so that the applied temperature is no longer 900 °C but 650 °C. This temperature was selected to account for the contribution of the eutectic mixture's melting. According to Figure IV-6-c, the Eut2M mixture also contributes to the densification process beyond 650 °C, but we make the hypothesis that contributions at lower temperatures will enable better densification compared to pure $LATP_{0.3}$. To confirm or refute this hypothesis, a $LATP_{0.3}$ powder was thermally treated by SPS according to this new program, along with a powder containing 5 wt% of Eut2M.

The displacement curves obtained for the two samples are presented in Figure IV-8-a. Initially, we can observe that the curves do not show significant change until 480 °C, which is the temperature range at which densification begins in both cases. From 530 °C onwards, the two curves evolve differently, as two densification phenomena occur in the temperature ranges of 530-570 °C (**zone 1**) and 570-630 °C (**zone 2**) in the case of the Eut2M addition. These two phenomena do not appear in the case of pure $LATP_{0.3}$, as the displacement curve remains linear from 480 °C until the end of the experiment.

By observing the derivative of the curve for the sample containing Eut2M (Figure IV-8-b), these two densification phenomena correspond to two peak temperatures at 544 °C and 585 °C. Surprisingly, these two temperatures do not correspond to those obtained during the SPS thermal treatment at 900 °C for the same sample (Figure IV-6-d). Based on the observed temperatures, the contribution at 544 °C may be due to the melting of the eutectic mixture, whereas the one at 585 °C corresponds to the melting of $LiPO_3$. This highlights that even though the eutectic mixture of salts was melted before being added to the $LATP_{0.3}$, the homogenisation

of the mixture is not sufficient during SPS for the entire mixture to melt at the eutectic melting temperature. Additionally, differences in melting temperatures are observed for the same sample, indicating a problem of repeatability, which we have not addressed yet.

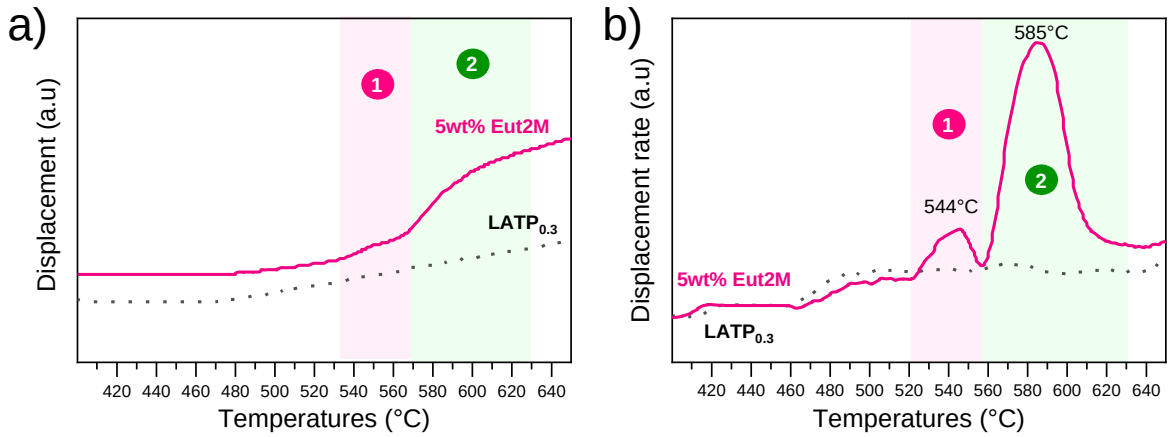

Figure IV-8: (a) Displacement of the lower piston as a function of temperature for $LATP_{0.3}$ + 5 wt% Eut1 (- - -) and $LATP_{0.3}$ + 5 wt% Eut2M (—). (b) The first derivative of the curves is also presented for these two samples. The heat treatment was conducted up to 650 °C, with a heating ramp of 50 °C/min, under primary vacuum.

Nevertheless, when comparing the obtained relative densities, i.e. 79.9 % for pure $LATP_{0.3}$ and 88.3 % for the mixture with 5wt % of Eut2M, the densification is better at 650 °C in the case of the Eut2M addition. Another way to visualize this improvement in terms of densification is by examining the microstructure of the two pellets using Scanning Electron Microscopy (SEM). For this purpose, the pellets were fractured in half to visualise a cross-sectional slice. Figure IV-9-a and Figure IV-9-b show the results for the pure $LATP_{0.3}$ pellet and the pellet with the Eut2M mixture, respectively. Visually, the size of most particles is similar across samples. However, aggregates composed of smaller particles are visible in the pure $LATP_{0.3}$ sample, suggesting less advanced densification. This difference, which is more pronounced macroscopically, may explain the observed variation in relative densities between the two samples.

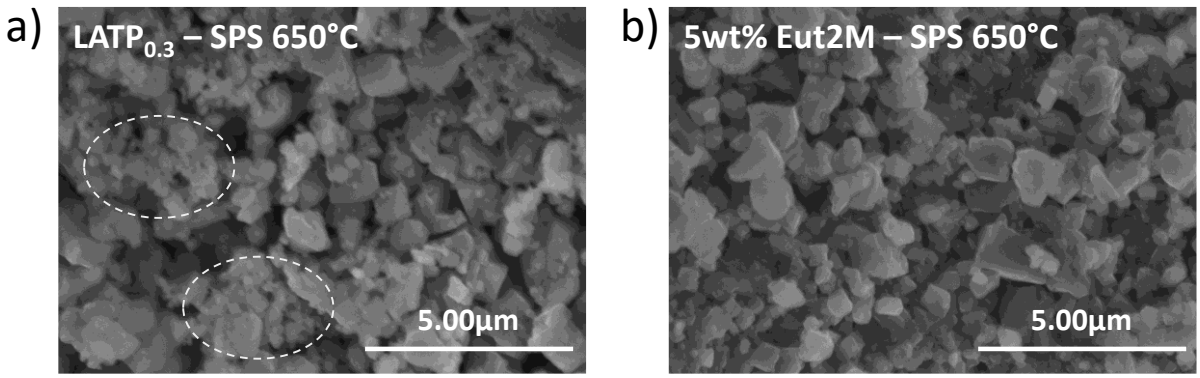

Figure IV-9: SEM images of (a) pure $LATP_{0.3}$ pellet and (b) pellet with 5 wt% Eut2M mixture after a heat treatment by SPS at 650 °C, for 1 min, with a heating ramp of 50 °C/min. The pellets were fractured in half to visualize a cross-sectional slice. The dotted circles indicate the aggregates of small particles observed in the pure $LATP_{0.3}$ pellet.

Given that the relative density is close to 90 % at 650 °C but does not exceed it, we tested the same powder in SPS using the same program but increasing the temperature to 700 °C instead of 650 °C. This 50 °C increase, combined with the addition of 5 wt% Eut2M, resulted in achieving a relative density of 93.4 %. In parallel, we also tested extending the dwell time at 650 °C to 10 minutes instead of 1 minute for a powder of the same composition. Similar to the effect of a 50 °C increase, the relative density obtained for this sample is 94.2 %.

The microstructures were also studied for these two samples, as with the samples treated at 650 °C for 1 minute. The SEM images presented in Figure IV-10-a and Figure IV-10-b show a similar microstructure whether achieved by increasing the temperature or extending the dwell time. Compared to Figure IV-9, no increase in particle size is observed; instead, a change in particle morphology from spherical to cubic and a fusion of particles with each other are noted. These morphologies (Figure IV-10-a and Figure IV-10-b) were compare to those of a pure $LATP_{0.3}$ pellet sintered by SPS at 900 °C (Figure IV-10-c). We observe that the particles in the mixture's samples are slightly smaller than those in pure $LATP_{0.3}$ sample, which can be attributed to a modest difference in relative density, around 3-4%. These SEM images indicate that densification has been effectively improved at lower temperatures with the addition of Eut2M.

It is noted that the microstructure of the pure $LATP_{0.3}$ pellet obtained by SPS is similar to that obtained by conventional sintering for the same temperature of heat treatment (Figure IV-10-d). However, the relative densities are smaller is the latter case (~90 %), suggesting that larger grains are expected at higher value of relative densities for the $LATP_{0.3}$ pellets conventionally sintered.

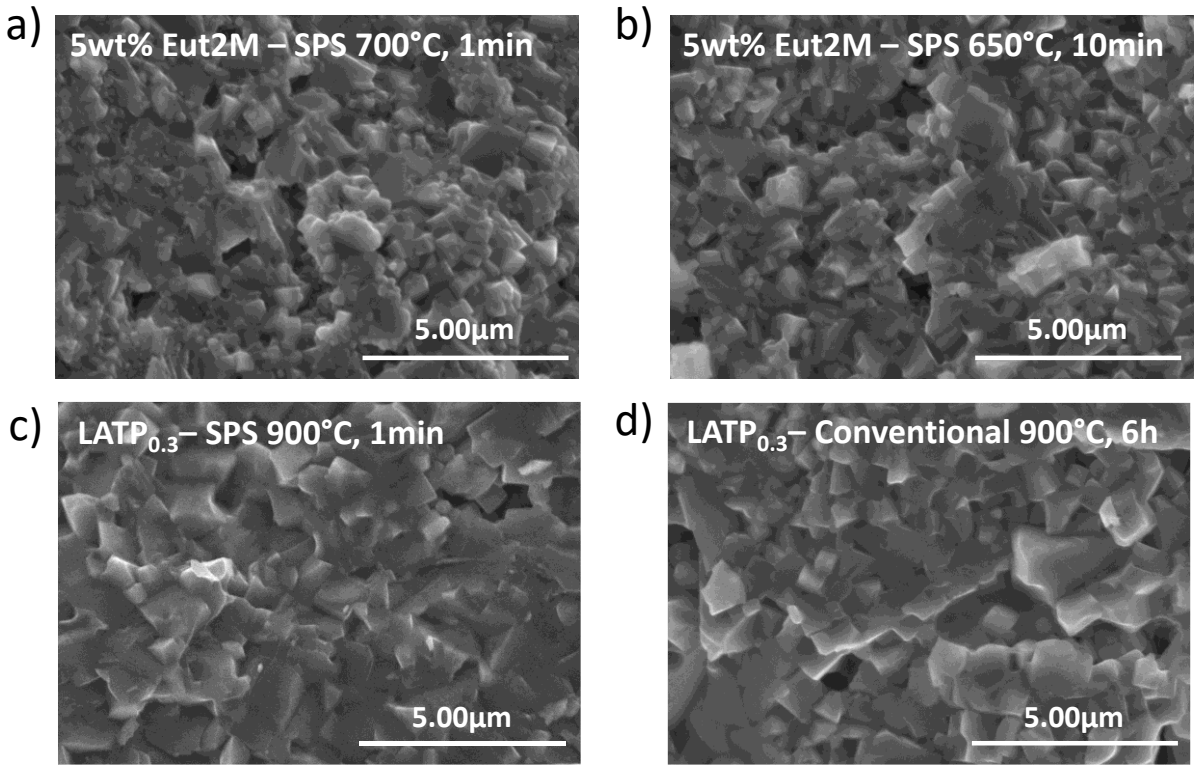

Figure IV-10: SEM images of (a) pellet with 5 wt% Eut2M mixture treated at 700 °C for 1 min; (b) pellet with 5 wt% Eut2M mixture treated at 650 °C for 10 min; (c) $LATP_{0.3}$ pellet treated at 900 °C for 1 min by SPS; and (d) $LATP_{0.3}$ pellet treated at 900 °C for hours by conventional sintering process. The pellets were fractured in half to visualise a cross-sectional slice.

The relative densities obtained in this section are summarised in Table 9. From both a density and microstructural perspective, two samples stand out: the one treated at 700 °C for 1 minute and the one treated at 650 °C for 10 minutes. Indeed, the relative density values corresponding are of the same order of magnitude as those obtained after heat treatment at 900 °C (Table 8), which is promising.

Samples	Methods	Relative density (%)
Pure $LATP_{0.3}$	650 °C, 1 min	**79.9**
5 wt% Eut2M	650 °C, 1 min	**88.3**
5 wt% Eut2M	700 °C, 1 min	**93.4**
5 wt% Eut2M	650 °C, 10 min	**94.2**

Table 9: Summary of samples, methods, and relative densities obtained after SPS.

A final point concerns the colour of the pellets depending on the applied temperature and the duration of the SPS program. As observed in Figure IV-11, the pellets remain white after heat treatment at 650 °C for 1 minute. Some grey/black traces are visible, corresponding to residual graphite. However, extending the duration at 650 °C results in the pellet turning various shades of blue. Similarly, increasing the temperature to 700 °C also causes the pellet to turn blue. In

contrast to a pellet treated at 900 °C (Figure IV-3), the blue obtained at these lower temperatures is lighter, indicating that the reduction of titanium is limited.

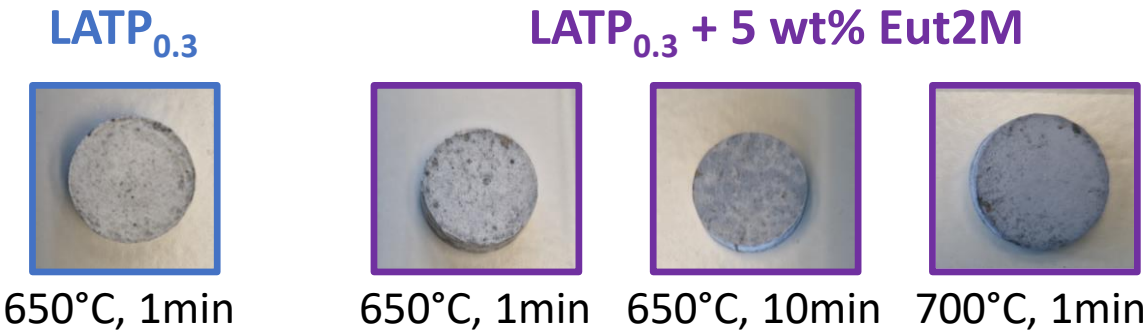

Figure IV-11: Colour variation of $LATP_{0.3}$ and $LATP_{0.3}$ + 5wt% Eut2M based on SPS program parameters.

As explained previously, this colour modification result on the partial reduction of Ti^{4+} to Ti^{3+} of LATP. A study of Courbaron et al.[119] performed a heat treatment at 700 °C during 12 hours under O_2 on LATP pellets in order to re-oxide the material. According to this study, this program would re-oxide all the Ti^{3+} formed. In our case, applying a heat treatment at a temperature higher than the salt's melting point would re-sinter the pellet, potentially altering its density and microstructure. To avoid this, the two pellets treated at 650 °C for 10 minutes and at 700 °C for 1 minute will be analysed by impedance as they are.

IV.3.2. Ionic conductivity properties of $LATP_{0.3}$ with additives

Finally, impedance measurements (EIS) were performed on the pellets composed of 5 wt% Eut2M treated at 750 °C for 1 minute and at 650 °C for 10 minutes without post-treatment under air conditions. The Nyquist Plots obtained for pure $LATP_{0.3}$ and for the mixtures are presented in Figure IV-12, respectively. As a reminder, the right intercept of the semi-circle with the Z' axis at low frequencies corresponds to the total resistivity of the system. Each impedance data point was normalised to the thickness and surface area of the respective pellets. The data in Figure IV-12 show a single semi-circle for the sample treated at 650 °C for 10 minutes, whereas two semi-circles are observed for the sample treated at 700 °C for 1 minute. These two semi-circles correspond to the contributions from the bulk (grains) and the grain boundaries to the total resistance of the system. The Nyquist plots were fitted with two circuits: The Debye equivalent circuit and the modified one. The Figure IV-12-a shows the fits using the Debye equivalent circuit. This model works well for the sample treated at 650 °C for 10 minutes ($\chi^2 = 10^{-4}$), but it is less effective for the other sample, as it does not account for the small semi-circle observed at high frequencies. The EIS points for the sample treated at 700 °C are well fit using

the second model (χ^2 = 10^{-4}), which consists of two resistances and two capacitances. In contrast, this model performs less effectively for the sample treated at 650 °C for 10 minutes as it does not account to the part at low frequencies.

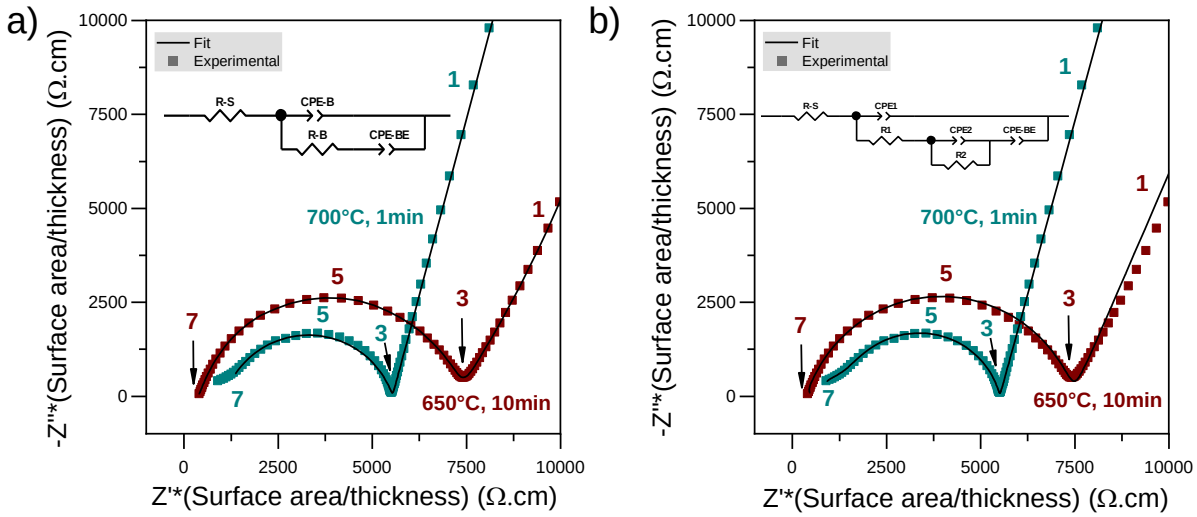

Figure IV-12: The Nyquist plots at 25 °C of the pellet with 5 wt% Eut2M mixture treated at 700 °C for 1 min (■) and the pellet with 5 wt% Eut2M mixture treated at 650 °C for 10 min (■). The EIS data were fitted with (a) the Debye equivalent circuit and (b) a modified Debye equivalent circuit. The numbers on the data indicate the power of frequency.

Based on the total resistance determined, the total conductivity is 1.10^{-4} S.cm^{-1} for the sample treated at 650 °C for 10 min and 2.10^{-4} S.cm^{-1} for the sample treated at 700 °C for 1 min, which are of the same order of magnitude. In comparison, the same order of magnitude in terms of ionic conductivity was obtained for LATP sintered at 900 °C by SPS in the literature[121,195]. However, the microstructure of the pellets consists predominantly of small grains (see Figure IV-10). The presence of numerous small grains can adversely affect the conductive properties, as a higher number of grain boundaries generally increases the overall resistance of the system[128]. The semi-circle at middle frequencies observed for the sample treated at 700 °C could be attributed to either an excessive number of grain boundaries or the presence of salts at the grain boundaries. Given that the microstructures are similar and the same percentage of salts is used for both samples, it is likely that the initial mixture was less homogeneous in the case of the sample treated at 700 °C.

Unlike in the previous chapters, the presence of Ti^{3+} indicates that the measured conductivity is not purely ionic but represents the sum of both ionic and electronic conductivity in the system. Further analyses on pellets with the same composition are necessary to ensure result reproducibility. Additionally, these pellets should be treated in air to specifically study the ionic conductivity of such systems.

V. Conclusion of Chapter IV

In this chapter, we studied salt mixtures that do not react and have eutectic melting temperatures around 600 °C, aiming to enhance the densification of $LATP_{0.3}$ at lower temperatures.

The challenge with using a salt mixture to melt at the eutectic temperature is ensuring that the contact between salt particles is more intimate than the contact between the salt particles and $LATP_{0.3}$. Two mixtures were studied, namely Eut1 (0.86 $LiPO_3$ – 0.14 Li_3PO_4) and Eut2 (0.845 $LiPO_3$ – 0.155 $Li_4P_2O_7$). We successfully addressed the challenge only for Eut2, which was pre-formed by melting and quenching. Therefore, Eut2 was selected for further investigation into its contribution to densification phenomena.

To this end, we considered two sintering methods: conventional sintering and Spark Plasma Sintering (SPS).

In the first case, the addition of Eut2 melted did not improve densification at lower temperatures due to the low ability of one of the salts in the mixture, $LiPO_3$, to densify $LATP_{0.3}$. We made the hypothesis that this was due to the low wettability of $LiPO_3$, which make the initial stage of liquid-phase sintering difficult.

In the case of SPS, this issue was partially resolved due to the constant application of pressure during the thermal treatment and the fast heating. Thus, by adjusting the temperature and the duration of its application, we were able to achieve relative densities exceeding 90% for pellets containing 5 wt% Eut2 melted treated at 650 °C for 10 minutes or 700 °C for 1 minute. Although further experiments are needed to confirm reproducibility, these results are promising, demonstrating that densification can occur at temperatures below 700°C. However, the properties related to conductivity require more thorough characterization. Currently, the total conductivities measured represent the combined ionic and electronic conductivities, as indicated by the coloration of the pellets, which suggests the presence of Ti^{3+}.

General conclusion and perspectives

In this study, strategies for improving the densification of LATP at lower temperatures were explored with the aim of making its use compatible with all-solid-state batteries. Several approaches were investigated, including particle size reduction, the use of Li-salts as sintering aids, and their combination with specific sintering techniques.

The first approach demonstrated the impact of particle size on $LATP_{0.3}$ sintering. The densification processes of two powders with significantly different primary particle sizes (nano and micron-scale) were compared. This comparison highlighted that decreasing particle size had a beneficial effect on sintering. Indeed, this size reduction accelerates the mechanisms occurring during sintering and lowers the sintering temperature from 950 °C (micron-sized particles) to 780 °C (nano-sized particles). Next, the impact of secondary particle size was investigated. Two micron-sized distributions were successfully obtained via spray drying. The spray drying synthesis method was adapted from the literature for this purpose but remains relatively rare in the case of $LATP_{0.3}$[169]. The key advantage of this method is that it combines the benefits of soft chemistry synthesis with the production of spherical particles[75]. The highest relative density was achieved with the smallest size distribution obtained (D50 = 4 µm), reaching 90 % after a heat treatment at 900 °C for 6h. This resulted in ionic conductivity of approximately 10^{-4} S/cm at room temperature. While this strategy improved densification, it was not sufficient to achieve even lower sintering temperatures, necessitating the exploration of other techniques.

For the second approach, we investigated the addition of Li-salts as sintering aids. Unlike other techniques used in the literature, this method does not require expensive equipment and allows for the densification of $LATP_{0.3}$ within a temperature range between 800 °C and 900 °C, while ensuring sufficient ionic conductivity at room temperature[143]. The origin of this improvement at lower temperatures was therefore studied. We started from the hypothesis that the chemical reactivity between $LATP_{0.3}$ and Li-salts plays a role in densification, as the formation of the same impurities was systematically observed at the end of sintering. The first section of this second part focused on determining the reactivity mechanism between $LATP_{0.3}$ and Li-salts. To do this, equimolar mixtures of Li-salts and $LATP_{0.3}$ were studied to maximise reactivity and better observe the reactions occurring at the interfaces. By combining several characterisation methods, we proposed a mechanism with two main reactivity steps.

1. The first step is the reaction of the initially added lithium salt with $LATP_{0.3}$. The temperature ranges at which this step occurs depends on the specific $LATP_{0.3}$-lithium salt system studied. Other factors impact the kinetics of this reaction, such as the decomposition of the salt at elevated temperatures or its melting temperature. This step leads to the formation of two new compounds, Li_3PO_4 and TiO_2, which were observed in the temperature range between 400 °C and 700 °C.
2. The second step occurs around 800 °C and is triggered by the reaction of Li_3PO_4, TiO_2, and $AlPO_4$ with $LATP_{0.3}$. It leads to the formation of $LiTiOPO_4$ and $Li_4P_2O_7$, along with another aluminium-based impurity that remains unidentified.

After generalising this mechanism with different Li-salts and confirming that it occurs even with small quantities of sintering aids, the relationship between reactivity and densification was highlighted. Indeed, we demonstrated that the origin of the successful densification of LATP at lower temperatures was due to the partial solubility of $LATP_{0.3}$ in $Li_4P_2O_7$ and the melting of this $LATP_{0.3}$-$Li_4P_2O_7$ mixture. The melting temperature of this mixture varies from 770 °C to 820 °C, depending on the amounts of $LATP_{0.3}$ and $Li_4P_2O_7$. It was also shown that directly adding $Li_4P_2O_7$ as the starting lithium salt was preferable, as it allowed for > 85 % relative density after a thermal treatment at 760 °C, while limiting the negative impact on ionic conductivity due to the formation of $LiTiOPO_4$. Microstructural analysis, however, revealed the presence of porosity, which can be adjusted by modifying the initial lithium salt particle size. By decreasing this particle size, we ultimately achieved a relative density greater than 85 % at 760 °C and an ionic conductivity of about 10^{-4} S/cm at room temperature with the addition of 5 wt% $Li_4P_2O_7$ to $LATP_{0.3}$. The originality of this work lies in the understanding of the densification mechanism involved when adding Li-salts. This insight is crucial because it allow us to conclude that the sintering temperature of $LATP_{0.3}$, when lithium salt that exhibit this reactivity are added, is controlled and limited by the melting temperature of the $LATP_{0.3}$-$Li_4P_2O_7$ mixture.

The third approach derives directly from the latter conclusions: we selected a eutectic mixture between $Li_4P_2O_7$ and $LiPO_3$ that does not react with LATP and reduces the melting temperature of $Li_4P_2O_7$. Two salt mixtures were prepared at this eutectic composition (0.86 $LiPO_3$ – 0.14 Li_3PO_4 and 0.845 $LiPO_3$ – 0.155 $Li_4P_2O_7$) and achieve melting temperatures around 600 °C[250]. One of the initial challenges was to successfully shape these mixtures to maximise homogeneity and maintain their eutectic composition, even in contact with $LATP_{0.3}$. This hurdle was successfully overcome for the 0.845 $LiPO_3$ – 0.155 $Li_4P_2O_7$ mixture through quenching, which

allowed to study its impact on the sintering of $LATP_{0.3}$. Conventional sintering with this eutectic mixture did not reduce the densification temperature of $LATP_{0.3}$. Indeed, the addition of a melting species does not necessarily lead to liquid-phase sintering, as the phase must be able to wet the particles, and the solid material must dissolve into the liquid[97]. To address this second challenge, we combined the addition of this salt mixture with Spark Plasma Sintering (SPS). The benefit of using this method in our case is that it applies pressure during thermal treatment, forcing the melting salt to effectively wet the particles. By varying the temperature parameters and dwell time, we ultimately achieved 94 % density in an $LATP_{0.3}$ pellet with 5 wt% salt after a thermal treatment at 650 °C for 10 minutes. The ionic conductivity obtained is on the order of 10^{-4} S/cm, although it includes a mix of ionic and electronic conductivity. Further efforts are required to verify the repeatability of these results and to ensure that the conductivity is purely ionic.

In summary, we successfully decreased the initial sintering temperature of $LATP_{0.3}$ from 1000-1100 °C, as reported in the literature, to 650 °C. This reduction was achieved progressively: first to 900 °C by modifying the particle size and morphology, then to 760 °C by adding 5 wt% $Li_4P_2O_7$, and finally to 650 °C by combining the addition of Li-salts with the SPS technique. To move forward, we could explore combining the first and third approaches (reducing particle size, adding Li-salts that melt at low temperatures, and employing SPS) to further lower the sintering temperature of $LATP_{0.3}$. Additionally, while Li-salts have been added by simple manual grinding so far, improving the final microstructure could be achieved by incorporating them using other methods. For instance, we could consider dissolving these Li-salts in a solution containing $LATP_{0.3}$ particles and atomizing them via Spray Drying to decrease salt particle agglomeration.

Overall, this doctoral work primarily focused on the densification of the solid electrolyte $LATP_{0.3}$. On one hand, it demonstrates that densification can be performed in temperature ranges which are compatible with certain active materials in the positive electrode of all-solid-state batteries[11]. This implies that significant efforts are required to integrate this strategy into the fabrication of composite positive electrodes. Specifically, it will be necessary to optimise the quantities of each component in the system and ensure that the addition of Li-salts does not degrade the active material or other compounds in the electrode (conductive additives, etc.). However, designing composite positive electrodes based on oxide solid electrolytes presents additional challenges. For example, these electrodes cannot accommodate the volume changes of active material particles, leading to stress and fractures within the solid electrolyte or,

conversely, loss of contact[251]. Moreover, when used as a separator, the solid electrolyte is in direct contact with Li metal, which limits the use of $LATP_{0.3}$ in its current form without a protective layer[252]. Nonetheless, this thesis work remains significant, as the strategies explored to decrease the sintering temperature can be applied to other materials, notably LLZO, which typically requires sintering greater than 1200 °C[112].

Appendix

A- $Li_4P_2O_7$ and $LiPO_3$ synthesis

The synthesis of $LiPO_3$ is based on the study by Bahman et al.[253] and involves dehydrating the compound LiH_2PO_4. This compound was placed in an aluminium crucible and then in a muffle furnace following this program: heating to 110 °C for 15 minutes with a ramp rate of 10 °C/min, followed by heating to 400 °C for 6 hours with a ramp rate of 5 °C/min. The cooling process was carried out by allowing the furnace to cool naturally. The powder was characterised by XRD. According the results in Appendix 1, the synthesised $LiPO_3$ is pure and it has a space group of *P*12/*n*1.

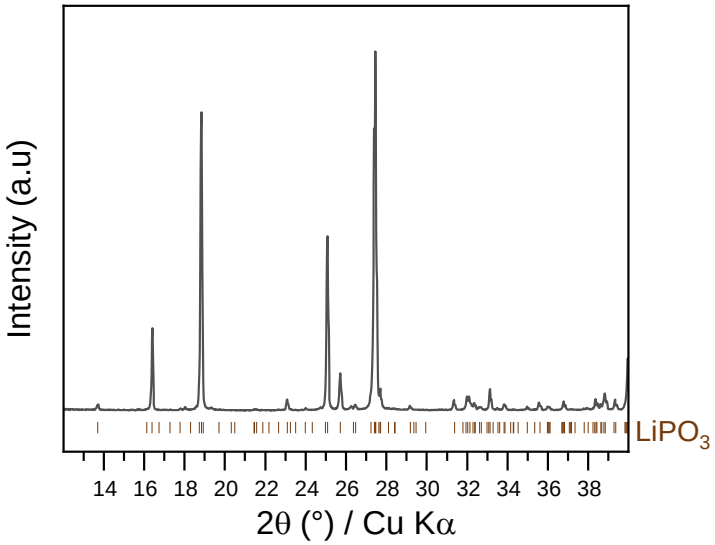

Appendix 1: XRD pattern of $LiPO_3$ powder acquired with standard conditions

$Li_4P_2O_7$ was synthesised by mixing equimolar amounts of $LiPO_3$ and Li_3PO_4 using a mortar. The mixture was then placed in an aluminium crucible and introduced into a muffle furnace. The powder was thermally treated at 750 °C for 1 hour, with a heating ramp rate of 2 °C/min. The cooling process was carried out by allowing the furnace to cool naturally. The powder was characterised by XRD and DTA analysis to confirm its nature and its melting temperature respectively.

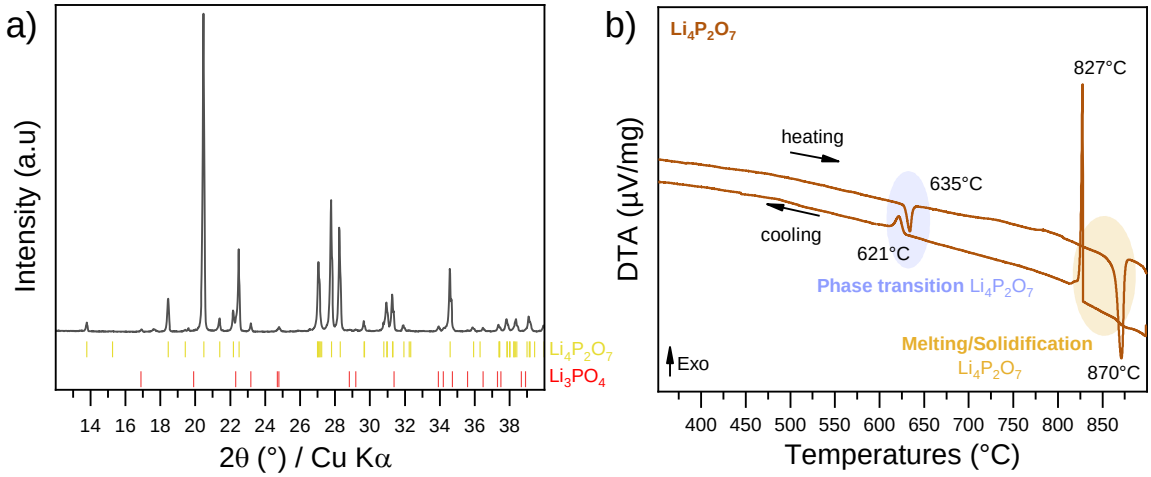

Appendix 2: (a) XRD pattern of $Li_4P_2O_7$ powder acquired with standard conditions. (b) DTA curves of $Li_4P_2O_7$ powder. The analysis was performed between 25 and 900 °C with a heating/cooling ramp of 5 °C/min, and under an airflow of 20 ml/min.

The synthesised $Li_4P_2O_7$ has a space group of *P*-1 and is not entirely pure, as a small amount of Li_3PO_4 is observed in Appendix 2-a. The melting temperature of $Li_4P_2O_7$ is 870 °C, as shown in Appendix 2-b, which is consistent with the literature[254].

B- Rietveld refinements

The following results refer to the $LATP_{0.3}$ + LiBr (1:1) sample analysed by high temperature X-ray diffraction (Chapter III).

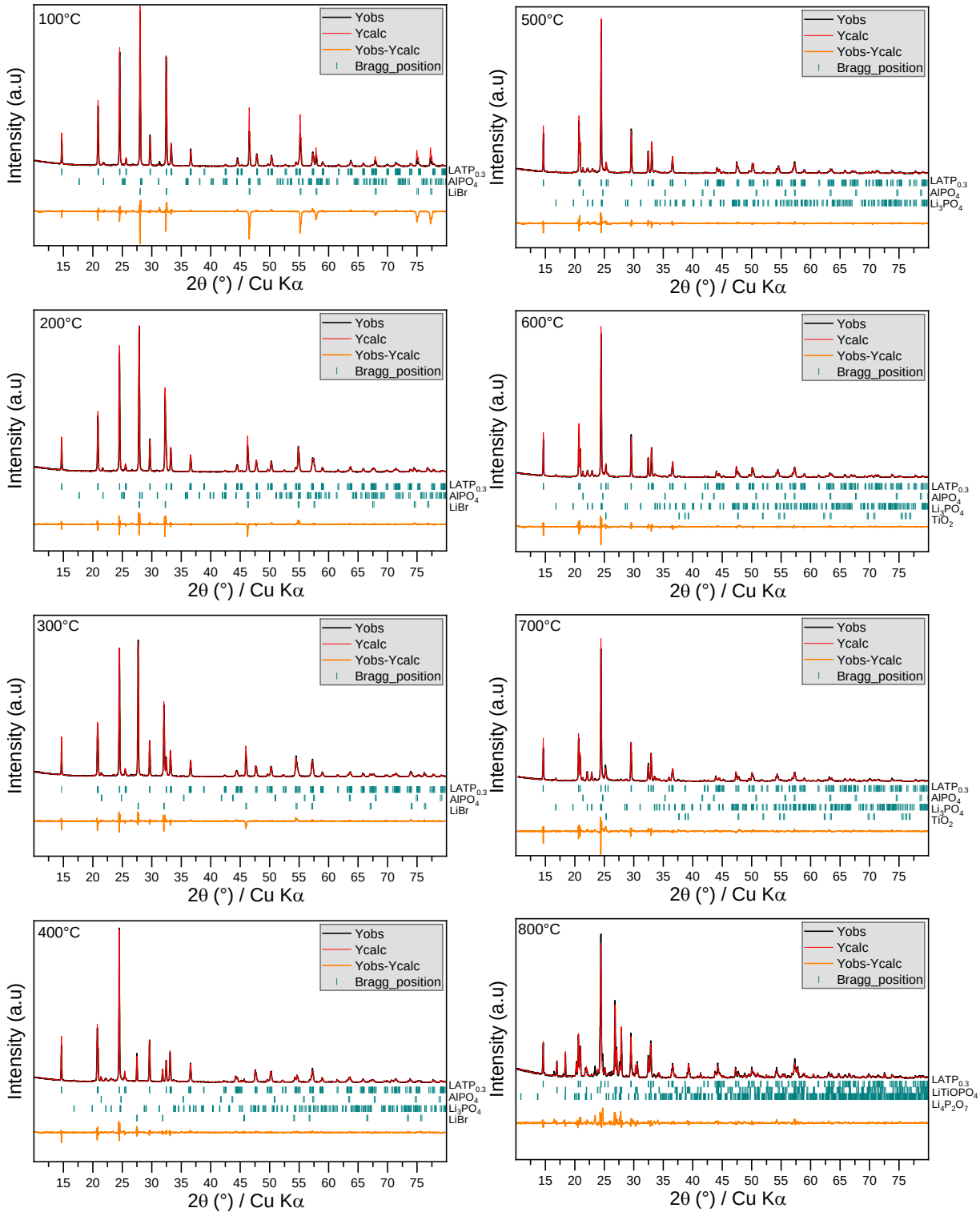

Appendix 3: Rietveld refinements of XRD patterns of mixture of $LATP_{0.3}$ + LiBr (1:1) obtained by high temperature X-Ray (100-800 °C).

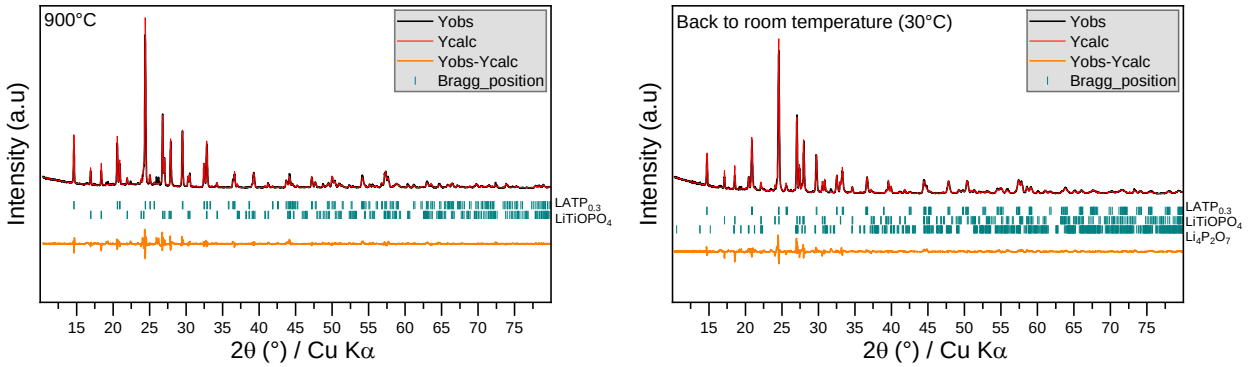

Appendix 4: Rietveld refinements of XRD patterns of mixture of $LATP_{0.3}$ + LiBr (1:1) obtained by high temperature X-Ray (900 °C and back to 30 °C). Experimental plots are shown in black lines, calculated in red lines, Bragg reflection peaks by blue vertical lines and difference plot by orange line.

100°C				
Phases	*a* (Å)	*b* (Å)	*c* (Å)	wt%
$LATP_{0.3}$ (***R*-3*c***)	8.4962(5)	8.4962(5)	20.861(3)	75.73 (±0.35)
$AlPO_4$ (***C*222$_1$**)	7.11(5)	7.06(5)	7.00(3)	1.41 (±0.46)
LiBr (***Fm*-3*m***)	5.51(0)	5.51(0)	5.51(0)	22.85 (±0.11)
χ^2 = 0.174; R_p = 15.5; R_{wp} = 27.7; R_{exp} = 66.86				

200°C				
$LATP_{0.3}$ (***R*-3*c***)	8.5015(4)	8.5015(4)	20.914(2)	70.81 (±1.93)
$AlPO_4$ (***C*222$_1$**)	7.15(7)	7.03(7)	7.06(3)	1.24 (±0.36)
LiBr (***Fm*-3*m***)	5.5472(1)	5.5472(1)	5.5472(1)	27.95 (±0.85)
χ^2 = 0.0241; R_p = 7.95; R_{wp} = 10.4; R_{exp} = 67.31				

300°C				
$LATP_{0.3}$ (***R*-3*c***)	8.5019(4)	8.5019(4)	20.971(1)	72.29 (±1.95)
$AlPO_4$ (***F*-43*m***)	7.166(6)	7.166(6)	7.166(6)	0.93 (±0.30)
LiBr (***Fm*-3*m***)	5.5808(1)	5.5808(1)	5.5808(1)	26.78 (±0.84)
χ^2 = 0.0220; R_p = 7.40; R_{wp} = 9.79; R_{exp} = 65.97				

400°C				
$LATP_{0.3}$ (***R*-3*c***)	8.5036(3)	8.5036(3)	21.028(2)	81.84 (±3.41)
$AlPO_4$ (***F*-43*m***)	7.183(4)	7.183(4)	7.183(4)	1.06 (±0.34)
LiBr (***Fm*-3*m***)	5.6213(5)	5.6213(5)	5.6213(5)	10.40 (±0.18)
Li_3PO_4 (***Pnma***)	10.54(1)	6.15(1)	4.929(7)	6.72 (±1.16)
χ^2 = 0.0171; R_p = 7.20; R_{wp} = 9.47; R_{exp} = 72.55				

500 °C				
$LATP_{0.3}$ (***R*-3*c***)	8.5030(4)	8.5030(4)	21.088(1)	91.67 (±3.57)
$AlPO_4$ (***F*-43*m***)	7.192(4)	7.192(4)	7.192(4)	1.10 (±0.32)
Li_3PO_4 (***Pnma***)	10.559(7)	6.170(4)	4.960(3)	7.23 (±0.97)
χ^2 = 0.0199; R_p = 7.73; R_{wp} = 10.1; R_{exp} = 73.24				

600 °C				
$LATP_{0.3}$ (***R*-3*c***)	8.5010(3)	8.5010(3)	21.146(2)	82.10 (±3.28)
$AlPO_4$ (***F*-43*m***)	7.196(3)	7.196(3)	7.196(3)	0.92 (±0.20)
Li_3PO_4 (***Pnma***)	10.549(5)	6.182(3)	4.974(2)	14.65 (±1.22)
TiO_2 (***I*4$_1$/*amd***)	3.819(5)	3.819(5)	9.17(1)	2.33 (±0.83)
χ^2 = 0.0230; R_p = 8.64; R_{wp} = 11.3; R_{exp} = 74.17				

700 °C				
$LATP_{0.3}$ (***R*-3*c***)	8.4993(4)	8.4993(4)	21.211(2)	83.05 (±2.58)
$AlPO_4$ (***F*-43*m***)	7.197(5)	7.197(5)	7.197(5)	0.57 (±0.26)
Li_3PO_4 (***Pnma***)	10.574(3)	6.196(2)	4.993(1)	14.49 (±1.13)
TiO_2 (***I*4$_1$/*amd***)	3.811(3)	3.811(3)	9.194(8)	1.90 (±0.04)
χ^2 = 0.0423; R_p = 11.7; R_{wp} = 15.1; R_{exp} = 73.52				

800 °C				
$LATP_{0.3}$ (***R*-3*c***)	8.4953(7)	8.4953(7)	21.281(3)	57.68 (±4.03)
$LiTiOPO_4$ (***Pnma***)	7.4547(6)	6.3931(5)	7.3346(7)	34.31 (±2.80)
$Li_4P_2O_7$ (***P*12$_1$/*n*1**)	8.865(5)	5.200(2)	13.367(8)	8.01 (±1.84)
χ^2 = 0.0559; R_p = 12.3; R_{wp} = 17.2; R_{exp} = 72.67				

900 °C				
$LATP_{0.3}$ (***R*-3*c***)	8.4959(5)	8.4959(5)	21.327(2)	56.02 (±3.53)
$LiTiOPO_4$ (***Pnma***)	7.4635(8)	6.3958(6)	7.356(1)	43.98 (±2.41)
$Li_4P_2O_7$ (***P*12$_1$/*n*1**)	-	-	-	-
χ^2 = 0.0323; R_p = 10.0; R_{wp} = 13.1; R_{exp} = 72.92				

Back to room temperature (30 °C)				
$LATP_{0.3}$ (***R*-3*c***)	8.49(1)	8.49(1)	21.327(2)	53.25 (±3.33)
$LiTiOPO_4$ (***Pnma***)	7.4017(8)	6.3729(6)	7.2409(9)	40.43 (±2.15)
$Li_4P_2O_7$ (***P*-1**)	8.636(8)	7.127(6)	5.1862(3)	6.31 (±0.21)
χ^2 = 0.0339; R_p = 9.46; R_{wp} = 12.9; R_{exp} = 69.85				

Appendix 5: Rietveld refinement results for the $LATP_{0.3}$ + LiBr (1:1) sample from 100 °C to 900 °C then back to 30 °C.

C- Materials and Method

a. X-Ray Diffraction

The analyses were carried out on a Bruker D8 Advance diffractometer in Bragg-Brentano θ-θ geometry, equipped with a LynxEye detector and a Cu emitter anode ($\lambda K_{\alpha 1}$ = 1.54056 Å, $\lambda K_{\alpha 2}$ = 1.54439 Å). All analysis was carried out with a fixed slit of 0.18 cm.

b. Laser granulometry

The particle size analysis experiments were performed using the AccuSizer™ 780/SIS model LE400-05. The analyses were conducted by adding a small amount of powder (a spatula tip) into 30 mL of pure ethanol under stirring.

c. Scanning electron microscopy

SEM images were obtained using a Hitachi S-3400N microscope. The analyses were carried out on non-metallised samples.

d. Thermogravimetric and Differential Thermal analysis

Thermogravimetric analyses (TGA) were performed using an SDT Q600 V20.9 Build 20 thermal analyser to determine mass loss during heat treatment. The samples were placed in an alumina crucible. Differential Thermal Analysis were carried out using a STA 2500 (NETZSCH) and the sample was introduced in an aluminium capsule.

e. Dilatometry

The dilatometry experiments were carried out using a Setsys Evolution CS Evo TMA dilatometer from the brand SETERAM. The analyses were conducted on pellets weighing between 150 mg and 200 mg, shaped using a uniaxial press with a pressure of 1.5 ton, and using an 8 mm die. During the analysis, the sample was sandwiched between two alumina disks to prevent contamination. A blank measurement was performed with the two disks before the analysis to subtract their contributions.

f. Wavelength Dispersive X-Ray Fluorescence

The analyses were conducted on powders compacted under 8 ton of pressure for 2 minutes using a uniaxial press. The pellets were analysed using a S8 Tiger spectrometer (Bruker) in 4 kW, with a Rhodium tube as an X-ray source.

g. Electrochemical Impedance Spectroscopy

The EIS measurements were carried out using a 1260 Solartron FRA device in a range of frequencies between 10^7 Hz and 10^{-1} Hz, with a perturbation of 10 mV at the open circuit voltage, recording 11 points per decade. Before analysis, the pellets were covered with a 20 nm layers of gold, serving as a blocking electrode. The pellets were assembled in a Swagelok-type cell using two stainless-steel. A spring was used in order to maintain the contact pressure.

h. Spray Drying

The experiments were carried out using the Büchi Mini Spray Dryer B-290.

i. High temperature X-Ray Diffraction

The equipment used was a Bruker D8 Advance diffractometer in Bragg-Brentano θ-θ geometry, equipped with a LynxEye detector and a Cu emitter anode ($\lambda K_{\alpha 1}$ = 1.54056 Å, $\lambda K_{\alpha 2}$ = 1.54439 Å). Pellets samples were placed on a ceramic support and modifications to the height of the sample were made to limit any shift in θ. All analysis was carried out with a fixed slit of 0.18 cm.

j. Raman spectroscopy

Raman spectroscopy was performed using the spectrometer LabRam HR800 (Horiba Jobin Yvon) using the 514 nm line of an Ar laser.

k. Solid-state Nuclear Magnetic Spectroscopy

Solid-state MAS NMR spectra were acquired on a Bruker AVANCE III 700 spectrometer (16.4 T magnet) operating at ν_0 = 283.29, 271.98 and 182.35 MHz for ^{31}P, ^{7}Li and ^{27}Al respectively, using a commercial Bruker triple-resonance MAS probe. Powder samples were transferred to ZrO_2 rotors and spun at a MAS rate of 20 kHz. ^{31}P, ^{7}Li and ^{27}Al chemical shifts were referenced to H_3PO_4, LiCl and $Al(NO_3)_3$, respectively. Two-dimensional 27Al multiple-quantum magic-angle spinning (MQMAS) NMR spectra were obtained by using an amplitude modulated Z-filter experiment (p1-t1 (MQ evolution)-p2-τ -p3-t2(acquire) sequence). The optimized pulse lengths of the 3Q excitation (p1) and reconversion (p2) were p1 = 4 μs and p2 = 2 μs whereas the soft π/2 Z-filter (p3) was set to 15 μs.

l. DFT calculations

All atomic positions were then relaxed with the VASP (Vienna Ab-initio Simulation Package) code[222] based on the Kohn-Sham Density Functional Theory (DFT) and using a plane-wave pseudopotential approach. The cells parameters were fixed to X-ray diffraction parameters during geometry optimizations. The NMR parameters were then calculated within Kohn-Sham DFT using the QUANTUM-ESPRESSO code[223], keeping the atomic positions equal to the values previously calculated with VASP. The PBE generalized gradient approximation[224] was used and the valence electrons were described by norm conserving pseudopotentials[225] in the Kleinman Bylander form[226]. The shielding tensor was computed using the Gauge Including Projector Augmented Wave (GIPAW) approach[227], which enables the reproduction of the results of a fully converged all electron calculation. The isotropic chemical shift δ_{iso} is defined as $\delta_{iso} = -[\sigma - \sigma_{ref}]$ where σ is the isotropic shielding and σ_{ref} is the isotropic shielding of the same nucleus in a reference system. In the present case, we used the comparison between the experimental δ_{iso} and calculated δ_{iso} ^{31}P chemical shift values for Li_3PO_4 and ^{27}Al for a-Al_2O_3.

m. Spark Plasma Sintering

The ground powders in Chapter IV, Section III were sintered by Spark Plasma Sintering (SPS) under vacuum (around 10 Pa) using a Dr. Sinter 515S Syntex setup and in a 15-mm diameter graphite die.

References

[1] “Chiffres clés du climat - France, Europe et Monde - Édition 2021 | Données et études statistiques,” can be found under https://www.statistiques.developpement-durable.gouv.fr/chiffres-cles-du-climat-france-europe-et-monde-edition-2021-0, **2021**.

[2] “Greenhouse gas emissions by gas,” can be found under https://ourworldindata.org/grapher/ghg-emissions-by-gas, **2024**.

[3] Intergovernmental Panel on Climate Change, “Global Warming of 1.5 ºC,” can be found under https://www.ipcc.ch/sr15/, **2019**.

[4] European Environment Agency, “High time to shift gear in transport sector,” can be found under https://www.eea.europa.eu/signals-archived/signals-2022/articles/high-time-to-shift-gear, **2022**.

[5] J. Janek, W. G. Zeier, *Nat Energy* **2016**, *1*, 1.

[6] J. G. Kim, B. Son, S. Mukherjee, N. Schuppert, A. Bates, O. Kwon, M. J. Choi, H. Y. Chung, S. Park, *Journal of Power Sources* **2015**, *282*, 299.

[7] Y. Zheng, Y. Yao, J. Ou, M. Li, D. Luo, H. Dou, Z. Li, K. Amine, A. Yu, Z. Chen, *Chem. Soc. Rev.* **2020**, *49*, 8790.

[8] N. Zhao, W. Khokhar, Z. Bi, C. Shi, X. Guo, L.-Z. Fan, C.-W. Nan, *Joule* **2019**, *3*, 1190.

[9] C. Luo, M. Yi, Z. Cao, W. Hui, Y. Wang, *ACS Appl. Electron. Mater.* **2024**, *6*, 641.

[10] T. Hupfer, E. C. Bucharsky, K. G. Schell, A. Senyshyn, M. Monchak, M. J. Hoffmann, H. Ehrenberg, *Solid State Ionics* **2016**, *288*, 235.

[11] C.-Y. Yu, J. Choi, V. Anandan, J.-H. Kim, *J. Phys. Chem. C* **2020**, *124*, 14963.

[12] Y. Liu, Q. Sun, D. Wang, K. Adair, J. Liang, X. Sun, *Journal of Power Sources* **2018**, *393*, 193.

[13] K. Waetzig, A. Rost, U. Langklotz, B. Matthey, J. Schilm, *Journal of the European Ceramic Society* **2016**, *36*, 1995.

[14] F. Zheng, M. Kotobuki, S. Song, M. O. Lai, L. Lu, *Journal of Power Sources* **2018**, *389*, 198.

[15] M. Armand, J.-M. Tarascon, *Nature* **2008**, *451*, 652.

[16] A. C. Luntz, J. Voss, K. Reuter, *J. Phys. Chem. Lett.* **2015**, *6*, 4599.

[17] J. B. Goodenough, *J Solid State Electrochem* **2012**, *16*, 2019.

[18] M. M. Thackeray, C. Wolverton, E. D. Isaacs, *Energy Environ. Sci.* **2012**, *5*, 7854.

[19] X. Yao, B. Huang, J. Yin, G. Peng, Z. Huang, C. Gao, D. Liu, X. Xu, *Chinese Phys. B* **2015**, *25*, 018802.

[20] Z. Zhang, Y. Shao, B. Lotsch, Y.-S. Hu, H. Li, J. Janek, L. F. Nazar, C.-W. Nan, J. Maier, M. Armand, L. Chen, *Energy Environ. Sci.* **2018**, *11*, 1945.

[21] L. Fan, S. Wei, S. Li, Q. Li, Y. Lu, *Advanced Energy Materials* **2018**, *8*, 1702657.

[22] J. Sung, J. Heo, D.-H. Kim, S. Jo, Y.-C. Ha, D. Kim, S. Ahn, J.-W. Park, *Materials Chemistry Frontiers* **2024**, *8*, 1861.

[23] A. Banerjee, X. Wang, C. Fang, E. A. Wu, Y. S. Meng, *Chem. Rev.* **2020**, *120*, 6878.

[24] J. Janek, W. G. Zeier, *Nat Energy* **2023**, *8*, 230.

[25] Y. Zhu, X. He, Y. Mo, *ACS Appl. Mater. Interfaces* **2015**, *7*, 23685.

[26] H. Xu, Y. Yu, Z. Wang, G. Shao, *ENERGY & ENVIRONMENTAL MATERIALS* **2019**, *2*, 234.

[27] Z. Moradi, A. Lanjan, R. Tyagi, S. Srinivasan, *Journal of Energy Storage* **2023**, *73*, 109048.

[28] A. Jonderian, E. McCalla, *Mater. Adv.* **2021**, *2*, 2846.

[29] N. J. Dudney, in *Lithium Batteries: Science and Technology* (Eds.: G.-A. Nazri, G. Pistoia), Springer US, Boston, MA, **2003**, pp. 624–642.

[30] Y. Zhu, X. He, Y. Mo, *J. Mater. Chem. A* **2016**, *4*, 3253.
[31] P. Yao, H. Yu, Z. Ding, Y. Liu, J. Lu, M. Lavorgna, J. Wu, X. Liu, *Front. Chem.* **2019**, *7*, DOI 10.3389/fchem.2019.00522.
[32] W. H. Meyer, *Advanced Materials* **1998**, *10*, 439.
[33] S. Ibrahim, M. M. Yassin, R. Ahmad, M. R. Johan, *Ionics* **2011**, *17*, 399.
[34] X. Zhu, K. Wang, Y. Xu, G. Zhang, S. Li, C. Li, X. Zhang, X. Sun, X. Ge, Y. Ma, *Energy Storage Materials* **2021**, *36*, 291.
[35] L. Meabe, T. V. Huynh, D. Mantione, L. Porcarelli, C. Li, L. A. O'Dell, H. Sardon, M. Armand, M. Forsyth, D. Mecerreyes, *Electrochimica Acta* **2019**, *302*, 414.
[36] M. Armand, *Solid State Ionics* **1983**, *9–10*, 745.
[37] X. Zhao, C. Wang, H. Liu, Y. Liang, L.-Z. Fan, *Batteries & Supercaps* **2023**, *6*, e202200502.
[38] A. Manuel Stephan, K. S. Nahm, *Polymer* **2006**, *47*, 5952.
[39] "Technologie de batteries - Bollore - Blue Solutions," can be found under https://www.blue-solutions.com/technologie-de-batteries/, **n.d.**
[40] Y. Kato, S. Hori, T. Saito, K. Suzuki, M. Hirayama, A. Mitsui, M. Yonemura, H. Iba, R. Kanno, *Nat Energy* **2016**, *1*, 1.
[41] Y. Seino, T. Ota, K. Takada, A. Hayashi, M. Tatsumisago, *Energy Environ. Sci.* **2014**, *7*, 627.
[42] C. Dietrich, D. A. Weber, S. J. Sedlmaier, S. Indris, S. P. Culver, D. Walter, J. Janek, W. G. Zeier, *J. Mater. Chem. A* **2017**, *5*, 18111.
[43] L. Zhou, K.-H. Park, X. Sun, F. Lalère, T. Adermann, P. Hartmann, L. F. Nazar, *ACS Energy Lett.* **2019**, *4*, 265.
[44] A. Machín, C. Morant, F. Márquez, *Batteries* **2024**, *10*, 29.
[45] S. P. Kammampata, M. A. Garakani, Z. Zhang, V. Thangadurai, in *Comprehensive Inorganic Chemistry III (Third Edition)* (Eds.: J. Reedijk, K. R. Poeppelmeier), Elsevier, Oxford, **2023**, pp. 658–680.
[46] A. M. Nolan, Y. Zhu, X. He, Q. Bai, Y. Mo, *Joule* **2018**, *2*, 2016.
[47] Y. Yu, X. Rui, M. Wu, in *Reference Module in Chemistry, Molecular Sciences and Chemical Engineering*, Elsevier, **2023**.
[48] Q. Zhang, D. Cao, Y. Ma, A. Natan, P. Aurora, H. Zhu, *Advanced Materials* **2019**, *31*, 1901131.
[49] S. Huang, P. Cao, in *Advanced Ceramics for Energy Storage, Thermoelectrics and Photonics* (Eds.: P. Cao, Z.-G. Chen, Z. Xia), Elsevier, **2023**, pp. 77–117.
[50] H. Sun, S. Kang, L. Cui, *Chemical Engineering Journal* **2023**, *454*, 140375.
[51] K. V. Kravchyk, D. T. Karabay, M. V. Kovalenko, *Sci Rep* **2022**, *12*, 1177.
[52] J.-H. Yin, H. Zhu, S.-J. Yu, Y.-B. Dong, Q.-Y. Wei, G.-Q. Xu, Y. Xiong, Y. Qian, *Advanced Engineering Materials* **2023**, *25*, 2300566.
[53] Y. Li, J.-T. Han, C.-A. Wang, H. Xie, J. B. Goodenough, *J. Mater. Chem.* **2012**, *22*, 15357.
[54] C. A. Geiger, E. Alekseev, B. Lazic, M. Fisch, T. Armbruster, R. Langner, M. Fechtelkord, N. Kim, T. Pettke, W. Weppner, *Inorg. Chem.* **2011**, *50*, 1089.
[55] Z. Zhang, X. Wang, X. Li, J. Zhao, G. Liu, W. Yu, X. Dong, J. Wang, *Materials Today Sustainability* **2023**, *21*, 100316.
[56] S. Rajendran, N. K. Thangavel, K. Mahankali, L. M. R. Arava, *ACS Appl. Energy Mater.* **2020**, *3*, 6775.
[57] X. Wang, J. Wang, F. Li, F. Zhu, C. Ma, *Ceramics International* **2020**, *46*, 18544.
[58] J. Xiao, B. Zhang, J. Liu, X. He, Z. Xiao, H. Qin, T. Liu, K. Amine, X. Ou, *Nano Energy* **2024**, *127*, 109730.

[59] H. Aono, E. Sugimoto, Y. Sadaoka, N. Imanaka, G. Adachi, *J. Electrochem. Soc.* **1990**, *137*, 1023.
[60] Y. Fu, H. Ming, S. Zhao, J. Guo, M. Chen, Q. Zhou, J. Zheng, *Electrochimica Acta* **2015**, *185*, 211.
[61] J. Fu, *Solid State Ionics* **1997**, *96*, 195.
[62] "Lithium-Ion Conducting Glass-Ceramics (LICGC^{TM}) - Ohara Corp," **2022**.
[63] P. Knauth, *Solid State Ionics* **2009**, *180*, 911.
[64] L. Li, Z. Zhang, L. Luo, R. You, J. Jiao, W. Huang, J. Wang, C. Li, X. Han, S. Chen, *Ionics* **2020**, *26*, 3815.
[65] J. B. Goodenough, H. Y. P. Hong, J. A. Kafalas, *Mate Res Bull* **1976**, *11*, 203.
[66] D. K. Agrawal, C.-Y. Huang, H. A. McKinstry, *Int J Thermophys* **1991**, *12*, 697.
[67] J. Alamo, *Solid State Ionics* **1993**, *63–65*, 547.
[68] K. Arbi, M. A. París, J. Sanz, *Dalton Trans.* **2011**, *40*, 10195.
[69] E. Morin, T. L. Mercier, M. Quarton, E. R. Losilla, M. a. G. Aranda, S. Bruque, *Powder Diffraction* **1999**, *14*, 53.
[70] C. Park, *Journal of Ceramic Processing Research* **2013**.
[71] R. D. Shannon, B. E. Taylor, A. D. English, T. Berzins, *Electrochimica Acta* **1977**, *22*, 783.
[72] B. Lang, B. Ziebarth, C. Elsässer, *Chem. Mater.* **2015**, *27*, 5040.
[73] K. Takada, M. Tansho, I. Yanase, T. Inada, A. Kajiyama, M. Kouguchi, S. Kondo, M. Watanabe, *Solid State Ionics* **2001**, *139*, 241.
[74] F. Öksüzoğlu, Ş. Ateş, O. M. Özkendir, G. Çelik, Y. R. Eker, H. Baveghar, *Ceramics International* **2024**, *50*, 31435.
[75] W. Xiao, J. Wang, L. Fan, J. Zhang, X. Li, *Energy Storage Materials* **2019**, *19*, 379.
[76] K. Arbi, M. Hoelzel, A. Kuhn, F. García-Alvarado, J. Sanz, *Inorg. Chem.* **2013**, *52*, 9290.
[77] M. Monchak, T. Hupfer, A. Senyshyn, H. Boysen, D. Chernyshov, T. Hansen, K. G. Schell, E. C. Bucharsky, M. J. Hoffmann, H. Ehrenberg, *Inorg. Chem.* **2016**, *55*, 2941.
[78] G. J. Redhammer, D. Rettenwander, S. Pristat, E. Dashjav, C. M. N. Kumar, D. Topa, F. Tietz, *Solid State Sciences* **2016**, *60*, 99.
[79] M. Pérez-Estébanez, J. Isasi-Marín, D. M. Többens, A. Rivera-Calzada, C. León, *Solid State Ionics* **2014**, *266*, 1.
[80] K. Arbi, M. Hoelzel, A. Kuhn, F. García-Alvarado, J. Sanz, *Phys. Chem. Chem. Phys.* **2014**, *16*, 18397.
[81] R. D. Shannon, C. T. Prewitt, *Acta Cryst B* **1970**, *26*, 1046.
[82] D. Case, A. J. McSloy, R. Sharpe, S. R. Yeandel, T. Bartlett, J. Cookson, E. Dashjav, F. Tietz, C. M. Naveen Kumar, P. Goddard, *Solid State Ionics* **2020**, *346*, 115192.
[83] R. DeWees, H. Wang, *ChemSusChem* **2019**, *12*, 3713.
[84] H. Aono, E. Sugimoto, Y. Sadaoka, N. Imanaka, G. Adachi, *Solid State Ionics* **1991**, *47*, 257.
[85] S. Yu, A. Mertens, X. Gao, D. C. Gunduz, R. Schierholz, S. Benning, F. Hausen, J. Mertens, H. Kungl, H. Tempel, R.-A. Eichel, *Funct. Mater. Lett.* **2016**, *09*, 1650066.
[86] G. Yan, S. Yu, J. F. Nonemacher, H. Tempel, H. Kungl, J. Malzbender, R.-A. Eichel, M. Krüger, *Ceramics International* **2019**, *45*, 14697.
[87] X. M. Wu, S. Chen, F. R. Mai, J. H. Zhao, Z. Q. He, *Ionics* **2013**, *19*, 589.
[88] H. Chen, H. Tao, X. Zhao, Q. Wu, *Journal of Non-Crystalline Solids* **2011**, *357*, 3267.
[89] L. Zhang, P. Chen, Z. Hu, C. Chen, *Chinese Journal of Chemical Physics* **2012**, *25*, 703.
[90] F. Ma, E. Zhao, S. Zhu, W. Yan, D. Sun, Y. Jin, C. Nan, *Solid State Ionics* **2016**, *295*, 7.

[91] Z. Yao, K. J. Zhu, K. Zhu, J. Zhang, X. Li, J. Chen, J. Wang, K. Yan, J. Liu, **2021**, DOI 10.21203/rs.3.rs-416213/v1.
[92] K. M. Kim, D. O. Shin, Y.-G. Lee, *Electrochimica Acta* **2015**, *176*, 1364.
[93] K. Arbi, W. Bucheli, R. Jiménez, J. Sanz, *Journal of the European Ceramic Society* **2015**, *5*, 1477.
[94] C. Luo, M. Yi, Z. Cao, W. Hui, Y. Wang, *ACS Appl. Electron. Mater.* **2024**, *6*, 641.
[95] D. Bernache-assollant, *Chimie-physique du frittage*, Lavoisier-Hermès, **1993**.
[96] R. M. German, *Liquid Phase Sintering*, Springer US, Boston, MA, **1985**.
[97] D. Bernache-assollant, J.-P. Bonnet, *Techniques de l'Ingénieur* **2005**.
[98] M. P. Groover, *Fundamentals of Modern Manufacturing: Materials, Processes, and Systems*, John Wiley & Sons, **2010**.
[99] M. A. Occhionero, J. W. Halloran, in *Materials Science Research: Volume 16 Sintering and Heterogeneous Catalysis* (Eds.: G. C. Kuczynski, A. E. Miller, G. A. Sargent), Springer US, Boston, MA, **1984**, pp. 89–102.
[100] D. Bernache-Assollant, J.-P. Bonnet, *Techniques de l'Ingénieur* **2005**.
[101] A. Mormeneo-Segarra, S. Ferrer-Nicomedes, N. Vicente-Agut, A. Barba-Juan, *Journal of the European Ceramic Society* **2024**, *44*, 5105.
[102] M. Bertrand, S. Rousselot, D. Aymé-Perrot, M. Dollé, *Mater. Adv.* **2021**, *2*, 2989.
[103] B. Davaasuren, F. Tietz, *Solid State Ionics* **2019**, *338*, 144.
[104] K. Waetzig, A. Rost, C. Heubner, M. Coeler, K. Nikolowski, M. Wolter, J. Schilm, *Journal of Alloys and Compounds* **2020**, *818*, 153237.
[105] H. Raj, T. Fabre, M. Lachal, A. Neveu, J. Jean, M. C. Steil, R. Bouchet, V. Pralong, *ACS Appl. Energy Mater.* **2023**, *6*, 1197.
[106] J. Liu, T. Liu, Y. Pu, M. Guan, Z. Tang, F. Ding, Z. Xu, Y. Li, *RSC Adv.* **2017**, *7*, 46545.
[107] G. Yan, S. Yu, J. F. Nonemacher, H. Tempel, H. Kungl, J. Malzbender, R.-A. Eichel, M. Krüger, *Ceramics International* **2019**, *45*, 14697.
[108] S. D. Jackman, R. A. Cutler, *Journal of Power Sources* **2012**, *218*, 65.
[109] S. Valiyaveettil-SobhanRaj, R. Cid, T. Thompson, F. Bonilla, G. A. López, F. Aguesse, M. Casas-Cabanas, *ACS Appl. Mater. Interfaces* **2023**, *15*, 13689.
[110] M. Trunec, K. Maca, in *Advanced Ceramics for Dentistry* (Eds.: J. Z. Shen, T. Kosmač), Butterworth-Heinemann, Oxford, **2014**, pp. 123–150.
[111] M. Dixit, C. Beamer, R. Amin, J. Shipley, R. Eklund, N. Muralidharan, L. Lindqvist, A. Fritz, R. Essehli, M. Balasubramanian, I. Belharouak, *ACS Energy Lett.* **2022**, *7*, 3936.
[112] R. Murugan, V. Thangadurai, W. Weppner, *Angewandte Chemie International Edition* **2007**, *46*, 7778.
[113] E. Rangasamy, J. Wolfenstine, J. Sakamoto, *Solid State Ionics* **2012**, *206*, 28.
[114] I. N. David, T. Thompson, J. Wolfenstine, J. L. Allen, J. Sakamoto, *Journal of the American Ceramic Society* **2015**, *98*, 1209.
[115] Y. Zhu, T. Wu, J. Sun, M. Kotobuki, *Solid State Ionics* **2020**, *350*, 115320.
[116] A. Paolella, W. Zhu, G. Bertoni, A. Perea, H. Demers, S. Savoie, G. Girard, N. Delaporte, A. Guerfi, M. Rumpel, H. Lorrmann, G. P. Demopoulos, K. Zaghib, *Advanced Materials Interfaces* **2020**, *7*, 2000164.
[117] J.-H. Yin, H. Zhu, S.-J. Yu, Y.-B. Dong, Q.-Y. Wei, G.-Q. Xu, Y. Xiong, Y. Qian, *Advanced Engineering Materials* **2023**, *25*, 2300566.
[118] K. G. Schell, E. C. Bucharsky, F. Lemke, M. J. Hoffmann, *Ionics* **2017**, *23*, 821.
[119] G. Courbaron, R. B. Nuernberg, J. S. Sevillano, U.-C. Chung, M. Duttine, C. Labrugère-Sarroste, J. Olchowka, D. Carlier, N. Delpuech, L. Croguennec, *Journal of Alloys and Compounds* **2024**, *985*, 174062.
[120] Z. A. Munir, U. Anselmi-Tamburini, M. Ohyanagi, *J Mater Sci* **2006**, *41*, 763.

[121] S. Duluard, A. Paillassa, L. Puech, P. Vinatier, V. Turq, P. Rozier, P. Lenormand, P.-L. Taberna, P. Simon, F. Ansart, *Journal of the European Ceramic Society* **2013**, *33*, 1145.
[122] R. Kali, A. Mukhopadhyay, *Journal of Power Sources* **2014**, *247*, 920.
[123] Y. Kobayashi, T. Takeuchi, M. Tabuchi, K. Ado, H. Kageyama, *Journal of Power Sources* **1999**, *81–82*, 853.
[124] S. S. Berbano, J. Guo, H. Guo, M. T. Lanagan, C. A. Randall, *Journal of the American Ceramic Society* **2017**, *100*, 2123.
[125] J.-P. Maria, X. Kang, R. D. Floyd, E. C. Dickey, H. Guo, J. Guo, A. Baker, S. Funihashi, C. A. Randall, *Journal of Materials Research* **2017**, *32*, 3205.
[126] Y. Liu, J. Liu, Q. Sun, D. Wang, K. R. Adair, J. Liang, C. Zhang, L. Zhang, S. Lu, H. Huang, X. Song, X. Sun, *ACS Appl. Mater. Interfaces* **2019**, *11*, 27890.
[127] M. Vinnichenko, K. Waetzig, A. Aurich, C. Baumgaertner, M. Herrmann, C. W. Ho, M. Kusnezoff, C. W. Lee, *Nanomaterials* **2022**, *12*, 3178.
[128] X. Li, Y. Zhou, J. Tang, S. Zhao, J. Zhang, X. Huang, B. Tian, *ACS Appl. Mater. Interfaces* **2023**, *15*, 36289.
[129] W. Lee, C. K. Lyon, J.-H. Seo, R. Lopez-Hallman, Y. Leng, C.-Y. Wang, M. A. Hickner, C. A. Randall, E. D. Gomez, *Advanced Functional Materials* **2019**, *29*, 1807872.
[130] K. Takashima, Y. Iwazaki, C. A. Randall, *Jpn. J. Appl. Phys.* **2021**, *60*, 126505.
[131] P. Jiang, P. Guo, Y. Shi, S. Li, K. Li, X. Y. Lu, Z. Zhang, D. He, J. Bian, X. Lu, *Materials Today Physics* **2021**, *20*, 100476.
[132] M. Y. Sengul, A. Ndayishimiye, W. Lee, J.-H. Seo, Z. Fan, Y. K. Shin, E. D. Gomez, C. A. Randall, A. C. T. van Duin, *Phys. Chem. Chem. Phys.* **2022**, *24*, 4125.
[133] H. Cai, T. Yu, D. Xie, B. Sun, J. Cheng, L. Li, X. Bao, H. Zhang, *Journal of Alloys and Compounds* **2023**, *939*, 168702.
[134] H. Leng, J. Huang, J. Nie, J. Luo, *Journal of Power Sources* **2018**, *391*, 170.
[135] M. Rumpel, L. Appold, J. Baber, W. Stracke, A. Flegler, G. Sextl, *Mater. Adv.* **2022**, *3*, 8157.
[136] S.-P. Shen, G. Tang, H.-J. Li, L. Zhang, J.-C. Zheng, Y. Luo, J.-P. Yue, Y. Shi, Z. Chen, *Ceramics International* **2022**, *48*, 36961.
[137] T. Zhu, Y. Lin, Z. Yang, D. Su, S. Ma, M. Han, F. Chen, *Journal of Power Sources* **2014**, *261*, 255.
[138] L. Xiong, Z. Ren, Y. Xu, S. Mao, P. Lei, M. Sun, *Solid State Ionics* **2017**, *309*, 22.
[139] K. Kwatek, W. Ślubowska, J. Trébosc, O. Lafon, J. L. Nowiński, *Journal of the European Ceramic Society* **2020**, *40*, 85.
[140] L. Dai, J. Wang, Z. Shi, L. Yu, J. Shi, *Ceramics International* **2021**, *47*, 11662.
[141] H. Bai, J. Hu, X. Li, Y. Duan, F. Shao, T. Kozawa, M. Naito, J. Zhang, *Ceramics International* **2018**, *44*, 6558.
[142] Y. E. Milián, N. Reinaga, M. Grágeda, S. Ushak, *J Sol-Gel Sci Technol* **2020**, *94*, 22.
[143] K. Waetzig, C. Heubner, M. Kusnezoff, *Crystals* **2020**, *10*, 408.
[144] K. Kwatek, M. Świniarski, J. L. Nowiński, *Journal of Solid State Chemistry* **2018**, *265*, 381.
[145] C.-Y. Yu, J. Choi, V. Anandan, J.-H. Kim, *J. Phys. Chem. C* **2020**, *124*, 14963.
[146] F. Ichihara, S. Miyoshi, T. Masuda, *Phys. Chem. Chem. Phys.* **2022**, *24*, 25878.
[147] L. Miara, A. Windmüller, C.-L. Tsai, W. D. Richards, Q. Ma, S. Uhlenbruck, O. Guillon, G. Ceder, *ACS Appl. Mater. Interfaces* **2016**, *8*, 26842.
[148] P.-Y. Yen, M.-L. Lee, D. H. Gregory, W.-R. Liu, *Ceramics International* **2020**, *46*, 20529.
[149] Q. Ma, Q. Xu, C.-L. Tsai, F. Tietz, O. Guillon, *Journal of the American Ceramic Society* **2016**, *99*, 410.

[150] K. Waetzig, A. Rost, C. Heubner, M. Coeler, K. Nikolowski, M. Wolter, J. Schilm, *Journal of Alloys and Compounds* **2020**, *818*, 153237.
[151] M. Cretin, P. Fabry, *Journal of the European Ceramic Society* **1999**, *19*, 2931.
[152] X. Liang, D. Han, Y. Wang, L. Lan, J. Mao, *RSC Adv.* **2018**, *8*, 40498.
[153] B. Key, D. J. Schroeder, B. J. Ingram, J. T. Vaughey, *Chem. Mater.* **2012**, *24*, 287.
[154] D. Campanella, S. Krachkovskiy, C. Faure, W. Zhu, Z. Feng, S. Savoie, G. Girard, H. Demers, A. Vijh, C. George, M. Armand, D. Belanger, A. Paolella, *ChemElectroChem* **2022**, *9*, e202200984.
[155] G. J. Redhammer, D. Rettenwander, S. Pristat, E. Dashjav, C. M. N. Kumar, D. Topa, F. Tietz, *Solid State Sciences* **2016**, *60*, 99.
[156] E. C. Bucharsky, K. G. Schell, A. Hintennach, M. J. Hoffmann, *Solid State Ionics* **2015**, *274*, 77.
[157] M. Pogosova, I. Krasnikova, A. Sergeev, A. Zhugayevych, K. Stevenson, *Journal of Power Sources* **2020**, *448*, 227367.
[158] D. Case, A. J. McSloy, R. Sharpe, S. R. Yeandel, T. Bartlett, J. Cookson, E. Dashjav, F. Tietz, C. M. Naveen Kumar, P. Goddard, *Solid State Ionics* **2020**, *346*, 115192.
[159] C. Park, S. Na, H. G. Park, K. Park, *ACS Appl. Mater. Interfaces* **2023**, *15*, 26985.
[160] N. Tolganbek, Y. Yerkinbekova, A. Khairullin, Z. Bakenov, K. Kanamura, A. Mentbayeva, *Ceramics International* **2021**, *47*, 18188.
[161] C. Herring, *Journal of Applied Physics* **1950**, *21*, 301.
[162] H. Song, R. L. Coble, R. J. Brook, in *Materials Science Research: Volume 16 Sintering and Heterogeneous Catalysis* (Eds.: G. C. Kuczynski, A. E. Miller, G. A. Sargent), Springer US, Boston, MA, **1984**, pp. 63–79.
[163] H. E. Exner, G. Petzow, in *Sintering and Catalysis* (Ed.: G. C. Kuczynski), Springer US, Boston, MA, **1975**, pp. 279–293.
[164] J. Fruhstorfer, C. G. Aneziris, *Ceramics International* **2017**, *43*, 13175.
[165] S.-J. L. Kang, in *Sintering* (Ed.: S.-J. L. Kang), Butterworth-Heinemann, Oxford, **2005**, pp. 117–135.
[166] N. Schiffmann, E. C. Bucharsky, K. G. Schell, C. A. Fritsch, M. Knapp, M. J. Hoffmann, *Ionics* **2021**, *27*, 2017.
[167] E. Zhao, F. Ma, Y. Jin, K. Kanamura, *Journal of Alloys and Compounds* **2016**, *680*, 646.
[168] L. Huang, Z. Wen, M. Wu, X. Wu, Y. Liu, X. Wang, *Journal of Power Sources* **2011**, *196*, 6943.
[169] M. Schroeder, S. Glatthaar, J. R. Binder, *Solid State Ionics* **2011**, *201*, 49.
[170] B. Yang, X. Li, H. Guo, Z. Wang, W. Xiao, *Journal of Alloys and Compounds* **2015**, *643*, 181.
[171] F. Ma, E. Zhao, S. Zhu, W. Yan, D. Sun, Y. Jin, C. Nan, *Solid State Ionics* **2016**, *295*, 7.
[172] K. Cal, K. Sollohub, *Journal of Pharmaceutical Sciences* **2010**, *99*, 575.
[173] A. Sosnik, K. P. Seremeta, *Advances in Colloid and Interface Science* **2015**, *223*, 40.
[174] D. Santos, A. C. Maurício, V. Sencadas, J. D. Santos, M. H. Fernandes, P. S. Gomes, D. Santos, A. C. Maurício, V. Sencadas, J. D. Santos, M. H. Fernandes, P. S. Gomes, in *Biomaterials - Physics and Chemistry - New Edition*, IntechOpen, **2017**.
[175] A. B. D. Nandiyanto, K. Okuyama, *Advanced Powder Technology* **2011**, *22*, 1.
[176] J. A. F. Plateau, *Statique expérimentale et théorique des liquides soumis aux seules forces moléculaires*, Gauthier-Villars, Paris, **1873**.
[177] Lord Rayleigh, *Proceedings of the London Mathematical Society* **1878**, *s1-10*, 4.
[178] C. Anandharamakrishnan, P. I. S, *Spray Drying Techniques for Food Ingredient Encapsulation*, John Wiley & Sons, **2015**.
[179] J. Karas, S. Pavloková, H. Hořavová, J. Gajdziok, *Pharmaceutics* **2023**, *15*, 496.

[180] X. Xu, Z. Wen, J. Wu, X. Yang, *Solid State Ionics* **2007**, *178*, 29.
[181] X. Xu, Z. Wen, X. Yang, J. Zhang, Z. Gu, *Solid State Ionics* **2006**, *177*, 2611.
[182] H. Kim, Y. Ding, P. A. Kohl, *Journal of Power Sources* **2012**, *198*, 281.
[183] R. A. Huggins, *Ionics* **2002**, *8*, 300.
[184] K. Kwatek, J. L. Nowiński, *Solid State Ionics* **2017**, *302*, 54.
[185] H. Aono, E. Sugimoto, Y. Sadaoka, N. Imanaka, G. Adachi, *Solid State Ionics* **1991**, *47*, 257.
[186] Q. Zhang, X. Zhang, Y. Zhang, Q. Shen, *Ionics* **2021**, *27*, 2473.
[187] K. Kwatek, J. L. Nowiński, *Ionics* **2019**, *25*, 41.
[188] Y. Kobayashi, M. Tabuchi, O. Nakamura, *Journal of Power Sources* **1997**, *68*, 407.
[189] K. Waetzig, C. Heubner, M. Kusnezoff, *Crystals* **2020**, *10*, 408.
[190] L. A. Sonnenberg, S. Chandra Paul, S. L. Wunder, M. J. Zdilla, *J. Phys. Chem. Lett.* **2024**, *15*, 782.
[191] S. V. Pershina, E. A. Il'ina, O. G. Reznitskikh, *Inorg. Chem.* **2017**, *56*, 9880.
[192] E. Il'ina, S. Pershina, B. Antonov, A. Pankratov, *Materials* **2021**, *14*, 7099.
[193] C. Liao, Z. Fu, L. Que, H. Tang, X. Wang, *RSC Advances* **2023**, *13*, 24174.
[194] R. K. Osterheld, *Journal of Inorganic and Nuclear Chemistry* **1968**, *30*, 3173.
[195] K. Waetzig, A. Rost, U. Langklotz, B. Matthey, J. Schilm, *Journal of the European Ceramic Society* **2016**, *36*, 1995.
[196] J. P. Gross, J. Malzbender, E. Dashjav, F. Tietz, R. Schwaiger, *J Mater Sci* **2022**, *57*, 925.
[197] T. Hupfer, E. C. Bucharsky, K. G. Schell, M. J. Hoffmann, *Solid State Ionics* **2017**, *302*, 49.
[198] P. Goj, B. Handke, P. Stoch, *Sci Rep* **2022**, *12*, 17495.
[199] E. Kartini, V. Yapriadi, H. Jodi, M. Manawan, C. Panghegar, Wahyudianingsih, *Progress in Natural Science: Materials International* **2020**, *30*, 168.
[200] B. H. Toby, *Powder Diffraction* **2006**, *21*, 67.
[201] V. I. Pet'kov, E. A. Asabina, I. A. Shchelokov, *Inorg Mater* **2013**, *49*, 502.
[202] M. Pérez-Estébanez, J. Isasi-Marín, D. M. Többens, A. Rivera-Calzada, C. León, *Solid State Ionics* **2014**, *266*, 1.
[203] M. Bertrand, S. Rousselot, D. Aymé-Perrot, M. Dollé, *Mater. Adv.* **2021**, *2*, 2989.
[204] J. Alamo, *Solid State Ionics* **1993**, *63–65*, 547.
[205] D. K. Agrawal, C.-Y. Huang, H. A. McKinstry, *Int J Thermophys* **1991**, *12*, 697.
[206] D. T. Qui, J. J. Capponi, M. Gondrand, M. Saïb, J. C. Joubert, R. D. Shannon, *Solid State Ionics* **1981**, *3–4*, 219.
[207] J. Kang, R. Gu, X. Guo, J. Li, H. Sun, L. Zhang, R. Jing, L. Jin, X. Wei, *Ceramics International* **2022**, *48*, 157.
[208] E. Dashjav, Q. Ma, Q. Xu, C.-L. Tsai, M. Giarola, G. Mariotto, F. Tietz, *Solid State Ionics* **2018**, *321*, 83.
[209] C. M. Burba, R. Frech, *Solid State Ionics* **2006**, *177*, 1489.
[210] W. Ślubowska, K. Kwatek, C. Jastrzębski, J. L. Nowiński, *Solid State Ionics* **2019**, *335*, 129.
[211] Y. Luo, X. Jiang, Y. Yu, L. Liu, X. Lin, Z. Wang, L. Han, Z. Luo, A. Lu, *Solid State Ionics* **2023**, *390*, 116111.
[212] F. D. Hardcastle, *Arkansas Academy of Science* **2011**, *65*, DOI 10.54119/jaas.2011.6504.
[213] Y. L. Du, Y. Deng, M. S. Zhang, *Journal of Physics and Chemistry of Solids* **2006**, *67*, 2405.
[214] T. Pichonat, C. Lethien, N. Tiercelin, S. Godey, E. Pichonat, P. Roussel, M. Colmont, P. A. Rolland, *Materials Chemistry and Physics* **2010**, *123*, 231.

[215] Y. Zeng, N. J. Szymanski, T. He, K. Jun, L. C. Gallington, H. Huo, C. J. Bartel, B. Ouyang, G. Ceder, *Science Advances* **2024**, *10*, eadj5431.
[216] K. Kwatek, W. Ślubowska, C. Ruiz, I. Sobrados, J. Sanz, J. E. Garbarczyk, J. L. Nowiński, *Journal of Alloys and Compounds* **2020**, *838*, 155623.
[217] K. Arbi, M. Hoelzel, A. Kuhn, F. García-Alvarado, J. Sanz, *Inorg. Chem.* **2013**, *52*, 9290.
[218] K. Arbi, S. Mandal, J. M. Rojo, J. Sanz, *Chem. Mater.* **2002**, *14*, 1091.
[219] C. Vinod Chandran, S. Pristat, E. Witt, F. Tietz, P. Heitjans, *J. Phys. Chem. C* **2016**, *120*, 8436.
[220] G. Courbaron, R. B. Nuernberg, J. S. Sevillano, U.-C. Chung, M. Duttine, C. Labrugère-Sarroste, J. Olchowka, D. Carlier, N. Delpuech, L. Croguennec, *Journal of Alloys and Compounds* **2024**, *985*, 174062.
[221] W. Ślubowska, L. Montagne, O. Lafon, F. Méar, K. Kwatek, *Nanomaterials* **2021**, *11*, 390.
[222] G. Kresse, J. Hafner, *Phys. Rev. B* **1994**, *49*, 14251.
[223] P. Giannozzi, S. Baroni, N. Bonini, M. Calandra, R. Car, C. Cavazzoni, D. Ceresoli, G. L. Chiarotti, M. Cococcioni, I. Dabo, A. Dal Corso, S. de Gironcoli, S. Fabris, G. Fratesi, R. Gebauer, U. Gerstmann, C. Gougoussis, A. Kokalj, M. Lazzeri, L. Martin-Samos, N. Marzari, F. Mauri, R. Mazzarello, S. Paolini, A. Pasquarello, L. Paulatto, C. Sbraccia, S. Scandolo, G. Sclauzero, A. P. Seitsonen, A. Smogunov, P. Umari, R. M. Wentzcovitch, *J Phys Condens Matter* **2009**, *21*, 395502.
[224] J. P. Perdew, K. Burke, M. Ernzerhof, *Phys. Rev. Lett.* **1996**, *77*, 3865.
[225] N. Troullier, J. L. Martins, *Phys. Rev. B* **1991**, *43*, 1993.
[226] L. Kleinman, D. M. Bylander, *Phys. Rev. Lett.* **1982**, *48*, 1425.
[227] C. J. Pickard, F. Mauri, *Phys. Rev. B* **2001**, *63*, 245101.
[228] A. Robertson, J. G. Fletcher, J. M. S. Skakle, A. R. West, *Journal of Solid State Chemistry* **1994**, *109*, 53.
[229] S. Miyoshi, Y. Nishihara, K. Takada, *ACS Appl. Energy Mater.* **2022**, *5*, 7515.
[230] K. Waetzig, A. Rost, C. Heubner, M. Coeler, K. Nikolowski, M. Wolter, J. Schilm, *Journal of Alloys and Compounds* **2020**, *818*, 153237.
[231] D. Campanella, S. Krachkovskiy, C. Faure, W. Zhu, Z. Feng, S. Savoie, G. Girard, H. Demers, A. Vijh, C. George, M. Armand, D. Belanger, A. Paolella, *ChemElectroChem* **2022**, *9*, e202200984.
[232] S. Yu, A. Mertens, X. Gao, D. C. Gunduz, R. Schierholz, S. Benning, F. Hausen, J. Mertens, H. Kungl, H. Tempel, R.-A. Eichel, *Funct. Mater. Lett.* **2016**, *09*, 1650066.
[233] L. Huang, Z. Wen, M. Wu, X. Wu, Y. Liu, X. Wang, *Journal of Power Sources* **2011**, *196*, 6943.
[234] M. N. Rahaman, *Ceramic Processing and Sintering*, CRC Press, Boca Raton, **2017**.
[235] E. C. Bucharsky, K. G. Schell, A. Hintennach, M. J. Hoffmann, *Solid State Ionics* **2015**, *274*, 77.
[236] K. G. Schell, E. C. Bucharsky, F. Lemke, M. J. Hoffmann, *Ionics* **2017**, *23*, 821.
[237] L. D. Prayogi, M. Faisal, E. Kartini, W. Honggowiranto, Supardi, *AIP Conference Proceedings* **2016**, *1710*, 030047.
[238] H. El-Shinawi, E. J. Cussen, S. A. Cussen, *Dalton Trans.* **2024**, *53*, 4139.
[239] M. M. Markowitz, R. F. Harris, W. N. Hawley, *Journal of Inorganic and Nuclear Chemistry* **1961**, *22*, 293.
[240] I. Auramou, R. Pascova, B. Samouneua, I. Gutzow, *Physics and Chemistry of Glasses* **1979**, *20*, 91.
[241] A. A. Raskovalov, O. L. Andreev, V. B. Malkov, *Journal of Non-Crystalline Solids* **2011**, *357*, 3153.

[242] P. Goj, B. Handke, P. Stoch, *Sci Rep* **2022**, *12*, 17495.
[243] Y. Le Godec, S. Le Floch, *Materials* **2023**, *16*, 997.
[244] Z. A. Munir, U. Anselmi-Tamburini, M. Ohyanagi, *J Mater Sci* **2006**, *41*, 763.
[245] C. Estournes, *Techniques de l'Ingénieur* **2006**.
[246] N. Chawake, L. D. Pinto, A. K. Srivastav, K. Akkiraju, B. S. Murty, R. S. Kottada, *Scripta Materialia* **2014**, *93*, 52.
[247] D. M. Hulbert, A. Anders, J. Andersson, E. J. Lavernia, A. K. Mukherjee, *Scripta Materialia* **2009**, *60*, 835.
[248] X. Xu, Z. Wen, X. Yang, L. Chen, *Materials Research Bulletin* **2008**, *43*, 2334.
[249] T. Tezuka, Y. Inagaki, S. Kodama, H. Takeda, I. Yanase, *Powder Technology* **2023**, *429*, 118870.
[250] M. M. Markowitz, R. F. Harris, W. N. Hawley, *Journal of Inorganic and Nuclear Chemistry* **1961**, *22*, 293.
[251] T. Famprikis, P. Canepa, J. A. Dawson, M. S. Islam, C. Masquelier, *Nat. Mater.* **2019**, *18*, 1278.
[252] L. Li, Z. Zhang, L. Luo, R. You, J. Jiao, W. Huang, J. Wang, C. Li, X. Han, S. Chen, *Ionics* **2020**, *26*, 3815.
[253] B. Yari, Production of LiPO3 From LiH2PO4 in a Ball-Mill Rotary-Kiln (BaMRoK) Reactor, phd, Polytechnique Montréal, **2019**.
[254] E. Kartini, V. Yapriadi, H. Jodi, M. Manawan, C. Panghegar, Wahyudianingsih, *Progress in Natural Science: Materials International* **2020**, *30*, 168.

Abstract

All-solid-state batteries are considered as a promising candidate technology for the deployment of electric vehicles. This system is composed of a negative electrode (metallic lithium), a solid electrolyte and a composite positive electrode. NaSICON-type materials, such as $Li_{1+x}Al_xTi_{2-x}(PO_4)_3$ (LATP), are considered promising solid electrolytes for all-solid-state batteries due to their good total ionic conductivity of 10^{-4} S/cm at room temperature and their stability at high potentials (4.1 V vs Li/Li^+). However, a critical issue concerns the processability of LATP as it requires densification through heat treatment above 900 °C, which leads to chemical reactivity and degradation of the composite positive electrode. The aim of this thesis is to explore strategies to lower the densification temperature of this solid electrolyte. To this end, two approaches were investigated: modifying LATP particle size and microstructure; and using Li-salts as sintering aids. In the first approach, we successfully synthesised LATP with different size distributions and morphologies and demonstrated that smaller particles enhance densification. In the second phase of this study, the systematic chemical reactivity observed between lithium salts and LATP was investigated through various characterisation methods (e.g thermodiffraction, Raman spectroscopy, Solid-state NMR, and TGA-DSC-MS). These results enabled us to propose a unified reactivity mechanism for multiple lithium salts demonstrating that the observed improvement in densification is due to the formation of side reaction products resulting from the decomposition of LATP. Based on this new understanding, the use of salt mixtures that do not react with LATP was proposed to enable liquid phase sintering at lower temperature. By combining the salts mixture with Spark Plasma Sintering, the densification temperature was successfully decreased to 650 °C, achieving a relative density of 94 % and a total conductivity in a range of 10^{-4} S/cm at room temperature. These promising results demonstrate the potential to densify LATP at relatively low temperature, making it compatible for use in the composite positive electrode of all-solid-state batteries.

Résumé

Les batteries tout-solide sont considérées comme une technologie prometteuse pour le déploiement des véhicules électriques. Ce système est composé d'une électrode négative (lithium métallique), d'un électrolyte solide et d'une électrode positive composite. Les matériaux de type NaSICON, tels que le $Li_{1+x}Al_xTi_{2-x}(PO_4)_3$ (LATP), sont considérés comme des électrolytes solides prometteurs pour les batteries tout-solide en raison de leur bonne conductivité ionique totale de 10^{-4} S/cm à température ambiante et de leur stabilité à hautes tensions (4,1 V par rapport à Li/Li^+). Cependant, un problème critique concerne la fabricabilité du LATP, car il nécessite une densification par traitement thermique au-dessus de 900 °C, ce qui conduit à une réactivité chimique et à une dégradation de l'électrode positive composite. L'objectif de cette thèse est d'explorer des stratégies pour diminuer la température de densification de cet électrolyte solide. À cette fin, deux approches ont été étudiées : la modification de la taille des particules et de la microstructure du LATP ; et l'utilisation de sels de lithium comme agents de frittage. Dans la première approche, nous avons réussi à synthétiser du LATP avec différentes distributions de taille et morphologies, et démontré que des particules plus petites améliorent la densification. Dans la seconde phase de cette étude, la réactivité chimique systématique observée entre les sels de lithium et le LATP a été examinée à l'aide de diverses méthodes de caractérisation (par exemple, thermodiffraction, spectroscopie Raman, RMN à l'état solide, et TGA-DSC-MS). Ces résultats nous ont permis de proposer un mécanisme de réactivité unifié pour plusieurs sels de lithium, démontrant que l'amélioration observée de la densification est due à la formation de produits de réactions secondaires résultant de la décomposition du LATP. Sur la base de cette nouvelle compréhension, l'utilisation de mélanges de sels ne réagissant pas avec le LATP a été proposée pour permettre le frittage en phase liquide à une température plus basse. En combinant ce mélange de sels avec le Spark Plasma Sintering, la température de densification a été réduite avec succès à 650 °C, atteignant une densité relative de 94 % et une conductivité totale de l'ordre de 10^{-4} S/cm à température ambiante. Ces résultats prometteurs démontrent le potentiel de densification du LATP à une température relativement basse, le rendant compatible pour une utilisation dans l'électrode positive composite des batteries tout-solide.